Electronic correlations in multiorbital systems

by

José María Pizarro Blanco

Submitted to the Department of Condensed Matter Physics
in partial fulfillment of the requirements
for the degree of

Doctor of Philosophy in Physics

at the

UNIVERSIDAD AUTÓNOMA DE MADRID

PhD Supervisor: Dr. Elena Bascones Fernández de Velasco
Instituto de Ciencia de Materiales de Madrid
Consejo Superior de Investigaciones Científicas

Madrid, Mar 2019

Acknowledgements

Para comenzar, me gustaría agradecer a mi directora, Leni Bascones, por la oportunidad de realizar esta tesis junto a ella. Gracias por haber tenido tanta paciencia y haberme enseñado tanto en estos años. Gracias también por haberme dado la oportunidad de viajar e intercambiar conocimientos con otros compañeros de profesión en diferentes conferencias y escuelas. Y gracias también por haberte preocupado por mi presente y futuro y para que pudiese salir adelante. Aprovecho y también te doy las gracias junto a Maria José Calderón y Belen Valenzuela por haberme permitido ayudar a fomentar la Ciencia y la Física de Materiales en diferentes eventos de divulgación.

También quiero agradecer a mi familia el apoyo durante estos años. A mis hermanos (y sobrinos), a mis tíos (en especial a mi tía Marisa) y demás por preocuparse por mí. Gracias a mi padre por todo el apoyo que me ha brindado durante años y por la confianza en que lograría ser un buen científico. Gracias también a Enrique y Mila.

Gracias a los compañeros y compañeras que me han ido acompañando en mi carrera científica. Gracias a Fer, Teje, a otro Fer, Carol, Gloria, Nadia, Miguel Ángel, Carlos, Jordi. Gracias también a los compañeros del ICMM por haber hecho este camino más ameno: Mónica, Fernando, Sigmund, Bea, Álvaro, José Carlos, Jorge, Guillem, Jesús y Jordi (otra vez).

I would also like to thank all of the co-workers from Frankfurt: Ying, Sananda, Emanuelle, Hendrik, Karim, Fabian, Vladislav, Steve, Kira, Anand, Thomas. Y por supuesto, gracias a Roser Valentí por acogerme en su grupo y permitirme aprender tantas cosas.

Por último, quiero dar las gracias a Laura por haber estado ahí durante todos estos años. Muchas gracias por haber estado ahí todos estos días y por haberme escuchado y animado. Y gracias por haberme ayudado en la escritura y revisión de esta tesis. Sin tí, esta tesis no habría salido adelante.

Para Laura

Electronic correlations in multiorbital systems

by

José María Pizarro Blanco

Abstract

The role of electronic correlations in Condensed Matter is at the heart of various important systems, like magnetic materials, superconductors, topological materials, optical lattices, etc. Electronic correlations are those which change the motion of individual electrons when considering the interaction with other electrons in the material. Among the available systems to study electronic correlation effects, in this thesis I focus on unconventional superconductors, specifically in high-T_c iron-based superconductors, and on two-dimensional materials, like the recent magic-angle twisted bilayer graphene or the itinerant ferromagnet Fe_3GeTe_2.

In the first chapter, I will briefly review the band theory and Fermi liquid theory for solid systems. In certain situations, the long-range character of the Coulomb interaction can be safely ignored, and short-range Coulomb interaction will result in various interesting behaviors, such as the Mott insulator and the Hund metal, which can change the expectations from band theory. I will constraint to onsite (local) correlations, i.e. those between electrons sitting in the same lattice site. I will also briefly review some of the most important properties of unconventional superconductors and two-dimensional materials.

In the second chapter, I will review the effects of local correlations in multiorbital systems. I will compare with experimental results for high-T_c iron-based superconductors with the expectations given by local correlations, arguing that the iron superconductors are in the Hund metal regime, in which the Hund's coupling plays a major role.

Last chapters are dedicated to the work done during this thesis. I studied the effects of local correlations in various high-T_c iron superconductors, as well as in the magic-angle twisted bilayer graphene. A brief chapter about my ongoing work in Fe_3GeTe_2 is presented at the end of the thesis. Through this thesis, I used the Slave-Spin Mean-Field technique to address the local correlations behavior in these multiorbital systems.

In the third chapter, we proposed to search a new family of high-T_c superconductors in the chromium analogues of iron-based superconductors. We argue that, due to the similar strength of electronic correlations, plus a superconducting instability driven by magnetic fluctuations, chromium-based pnictides and chalcogenides could host unconventional superconductivity. This argument is based on the fact that iron-based superconductors can be viewed as electron-doped Mott insulators, where the strength of correlations increases when doping these iron superconductors with holes, and decreases when doping them with electrons. In this picture, chromium pnictides and chalcogenides will be the hole-doped Mott insulator, and we found a similar trend: electronic correlations increase when doping the cromium-based systems with electrons (and decrease when doping with holes).

In the fourth chapter, I studied the strength of local correlations in the quasi-1D two-leg ladder iron-based superconductor $BaFe_2S_3$ for two different pressures. Contrary to other iron-based superconductors, $BaFe_2S_3$ (and related materials) is an insulator. Other authors

have pointed out that these quasi-1D systems are Mott insulators. In this chapter, I calculated the strength of local correlations to check the behavior of these systems at $T = 0\,K$. I found a metallic behavior instead, so that we concluded by stating that the insulating behavior could be driven by finite temperature effects. I found a substantial Fermi surface reconstruction due to local correlations, contrary to what happen in other iron-based superconductors.

In the fifth chapter, I studied the nature of the insulating states in magic-angle twisted bilayer graphene. I implemented the Zeeman effect in the Slave-Spin Mean-Field formalism to address the behavior of the insulating states when varying an onsite magnetic field in the local correlations picture. I found that the behavior is opposite to the experimental evidences. We argued that local correlations by themselves cannot explain the insulating states in magic-angle twisted bilayer graphene. We reviewed the last works done in non-local correlations in other lattices, concluding that the insulating states in magic-angle twisted bilayer graphene could be explained by using the non-local correlations picture.

In the sixth chapter, I obtained the band structure and tight-binding model of the 2D itinerant ferromagnet Fe_3GeTe_2. This is a brief chapter about the current status on my work in this system.

A final chapter is devoted to the conclusions and a final overview that can be extracted from this thesis. Various appendices indicate the details of the techniques used during this thesis, as well as some interesting mathematical proofs.

Keywords: Unconventional superconductivity, strongly correlated electron systems, Mott insulator, multiorbital systems, Hund metal, metal-to-insulator transition, many-body techniques, Slave-Spin Mean Field formalism, local correlations, magic-angle twisted bilayer graphene.

Correlaciones electrónicas en sistemas multi-orbitales

por

José María Pizarro Blanco

Resumen

Las correlaciones electrónicas en Física de la Materia Condensada juegan un papel fundamental en varios sistemas importantes, como son los materiales magnéticos, los superconductores, los materiales topológicos, las redes ópticas, etc. Las correlaciones electrónicas son aquellas que modifican el movimiento de electrones individuales cuando se considera su interacción con otros electrones dentro del material. Dentro de los sistemas disponibles para estudiar los efectos de las correlaciones electrónicas, en esta tesis voy a centrarme en los superconductores no convencionales, específicamente en los superconductores de alta T_c basados en hierro, y en sistemas bidimensionales, como el recientemente descubierto grafeno bicapa rotado en ángulo mágico o el ferromagneto itinerante Fe_3GeTe_2.

En el primer capítulo, resumiré brevemente la teoría de bandas y la teoría del líquido de Fermi para sistemas sólidos. En ciertas situaciones, el cáracter de largo alcance de la interacción de Coulomb puede ignorarse, y la interacción de Coulomb de corto alcance resulta en varios comportamientos interesantes, tales como el aislante de Mott y el metal de Hund, los cuales cambian las expectativas dadas por la teoría de bandas. Me centraré en las correlaciones en el mismo sitio (locales), es decir, aquellas entre electrones que están localizados en el mismo sitio de la red. También resumiré brevemente algunos de las propiedades más importantes de los superconductores no convencionales y de los materiales bidimensionales.

En el segundo capítulo, repasaré los efectos de las correlaciones locales en sistemas multi-orbitales. Compararé los resultados experimentales para los superconductores de alta T_c basados en hierro con las expectativas dadas por las correlaciones locales, y argumentaré que los superconductores de hierro están en el régimen del metal de Hund, en el cual el acoplo Hund juega un papel esencial.

Los últimos capítulos están dedicados a los trabajos realizados durante esta tesis. Estudié los efectos de las correlaciones locales en varios superconductores de alta T_c de hierro, así como en el grafeno bicapa rotado en ángulo mágico. Al final de la tesis hay un capítulo dedicado a mi trabajo actual en el Fe_3GeTe_2. A lo largo de la tesis, he usado la técnica de Espines Esclavos en Campo Medio para estudiar el comportamiento de las correlaciones locales en estos sistemas multi-orbitales.

En el tercer capítulo, propusimos buscar una nueva familia de superconductores de alta T_c en sistemas de cromo, análogos a los superconductores basados en hierro. Argumentamos que debido a que las correlaciones electrónicas tienen una magnitud similar, y asumiendo que la inestabilidad superconductora es debida a fluctuaciones magnéticas, los pnicturos y calcogenuros basados en cromo podrían dar lugar a una fase superconductora no convencional. Este argumento está fundamentado en el hecho de que los superconductores basados en hierro pueden verse como aislantes de Mott dopados con electrones en donde el valor de las correlaciones electrónicas aumentan cuando se dopan estos superconductores de hierro con huecos, mientras que disminuyen cuando se dopan con electrones. De acuerdo a esta idea, los

pnicturos y calcogenuros de cromo se comportan como aislantes de Mott dopados con huecos, y encontramos unas tendencias similares: las correlaciones electrónicas aumentan cuando se dopan los sistemas basados en cromo con electrones (y disminuyen cuando se dopan con huecos).

En el capítulo cuarto, estudié el valor de las correlaciones electrónicas en el superconductor basado en hierro quasi-1D en escalera de dos patas $BaFe_2S_3$ para dos presiones distintas. Al contrario que en otros superconductores basados en hierro, $BaFe_2S_3$ (y otros materiales relacionados) es un aislante. Otros autores señalaron que estos sistemas quasi-1D son aislantes de Mott. En este capítulo, calculé el valor de las correlaciones electrónicas para estudiar el comportamiento de estos sistemas a $T = 0\,K$. Encontré un comportamiento metálico en vez de aislante, por lo que concluimos que el comportamiento aislante en este sistema podría ser debido a los efectos de incluir una temperatura finita. Encontré una reconstrucción substancial de la superficie de Fermi debida a las correlaciones electrónicas, diferente a lo que sucede en otros superconductores basados en hierro.

En el quinto capítulo, estudié la naturaleza de los estados aislantes en el grafeno bicapa rotado en ángulo mágico. Implementé el efecto Zeeman en el formalismo de Espines Esclavos en Campo Medio para estudiar el comportamiento de estos estados aislantes cuando un campo magnético en el mismo sitio varía, considerando solo las correlaciones locales. Encontré que el comportamiento es el opuesto al obtenido experimentalmente. Argumentamos que las correlaciones locales por sí solas no pueden explicar los estados aislantes en el grafeno bicapa rotado en ángulo mágico. Examinamos los últimos trabajos hechos en otras redes para las correlaciones no locales, y concluimos que los estados aislantes en el grafeno bicapa rotado en ángulo mágico podrían explicarse teniendo en cuenta las correlaciones no locales.

En el capítulo sexto, obtuve la estructura de bandas y el modelo de enlaces fuertes del ferromagneto itinerante 2D Fe_3GeTe_2. Éste es un capítulo breve sobre el estado actual de mi trabajo en dicho material.

El capítulo final está dedicado a las conclusiones y un resumen final de las ideas que pueden extraerse de esta tesis. Varios apéndices indican los detalles de las técnicas usadas durante esta tesis, así como algunas demostraciones matemáticas interesantes.

Palabras clave: Superconductividad no convencional, sistemas de electrones fuertemente correlacionados, aislante de Mott, metal de Hund, transición metal-aislante, técnicas de muchos cuerpos, formalismo de espines esclavos en campo medio, correlaciones locales, grafeno bicapa rotado en ángulo mágico.

Contents

List of Figures

Abbreviations

BZ	**B**rillouin **Z**one
FT	**F**ourier **T**ransformation
DOS	**D**ensity **O**f **S**tates
DFT	**D**ensity **F**unctional **T**heory
LDA	**L**ocal **D**ensity **A**pproximation
GGA	**G**eneralized **G**radient **A**pproximation
FLT	**F**ermi-**L**iquid **T**heory
SCES	**S**trongly **C**orrelated **E**lectron **S**ystems
FeSCs	Iron-based superconductors
PM	**P**ara**m**agnetism
AFM	**A**ntiferro**m**agnetism
FM	**F**erro**m**agnetism
NM	**N**on-**M**agnetic
DMFT	**D**ynamical **M**ean-**F**ield **T**heory
SSMF	**S**lave-**S**pin **M**ean-**F**ield
CDMFT	**C**luster **D**ynamical **M**ean-**F**ield **T**heory
GA	**G**utzwiller **A**pproximation
RPA	**R**andom **P**hase **A**pproximation
cRPA	**c**onstrained **R**andom **P**hase **A**pproximation
OSMP	**O**rbital **S**elective **M**ott **P**hase
OSMT	**O**rbital **S**elective **M**ott **T**ransition
PES	**P**hoto**E**mission **S**pectroscopy
ARPES	**A**ngle-**R**esolved **P**hoto**E**mission **S**pectroscopy

QOs	**Q**uantum **O**scillations
MA-TBG	**M**agic-**A**ngle **T**wisted **B**ilayer **G**raphene
TBG	**T**wisted **B**ilayer **G**raphene
TTG	**T**wisted **T**rilayer **G**raphene
QCP	**Q**uantum **C**ritical **P**oint
hBN	**h**exagonal **B**oron **N**itride
TMDC	**T**ransition **M**etal **Dic**halcogenides
TMMC	**T**ransition **M**etal **Mono**chalcogenides
TMTC	**T**ransition **M**etal **Tri**chalcogenides
vdW	**v**an-**d**er-**W**aals
BCS	**B**ardeen-**C**ooper-**S**chrieffer
MLWF	**M**aximally-**L**ocalized **W**annier **F**unctions
VASP	**V**ienna **a**b-initio **S**imulation **P**ackage
PBE	**P**erdew-**B**urke-**E**rnzerhof
fRG	**f**unctional **R**enormalization **G**roup
APW	**A**ugmented **P**lane **W**aves
LAPW	**L**inearized **A**ugmented **P**lane **W**aves

Chapter 1

Introduction

1.1 Motivation of this thesis

A solid material is a system formed by an infinite arrange of atoms ordered in a specific pattern, called the lattice [1]. The material can be obtained by infinitely reproducing the unit cell in the real space, which is the most basic unit arrangement of atoms that describes the system. Each material has a different unit cell, with a different symmetry pattern and/or formed by different atoms. In a first approximation, ions (the atomic nucleus plus the core electrons) in the unit cell are siting motionless in their sites (Born-Oppenheimer approximation), and valence electrons will move through the system according to the band theory of solids.

In band theory, the eigenstates and eigenvalues satisfy the Bloch theorem, which states that electrons move in the average periodic potential created by the motionless atoms. The eigenvalues are also called electronic band energies $E_{k\nu\sigma}$, and they are defined in the k-space in the so called first Brillouin zone (BZ), which is the Fourier transformed (FT) unit cell, ν is the band index and σ is the spin index. At the practical level, the electronic band energies (or equivalently the band structure) are obtained by Density Functional Theory (DFT) calculations, explained more in detail later on and in **Appendix A**. In this framework, the electronic band structure can be extracted from the hybridization of atomic-like orbitals s, p, d, f,..., which come from each atom of the unit cell. The number of bands will be determined by the number of atoms in the unit cell N_{uc}, the number of orbitals N of each atom (where the total number of orbitals per unit cell can be alternatively defined as $N_{orb} = N_{uc}N$) and the spin degree of freedom for a given system. In DFT calculations, some effects coming from the electron-electron repulsion are included in the average periodic potential in which electrons move.

The number of (valence) electrons per unit cell is given by the total number of valence electrons coming from each atom in the unit cell. Thus, the band energies are filled bottom-up until all the electrons are distributed (following the Pauli exclusion principle) in the band structure. At $T = 0\,K$, the last filled band energy is defined as the Fermi energy ε_F. The Fermi energy is defined as the chemical potential at zero temperature, $\varepsilon_F = \mu(T = 0\,K)$, where the chemical potential is the change in energy when a new particle is added to the system. At finite and low temperature T, electrons distribute in the band energies following the Fermi-Dirac distribution function.

A major success of band theory is the ability to predict a metallic or insulating behavior for a given material. Then, if ε_F crosses the bands, the system is a metal (FIGURE 1.1**(a)**), while if there is an energy gap between ε_F and the next available energy, the system is an insulator (FIGURE 1.1**(c)**). Then, for an odd number of electrons per unit cell, the system will be always behave as a metal, whether if it has an even number of electrons per unit cell, band theory predicts that the system can behave as a metal or an insulator.

When ε_F crosses the bands, the closed surfaces in the first BZ with band energies $E_{k\nu\sigma} = \varepsilon_F$ are defined as the Fermi surface. The notation hole- or electron-pocket is used to denominate the closed surfaces which have positive or negative curvature for $E_{k\nu\sigma}$ close to ε_F, respectively, see FIGURE 1.1**(b)**. For a given band E_k, the electron effective mass m_0 can be defined as $m_0 = |\nabla_k^2 E_k/\hbar|^{-1}$. This parameter states the variation of the electron mass when the electron is moving in the periodic potential of a solid.

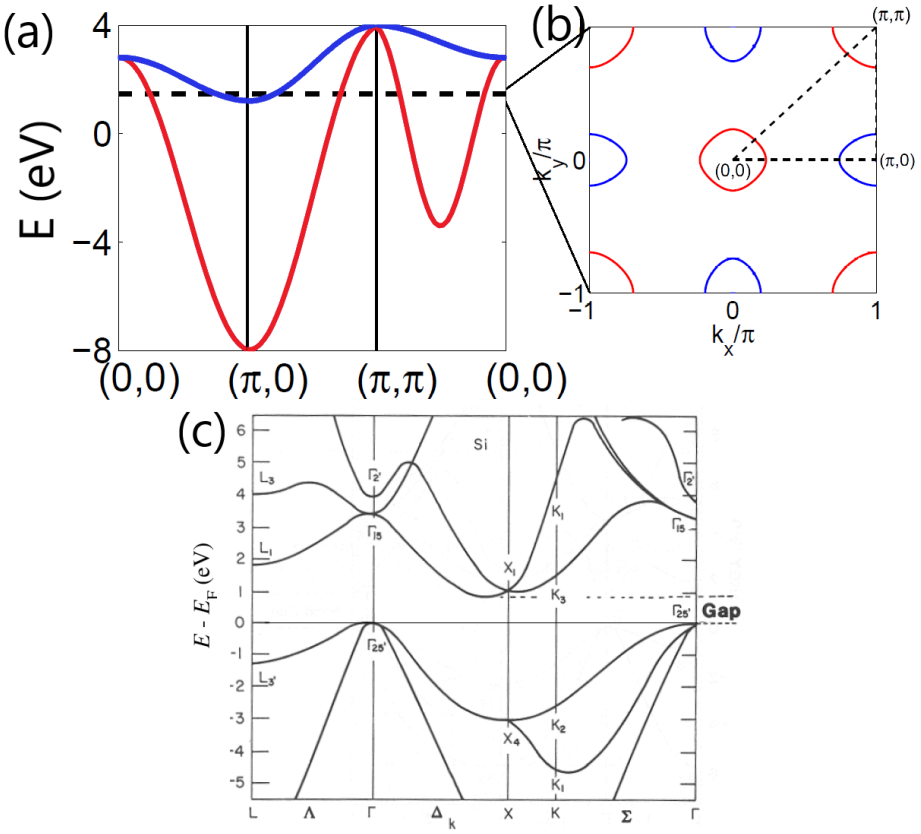

FIGURE 1.1: **(a)** Band structure (dashed black line marks ε_F) and **(b)** Fermi surface for a model proposed for metallic $LaFeAsO$ in the unfolded BZ (see **Section 1.5.2**). The Fermi surface is formed by various hole- (red lines) and electron-pockets (blue lines). Dashed black line in the Fermi surface marks the $\vec{k}$-path followed to obtain the band structure. Taken and adapted from [2]. **(c)** Band structure calculation for semiconducting silicon (ε_F fixed at $0\,eV$). A (indirect) gap opens at ε_F, where $gap \sim 1\,eV$. Taken and adapted from [3].

In band theory, when a new particle (hole or electron) is added to the system, ε_F shift downwards or upwards and the Fermi surface changes. This shift is said to be a rigid-band shift, i.e. the band structure remains unchanged while ε_F moves. The parent compound of a material is defined as the system with no external particles added and no external perturbations, such as pressure, magnetic or electric fields.

A priori, the Fermi level shift when new particles are added into the system should not be rigid, due to the fact that the new particle will interact with the other electrons in the material, and hence the band structure should change. Nevertheless, band theory and rigid-band shift work on the basis of the Fermi liquid theory (FLT) for solids [4, 5], see **Section 1.2.2**. FLT justifies the success of band predictions in most of the materials. In this framework, the excitations (i.e. when a new particle is added to the system) are described as single-particle states in the low T and low energy regime. These excitations have a finite lifetime, which in the FLT at low T will be large enough close to the Fermi level to legitimate the single-particle description. In FLT, the low temperature-dependent electronic properties, such as the resistivity $\rho(T)$, the specific heat $C(T)$ or the susceptibility $\chi(T)$, can be obtained and compared with experimental results.

However, there are some situations in which FLT, and hence the band theory can fail. In these cases, the experimentally observed band structure and electronic properties deviate from the DFT calculations. For example, the observed band structure of some metals is much narrower than calculated using DFT [6], or an expected metallic material behaves as an insulator [7]. These behaviors result from the effects of the electronic correlations. Including these electronic correlations will describe how electrons change their motion through the material when they interact with other electrons. Then, further models and approximations beyond DFT are needed to describe such new systems, usually called strongly correlated electron systems (SCES) [4, 5, 8]. This is the case for the previously commented situations, when the band structure narrows in a metal or when an expected metal behaves as an insulator, the so called Mott insulator [7].

Among the systems which show increased electronic correlation effects, in this thesis I will focus on high-T_c iron-based superconductors (FeSCs) [5, 9] and 2D materials [10, 11], specifically in magic-angle twisted bilayer graphene (MA-TBG) and Fe_3GeTe_2 (FGT). I will specifically focus on studying such systems when considering the interaction between electrons in the same lattice site, in the so called local approximation (see next section). A major question that I would like to answer through this thesis is: *what is the strength of these electronic correlations and how does it relate with the experimental properties observed?*. This question is crucial in order to understand the origin of various phases, like magnetism, superconductivity, etc, that appear in such systems

The strength of electronic correlations can be modeled by a parameter called the quasiparticle weight Z. Alternatively, in the local approximation, the effective mass renormalization, or mass enhancement can be defined as $m^*/m_0 = 1/Z$, where m_0 is the non-correlated electron mass obtained from DFT [4, 5]. The quasiparticle weight is a well defined quantity (for a metal) in the FLT and ranges from $0 < Z < 1$. For $0.7 < Z \leq 1$, the general expectations from band theory are recovered, and the system is said to be weakly correlated. For $Z < 1$, the system start to become more and more correlated, progresively entering in the regime which is known as the correlated metal. When the system becomes the special insulator, called the Mott insulator, $Z = 0$. In this situation, FLT breaks down and further approximations are needed to describe the physics of the system. Due to the relation between Z and m^* found in the local approximation, Z can be identified as a renormalization pre-factor of the band structure $\sim ZE_k$, hence when electronic correlations increase, the bands become narrower. We will later see that this effect translates into a non-rigid shift when the chemical potential varies because Z depends on the electronic filling.

The mass renormalization $m^*/m_0 = 1/Z$ gives a physical explanation of what is occurring in the system: at $m^* = m_0$ ($Z = 1$), the electron has an effective mass which is equal to

the non-correlated one; when correlations increase, $m^* > m_0$ ($Z < 1$), the electrons start to become heavier, so their motion is stopped progresively, increasing the resistivity of the material; at $m^* \to \infty$ ($Z = 0$), electrons are infinitively heavy, so they will prefer to stay motionless in the system, and the material becomes an insulator. Note that this description is based on the Brinkman-Rice picture of the Mott transition (see next sections).

The metal-to-insulator transition described above, also called the Mott transition, is at the heart of various SCES, such as unconventional superconductors, various two-dimensional (2D) materials, see **Section 1.3**, or for ultra-cold atoms in optical lattices.

1.2 Many-body hamiltonian and the concept of correlation

In this section, I will formally introduce the hamiltonian which describes a solid material, also called a many-body hamiltonian, and the concept of electronic correlations. I will follow a similar derivation as the ones done in [11–13].

The hamiltonian of a solid material, with N_I ions and N_{el} electrons, can be written as:

$$H = \underbrace{-\frac{\hbar}{2M}\sum_{\alpha}^{N_I}\nabla_{\alpha}^2}_{T_I} \underbrace{-\frac{\hbar}{2m}\sum_{i}^{N_{el}}\nabla_{i}^2}_{T_{el}} + \underbrace{\sum_{\alpha\neq\beta}^{N_I}\frac{Z_\alpha Z_\beta e^2}{|\vec{R}_\alpha - \vec{R}_\beta|}}_{V_{I-I}} \underbrace{-\sum_{\alpha}^{N_I}\sum_{i}^{N_{el}}\frac{Z_\alpha e^2}{|\vec{r}_i - \vec{R}_\alpha|}}_{V_{I-el}} + \underbrace{\sum_{i\neq j}^{N_{el}}\frac{e^2}{|\vec{r}_i - \vec{r}_j|}}_{V_{el-el}} \tag{1.1}$$

where atomic units $\varepsilon_0 = 1/4\pi$) have been used. M and m are the free ion and electron masses, $\vec{R}_\alpha$ is the ion α position, $\vec{r}_i$ is the electron i position and Z_α is the atomic number of the α ion. Various kinetic and interaction energy operators have been defined: T_I is the ionic kinetic energy, T_{el} is the electronic kinetic energy, V_{I-I} is the ion-ion interaction, V_{I-el} is the ion-electron interaction and V_{el-el} is the electron-electron interaction.

Due to the massive character of ions when compared with electrons ($M \gg m$), ions move much slowly than electrons, so in a first approximation, ions can be treated as sitting motionless, considering T_I as a perturbation $H = H_{BO} + T_I$ (Born-Oppenheimer approximation), where:

$$H_{BO} = \underbrace{T_{el}}_{\hat{T}} + \underbrace{V_{I-I} + V_{I-el}}_{\hat{V}_{ext}} + \underbrace{V_{el-el}}_{\hat{V}_{ee}} \tag{1.2}$$

The hamiltonian $H_{BO} = \hat{T} + \hat{V}_{ext} + \hat{V}_{ee}$, with $\hat{T}$ being the kinetic energy of the electrons, $\hat{V}_{ext}$ the external potential generated by the ions in which the electrons are moving and $\hat{V}_{ee}$ is the electron-electron interaction. From now on, T_I effects will be neglected.

DFT is the most widely used approximation to solve the many-body hamiltonian Eq. (1.2), see **Appendix A**. DFT allows to calculate the band structure $E_{k\nu\sigma}$ for different materials. Each atom in the unit cell is considered to contribute with its atomic orbitals. The number of bands ν equals the number of orbitals per unit cell and spin $2N_{orb}$. When treating $\hat{T}$, the eigenstates are described as a linear combination of single-particle states, hence the electrons will behave almost independently of each other (they are not electronically correlated). Also,

when treating $\hat{V}_{ee}$, a Hartree-like approximation is made, and hence the exchange effects are almost neglected. Thus, the DFT hamiltonian H_0 can be written as:

$$H_0 = \hat{T}^{noncorr} + \hat{V}_{ext} + \hat{V}_{ee}^{H} + \hat{V}_{XC} \tag{1.3}$$

where $\hat{T}^{noncorr}$ refers to the non-correlated kinetic energy of the electrons, $\hat{V}_{ee}^{H}$ is the electron-electron interaction in the Hartree approximation and $\hat{V}_{XC}$ encodes the electronic correlation and the exchange effects. In the most common DFT approaches, such as local density approximation (LDA) or generalized gradient approximation (GGA), $\hat{V}_{XC}$ is approximated by different functions, see **Appendix A** for a brief discussion, and biggest correlation and exchanges effects are neglected. Thus, we can conclude by considering the most common DFT band structure calculations (LDA or GGA) as the weakly correlated limit, and adding new particles to the system will rigidly shift (i.e. the band structure remains unchanged) the Fermi energy ε_F.

1.2.1 Tight-binding models

The hamiltonian Eq. (1.3) can be translated into a tight-binding model [1, 12]. During this thesis, I will mainly use the second quantization notation. For a tight-binding model in the second quantization notation, H_0 is encoded in the hopping integrals t_{mn}^{ij}. These hopping integrals describe the possible hopping processes for an electron in an orbital n at the lattice site j which hops to an orbital m in a lattice site i. Then, H_0 can be written as:

$$H_0 = \sum_{mn}\sum_{ij}\sum_{\sigma} t_{mn}^{ij} d_{im\sigma}^{\dagger} d_{jn\sigma} \tag{1.4}$$

where $d_{im\sigma}$ ($d_{im\sigma}^{\dagger}$) annihilates (creates) an electron in a lattice site $\vec{i}$, in a orbital m and with spin σ. $\sum_{ij}$ runs for all the neighbors around the considered origin lattice site. t_{mn}^{ij} can be complex numbers and they usually receive names such as nearest or first neighbor, next-nearest or second neighbor, etc., refering to the distance from the origin. Tight-binding models will only include up to a certain number of neighbor hoppings.

The dispersion relations ε_{kmn} are defined by the FT of the hopping terms in Eq. (1.4), as shown in Eq. (1.5), and the band structure $E_{k\nu}$ is obtained by diagonalizing the hamiltonian defined by $H_0 = \sum_{kmn\sigma} \varepsilon_{kmn} d_{km\sigma}^{\dagger} d_{kn\sigma}$. Tight-binding models can be used as simple models to address different physical behaviors, as for example, when considering the 2D square lattice, in a single-orbital system with only nearest neighbors t included:

$$\varepsilon_{kmn} = \sum_{ij} t_{mn}^{ij} e^{-i\vec{k}\cdot\vec{ij}} \;\rightarrow\; \varepsilon_k^{2D\,square} = 2t\,(\cos k_x + \cos k_y) \tag{1.5}$$

Tight-binding models are applied to study real materials. In order to calculate the hopping parameters for a real material, a procedure called Wannier parametrization is used, see **Section A.2**. In this procedure, a set of targeted band energies $E_{k\nu}$ are fitted to a set of hopping integrals t_{mn}^{ij}. The goal of a Wannier parametrization is to be able to reduce the original ν bands problem, to a smaller set of bands which gives enough information to explain the physics in a given material. Usually, bands around the Fermi level and well separated by

a gap from next bands can be targeted to obtain the tight-binding model, see red bands in FIGURE 1.2**(a)**. In some cases, there is not a clear gap between the targeted bands and the next bands (they are said to be entangled), and the procedure will give a less accurate result, see FIGURE 1.2**(b)**. The orbitals for which t^{ij}_{mn} are obtained are called Wannier orbitals, and they are not necessarily the same as the atomic orbitals. The degree of similarities between Wannier and atomic orbitals depend on how entangled the targeted and untargeted bands are. In most of the cases, and through all this thesis, I will focus on Wannier orbitals which have the same symmetry than the atomic orbitals, hence we can distinguish Wannier orbitals like s, p_x, p_y and p_z, d_{zx}, d_{yz}, $d_{x^2-y^2}$, d_{z^2} or d_{xy}, etc, depending on their quantum angular momentum numbers $l = 1, 2, \ldots$ and $m_l = -l, \ldots, +l$

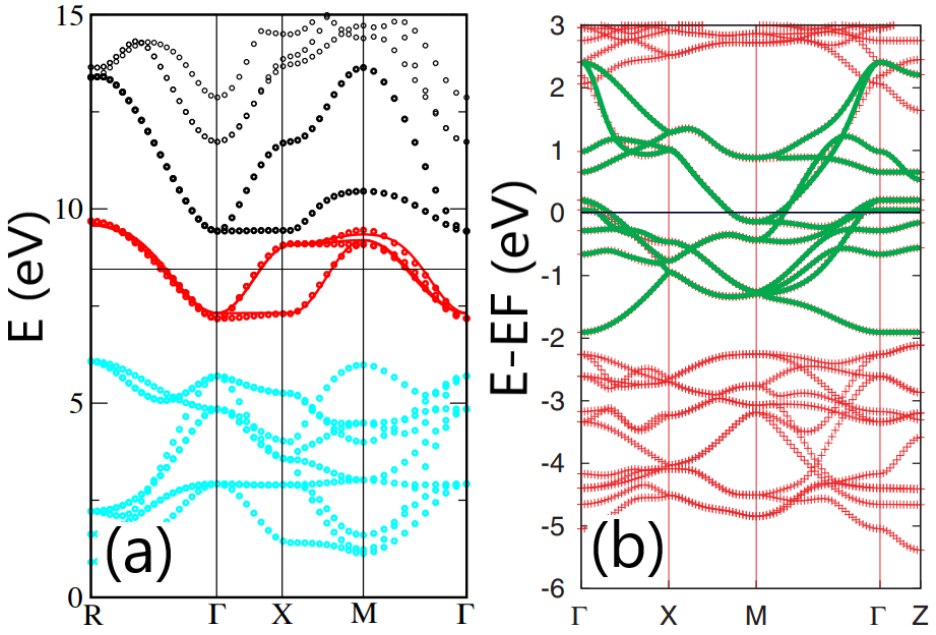

FIGURE 1.2: **(a)** Disentangled bands (red points) and Wannier parametrization fitting (red lines) for $SrVO_3$. The perfect fitting is done in a set of bands which are well separated from other untargeted bands. **(b)** Same for $LaFeAsO$ in the folded BZ, see **Section 1.5.2**, which shows some entanglement between the Fe d bands around the Fermi level and the next bands. The Wannier fitting (green lines) is done in a set of bands which are entangled with other untargeted bands. The fitting shows discrepancies in certain areas (see $E - E_F \sim 2\,eV$), but the Wannier fitting gives good enough results to address the electronic properties at low energies. Taken and adapted from [14].

In principle, the orbitals with the same l and different m_l will be energetically degenerated in each atom. However, due to the environment that surrounds each lattice site in the unit cell, a crystal field splting ϵ_m appears, which is $\epsilon_m = t^{ij=0}_{mm}$. i.e. an onsite energy which breaks the m_l-orbital degeneracy [5, 8]. The crystal field splitting is an electrostatic interaction between the electrons in each site with their surrounding ions. Different crystal structure symmetries will have different crystal fields. As an example in perovskite structures (see FIGURE 1.3), for d orbitals in a cubic symmetry, the crystal field effect breaks the degeneracy between (d_{zx}, d_{yz}, d_{xy}) (also called t_{2g} orbitals) and $(d_{x^2-y^2}, d_{z^2})$ (also called e_g orbitals), while for d-orbitals in a tetragonal symmetry, all the orbitals except (d_{zx}, d_{yz}) are non-degenerated.

The total bandwidth W of a given band structure is the difference between the minimum and maximum band energies (for example, in FIGURE 1.1**(a)**, $W = 12\,eV$). It is related with the hopping integrals t^{ij}_{mn}, so W approximately states the kinetic energy of the electrons in a given material. In a multiorbital system, each orbital will approximately contribute to

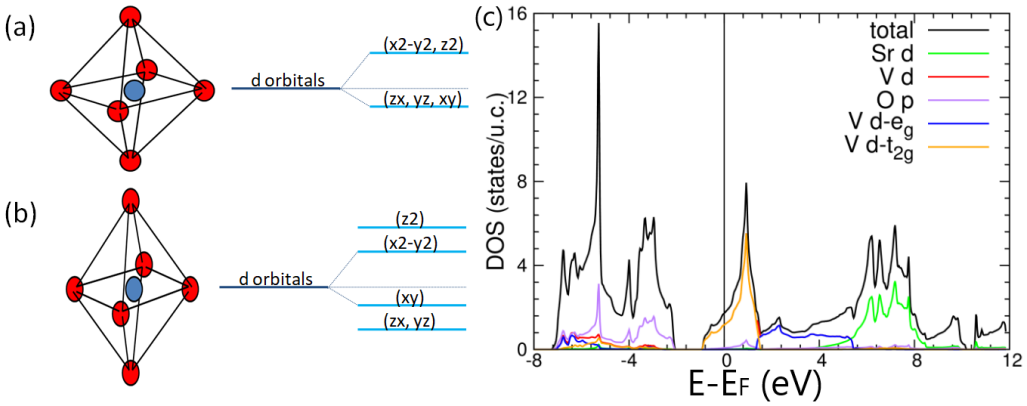

FIGURE 1.3: Crystal field splitting in **(a)** cubic and **(b)** tetragonal symmetries for perovskite crystal structures. The original d orbitals (marked as a dark blue line) become non-degenerated due to environment and the shape of each orbital (marked as light blue lines). Taken and adapted from [5]. **(c)** Total (black lines) and orbital-resolved (colored lines) DOS for $SrVO_3$. d orbitals from V are mostly located from $-1\,eV$ to $5\,eV$. Figure obtained by GGA DFT calculations implemented in the WIEN2K code.

the band structure in a certain energy window. This energy window can be identified as an orbital-resolved bandwidth W_m. These parameters will be useful when talking about the strength of electronic correlations in the next chapters. In FIGURE 1.3**(c)**, I show the total and orbital-resolved density of states (DOS) for the $SrVO_3$, where $W \approx 18\,eV$, and V d orbitals are mainly contributing around the Fermi level, with $W_{V\,d} \approx 6\,eV$, $W_{V\,d\,e_g} \approx 3.5\,eV$ and $W_{V\,d\,t_{2g}} \approx 2.5\,eV$. The DOS is defined as the number of accessible states per energy by the electrons of a given material, so it gives the degeneracy of a given band energy $E_{k\nu}$.

1.2.2 Fermi liquid theory (FLT)

In this section, I will review the FLT for solid state systems, by following [4, 5]. I have already mentioned that it is not trivial to see that, when adding a new electron into a material, the band structure remains unchanged while the Fermi level is rigidly shifted. FLT justifies the applicability of this single-particle states approximation for DFT band structure calculations for most of the materials. FLT is a low energy and low temperature theory, in which there is a one-to-one correspondence between the low energy excitations (called quasiparticles) and the real particles of the system. Then, the quasiparticles have the same charge $|e|$ and spin 1/2 than the real particles. FLT is a phenomenological theory, but it can be justified by perturbative arguments (by using Green's function formalism, see the end of this section), so it is not restricted to weak interactions. FLT fails when dealing with various situations, such as for Mott insulators, Luttinger liquids, strange metal phases, etc.

In FLT, for a non-interacting hamiltonian H_0, the interactions between electrons $\hat{U}$ are adiabatically turned on, i.e. the ground state of H_0 evolves smoothly with $\hat{U}$, until there is a direct connection with the ground state of the interacting hamiltonian $H_0 + \hat{U}$. For magnetic or superconducting phase transitions, the Mott transition, etc, FLT breaks down.

Then, let's assume a many-body system with N particles and the ground states of the non-interacting $|\Psi_{gs}>$ and interacting $|\Psi^*_{gs}>$ hamiltonians are connected adiabatically. If a new particle is added to H_0, the new state will be $|P>= c^\dagger_{k\sigma}|\Psi_{gs}>$, where $c^\dagger_{k\sigma}$ creates a particle in a excited state of the non-interacting hamiltonian H_0 with k and spin σ. When

$\hat{U}$ is turned on, the system evolves adiabatically from its initial state $|P>$ to a final state $|QP>=\hat{U}|P>$. Then, quasiparticles can be defined as the elementary excitations of the interacting hamiltonian $|QP>=a^{\dagger}_{k\sigma}|\Psi^{*}_{gs}>$, where $a^{\dagger}_{k\sigma}$ creates a quasiparticle in a excited state of the interacting hamiltonian $H_0+\hat{U}$ with k and spin σ, with $a^{\dagger}_{k\sigma}=\hat{U}c^{\dagger}_{k\sigma}\hat{U}^{\dagger}$. Thus, the elementary excitations of the interacting system $(H_0+\hat{U})$ are the quasiparticles, and not the real particles.

The electronic particle operator $c_{k\sigma}$ can be written in a perturbative way in terms of $\hat{U}$, not restricted to weak $\hat{U}$ (and dropping out the spin indices σ for simplicity):

$$c^{\dagger}_{k}=\sqrt{Z_k}a^{\dagger}_{k}+\underbrace{\sum_{k_4+k_3=k_2+k}A(k_4,k_3,k_2,k)a^{\dagger}_{k_4}a^{\dagger}_{k_3}a_{k_2}+\cdots}_{decay\ proccesses} \tag{1.6}$$

Z_k is defined as the quasiparticle weight (mentioned in the previous section), and it is given by $Z_k=|<\Psi^{*}_{gs}|a_k c^{\dagger}_{k}|\Psi^{*}_{gs}>|^2>0$, so it is the overlap between particle and quasiparticle states. The quasiparticle weight takes values $0<Z_k<1$, so when $Z_k\approx 1$, the weakly correlated limit is recovered, whether for $Z_k=0$, FLT breaks down. When Z_k decreases, the strength of correlations increases. Then, Z_k can be used to measure the strength of electronic correlations. Higher-order terms in Eq. (1.6) describe the decay processes of an electron into several exciations. Then, there is a part of the electron that cannot be expressed in terms of quasiparticles. This is the so called incoherent part. As a consequence, the quasiparticles will have a finite lifetime τ.

The single-particle states approximation makes sense if Z_k is a finite number and if the quasiparticles live long enough. It can be shown that in 3D and at low ω ($|\omega-\mu|\ll\mu$) and low T ($T\ll\mu=k_B T_F$):

$$\frac{1}{\tau}\propto(\omega-\mu)^2+T^2 \tag{1.7}$$

where ω is the frequency of the elementary excitations, μ is the chemical potential (the change in the total energy when an excitation is created in the system) and T_F is the characteristic temperature of the Fermi liquid metal (Fermi temperature). The quadratic dependencies ensure the long-lived quasiparticles at low T and energies. The quasiparticle stability requires that $\Gamma/\omega\sim\omega\ll 1$, which is satisfied for 3D[1], see Eq. (1.7). Then, the stability condition states that the decay rate of the quasiparticles have to be much smaller than their characteristic energies.

The quasiparticle weight Z_k is obtained from the excitation spectra. The excitation spectra, or alternatively the spectral function $A(k,\omega)$, is the distribution of excitations which are created when a particle (real electrons) is added/removed from the system. It can be measured by photoemission spectroscopy (PES). The spectral functions for a non-interacting and interacting system are shown in FIGURE 1.4. For a non-interacting system, $A(k,\omega)$ is a delta function. For an interacting system, the excitation spectra is formed by the so called quasiparticle peak (also called the coherent part), plus a continuum of states which are excited by the added/removed particle (the incoherent part). The continuum of states is the contribution of the decay proccesses, see Eq. (1.6). The delta function adquires a width Γ related

[1] In 2D $\Gamma/\omega\sim\omega\ln\omega$ and stability can be recovered. Interestingly, in 1D systems, $\Gamma/\omega\sim const$, so quasiparticles are not stable, and hence FLT breaks down. This is the situation for the Luttinger liquids.

with the decay of a quasiparticle which is not an eigenstate of the interacting hamiltonian, $\Gamma = 1/\tau$.

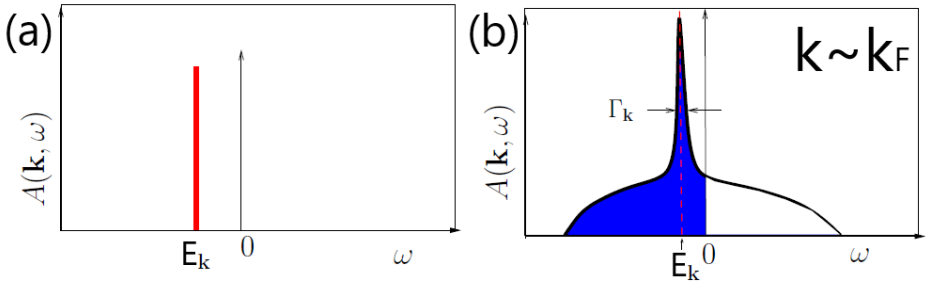

FIGURE 1.4: **(a)** Spectral function for a non-interacting hamiltonian. In this case, $A(k,\omega)$ is a delta function for $\omega = E_k$. **(b)** Spectral function for the interacting hamiltonian. The quasiparticle peak can be identified at $\omega = E_k$ with a width Γ. Apart from the quasiparticle peak, there is a continuum of excitation energies for $\omega > E_k$ and $< E_k$. Taken and adapted from [4].

The spectral function can be written in terms of the retarded propagator $G(k,\omega)$:

$$A(k,\omega) = -\frac{1}{\pi} Im\, G(k,\omega) \tag{1.8}$$

In Green's function formalism, the retarded propagator $G(k,\omega)$ is the probability amplitude for a particle being added/removed from the system, moving through it and ending in a state (k,ω). Then, $G(k,\omega)$ describes the propagation of a particle when it moves through a material, interacting with other electrons. It is a complex quantity which encodes all the information about the full interacting hailtonian $H_0 + \hat{U}$. $G(k,\omega)$ can be written using the Dyson equation:

$$G(k,\omega) = \frac{1}{\omega - \varepsilon_k^0 + \mu - \Sigma(k,\omega)} = \frac{1}{\omega - \varepsilon_k' + \mu - i\, Im\, \Sigma(k,\omega)} \tag{1.9}$$

where ε_k^0 is the dispersion energies of the non-interacting system (see Eq. (1.5)), $\varepsilon_k' = \varepsilon_k^0 + Re\,\Sigma(k,\omega)$, μ is the chemical potential and $\Sigma(k,\omega)$ is the self-energy. The self-energy is a complex quantity which accounts for the effects of $\hat{U}$ not included in the hamiltonian H_0, so it will describe the quantities that we have previously seen for the quasiparticles, Z_k and τ. We will see in the next paragraphs that $Re\,\Sigma(k,\omega)$ is related with Z_k and $Im\,\Sigma(k,\omega)$ with τ.

The poles ω_{pole} of $G(k,\omega)$ (i.e. the ω values at which $G(k,\omega)$ diverges) will describe the energies of the excitations of the interacting system, i.e. the quasiparticles. In FLT, the stability conditation states that $\Gamma/\omega = 1/\tau\omega \ll 1$. By definition $1/\tau = Im\Sigma(k,\omega)$, then the applicability of FLT requires that $Im\Sigma(k,\omega)/\omega \ll 1$ and $Im\,\Sigma(k,\omega) \ll \varepsilon_k'$. For $T = 0\,K$ and small frequencies (note that $\Sigma(k,\omega) \approx Re\,\Sigma(k,\omega)$), $\Sigma(k,\omega)$ can be Taylor expanded and retain only up to linear-ω terms [15]:

$$\Sigma(k,\omega) \approx Re\,\Sigma(k,0) + \omega \left.\frac{\partial Re\,\Sigma(k,\omega)}{\partial\omega}\right|_{\omega\to 0} \tag{1.10}$$

where the quasiparticle weight Z_k is defined as:

$$Z_k = \frac{1}{1 - \left.\frac{\partial Re\,\Sigma(k,\omega)}{\partial\omega}\right|_{\omega\to 0}} \tag{1.11}$$

and $\Sigma(k,\omega) \approx Re\,\Sigma(k,0) + \omega(1-1/Z_k)$, so in the FLT the real part of the self-energy depends linearly on ω with a factor which depends on the quasiparticle weight Z_k. The propagator is redefined as:

$$G(k,\omega) = \frac{Z_k}{\omega - Z_k(\varepsilon'_k - \mu)} \tag{1.12}$$

Eq. (1.12) features a pole at $\omega_{pole} = Z_k(\varepsilon'_k - \mu)$, where Z_k plays the role of weighting this pole (hence the name of Z_k). It appears as a pre-factor of ε'_k, so the energies will suffer a renormalization due to this Z_k.

Around the Fermi surface k_F, $\Sigma(k,\omega)$ can be further expanded to obtain the effective mass renormalization, $(m^*/m_0)_k \approx (1 - \left.\frac{\partial Re\,\Sigma(k,\omega)}{\partial\omega}\right|_{k\to k_F})/(1 - \left.\partial Re\,\Sigma(k,\omega)/\partial\omega\right|_{\omega\to 0})$. If $\Sigma(k,\omega)$ is k-independent (as I will discuss in **Section 1.3** and during a great part of the thesis), $1 - \left.\partial\Sigma'(k,0)/\partial k\right|_{k\to k_F} = 1$, and then:

$$\frac{m^*}{m_0} = \frac{1}{Z} \tag{1.13}$$

In this case, the mass renormalization for k-independent self-energy gives a clear physical meaning for Z: at $m^* = m_0$ ($Z = 1$), the electron has an effective mass which is equal to the non-correlated one, so the system behaves as a non-correlated metal, $m^* < m_0$ ($Z < 1$), the electrons become heavier, so the system progresively moves from a weakly correlated metal ($0.7 < Z \leq 1$) to a moderately ($0.3 < Z \lesssim 0.7$), and then a strongly ($0 < Z \lesssim 0.3$) correlated metal; at $m^* \to \infty$ ($Z = 0$), electrons are infinitively heavy, so they will prefer to sit motionless in the material, and the system behaves as an insulator. Now, we will see how to measure the mass renormalization.

Measurable thermodynamic quantities can be extracted by using the Landau's free energy functional $F[\delta\hat{n}_k]$, where $\hat{n}_k = a_k^\dagger a_k$ is the quasiparticle number operator. This functional is obtained by an expansion of $H_0 + \hat{U}$ around the equilibrium density of quasiparticles, which is a small quantity:

$$F[\delta\hat{n}_k] = F_{gs} + \sum_k \underbrace{\left.\frac{\partial F}{\partial\delta\hat{n}_k}\right|_{\delta\hat{n}_k\to 0}}_{E_k^*} \delta\hat{n}_k + \sum_{kk'} \underbrace{\left.\frac{\partial^2 F}{\partial\delta\hat{n}_k\partial\delta\hat{n}_{k'}}\right|_{\delta\hat{n}_{k,k'}\to 0}}_{f_{k,k'}} \delta\hat{n}_k\delta\hat{n}_{k'} + \cdots \tag{1.14}$$

where $\delta\hat{n}_k$ is the deviation from the equilibrium density of quasiparticles, F_{gs} refers to the non-interacting ground state free energy (system without quasiparticles), E_k^* is the single-quasiparticle energy and $f_{k,k'}$ is the residual quasiparticle-quasiparticle interaction (gives the decay processes). They are related with quantities such as the quasiparticle weight Z_k, the mass renormalization m^*/m_0, the lifetime τ, etc. Here, I will just mention that the electronic excitation terms of various thermodynamics quantities, like the specific heat $C(T)$, the resistivity $\rho(T)$ or the spin susceptibility $\chi^s(T)$, can be obtained as:

$$\begin{cases} C(T) \sim \gamma T^2 \\ \rho(T) \sim \rho_0 + AT^2 \\ \chi^s(T) \sim const. = \chi_0^s \end{cases} \tag{1.15}$$

The factors γ, A and χ_0^s can be obtained from E_k^* and $f_{k,k'}$. They depend on the effective mass renormalization as $\gamma \propto m^*$, $A \propto (m^*)^2$ and $\chi_0^s \propto m^*$, so they increases when electronic correlations increase. Then, the ratio $m^*/m_0 = 1/Z$ can be obtained when comparing the experimental values of γ, A and χ_0^s with the results calculated in DFT, e.g. $m^*/m_0 = \gamma^{exp}/\gamma^{DFT}$ (see next chapter). When comparing with the experimental results, Eq. (1.15) could show other T dependencies, like electron-phonon contributions (for example, βT^4 term in $C(T)$), or from non-Fermi liquid behaviors. In **Section 2.3.1**, we will further discuss the experimental results for the quantities of Eq. (1.15) in FeSCs.

1.3 Single-orbital systems

A first approximation to study the physics of many SCES is the so called Hubbard model. In the spatially localized Wannier orbital basis, Eq. (1.3) can be rewritten in second quantization to include strong correlation/interaction effects. In the real space [13]:

$$H = \underbrace{\sum_{mn}\sum_{ij}\sum_{\sigma} t_{mn}^{ij} d_{im\sigma}^{\dagger} d_{jn\sigma}}_{weakly correlated\ H_0} + \underbrace{\frac{1}{2}\sum_{mm'nn'}\sum_{ijkl}\sum_{\sigma\sigma'} U_{mnm'n'}^{ijkl} d_{im\sigma}^{\dagger} d_{jn\sigma'}^{\dagger} d_{lm'\sigma'} d_{kn'\sigma}}_{correlated\ \hat{U}} \tag{1.16}$$

where $U_{mm'nn'}^{ijkl}$ is the interaction integral between electrons initially with $lm'\sigma'$, and $kn'\sigma$ and which end in $im\sigma$ and $jn\sigma'$. This is the electronic correlations term $\hat{U}$.

In the k-space, and taking into account the momentum conservation:

$$H = \sum_{k}\sum_{mn}\sum_{\sigma} \varepsilon_{kmn} d_{km\sigma}^{\dagger} d_{kn\sigma} + \frac{1}{2}\sum_{mm'nn'}\sum_{kk'Q}\sum_{\sigma\sigma'} U_{mnm'n'}^{Q} d_{k+Q\,m\sigma}^{\dagger} d_{k'-Q\,n\sigma}^{\dagger} d_{k'\,m'\sigma'} d_{k\,n'\sigma} \tag{1.17}$$

where Q gives the momentum exchange due to the interaction U^Q. Eq. (1.16) and Eq. (1.17) are equivalent. When the $\hat{U}$ effect is strong enough, DFT band structure calculations fail, and further approximations have to be taken into account.

Two main regimenes can be differentiated when looking into the range of the electronic interaction $\hat{U}$: short- and long-range interactions [4]. Like the Coulomb interaction between electrons goes like $\sim 1/r$, it has a long-range character. However, other electrons in the system can screen this Coulomb interaction, reducing its long-range character. In order to have this situation, there has to be a minimum electron density needed to screen this interaction. When the screening is large enough, the long range character of the Coulomb interaction can be safely ignored, and short-range interactions will dominate the physics of the system.

During this thesis, I will focus on studying short-range interactions, in the limit of onsite interactions. The onsite interactions are restricted to the electrons in the same lattice site. These interactions do not necessarily imply an ordering of the system. In the case of the onsite interactions:

$$U^{ijkl}_{mnm'n'} = U_{mnm'n'}\delta^{ij}\delta^{ik}\delta^{il} \tag{1.18}$$

For a single-orbital system, the so called Hubbard model can be derived:

$$H = \sum_{ij,\sigma}(t^{ij}d^{\dagger}_{i\sigma}d_{j\sigma} + h.c.) + U\sum_{i}\widehat{n}_{i\uparrow}\widehat{n}_{i\downarrow} \tag{1.19}$$

In this model, U gives the onsite interaction (also called Hubbard interaction) and $\widehat{n}_{i\sigma} = d^{\dagger}_{i\sigma}d_{i\sigma}$ is the occupation number operator. The onsite interaction term gives the repulstion energy between two electrons which are in the same lattice site. We will see in the next section that due to the onsite interaction U, double occupied lattice sites (i.e. two electrons with opposite spins in the same lattice site) will be suppressed, as shown in FIGURE 1.6.

Within the limit of onsite interactions, two situations can be separated: local and non-local correlations. In the local correlations picture, only correlations between electrons in the same lattice site (also called onsite correlations) are considered, and further neighbor correlations are neglected. In this case, $\Sigma(\omega)$ is k-independent, and hence all the observables, like Z. In the non-local correlations picture, the correlations between an electron in a site with those in neighbor sites are also included, then $\Sigma(k,\omega)$ is k-dependent and also other observables as Z_k.

Although the Hubbard model Eq. (1.19) looks quite simple, it can capture the essential physics behind complicated systems, such as the high-T_c cuprates [7] or ultra-cold atoms in optical lattices [16]. The most suprising feature of this model is the Mott transition. In various materials, DFT band structure shows a metallic behavior (with an odd number of electrons per unit cell), but the experiments remark their insulating behavior in the paramagnetic (PM) state. This insulating behavior comes from local correlation effects, and it is known as the Mott insulator. We will further explore this insulating state in the next sections.

1.3.1 The Mott transition

Let's consider a simple model to see the effect of U [5, 8]. Suppose a single-orbital system, where only nearest neighbor hoppings t are included. Consider the large-U limit, with $t \approx 0$. Each lattice site can hold 2 electrons with different spin. Due to the effect of U, 2 electrons in the same lattice site will repel each other. Then, adding the second electron in an already occupied lattice site (also called double occupancy) costs an energy U, see FIGURE 1.5**(a)**. This results in the non-rigid band shift, i.e. both the chemical potential and the energies change when adding extra particles into the system. Now, when considering the hopping $t \neq 0$, the non-degenerated energy levels of FIGURE 1.5**(a)** will adquire a width, as shown in FIGURE 1.5**(b)**. These are the so called Hubbard bands, which belong to the continuum of states which is not in the quasiparticle state, see **Section 1.2.2**. Note that the Hubbard bands represent non-degenerated single and double occupied bands which cannot

be explained by the single-particle approximation done in band theory, in constrast to typical band insulators (see FIGURE 1.1**(c)**).

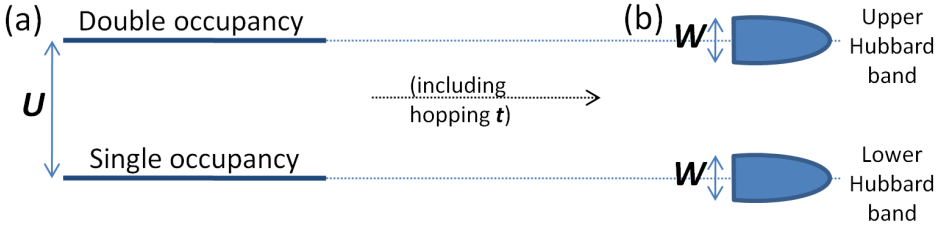

FIGURE 1.5: **(a)** Energy levels in the large-U limit (i.e. $t \approx 0$) for an atom, where adding a second electron will cost an energy U. These energy levels are labeled by single and double occupancy, so they have a single slot for electrons. **(b)** When including the hoppings, these energy levels adquire a width of the order of the bandwidth W. The dispersive single and double occupancy levels are also called Hubbard bands, which belong to the continuum of states which are not in the quasiparticle state. Adapted from [5].

Now, let's assume that the system is at half-filling, i.e. the number of electrons per atom is $n_e = 1$. Considering the ratio U/W (which is the ratio between the interaction energy and the effective kinetic energy), with W the bandwidth, two regimenes can be differentiated: when $W \gg U$, the kinetic energy gain is larger than the interaction energy cost for the double occupancy, hence the electrons will move almost freely through the lattice (FIGURE 1.6**(a)**), while if $W \ll U$, the interaction energy cost wins over the kinetic energy, so electrons in the same site repels each other, hence sitting motionless at each lattice site (FIGURE 1.6**(b)**)[2].

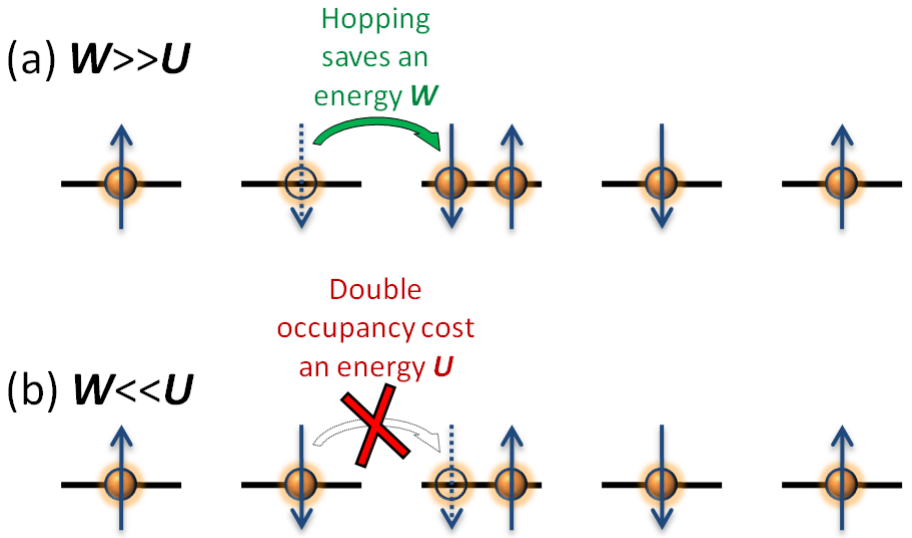

FIGURE 1.6: Sketch of the Mott transition in a single-orbital system at half-filling, where the effective kinetic energy is identified by the total bandwidth W. **(a)** $W \gg U$, the system behaves as a metal and **(b)** $W \ll U$, the system becomes a Mott insulator. Adapted from [5].

[2]Note that in a model like this one, non-local AFM correlations (note that the spins in FIGURE 1.6 are distributed anti-parallel from one atom to another, see **Section 1.3.2**) will tend to stabilize the Mott insulating state at an infinitesimal $U \approx 0$, hence the limit U/W does not make sense. However, in the local correlations picture, there is not such magnetic correlations playing any role, and the Mott transition is displaced to $U > 0$.

If only the hopping amplitudes are considered, a metallic solution is found. By introducing the onsite interaction, at a certain value of U, the metal-insulator transition can occur without any symmetry breaking. Thus, the system does not necessarily order magnetically. This is what is called the Mott transition, while the insulator is called Mott insulator. The Mott transition will occur at a critical interaction $U_c \simeq W$ and the gap will be of the order of $gap \sim U - W$ [17]. In FIGURE 1.7**(a)**, I have sketched the Mott transition explained above. Note that this transition will only occur at half-filling, once the system is doped (with holes or electrons) away from half-filling, the system behaves metallically (the chemical potential lies in a partially filled Hubbard band), so that the Mott insulator is only found at half-filling.

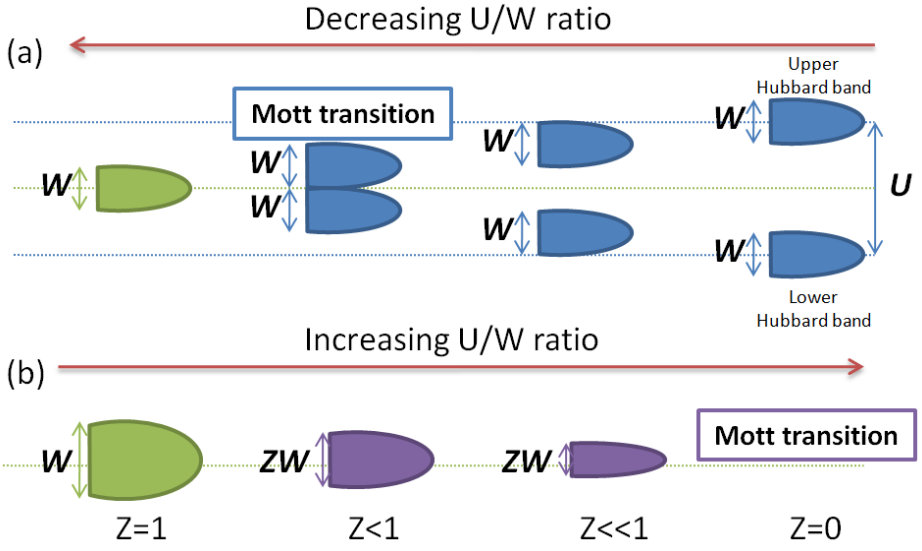

FIGURE 1.7: Sketches of the **(a)** Mott-Hubbard and **(b)** Brinkman-Rice metal-to-insulator transitions. Green dotted line marks the chemical potential μ when the system is at half-filling $n_e = 1$. In the Mott-Hubbard transition, the system starts in the Mott insulating state, and the kinetic energy W is progresively turned on. U_c is defined at the energy at which the upper and lower Hubbard bands merge. In this picture, the metallic phases are not properly described, and U effect is overestimated. In the Brinkman-Rice transition, the system starts in the non-correlated metallic state, and the interaction U is progresively turned on. U_c is defined at the energy at which the quasiparticle peak disappears ($Z = 0$). In this picture, the Mott insulating phase cannot be described, and U effect is understimated. Adapted from [5].

This previous picture is what can be alternatively called the Mott-Hubbard transition [8]. It starts from the insulating state, by considering the Hubbard bands and progresively turns on the kinetic energy W. In this picture, all the spectral weight goes to the Hubbard bands. Thus, while it captures the essence of the Mott transition, it does not properly describe the metallic state.

An alternative point of view starts from the metallic side and turns on the interactions U [5, 8]. In this picture, the ground state wavefunction of the interacting system $|\Psi^*_{gs}>$ evolves with a variational parameter η, which is related with the concentration of double occupied states. At $U = 0$, $\eta = 1$ and at $U \to \infty$, $\eta = 0$. This variational parameter η is also related with the quasiparticle weight Z, see **Section 1.2.2**.

This is the so called Brinkman-Rice transition [8]. In FIGURE 1.7**(b)**, I have sketched such transition, where the quasiparticle weight Z (which appears as a renormalization factor of the bandwidth $\sim ZW$) is progresively reduced until it disappears at the Mott transition

at $U_c \simeq 2W$. However, this picture is based on the FLT for solids, and hence it cannot provide further information about the Mott insulator and the Hubbard bands (e.g., the gap magnitude cannot be obtained), and U effect is understimated.

The quasiparticle weight Z is the order parameter of the Mott transition [5]. In the local correlations picture, it can be shown that $1/Z = m^*/m_0$, see Eq. (1.13), where m_0 is the non-correlated effective mass (i.e. obtained from the tight-binding model, see **Section 1.2.1**) and m^* is the correlated effective mass. The quasiparticle weight evolves from $Z = 1$ ($m^* = m_0$) in the non-correlated metal to $Z = 0$ ($m^* \to \infty$) in the Mott insulator. When $0.7 < Z \leq 1$ ($1 \leq m^*/m_0 < 1.4$), the system is said to be a weakly correlated metal, and descriptions based on a DFT band structure calculations and tight-binding models will give good predictions. At $0 < Z \lesssim 0.3$ ($3 \lesssim m^*/m_0 < \infty$) is in a strongly correlated metallic state, and DFT calculations and tight-binding models will leave out the most important local correlations effects. In between, a moderately correlated metal exits with $0.3 < Z \lesssim 0.7$ ($1.4 \lesssim m^*/m_0 < 3$).

The behavior explained above for local correlations is robust against any considered tight-binding model, as shown in FIGURE 1.8 for 2D square and triangular lattices, at half-filling $n_e = 1$ and only nearest neighbor hoppings t included, and solved using the slave-spin mean-field (SSMF) formalism, see **Section 1.4.1**, and the detailed discussion in **Appendix B**. Only the energy scales at which the effects occur will change from one model to another. For FIGURE 1.8, the total bandwidth for each lattice is $W^{square} = 8t$ and $W^{triangular} = 9t$, and hence $U_c^{square} \sim 13t < U_c^{triangular} \sim 15.6t$ (note that $U_c^{square} \sim 1.6W$ and $U_c^{triangular} \sim 1.7W$).

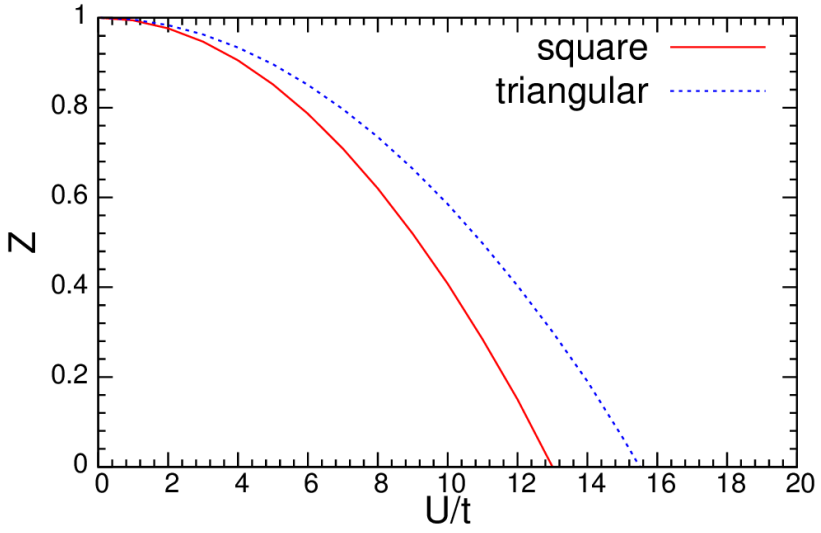

FIGURE 1.8: Z versus U/t comparison between 2D square and triangular single-orbital tight-binding models at half-filling. Only nearest neighbor hoppings t are considered. The triangular lattice is less correlated than the square (it requires a bigger U_c to become a Mott insulator) due to its larger bandwidth $W^{triangular} = 9t > W^{square} = 8t$. I have obtained $U_c^{square} \sim 13t$ and $U_c^{triangular} \sim 15.6t$. Figure obtained using SSMF $U(1)$ formalism, see **Appendix B**.

A more complete description requires both Mott-Hubbard and Brinkman-Rice pictures being applied at the same time, and it is provided by numerical calculations using Dynamical Mean-Field Theory (DMFT) [17]. A description of DMFT calculations is presented in **Section 1.4.1**. In DMFT close to the transition for a given U/W value, two solutions are

possible: a metallic one where the Hubbard bands start to form, with a fully gap ($\sim U - W$) opening at $U_{c1} \sim W$, and an insulating one where the quasiparticle peak disappears at $U_{c2} \sim 2W$. The Mott transition is then defined as the minimum of the Landau's free energy F, which at $T = 0\,K$ coincides with U_{c2}, and results in a first order transition (for finite T, see **Section 1.3.3**).

In FIGURE 1.9**(a)**, the DMFT spectral function for the Mott transition in the Bethe lattice[3] can be seen [17]. When the ratio U/W increases, the quasiparticle peak at $\omega = 0$ narrows, while the Hubbard bands start to form around $\omega \approx \pm 2D$ (where $D = W/2$ is the half-bandwidth), and a gap opens between them, at U_{c1} as previously pointed out. The narrowing of the quasiparticle peak with increasing U/W is related with the decrease (increase) of Z (m^*/m_0), hence with the narrowing of the band energies. In FIGURE 1.9**(b)**, the photoemission spectra, i.e. the spectral function $A(\omega)$, see **Section 1.2.2**) for $SrVO_3$ (and Ca-doped $SrVO_3$) clearly shows the coexistance of the quasiparticle peak and the Hubbard bands [18].

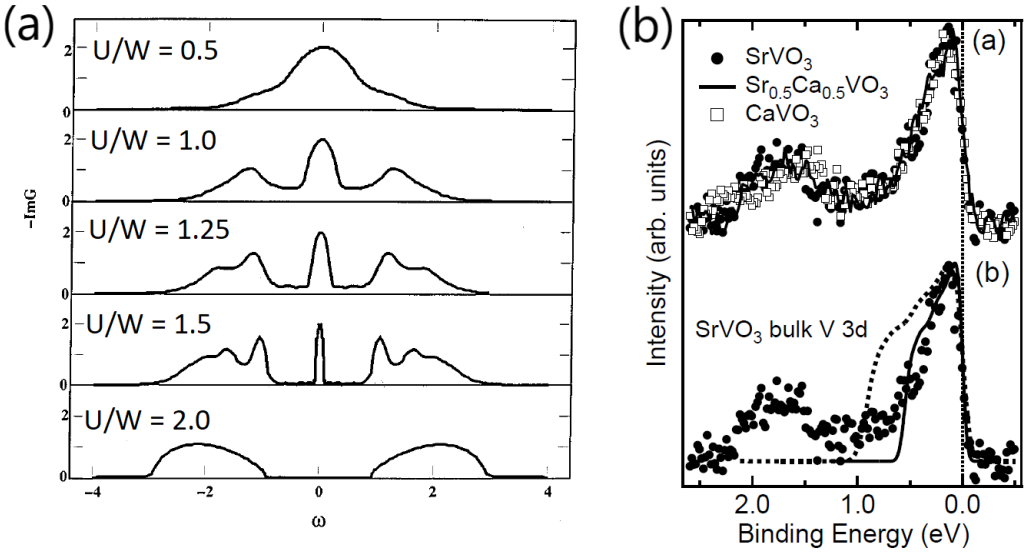

FIGURE 1.9: **(a)** DMFT spectral function for a single orbital in the Bethe lattice. ω is in units of the half-bandwidth $D = W/2$. Modified from [17] to include the ratio U/W. At $U_{c1} \sim W$ a gap ($\sim U - W$) fully opens between the Hubbard bands, and at $U_{c2} \sim 2W$ the quasiparticle peak dissapears, i.e. $Z = 0$. At $T = 0\,K$, the Mott transition occurs at $U_c = U_{c2} \sim 2W$. **(b)** Photoemission spectra of the strontium vanadate $SrVO_3$, where the quasiparticle peak (around $\sim 0.3\,eV$) and the lower Hubbard band (around $\sim 2\,eV$) can be clearly seen. Taken from [18].

An important result from this improved perspective is the fact that Z vanishes at the Mott transition, while double occupancy does not (see next section) [17]. Thus, Z is the correct order parameter of the Mott transition. In the Brinkman-Rice picture and for a single-orbital system, when $Z = 0$, the local total charge correlations C_{n_T} (which are the fluctuations around the equilibrium charge in each site) are also 0, hence the Mott insulator implies a localization of the local charge. Another important property is that local spin correlations C_S (which are the fluctuations around the equilibrium spin in each site) are maximum at the Mott insulator, signaling that atoms are in a local high-spin state (each atom is maximally

[3]The Bethe lattice is an infinite dimensional hypercubic lattice, where $\varepsilon_k = 2t\sum_{d=1}^{\infty}\cos k_d$ and it has a semicircular DOS. It is widely used in DMFT calculations due to the fact that this technique is exact in infinite dimensions.

spin polarized). In FIGURE 1.10, I present the color maps for Z, C_{n_T} and C_S in the U/W versus the number of electrons per atom n_e phase diagram, for the 2D square lattice with only nearest neighbor hoppings t [5]. These plots are obtained by using the SSMF formalism. Except for half-filling $n_e = 1$, the system will behave as a metal. Yellow-red areas in FIGURE 1.10**(a)** mark the weakly and moderately correlated metal, while purple region marks the strongly correlated metal behavior, in which $0 < Z \lesssim 0.3$. In this situation, DFT band structure calculations will fail when predicting the correct band structure, due to the large renormalization.

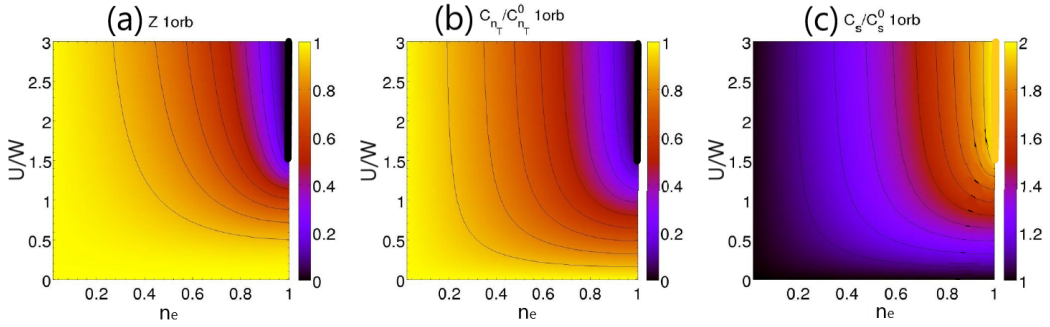

FIGURE 1.10: Color maps for **(a)** Z, **(b)** local total charge correlations C_{n_T} and **(c)** local spin correlations C_S in the U/W versus n_e phase diagram. Solved using a 2D square lattice with only nearest neighbor hoppings in the SSMF Z_2 formalism. The Mott transition is marked by a thick line at $n_e = 1$. When the Mott transition is reached, $Z = 0$, charge fluctuations are suppressed and the atoms become maximally spin polarized. Taken and adapted from [5].

Calculating Z and when possible, comparing with the experiment, is then an important first step in any SCES, in order to know the degree of electronic localization, and hence the most suitable space (real space using Eq. (1.16), or k-space using (1.17)) to describe the system.

1.3.2 Short-range magnetic correlations for the Mott insulator

In the previous sections, we have discussed the Mott transition without the presence of any magnetic (or orbital) tendencies. This emphasizes that the Mott insulator does not necessarily require any magnetic tendency. Nevertheless, short-range magnetic correlations can be promoted. In order to treat magnetic correlations, we have to go beyond local correlations approximation, including neighbor correlations into the calculations (this is the so called non-local correlations picture). In this section, I will briefly discuss the short-range magnetic correlations in the large-U limit, i.e. deep in the Mott insulating phase [8].

At half-filling, Eq. (1.19) in the large-U limit can be rewritten as the Heisenberg hamiltonian:

$$H = J \sum_{ij} \vec{S}_i \cdot \vec{S}_j \tag{1.20}$$

where $J = 4t^2/U$ (obtained from second order perturbation theory for the hopping term t) is the exchange interaction and $\vec{S}_i$ are the spin operators in each lattice site i. Note that J can depend on i, j if second, or higher-order neighbor exchanges are included, resulting in a similar hamiltonian to Eq. (1.20), but placing J_{ij} inside the summatory. When including a modified hopping hamiltonian in a second step [8], it receives the name of $t - J$ model. If $J > 0$,

antiferromagnetic (AFM) correlations are promoted, and hence the spins in neighboring lattice sites will align antiparallel, while if $J < 0$, ferromagnetic (FM) correlations are then promoted, so there is a parallel alignement. Note again that this tendencies do not require a long-range order.

In the case of single-orbital systems, AFM correlations are always promoted. This occurs because a virtual hopping process (as the one described in FIGURE 1.6) creates an intermediate empty and doubly occupied state, with an energy U. The associated energy gain if the spins of neighboring sites are antiparallel is $\sim -t^2/U$ (calculated from second-order perturbation theory for the hopping), while for parallel spins is zero (due to the Pauli exclusion principle). Then, due to the energy gain, AFM correlations are promoted. Due to this virtual proccesses, double occupancy at the Mott insulator is not strictly zero, as anticipated in the previous section [17]. Depending on the lattice symmetry, magnetic frustration varies, so the tendency towards the AFM correlations in higher frustrated lattices will decrease, but the character of these correlations will remain AFM.

1.3.3 Temperature effect in local and non-local correlated systems

In this section, I will review the behavior of the Mott transition in both local and non-local correlation pictures with the temperature T, mainly following [19–21]. The behavior of the Mott transition will change with T. FIGURE 1.11 shows the T vs $U_r = (U - U_c)/U_c$ phase diagram for both local and non-local correlations solved by cellular DMFT (cellDMFT) for a single-orbital at half-filling system in a 2D square lattice. In cellDMFT, non-local correlations between electrons in different real space sites are taken into account. The range of these non-local correlations depends on the size of the cluster used (in FIGURE 1.11, it is a 2×2 cluster in the square lattice). The Mott transition at finite T is given by U_c, defined as the minimum in the Landau's free energy F.

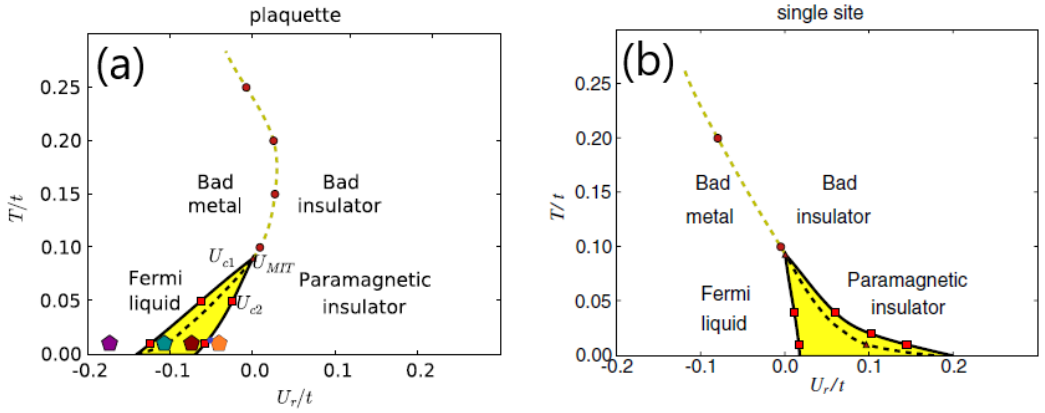

FIGURE 1.11: T/t versus U_r/t (with $U_r = (U - U_c)/U_c$) phase diagram for **(a)** non-local and **(b)** local correlations in the square lattice. Yellow area (in between $U_{c\,1}$ and $U_{c\,2}$ lines) marks the coexistance of both metallic and insulating behaviors. Dashed line inside the yellow region marks the Mott transition U_c. In both cases, a critical point appears at $T/t \approx 0.1$. Above $T/t = 0.1$, there is a crossover between a bad metal and bad insulator. Orange hexagon marks the pseudogap region. Taken and adapted from [19].

A main feature of non-local correlations when compared with local correlations is that both $U_{c\,1}$ (in local correlations describes a fully opened gap between the Hubbard bands) and $U_{c\,2}$ (in local correlations, the quasiparticle peak disappears), and hence U_c decrease. In CDMFT

calculation for a 2D square lattice at half-filling, $U_c^{nonlocal} \sim 6t$, while $U_c^{local} \sim 12t$. $U_c^{nonlocal}$ increases approaching U_c^{local} if the system is more frustrated, i.e. if the magnetic non-local correlations are suppressed. Frustration occurs, for example, when adding further neighbor hoppings t' to the tight-binding model for the 2D square lattice Eq. (1.4).

In FIGURE 1.11, most left-sided line marks $U_{c\,1}$, while right-sided line marks $U_{c\,2}$. Yellow area marks the coexistence of both metallic (quasiparticle peak) and insulating (gap separating the Hubbard bands) states, and dashed line marks the Mott transition U_c. These three lines end in a second order critical point, and at larger T there exist a crossover between bad metallic and bad insulating behavior (dashed yellow line). At large T and U, local correlations dominate the physics behavior. The Mott insulating state is the ground state for both local and non-local correlations pictures [19]. At lower T and U, the behavior is different for both cases. For local correlations, the metallic state is the ground state, whether for non-local correlations, the Mott insulator is the ground state due to AFM short-range correlations [19].

Close to critical interaction for the Mott transition in the non-local correlations picture $U_c^{nonlocal}$ (see orange pentagon in FIGURE 1.11**(a)**), the system shows a small gap in $A(k,\omega)$ at the chemical potential, but without the disappearance of the quasiparticle peak, which is splitted. This regime is totally different from local correlations, where once the Mott insulating phase is reached, the Mott gap is fully open ($\sim U - W$) and the quasiparticle peak vanish [17]. For $U > U_c^{nonlocal}$, the gap is fully formed and it recovers the local correlations expectations, with $gap \sim U - W$.

1.4 Multiorbital systems

The Hubbard hamiltonian of Eq. (1.19) describes a single-orbital system for onsite interactions. In order to generalize this model to the multiorbital case, we have to take into account various considerations [22]. From Eq. (1.18), it can be seen that there are, in principle, N^4 different spin-independent interaction terms $U_{mnm'n'}$. However, not all of them are allowed (due to the Pauli exclusion principle) or independent from each other. For example, $U_{mnm'n'} \equiv U_{m'nmn'} \equiv U_{mn'm'n} \equiv U_{m'n'mn}$. Also, terms which only mix three different orbitals, such as $U_{mmnn'}$, vanish. In conclusion, there are four independent interaction terms:

$$\begin{cases} U_{mm} = U_{mmmm} \\ U'_{mn} = U_{mnmn} \\ J_{H\,mn} = U_{mnnm} \\ J'_{mn} = U_{mmnn} \end{cases} \tag{1.21}$$

where the parameters are defined as (see below for the interacting hamiltonian form and the inclusion of the spin indices): U_{mm} is the intraorbital interaction, U'_{mn} is the interorbital interaction for electrons with anti-parallel spins, $U'_{mn} - J_{H\,mn}$ is the interorbital interaction for electrons with parallel spins, $J_{H\,mn}$ is the Hund's coupling and J'_{mn} is the pair-hopping term. The Hund's coupling term comes from two contributions, the interorbital interaction for electrons with anti-parallel spins and the spin-flip term, in which the electrons jump from one atom to another flipping their spin.

Then, the multiorbital system is described by the so called Hubbard-Kanamori hamiltonian:

$$
\begin{aligned}
H = & \underbrace{\sum_{ij,mn,\sigma} \left(t_{mn}^{ij} + \delta_{mn}\delta_{ij=0}\epsilon_m \right) d_{im\sigma}^{\dagger} d_{jn\sigma}}_{H_0} \\
& \underbrace{+ \sum_{i,m} U_{mm} \hat{n}_{im\uparrow}\hat{n}_{im\downarrow} + \sum_{i,m<n,\sigma} U'_{mn} \hat{n}_{im\sigma}\hat{n}_{in\bar{\sigma}} + \sum_{i,m<n,\sigma} \left(U'_{mn} - J_{H\,mn} \right) \hat{n}_{im\sigma}\hat{n}_{in\sigma}}_{H_{dens}} \\
& \underbrace{- \sum_{i,m<m'} J_{H\,mn} d_{im\uparrow}^{\dagger} d_{im\downarrow} d_{in\downarrow}^{\dagger} d_{in\uparrow} + \sum_{i,m\neq n,\sigma\neq\sigma'} \frac{J'_{mn}}{2} d_{im\sigma}^{\dagger} d_{im\sigma'}^{\dagger} d_{in'\sigma'} d_{in'\sigma}}_{H_{add}}
\end{aligned}
\tag{1.22}
$$

where $H = H_0 + H_{dens} + H_{add}$, with H_0 describing the tight-binding model, H_{dens} being the density-density interaction hamiltonian and H_{add} including both spin-flip and pair-hopping processes. $H = H_0 + H_{dens}$ is also known as the Ising hamiltonian, and the essential physical effects discussed in this thesis are encoded in it. The study of the Ising hamiltonian will be central during this thesis.

In a first approximation, interactions can be written orbital-independent U, U', J_H and J'. Even if this approximation looks very crude, it gives good enough results in many materials. If the system is rotationally invatiant, the relations $U' = U - 2J_H$ and $J' = J_H$ can be invoked [23]. Even if the system is not fully rotationally invariant, these relations approximately hold for various materials, such as FeSCs. Thus, the effects of local correlations have been reduced to 2 independent parameters, U and J_H. For real materials, these parameters can be estimated by using constraint Random Phase Approximation (cRPA) calculations [24], or by comparing with experiments and taking the most appropiated interaction parameter values [9, 25] (see **Chapter 4**).

When solving Eq. (1.22) considering only local correlations, new interesting features appear due to the addition of the orbital degree of freedom:

- The Mott transition occurs not only at half-filling, but also at other integer fillings n_e, where n_e is the number of electrons per atom.
- A new interaction energy scale emerges, the Hund's coupling J_H, and its role in the metallic and Mott insulating states is crucial and depends on the specific n_e/N value, where N is the number of orbitals per atom.
- If the orbitals are non-equivalent, they will behave differently with $(U, J_H, n_e/N)$, so there is an orbital selectivity of the electronic correlations. This can be translated into an orbital dependent quasiparticle weight Z_m.

These consequences are more extensively discussed in **Chapter 2**. Up to now, it is important to note that the appearance of the Hund's coupling, and the phenomenology resulting from it, led the scientific community to introduce a new type of correlated metallic state, the Hund metal [5, 9, 15, 26–37]. . The interplay and possible connections between Hund metals and Mott insulators are also discussed in **Chapter 2**. In Hund metals, a bad metallic behavior (i.e. higher resistivity which comes from an increase of the mass enhancements, see Eq. (1.15)) is promoted for increasing J_H, the atoms are highly (local) spin polarized and there is an orbital decoupling (different orbitals will be decoupled from each other).

Finally, orbital selectivity of the electronic correlations can make the system enters in an orbital selective Mott phase (OSMP), as studied by several authors [6, 38–41]. The OSMP is realised when some $Z_m = 0$ while others remain finite $Z_{n\neq m} \neq 0$, see **Section 2.2.4**. The Hund's coupling promotes orbital decoupling favouring this situation. Nevertheless, in the presence of finite interorbital hoppings t_{mn}, the OSMP evolves into a system in which both weakly ($0.7 < Z \leq 1$) and strongly correlated ($0 < Z \lesssim 0.3$), and even moderately correlated ($0.3 < Z \lesssim 0.7$) electrons coexist in different orbitals at the same time [5, 9, 15, 36, 37].

Different experimental probes [9, 15, 33, 34, 42–44] can be tested to check the effect of the correlations in multiorbital system, similarly to the single-orbital case: angle-resolved photoemission spectroscopy (ARPES), low-T specific heat, optical conductivity, resistivity and magnetic susceptibility measurements, etc., see Eq. (1.15). All of these experimental techniques are sensible to the band structure (specially ARPES), and hence to the possible renormalization or deviations from the DFT calculated band structure, hence they are sensible to $(m^*/m_0)_m$. Thus, quasiparticle weights Z_m ($1/Z_m = (m^*/m_0)_m$) can be extracted. In **Section 2.3.1**, we will get into more details when studying FeSCs and the role of electronic correlations in these materials.

In the next section, I will briefly review some of the most widely used techniques to study local correlations in multiorbital systems, which are able to study the the Mott insulator and Hund metal phenomenology in such multiorbital systems.

1.4.1 Brief description of local correlations theoretical techniques

Various theoretical techniques have been developed to calculate the effect of the local correlations. DMFT [17] is a technique specially adequate to address the Mott transition and the strength of correlations. This technique is able to calculate the local spectral function $A(\omega)$ with the information related with the quasiparticle peak and the continuum of states at the same time. In DMFT, localized electrons in a lattice site interact with a bath of delocalized electrons, thus capturing the real space localized and delocalized character of the electrons in a SCES. This means that DMFT can capture at the same time the role played by the localized electrons, which contribute to the Hubbard bands, and the delocalized ones, which contribute to the quasiparticle peak.

Other techniques, such as Gutzwiller approximation (GA) [8] or slave-particle mean-field techniques [25, 38, 45–47], like slave-boson [45], slave-rotor [46] or slave-spin [25, 38, 47], are based on the Brinkman-Rice picture of the Mott transition, hence they follow the FLT. They are nevertheless very useful. They can trace down Z_m when going from the non-correlated metal $Z_m = 1$ to the Mott transition, where all $Z_m = 0$. These techniques are computationally faster and they are easier to implement. The basic approximation behind GA is the projection out of the double occupied states when the system progresively approaches the Mott transition. The projection out of double occupied states is made by finding the variational parameter η for the interacting ground state $|\Psi^*_{gs}>$. For slave-particle mean-field techniques, Z_m appear as multiplying pre-factors of ε_{kmn} by doing an changing from the original Hilbert basis $\left\{d^\dagger_{im\sigma}, d_{im\sigma}\right\}$ to a new expanded space, where more degrees of freedom are added to obtain these pre-factors in the hamiltonian.

During this thesis, I will use the slave-spin mean-field (SSMF) formalisms to explore the effects of local correlations in multiorbital systems, specifically in FeSCs and 2D materials. Up to date, H_{add}, i.e. the pair-hopping and spin-flip terms, seeEq. (1.22), is not considered

in the calculations, due to the fact that it is unknown how to include it, see **Appendix B**. In this technique, the original Hilbert space is expanded in a new space with pseudospin operators $\left\{O^{\dagger}_{im\sigma}, O_{im\sigma}\right\}$ and auxiliary fermion operators $\left\{f^{\dagger}_{im\sigma}, f_{im\sigma}\right\}$. After doing a couple of mean-field approaches, H_0 is rewritten for the auxiliary fermion operators H_f, while H_{dens} is rewritten for pseudospin operators H_{PS}. Both non-interacting H_0 and interacting H_{dens} hamiltonians have been then separated for each degree of freedom, $H = H_f + H_{PS}$, where these two hamiltonians are coupled via a set of orbital-dependent parameters, called Lagrange multipliers λ_m. The hamiltonians H_f and H_{PS}, written in Eq. (1.23) in the k-space, have to be solved self-consistenly. The values of Z_m and λ_m depend on the values of the pseudospin operators. A more extense and detailed discussion, as well as the derivation of Eq. (1.23), can be seen in **Appendix B**.

$$\begin{cases} H_f = \sum\limits_{k,mn,\sigma} \sqrt{Z_{m\sigma} Z_{n\sigma}}\varepsilon_{kmn} f^{\dagger}_{km\sigma} f_{kn\sigma} + \sum\limits_{k,m,\sigma} \left(\epsilon_m - \mu - \lambda_{m\sigma} + \lambda^0_{m\sigma}\right) f^{\dagger}_{km\sigma} f_{km\sigma} \\ H_{PS} = \sum\limits_{m,\sigma} h_{m\sigma}\left(O^{\dagger}_{m\sigma} + O_{m\sigma}\right) + \sum\limits_{m,\sigma} \lambda_{m\sigma}\left(S^z_{m\sigma} + \dfrac{1}{2}\right) + H^{PS}_{dens} \end{cases} \tag{1.23}$$

$\lambda^0_{m\sigma}$ is a correction factor which appear to recover the non-interacting limit, and H^{PS}_{dens} is the H_{dens} hamiltonian rewritten for pseudospin operators, see Eq. (B.9). Here, $Z_{m\sigma}$ appear as pre-factors which renormalize the band structure, as already pointed out.

Compared with other slave-particle theories, the SSMF formalisms [25, 38, 47] allow to treat multiorbital systems in an economical way, using only $2N$ pseudospin operators, while the slave-boson technique [45] normally increases its number of variables in an exponential way with N. The SSMF formalisms permit a treatment of non-degenerated orbitals problem, while slave-rotor technique [46] cannot account for such systems. During the last decade, the SSMF technique has become an useful tool to study the strength of correlations in multiorbital systems, specially by comparing SSMF with experimental results in FeSCs, see **Chapter 2**.

1.5 Unconventional superconductors

Superconductors are materials in which the resistivity at a certain critical temperature T_c goes to zero. They also repel the magnetic field (Meissner effect) [48]. In all the superconductors, the electrons are said to be paired, forming the so called Cooper pairs, and moving through the material without resistance.

Within all the superconductors, two main families can be distinguished: conventional and unconventional superconductors. Conventional superconductors are those systems in which the pairing instability is due to phonons, while for unconventional superconductors is still under debate. According to the Bardeen-Cooper-Schrieffer (BCS) theory for conventional superconductors, electron-phonon coupling is the responsible of this pairing instability. The pairing instability in unconventional superconductors is not yet known, and it is accepted that it does not occur due to phonons. It is believed that magnetic fluctuations play a major role [4]. Nowadays, the record T_c belongs to conventional superconductors, with $T_c^{max} \sim 260\,K$ at huge pressures $\sim 190 - 200\,GPa$ in LaH_x [49]. At ambient pressure, the maximum T_c is

found in unconventional superconductors, specifically in a high-T_c cuprate superconductor, $Hg_{0.8}Cu_{0.2}Ba_2Ca_2Cu_3O_{8+\delta}$ with $T_c^{max} \sim 134\,K$ [50].

A key difference between conventional and unconventional superconductors is the initial theory that explain the non-superconducting compound. In conventional superconductors, the non-superconducting (metallic) phase can be properly described by FLT and DFT band structure calculations. In most unconventional superconductors, the electronic correlations are important in the non-superconducting phase. For example, the parent compound (i.e. the system without doping or external perturbations) of the cuprates [51] or organic superconductors [52] are Mott insulators, while the parent compound of the heavy-fermion superconductors [51] or FeSCs [9, 53] are correlated metals. They also have a tendency to show ordered phases, such as magnetism (see below). In this thesis, I will focus on studying the non-superconducting (and not ordered) phase for various unconventional superconductors, specifically in FeSCs, as well as in 2D materials such as MA-TBG, see **Section 1.6.1**.

Generally, something similar occurs in most of the unconventional superconductors (see FIGURE 1.12): the parent (and at ambient pressure) compound develops a magnetic order, normally antiferromagnetic (AFM) or ferromagnetic (FM) (this is not strictly true in all the unconventional superconductors, as for example in $\kappa - (ET)_2Cu_2(CN)_3$ [52], as shown in FIGURE 1.12**(d)** or in $FeSe$ [54]), which disappears once doping or pressure is applied. When the magnetic dome disappears, a superconducting dome emerges. More complicated situations may also appear [51, 54]: presence of a pseudogap state, strange metal behaviors, asymmetry for electron and hole dopings, etc. However, the previous behavior of magnetism being supressed plus superconductivity emerging, seems to be robust feature in most of these systems, so in this introduction, I will focus the discussion around this general situation, specifically for AFM systems.

By following the phase diagram, it has been proposed that magnetic fluctuations are playing a major role in the superconducting instability [4]. An important question emerges when studying the strength of electronic correlations in order to describe the magnetic phase: should the model which describes the magnetism starts from a weakly correlated regime for delocalized electrons or from a strongly correlated regime for localized spins (as described in **Section 1.3.2**) to describe the magnetism [9]? Answering this question is crucial to understand the initial model used to describe the unconventional superconductivity.

In the weakly correlated limit, for highly delocalized electrons, magnetism is described by a tendency to diverge for the spin susceptibility χ_{spin} [8]. The spin susceptibility is derived from the Fermi surface, in which nesting features (a portion of the Fermi surface can be superposed on another portion when displaced by a wavevector $\vec{Q}$, called the nesting vector) promote the magnetic instability. For $\vec{Q} = \vec{0}$, the system shows FM behavior, while for non-zero $\vec{Q}$ it shows different AFM orders. In FIGURE 1.13**(a)**, calculations for χ_{spin} are shown for the same model as in FIGURE 1.1**(a)-(b)** for $LaFeAsO$, where only the 2D square layers of Fe atoms is considered (see discussion in **Section 1.5.2**). $\vec{Q} = (\pi, 0)$ and $(0, \pi)$, which is recognised as a stripe-like AFM order (parallel spin alignement in one axis defined by $\vec{Q}$, while antiparallel alignement in the perpendicular axis), see **Section 1.5.2**.

In the strongly correlated limit (large-U limit), for totally localized spins, magnetism is described by the minimum in the ground state energy obtained from a Heisenberg-like hamiltonian, similar to Eq. (1.20) [8]. In FIGURE 1.13**(b)**, Heisenberg model results for first J_1 and second J_2 neighbor exchanges are presented for the same compound as in FIGURE 1.13**(a)**, $LaFeAsO$. Depending on the ratio $J_1/2J_2$, different AFM order are promoted. For the ground state energy (right part of FIGURE 1.13**(b)**), $J_2 > J_1/2$ and γ refers to the angle

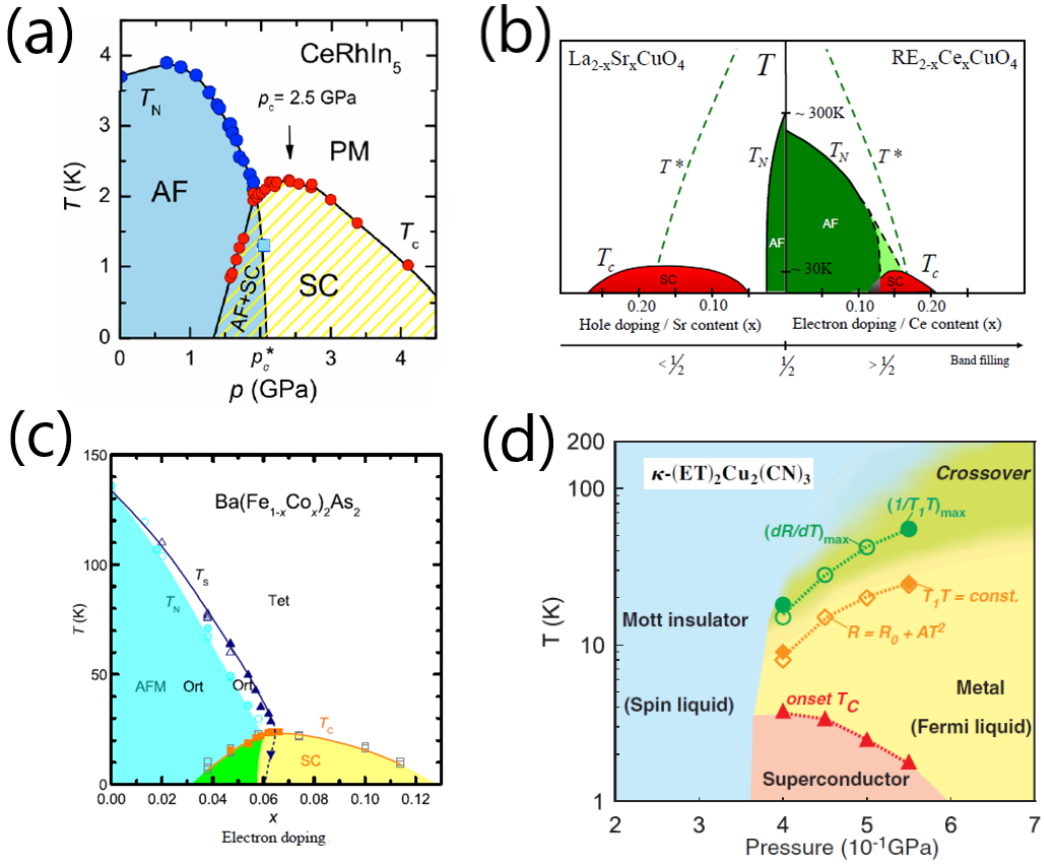

FIGURE 1.12: Phase diagrams for compounds belonging to the various families of unconventional superconductors: **(a)** heavy-fermion superconductors, **(b)** cuprates, **(c)** FeSCs and **(d)** organic superconductors. The superconducting dome usually emerges when an AFM phase is suppressed by doping or pressure. Both phases may coexist. Different metallic and insulating behaviors have been seen in these compounds. For the cuprates, an additional line T^* marks the existence of the pseudogap phase. For FeSCs, there is a tetragonal-to-orthorhombic transition at T_s as a prelude of the AFM phase, which is called the nematic transition. Both the nematic and AFM phases are suppressed with doping or when pressure is applied. In the organic superconductor case, the Mott insulating state can be accompanied by a spin liquid phase, which also suppress when doping or pressure is applied. Taken and adapted from [51, 52].

in the vertex of the 2D square lattice of Fe atoms, where for a perfect square $\gamma = 90\,°$, all the magnetic orders are degenerated. For $\gamma > 90\,°$, the AFM2 order (recognised as the checkerboard AFM order) is always the ground state.

In **Chapter 2**, we will explore the ongoing work in the moderately to strongly correlated metallic regime [9].

The superconducting order parameter (related with the supercoducting gap) ϕ, in absence of spin-orbit coupling, can be decoupled into $\phi = \psi^{orbital}\varphi^{spin}$, where ψ states the orbital symmetry (dictated by $L = 0, 1, 2, \ldots$) and φ the spin symmetry. Two different types of superconducting order parameter can be distinguished, spin-singlet, for which the orbital part has s-, d-, ... wave symmetry, and spin-triplet, for which it has p-, f-, ... wave symmetry. Spin-singlet superconducting order parameter is promoted by AFM correlations, while spin-triplet is promoted by FM correlations [4].

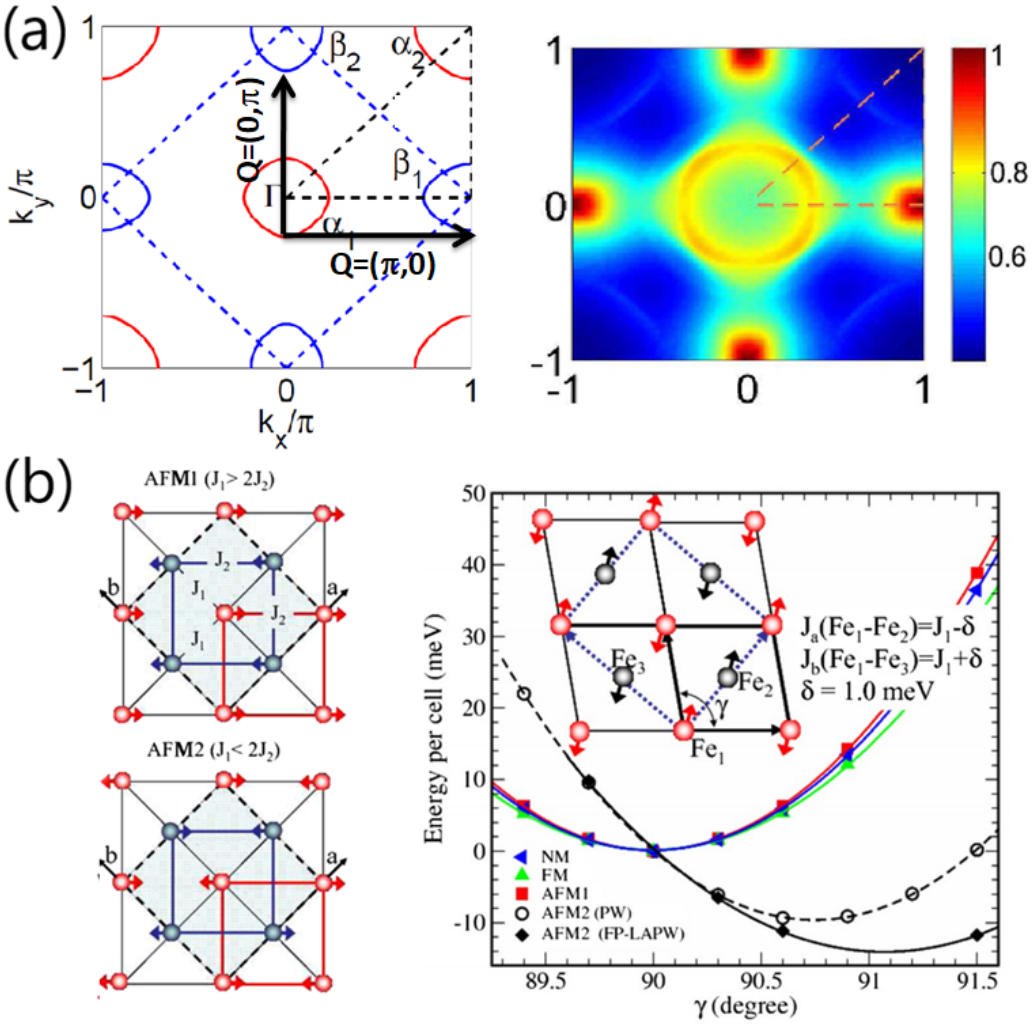

FIGURE 1.13: **(a)** Weakly correlated picture of magnetism for FeSCs, where the Fermi surface is plotted at the left and χ_{spin} is plotted at the right. Nesting vector is given by $\vec{Q} = (\pm\pi, 0)$ or $(0, \pm\pi)$, signaling a stripe-like AFM order. The scattering originates between α hole pockets $(0, 0)$ and β electron pockets at $(\pm\pi, 0)$ and $(0, \pm\pi)$. Taken and adapted from [2]. **(b)** Localized picture of magnetism for FeSCs, where the Heisenberg exchanges are plotted in the left and the energy per unit cell in terms of γ (where γ is the angle defined in the INSET) is plotted in the right. Depending on the ratio J_1/J_2, one or another AFM order is promoted, and for $J_2 > J_1/2$, AFM2 (checkerboard AFM) is always the ground state for $\gamma > 90\,°$. Taken and adapted from [55].

Spin fluctuation pairing theory is a weakly correlated theory in which spin fluctuations χ_{spin} enhance the pairing instabitility [56]. The symmetry of the superconducting order parameter is given by the largest eigenvalue of the pairing vertex $\Gamma_{\nu\mu}(\vec{k}, \vec{k'})$, where $\Gamma_{\nu\mu}$ is a scattering matrix (for two bands ν and μ which are connected by $\vec{Q}$) which depends on the interaction parameters and on the spin and the charge susceptibilities. The largest eigenvalue of $\Gamma_{\nu\mu}$ gives the largest contribution from spin fluctuations to the pairing instability.

In the case of strongly correlated theories, exchanges J_i are decoupled in the superconducting pairing channel with a mean-field approach. The superconducting order parameter symmetry will depend on the exchanges J_i.

In the next sections, I will very briefly discuss the general phenomenology of heavy-fermion and high-T_c cuprates superconductors, and more in detail about FeSCs.

1.5.1 Cuprates & other unconventional superconductors

The heavy-fermion superconductors were discovered in 1978 [57], in $CeCu_2Si_2$. In these systems [51], the T_c is usually low (not larger than $\sim 2K$) and the magnetic moment is high, in contrast with conventional superconductors, which do not show any magnetic moments preceeding the superconducting phase. In some of these compounds the effective masses can be up to thousands times the one expected from DFT calculations (they are strongly correlated metals), hence the name of the family. The crystal structure of heavy-fermion superconductors is formed by layers of the rare-earth element. In this system, both itinerant (coming from the f orbitals) and localized electrons coexist at the same time.

There are some heavy-fermion superconductors which show AFM ordering, and superconductivity emerges when magnetism is suppressed, such as $CeRhIn_5$ as shown in FIGURE 1.3**(a)**, while others show a FM order, like UGe_2 or $URhGe$. In the latter case, superconductivity is completely inside the FM dome [58], while for AFM compounds some coexistance between AFM order and superconductivity appears in some compounds [59], as shown in FIGURE 1.12**(a)**.

Later in 1986 [60], Bednorz and Muller gave birth to a new (and the most famous) family of unconventional superconductors, the high-T_c cuprates. They discovered superconductivity in $Ba_xLa_{2-x}CuO_4$ with $T_c \sim 30\,K$. Rapidly since then, a lot of effort for finding new superconductors in these family rose up T_c to $93\,K$ in $YBa_2Cu_3O_7$ (equivalently called YBCO, or Y-123) [61]. Up to date, the largest T_c in the cuprates was found in Hg-1223 under pressure, with $T_c \approx 164\,K$ [62]. The parent compound, i.e. the undoped system (see below), of high-T_c cuprates shows a Mott insulating behavior, and a checkerboard AFM phase for $T < T_N \sim 300\,K$, see FIGURE 1.14**(a)**. The unconventional superconducting dome emerges around the AFM phase for both electron- and hole-doped cuprates, as shown in FIGURE 1.12**(b)**. These systems are still under a huge debate about the physics and different phases that appear in them, as shown in FIGURE 1.14**(a)** for hole-doped cuprates.

The crystal structure of the cuprates is formed by square layers of CuO_2 and spacer layers [63]. In FIGURE 1.14**(b)**, the crystal structure of Hg-1201 is shown, where the spacer layers are made of Ba, Hg and O. CuO_2 layers control the physics of the cuprates. In the undoped systems [7], Cu atoms are filled with $n_e = 9$ electrons in 5 d orbitals, where $d_{x^2-y^2}$ remains at half-filling. This $d_{x^2-y^2}$ orbital is well separated from other orbitals, due to crystal field effects. Thus, the system is effectively behaving as a single-orbital system with one electron per site. Due to its quasi-2D crystal structure, cuprates can be modeled using a 2D square tight-binding model. As expected from the non-interacting limit, the system should behaves as a metal, with the Fermi level crossing the bands. Suprisingly, the undoped compounds are insulators, while at a certain doping, there is a insulator-to-metal transition.

More specifically, $d_{x^2-y^2}$ orbital hybridizes with p_x and p_y orbitals coming from O, forming bonding and antibonding orbitals as a linear combination in the CuO_2 plane. The CuO_2 antibonding orbital will remain at half-filling, then, single-band undoped cuprates can be seen as Mott insulators, as explained in **Section 1.3**. In fact, it is a charge-transfer (Mott) insulator, because the smallest direct gap opens between the valence O p bands and the upper Hubbard band (U pushes the lower Hubbard band below the valence O p band). Nevertheless, cuprates are generally referred to as Mott insulators.

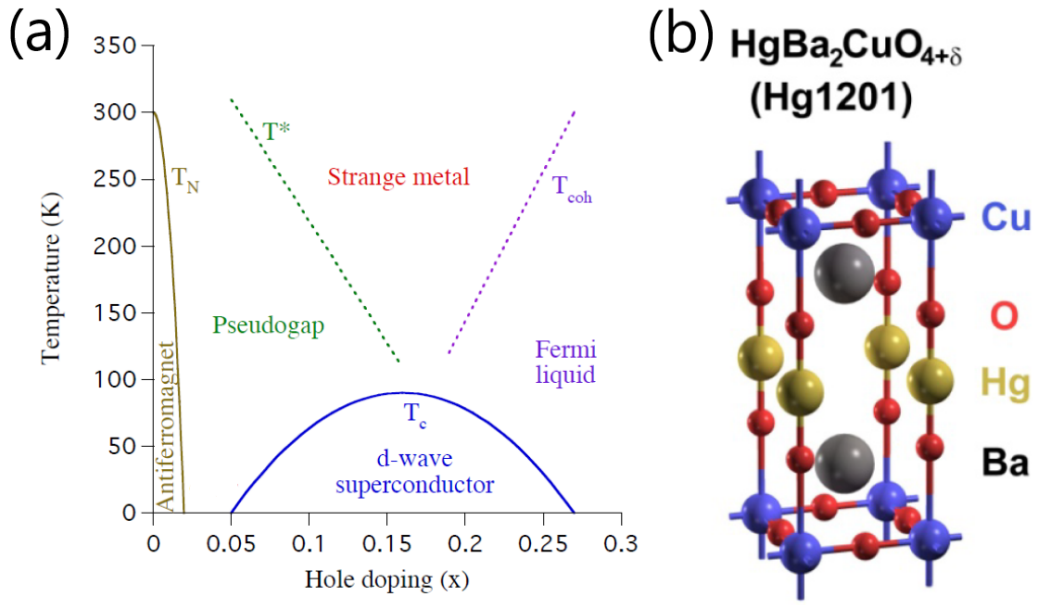

FIGURE 1.14: **(a)** Sketch of the hole-doped phase diagram for the cuprates, where various phases can be seen, like AFM checkerboard phase with a characteristic T_N, pseudogap state with T^*, the unconventional superconducting dome with T_c and the strange metal and Fermi liquid metal states. Taken and adapted from [51]. **(b)** Crystal structure of Hg-1201 cuprate superconductor, where CuO_2 layer is known to control the electronic properties of the cuprates. Taken and adapted from [63].

The undoped compound shows an AFM phase with checkerboard pattern $\vec{Q} = (\pi, \pi)$, as anticipated for 2D square lattices in **Section 1.3.2** for Heisenberg-like models [8]. In such a situation, AFM correlations are promoted for $J > 0$. The AFM phase is suppressed with doping.

The superconducting order parameter symmetry has been measured to be d-wave like, specifically $d_{x^2-y^2}$ [4]. It is believed that magnetic correlations are behind the pairing enhancement. As the undoped compound is a Mott insulator, most of the theories work with strongly correlated models, such as the Heisenberg-like models, like Eq. (1.20). Nevertheless, there are also weakly correlated models applied for the overdoped superconducing dome, i.e. the part which is closer to the Fermi liquid metal.

For the doped compound, at $T^* > T_N$ there is a crossover into an exotic pseudogap state [64–66]. In this state, the Fermi surface as observed in ARPES, exhibits an arc of gapless excitations, i.e. it is not closed in the BZ, as shown in FIGURE 1.15**(a)**. The Fermi surface in the weakly correlated metal state (see purple region in FIGURE 1.14**(a)**) is plotted in the background as a black line. There is still a lot of discussion about the origin of the pseudogap state and how it is the complete Fermi surface.

The strange metal regime is a metallic state with a linear-T term in the resistivity. This term does not follow the FLT expectations, see Eq. (1.15). A lot of effort has been put to understand this phase, and its origin it is believed to be related with the presence of a quantum critical point (QCP) inside the superconducting dome [67]. A QCP is a critical point found at $T = 0\,K$ which is driven by quantum fluctuations. The QCP has consequences at $T > 0\,K$, as shown in the phase diagram of FIGURE 1.15**(b)**.

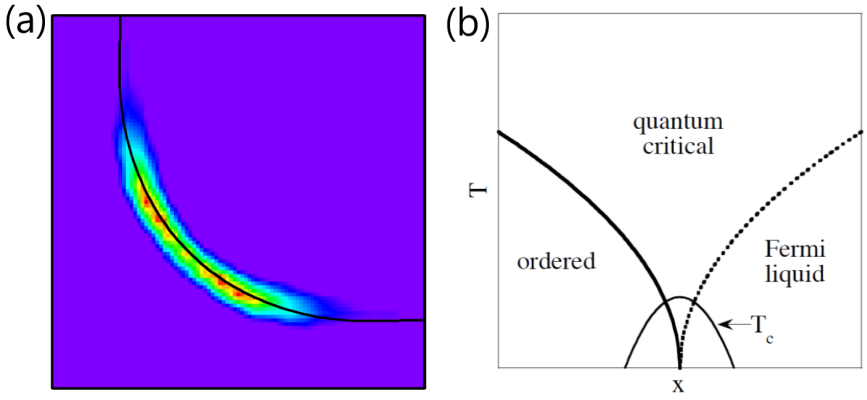

FIGURE 1.15: **(a)** Unclosed Fermi arcs appearing in the pseudogap state of cuprates. The Fermi surface of the normal metallic state is plotted in the background. **(b)** QCP phase diagram for the cuprates. The influence of the QCP at $T = 0\,K$ can be seen for $T > 0\,K$. Taken and adapted from [51].

1.5.2 Iron-based superconductors

In 2008 [68], high-T_c superconductivity was found in a new family of compounds, the FeSCs. They discovered $T_c^{max} \sim 26\,K$, in electron-doped $LaFeAsO$. Different crystal structures have been obtained, but they all share the same $FePn$ or $FeCh$ (with $Pn = As$, P and $Ch = S$, Se) layer, where Fe atoms are tetrahedrally coordinated by Pn or Ch atoms [53]. Usually, FeSCs are named according to their chemical formula, hence 1111 iron pnictide will refer to $LaFeAsO$ or to a related compound. Among the different compounds, it can be distinguished 1111 (like $LaFeAsO$), 111 (like $LiFeAs$), 122 (like $BaFe_2As_2$), 11 (like $FeSe$), 1144 (like $KCsFe_4As_4$), etc, iron pnictides or chalcogenides. I will study and discuss more in detail the 123 FeSCs compounds in **Chapter 4**, which shows various important differences with the other FeSCs compounds. I will focus in this introduction in the discussion for 1111 and 122 FeSCs.

FIGURE 1.16**(a)** shows the crystal structure for the 122 FeSCs, $BaFe_2As_2$ [69]. In this crystal structure, $FeAs$ (or $FeCh$) layer is sandwiched between spacers (in the case of the figure, the spacers are Ba atoms), similar to what happens in high-T_c cuprates. There are 2 Fe atoms per unit cell, as seen in FIGURE 1.16**(b)** for the $FeAs$ plane. Pnictogen and chalcogen atoms are tetrahedrally coordinating the Fe atoms.

The parent compound of FeSCs is metallic [9, 53]. The physics in FeSCs is controlled by Fe orbitals, see FIGURE 1.17**(a)**. In FIGURE 1.17**(a)**, the total and orbital-resolved DOS is plotted for $LaFeAsO$, where the interstitial refers to the electronic charge in between Fe atoms (this effect comes from As p orbitals influence). All the 5 d contributes around the Fermi level [70, 71], with similar crystal field energies, so effective tight-binding models should include, at least, 5 d orbitals [72–74], see FIGURE 1.17**(b)**, in contrast to single-orbital cuprates. When only taking into account the Fe atoms, the total number of bands is 10 (2 Fe atoms $\times$ 5 d orbitals). The parent compound has 6 electrons per Fe atom, $n_e = 6$ (which is one extra electron than half-filling, which is defined as $n_e = N = 5$, where N is the number of d orbitals per Fe atom). Some authors have argued about the importance of the Pn or Ch atoms, and there are claims that p orbitals should be included in the minimal tight-binding model, giving rise to the d, dp and dpp models. In any case, d model is shown to give good enough predictions for most FeSCs, and here I will focus on the d model phenomenology. Total bandwidth is estimated $W \sim 4 - 5\,eV$ for d models. In the tetragonal phase, d_{zx} and

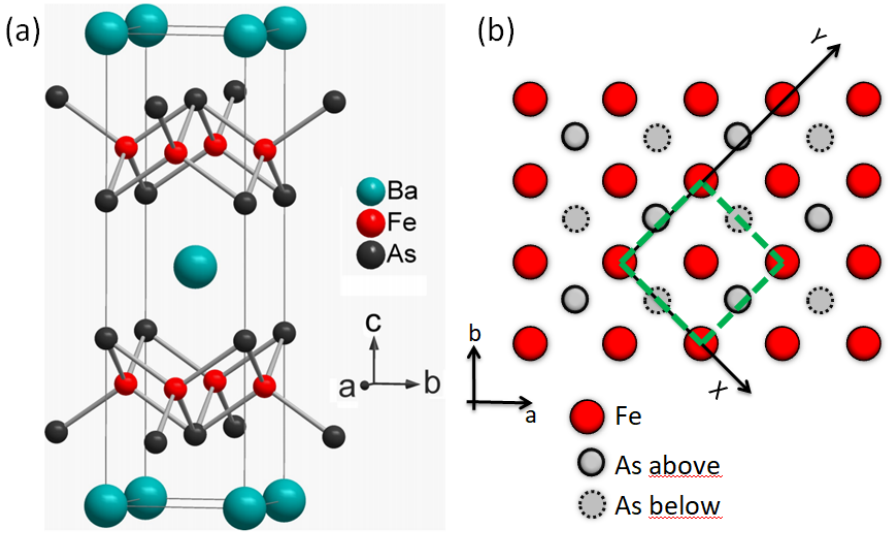

FIGURE 1.16: **(a)** Crystal structure and Fe layer in 122 iron arsenide $BaFe_2As_2$, where $FeAs$ layers are separated by spacer Ba. Taken and adapted from [69]. **(b)** $FeAs$ layer with unit cell (green dashed line) included with 2 Fe atoms per unit cell. Fe atoms form a 2D square lattice and are tetrahedrally coordinated by As atoms. Adapted from [5].

d_{yz} are degenerated, as shown in FIGURE 1.3**(b)**. Fermi surfaces shows a quasi-2D behavior, see FIGURE 1.17**(c)**, where almost cylindrical pockets along Z can be seen. Then, the tight-binding model for FeSCs is usually written for the 2D square layer of Fe atoms. The BZ for the 2 Fe atoms in the unit cell is also called folded BZ (see next paragraph), and it is formed by two hole pockets centered at $\Gamma = (0,0)$ and two electron pockets at $M = (\pi,\pi)$. In FIGURE 1.17**(d)**, I present the 2D Wannier parametrization of the 3D bands obtained for $FeSe$. Some discrepancies can be seen, but both the bandwidth and the Fermi surface obtained in DFT calculations are approximately reproduced by the Wannier tight-binding fitting.

An useful procedure can be done to reduce the difficulty of the problem, the so called unfolding of the BZ [74]. This is a 45° rotation plus an unfold in the y direction of the unit cell. By this procedure, the BZ has enlarged, while the unit cell is reduced, with respect to their original shapes in the folded BZ. After this unfolding, the number of atoms in the unit cell is reduced to 1 Fe atom. So instead of having 10 bands, 5 bands are obtained for the Fe atom with 5 d orbitals. In FIGURE 1.18**(a)**-**(b)**, I have sketched this procedure, labeling each folded and unfolded BZ situation with $2Fe$ or $1Fe$, respectively. I also show the resulting BZs in both folded and unfolded cases in FIGURE 1.18**(c)**. The 2D Fermi surface for both cases are shown in FIGURE 1.18**(d)**, **(e)**, where two hole pockets are centered at Γ for both cases, whether two electron pockets appear at M_{2Fe} and X_{1Fe}/Y_{1Fe}.

Most of the FeSCs are AFM metals with $T_N \sim 100-150\,K$ with a stripe-like order $\vec{Q} = (\pi, 0)$ and $(0,\pi)$ for the unfolded BZ [9], as shown in FIGURE 1.18**(f)**. Due to its metallic character, some approaches are based on a weakly correlated picture of magnetism [2, 77–79], in which χ_{spin} is peaked at $\vec{Q}$, as shown in FIGURE 1.13**(a)**, with $\vec{Q}$ being the scattering between Γ hole and X/Y electron pockets. On the other hand, there are calculations in the large-U limit [55, 80] for FeSCs with first J_1 and second J_2 neighbor exchanges, where the $(\pi, 0)$ ground state requires $J_2 > J_1/2$, as shown in FIGURE 1.13**(b)**. The magnetic moment measured by neutron scattering experiments is $\sim 0.5 - 1\,\mu_B$ per Fe atom. From the large-U limit

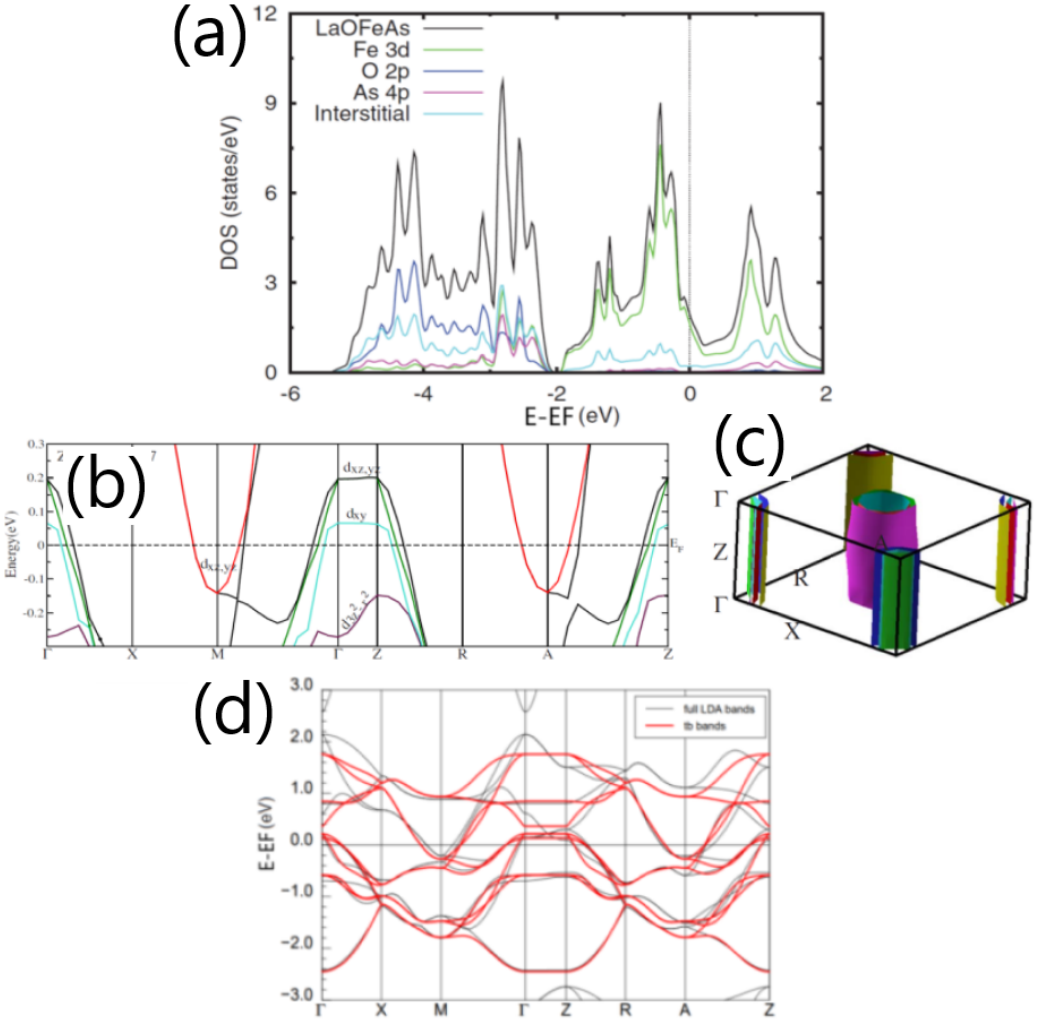

FIGURE 1.17: **(a)** Total (black line) and orbital-resolved (color lines) DOS. Fe d orbitals mostly contribute between -2 and $2\,eV$, with a small contribution from electronic charge in the interstitial region of Fe atoms. **(b)** DFT band structure around the Fermi level with d orbital character included, and **(c)** 3D Fermi surface for undoped $LaFeAsO$ at $n_e = 6$, remarking the quasi-2D character of FeSCs. Taken and adapted from [71]. **(d)** 2D Wannier tight-binding fitting (red line) of the 3D band structure (black line) for $FeSe$. Taken and adapted from [75].

calculations, the expected magnetic moment should be $= 4\,\mu_B/Fe$, much larger than the observed experimentally. On the other hand, DFT calculations predicted magnetic moments $\sim 1.5 - 2\,\mu_B/Fe$, also larger than the obtained experimentally.

ARPES and quantum oscillations (QOs) experiments [42] showed the existence of quasi-particles with $m^*/m_0 \sim 2 - 3$ ($Z \sim 0.3 - 0.5$) for the parent compound of FeSCs, hence emphasising the importance of electronic correlations. Due to the multiorbital character of FeSCs, it has been argued that both weakly and strongly correlated electrons coexist at the same time in different orbitals. In this situation, magnetic moments at Fe sites appear due to Hund's coupling J_H polarization [35]. I will discuss more in detail these ideas in **Chapter 2**.

AFM transition follows a previous tetragonal-to-orthorombic structural transition at $T_s \geq T_N$, also known as nematic transition [54], which breaks the x and y symmetry, hence the degeneracy between d_{zx} and d_{yz} orbitals. It has an electronic origin, rather than driven by

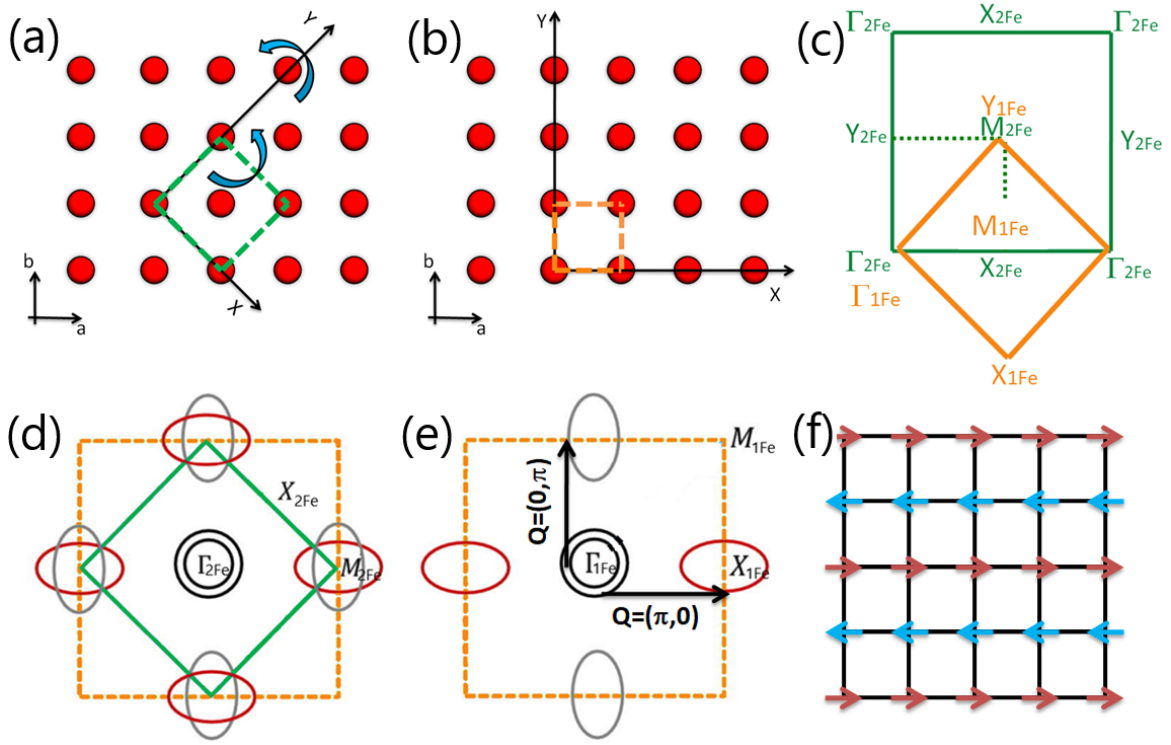

FIGURE 1.18: **(a)**, **(b)** Sketch of the unfolding procedure, with unit cell included in both the folded (green dashed lines) and unfolded BZ (orange dashed lines), **(c)** folded (green square) and unfolded (orange square) BZs. Adapted from [5]. 2D Fermi surfaces in both **(d)** folded and **(e)** unfolded BZ for FeSCs. Taken and adapted from [76]. I included the nesting vectors $\vec{Q} = (\pi, 0)$ and $(0, \pi)$. **(f)** Stripe-like AFM order in 2D square of Fe atoms. Note that stripe aligned in X or Y directions is equivalent for the tetragonal phase (Fe atoms form a perfect square). Adapted from [5]

phonons. Whether it comes from orbital/charge fluctuations or spin fluctuations is something still under debate. The spin fluctuations seem more plausible due to the fact that magnetism and nematic phases suppresses following the same trend.

Due to the metallic character of FeSCs, spin fluctuation pairing theory was proposed to obtain the superconducting order parameter in FeSCs [56]. Magnetic fluctuations with $\vec{Q} = (\pi, 0)$ promotes a spin-singlet superconducting order parameter [77]. Experiments confirmed the spin-singlet superconducting order parameter symmetry. In FIGURE 1.19, the $s_{\pm}$-wave symmetry proposed for FeSCs is shown. $s_{\pm}$-wave symmetry is present on most of the FeSCs.

I conclude by noting that there are still many questions open in FeSCs, in particular for the initial model needed to describe magnetism. In future chapters, I will study local correlations in order to shed light about the strength of such correlations in these systems.

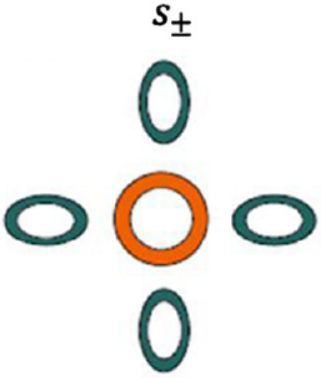

FIGURE 1.19: Schematic superconducting order parameter $s_{\pm}$ symmetry obtained for FeSCs. The different color marks the different sign for the superconducting order parameter. Taken and adapted from [56].

1.6 2D materials

In this section, I will follow the discussion made in [10, 11] for the role of electronic correlations in 2D materials. In the last decades, 2D materials have received a lot of attention, specially since the discovery of how to produce graphene by exfoliating graphite. 2D materials can be grouped in: graphene-like systems, hexagonal boron nitride (hBN), phosphorene, transition metal dichalcogenides (TMDCs), such as MoX_2, NbX_2, TaX_2, etc (with $X = S$ or Se), transition metal monochalcogenides (TMMCs), like $FeSe$ and SnS, and transition metal trichalcogenides (TMTCs), such as TiS_3. Other 2D materials, like Fe_3GeTe_2, have been recently isolated. These systems are simple to produce in a 2D version due to the weak van-der-Waals (vdW) forces acting between the layers that form the 3D system, which permit an easy exfoliation of the layers from the bulk crystal, and an easy adaptation to the substrates. Then, it is also simple to build a huge variety of heterostructures to produce different technological devices. In FIGURE 1.20, the crystal structure and band structure of various 2D materials, such as graphene, hBN, phosphorene and MoS_2, are presented.

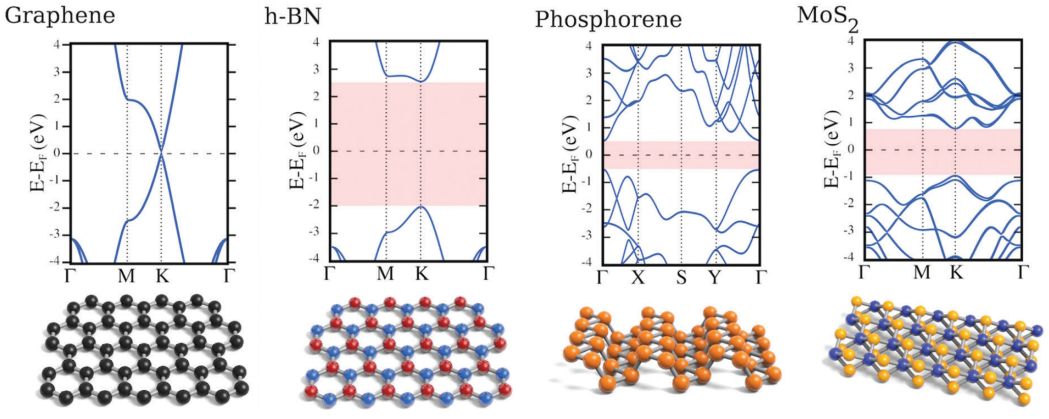

FIGURE 1.20: Crystal and band structures for various 2D materials: **(a)** graphene, **(b)** hBN, **(c)** phosphorene and **(d)** MoS_2. Graphene shows the famous Dirac points at K due to the hexagonal symmetry of its lattice. The Fermi velocity (in the non-interacting limit) $v_0 = \nabla_k E_k = 10^6\, m\, s^{-1}$ indicates the huge mobility of the electrons in graphene. The other compounds are semiconductors whose gap can be tuned in different ways (see main text). Taken and adapted from [10].

One of the most important properties of 2D materials is that they are very sensible to changes in the enviroment that surrounds the surface (because the portion of atoms in the surface is comparable to those in the volume). Then, the number of layers N_L, different substrates, or dielectric environments, and strain effects will change the electronic properties (in addition to doping or pressure). Moreover, doping can be induced in a non-invasive way by an external gate voltage, rather than by implementation or diffusion as in 3D materials. In FIGURE 1.21**(a)** and **(b)**, the bandgap evolution for phosphorene [81] in terms of N_L and for MoS_2 in terms of strain [82], respectively, are shown.

The interaction effects will be important in some of these systems. In FIGURE 1.21**(c)** and **(d)**, we can see the phase diagrams of $1T - TaS_2$ when pressure is applied [83] and the hole-doped magic-angle twisted bilayer graphene (MA-TBG) [84]. Superconducting domes emerge in both cases when the Mott insulating phase is suppressed, similar to what happens in high-T_c cuprate superconductors.

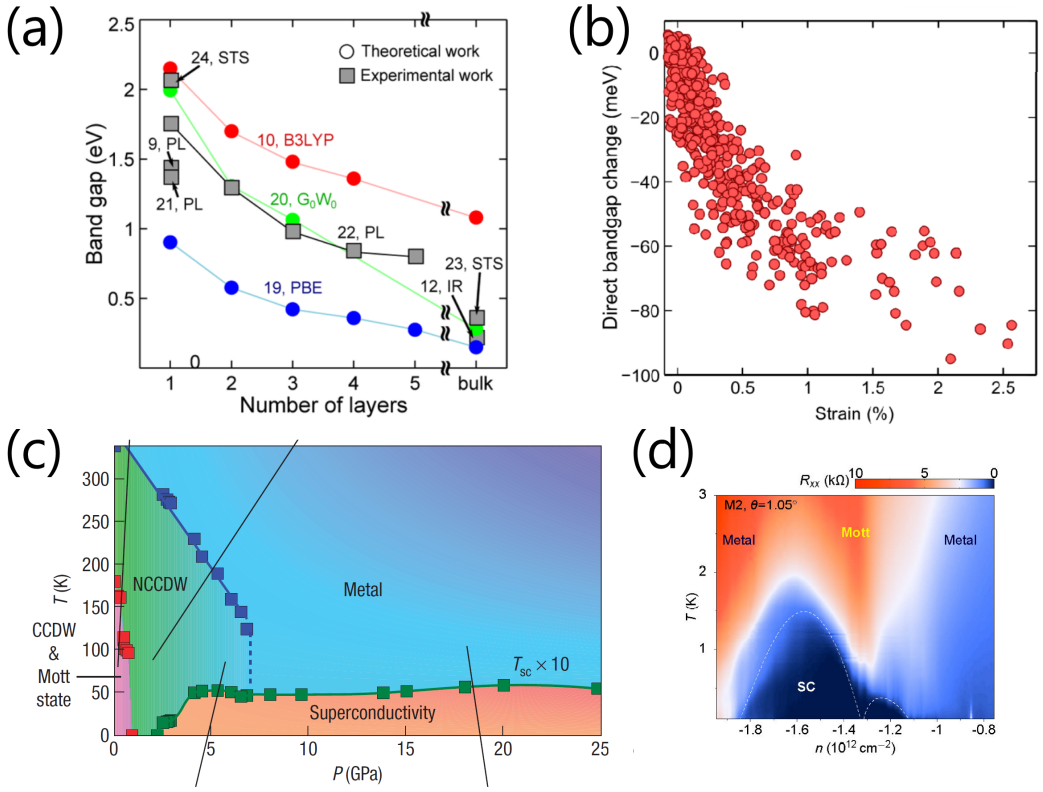

FIGURE 1.21: **(a)** Band gap versus N_L for phosphorene. Both theoretical and experimental results are included. Band gap shows a exponential decay with N_L. Taken from [81]. **(b)** Direct band gap verus strain for MoS_2. Again, band gap shows a exponential decay with strain. Taken from [82]. **(c)**, **(d)** Pressure and doping phase diagrams for $1T-TaS_2$ and MA-TBG, respectively. Both compounds show a rich phase diagram, where superconductivity emerges when a Mott insulating state is supressed. Non-invasive doping can be induced in 2D materials by an external gate voltage. Taken and adapted from [83, 84].

There are still a lot of questions open for the role of the electronic correlations in 2D materials. In this thesis, I am going to focus on studying the effect of local correlations in MA-TBG, and some properties of Fe_3GeTe_2 (FGT). Here, I will briefly discuss the basic phenomenology of MA-TBG, and in **Chapter 5** we will get more into the details after the works by *Cao et al.* were published [84, 85]. In **Chapter 6**, I will study FGT and the current status of our calculations in this system.

1.6.1 Twisted bilayer graphene (TBG)

In this section, I will discuss the known phenomenology of twisted bilayer graphene systems [86–93], before the discoveries by Pablo Jarillo's group [84, 85].

Graphene is formed by a hexagonal lattice of carbon atoms, in which the unit cell is made of two carbon atoms, usually called A and B. The band structure of graphene is formed by two linear dispersions which cross at the so called Dirac points, which corresponds to the K and K' points of the hexagonal BZ (see below) [94]. The region close to each Dirac point is called valley, and these two valleys K and K' are spin-degenerated.

Twisted graphene systems are heterostructures of N_L graphene layers rotated by a certain set of angles θ_{N_L-1}. In these circumstances, a moiré pattern (also called superlattice) emerges, which is described by the alignement of atoms in each graphene layer. For example, in twisted bilayer graphene (TBG), we can distinguish between AA regions, where A atom of the bottom graphene layer is aligned with the A atom of the top layer, AB (and BA) regions, where A (B) atom of the bottom layer is aligned with B (A) atom of the top one, see FIGURE 1.22**(a)**. Similar reasoning will result for twisted trilayer graphene (TTG) [95]. Note that twisted heterostructures might be built of different 2D materials. During this thesis I will focus on TBG.

FIGURE 1.22**(a)** shows the corresponding superlattice that emerges in TBG, where AA regions form a triangular symmetry superlattice and AB/BA regions form a hexagonal symmetry superlattice. The superatomic distance λ depends on the rotation angle θ, $\lambda \sim a/(2\sin(\theta/2))$, where $a = 2.46\,\text{Å}$ is the graphene lattice parameter. Due to the emergence of a larger superlattice, the BZ is reduced, which receives the name of mini-BZ, see FIGURE 1.22**(b)**. In the band structure of TBG, there are two doubly-degenerated Dirac points located at K_ξ^l with $l = 1, 2$ being the layer index for each $\xi = \pm$ valley [89, 93]. The parent compound of TBG has the Fermi level ε_F located at these Dirac points (similar to single-layer graphene).

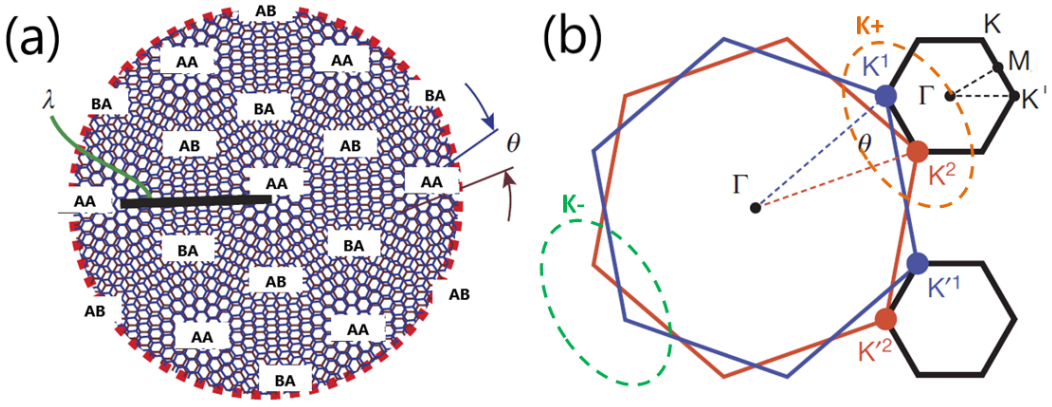

FIGURE 1.22: **(a)** Superlattice and **(b)** resulting mini-BZ (black hexagons) of TBG at a given rotation angle θ. The size of the mini-BZ is inversely proportional to the size of the superlattice λ. AA, AB and BA regions included as a eye-guide. There are two doubly-degenerated Dirac points located at K_ξ^l with $l = 1, 2$ being the layer index for each $\xi = \pm$ valley. Taken and adapted from [85].

An interesting behavior appears for the band structure in terms of the rotation angle θ, see FIGURE 1.23. Two different regimes can be found: for $\theta > 6\,°$, both graphene layers behave independently of each other, while for smaller angles $\theta < 6\,°$, both layers start to interact.

The layer interaction is identified by a hybridization hopping, which will produce gaps, called the superlattice gaps, in the band structure. Assuming that there is no corrugations (out-of-plane distortions in the interlayer space in such a way that the distance is the widest in AA regions and the narrowest in AB/BA regions between the two layers) this behavior can be understood by an angle-dependent hybridization hopping $w(\theta)$ between the layers, where around the Dirac points [89]:

$$w(\theta) \approx \begin{cases} 0 & if\ \theta > 6\,^\circ \\ \dfrac{\hbar v_0 k_\theta}{2} & if\ \theta < 6\,^\circ \end{cases} \tag{1.24}$$

With $k_\theta \propto \sin\theta$ and $v_0 = 10^6 ms^{-1}$ the Fermi velocity of non-interacting single-layer graphene (proportional to m_0). In the hybridized case, the hybridization gaps appear between the bands around the Fermi level and the higher-in-energy bands, see FIGURE 1.23**(b)**. For a set of slightly incommensurate angles below $2\,^\circ$, the bandwidth W of the bands around the Fermi level strongly reduces down to a few dozens of meV, see FIGURE 1.23**(c)**. In this situation, the renormalized (due to the interacting layers) Fermi velocity of TBG is $v_F \to 0$. The angles at which these flat bands emerge are called the magic angles θ^{magic}, see FIGURE 1.23**(d)**. The first magic angle occurs at $\theta_1^{magic} \approx 1.05\,^\circ$.

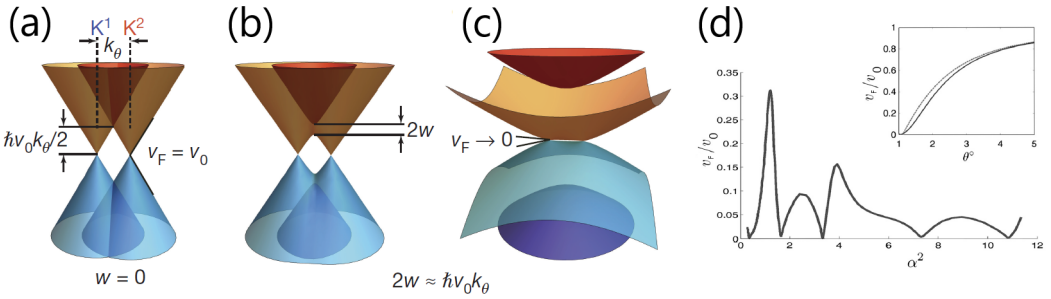

FIGURE 1.23: **(a)-(c)** Sketch of the band evolution for TBG. For $\theta > 6\,^\circ$, two independent graphene layers are obtained, as shown in **(a)**. For $\theta < 6\,^\circ$, hybridization gaps of size $\approx 2w$ emerge between the bands around the Fermi level and the higher in energy bands. For even smaller angles $\theta < 2\,^\circ$, a set of incommensurate magic angles appears at which $v_F \to 0$, and flat bands emerge. Taken and adapted from [85]. **(d)** v_F/v_0 in terms of $\alpha^2 \sim \theta^{-2}$, showing the cyclic behavior of v_F/v_0. The first magic angle appears at $\theta_1^{magic} \approx 1.05\,^\circ$. INSET: v_F/v_0 versus θ, where it can be seen the dependence with the rotation angle, for $\theta > 6\,^\circ$, $v_F \sim v_0$, and both graphene layers behave as isolated one from another. Taken from [89].

A popular approach to describe the band structure of TBG, based on a low-energy model (also called low-energy continuum model), is used to describe the flat bands dispersion around the Dirac points [89, 93]. It can be shown that the intervalley hopping parameters will decay exponentially, hence there is an approximate ξ valley degeneracy for K_ξ^l Dirac points. Adding the spin degree of freedom, the TBG non-interacting hamiltonian can be build by 4×4 block matrices, with non-zero diagonal 4×4 blocks H_ξ, and zero off-diagonal blocks. The derivation of the non-interacting hamiltonian for the other valley H_- can be done by changing $\vec{k} \to -\vec{k}$ in the equations of H_+ (see below). H_ξ is written in the lattice sites basis of each layer, $\{A_1, B_1, A_2, B_2\}$:

$$H_0 \approx \begin{pmatrix} H_+ & 0 \\ 0 & H_- \end{pmatrix} \to H_\xi \approx \begin{pmatrix} h^1 & h^{\theta\,\dagger} \\ h^\theta & h^2 \end{pmatrix} \tag{1.25}$$

where h^l (with $l = 1, 2$) are the intralayer hamiltonians and h^θ is the interlayer hamiltonian. These terms can be written as:

$$\begin{aligned} h^l &= -\hbar v_0 \left(\vec{k} - \vec{K}_\xi^l\right) \cdot (\xi\sigma_x, \sigma_y) \\ h^\theta &= \begin{pmatrix} h_{A_2A_1} & h_{A_2B_1} \\ h_{B_2A_1} & h_{B_2B_1} \end{pmatrix} \end{aligned} \tag{1.26}$$

where σ_x and σ_y are the 2×2 Pauli spin matrices. h_{ij} terms depend on the angle-dependent interlayer hopping $w(\theta)$. In fact, it can be proved there are two angle-dependent interlayer hoppings w and w' contributing to the diagonal and off-diagonal elements of h^θ, respectively. $w' \neq w$ accounts for corrugation effects in TBG [93]. If the two graphene layers do not have any interlayer corrugation, then $w' \neq w$. In FIGURE 1.24, the band structure close to the Dirac points is shown for both cases at the first magic angle are shown. Note that for $w' = w$, there is no superlattice gap (the gap between the flat bands and the next bands) in the valence ($E < \varepsilon_F$) part, but for $w' \neq w$ both superlattice gaps are recovered, hence remarking the importance of corrugation effects in MA-TBG. The resulting flat bands show a very flat dispersion around K^l, and reach extreme values at Γ. Note that the Fermi level ε_F is located at the Dirac points K^l. In total, there are 4 bands forming the flat bands.

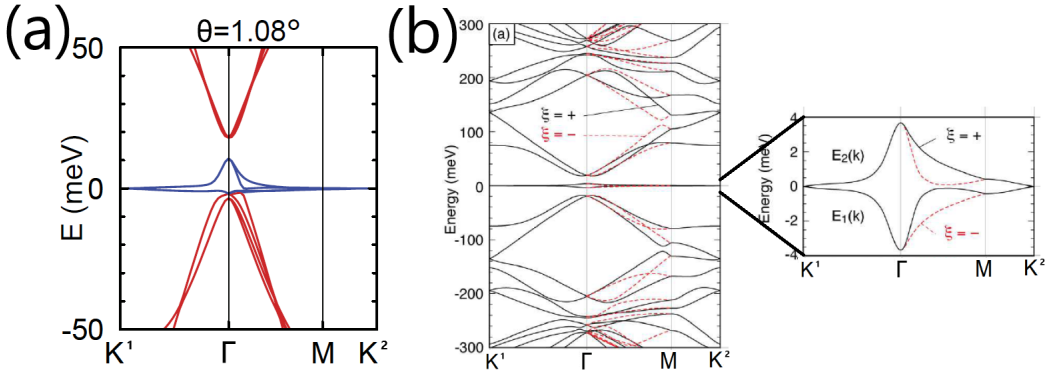

FIGURE 1.24: Flat bands at the first magic angle for **(a)** non-corrugated and **(b)** corrugated effects included in the low-energy continuum model. The flat bands around K^l with $l = 1, 2$ show a parabolic dispersion, and reach extreme values at Γ. Dirac points at K^l are doubly-valley degenerated. In total, there are 4 bands forming the flat bands. Taken and adapted from [85, 93].

In **Chapter 5**, I will discuss more extensively the current status of MA-TBG experimental and theoretical advances.

1.7 Organization of this thesis

In **Chapter 2**, I will present an introduction to the electronic correlations in multiorbital systems by considering only the effects of local correlations. First, I will focus in the case of equivalent orbitals systems, and I will review the behaviour of Z_m in terms of U, J_H and n_e/N. A new regime called the Hund metal is found for a certain region of the $(U, J_H, n_e/N)$ space. This metallic state shows sizable electronic correlations (Z_m values are low), the atoms are maximally spin polarized and there is an orbital decoupling behavior. Secondly, I will study the effect of local correlations in real materials, with special focus on FeSCs.

The experimental features to identify the local correlation effects in real materials are also presented at this point.

Chapters 3, **4**, **5** and **6** are devoted to present the contributions done during the thesis.

In **Chapter 3** [96], I will show the results obtained for the chromium pnictide analogue of the FeSCs, where Cr atoms are considered instead of Fe ones. The main idea in this work is to present a plausible new unconventional superconducting family based on chromium instead of iron, where the main difference is the electronic filling of each transition metal atom ($n_e = 6$ electrons in 5 d orbitals in Fe, and $n_e = 4$ in 5 d orbitals in Cr). We proposed that, for a similar crystal and band structure, and a similar strength of the electronic correlations, Cr-based materials could host unconventional superconductivity. First, I will check if the behavior of increasing electronic correlations when moving towards half-filling ($n_e = 5$ electrons in 5 d orbitals) in a multiorbital system (see **Chapter 2**) occurs for a 5 d orbitals tight-binding model (proposed for FeSCs) from both $n_e = 6$ and $n_e = 4$. As an example, we considered $LaCrAsO$. Then, DFT band structure calculations, and a Slater-Koster tight-binding model are obained for $LaCrAsO$. I will study the effects of local correlations by using SSMF Z_2 formulation. The magnetic and superconducting instabilities are studied using the renormalized band structure and by using multiorbital Random Phase Approximation (RPA). We will conclude by stating that, due to the presence of similar values for Z_m, and AFM tendencies, a new family of unconventional superconductors might be found in Cr pnictides and chalcogenides.

In **Chapter 4** [97], I will study the effect of local correlations in the quasi-one dimensional 123 FeSC, $BaFe_2S_3$. The differences of this material with respect to other FeSCs is that the crystal structure is quasi-1D and the parent compound is an insulator. The superconductivity emerges when applying pressure at the same time that the metallicity is recovered. I use the tight-binding proposed for this material [98] for zero pressure and the pressure around which superconductivity emerges. I will calculate local correlations by using SSMF $U(1)$ formulation. At zero pressure, the system shows very strong correlations ($Z_m \sim 0.03 - 0.06$) for d_{zx}- and d_{yz}-like orbitals, much stronger than in other quasi-2D FeSCs. For the pressure at which superconductivity emerges, Z_m values are close to those of other FeSCs. I will show that, contrary to other FeSCs, the Fermi surface suffers a huge reconstruction due to local correlations. This reconstruction will affect the typical weakly correlated approaches, which are based on the Fermi surface topology.

In **Chapter 5** [99], I will study the nature of the insulating states found in MA-TBG. I will consider a hexagonal lattice symmetry with two orbitals and nearest neighbor hoppings ($t \sim 2meV$) tight-binding model, in order to mimic the four bands obtained for the flat bands. A discussion about the current status of experimental and theoretical calculations in MA-TBG is presented. I will check if the experimental observations [85] can be explained in terms of a Mott insulating state including only local correlations, in particular: increasing the external magnetic field B and the temperature T promotes metallicity, and the gap found $\sim 0.3\,meV$ is two orders of magnitude smaller than the bandwidth $\sim 10\,meV$. For this work, I have implemented the Zeeman term in the SSMF $U(1)$ formalism and study the effect of B in the $Z_{m\sigma}$. I will conclude by stating that local correlations cannot explain the experimental features. We will propose to go beyond local correlations, including non-local correlations to explain the behavior found in this system.

In **Chapter 6**, I will present my current calculations in the 2D room-temperature itinerant ferromagnet Fe_3GeTe_2 (FGT). I will comment the recent results in bulk and low dimensional

FGT, and the importance of finding a room-temperature ferromagnet free of rare-earth elements. I will perform DFT calculations for this material, and I will compare the band structure for bulk and single-layer FGT. I will then derive the Wannier tight-binding model for single-layer FGT, including Fe d, Ge p and Te p orbitals.

The final **Chapter 7** is devoted to the conclusions extracted from this thesis.

In the Apendices section, **Appendix A** gives a brief introduction of DFT and Wannier parametrization calculations, **Appendix B** gets into the physical details and mathematical derivations of SSMF, and **Appendix C** gives some useful mathematical proofs.

Chapter 2

Local electronic correlations in multiorbital systems: the Hund metal

2.1 Introduction

In this chapter, I summarize the most important results for local correlations in multiorbital systems. I will follow the discussions in [5, 9, 15, 26–37, 100–104]. But before starting the discussion for multiorbital systems, I am going to summarize some results from the previous chapter for the effects of local correlations in single-orbital systems, see **Section 1.3**.

I have already presented the Hubbard hamiltonian in Eq. (1.19) for onsite interactions and single-orbital systems [105–108]. The local correlations physics which control this hamiltonian will depend on the ratio U/W, with U being the onsite Hubbard interaction (related with the double occupancy interaction energy cost) and W the bandwidth (related with the kinetic energy gain of the electrons when they hop through the system). At half-filling (one electron per atom, i.e. $n_e = 1$), the system can undergo a metal-to-insulator transition, called the Mott transition, at a critical interaction U_c at which the electrons become localized at the atomic sites. The U_c value depends only weakly on the lattice symmetry, and it ranges $U_c \sim 1.5 - 2W$ at $T = 0\,K$ [17]. The insulating state is called the Mott insulator. Out of half-filling ($n_e > 1$ or $n_e < 1$), the system is metallic for all U.

The quasiparticle weight Z is the order parameter for the Mott transition [5]. In the local correlations picture, it can be shown that $1/Z = m^*/m_0$, see Eq. (1.13), where m_0 is the non-correlated effective mass (obtained from the tight-binding model) and m^* is the correlated effective mass. The quasiparticle weight evolves from $Z = 1$ ($m^* = m_0$) in the non-correlated metal to $Z = 0$ ($m^* \to \infty$) in the Mott insulator. When $0.7 < Z \leq 1$ ($1 \leq m^*/m_0 < 1.4$), the system is said to be a weakly correlated metal, and descriptions based on a DFT band structure calculations and tight-binding models will give good predictions. At $0 < Z \lesssim 0.3$ ($3 \lesssim m^*/m_0 < \infty$), the system is a strongly correlated metal, and DFT calculations and tight-binding models will leave out the most important local correlations effects. In between, a moderately correlated metal exits with $0.3 < Z \lesssim 0.7$ ($1.4 \lesssim m^*/m_0 < 3$).

In the Brinkman-Rice picture of the Mott tansition[1] [4, 5], Z acts as a renormalization prefactor of the band energy, hence when Z is reduced the bandwidth W will also shrink, see FIGURE 1.7**(b)**. When varying the filling of the system (for example, by doping), this will produce a non-rigid band shift of the Fermi level ε_F, in contrast with what happens in the non-correlated limit, where ε_F is rigidly shifted when the filling varies.

In single-orbital systems, the Mott insulating state is characterized by a vanishing quasiparticle weight $Z = 0$ and a suppression of local charge correlations C_{n_T}, see FIGURE 1.10. Due to the clear relation between Z and C_{n_T}, a low Z value signals the charge localization in each atom, with a low C_{n_T} value. We will see that in multiorbital systems, this equivalence is not straightforward.

In order to study local correlations effects in multiorbital systems, I will discuss the solutions for Eq. (1.21), mainly using slave-spin mean-field (SSMF) formalisms, which are briefly described in **Section 1.4.1**, and more in detail in **Appendix B**.

In the SSMF framework, H_{add} is neglected, see Eq. (1.22). Up to date, it is not known how to properly include it in SSMF calculations. Also, I will assume: (i) orbital-independent interactions U, U', J_H and J' and (ii) rotational invariance relations are invoked $U' = U - 2J_H$ and $J' = J_H$ (even if the orbitals are not fully spherical) [23]. U and J_H are positive (see **Chapter 5** for negative J_H discussion), and the maximum value $J_H/U = 1/3$, which occurrs to maintain the interaction $(U - 3J_H)$ (see Eq. (1.22)) repulsive. In SSMF, the two coupled hamiltonians of Eq. (1.23) have to be solved self-consistenly, as described in **Section B.5**. Then, for spin-degenerated systems, the orbital-dependent quasiparticle weights Z_m can be obtained in terms of the interaction parameters U and J_H, as well as in terms of the number of electrons per atom n_e and the number of orbitals per atom N. Equivalently, I will use the total filling per atom, orbital and spin $x = n_e/2N$ defined between $x \in [0, 1]$, where $x = 0$ is the fully-emptied, $x = 1$ is the totally-filled and $x = 1/2$ is the half-filled system.

In a multiorbital system, we can define other useful quantities, such as the orbital filling per spin $n_{m\sigma}$ ($n_{m\sigma} \in [0, 1]$, with $n_{m\sigma} = 0$ being the emptied orbital and $n_{m\sigma} = 1$ the totally occupied orbital), and the orbital-resolved bandwidth W_m, which is an estimation of the energy window in which each orbital contributes to the band structure, see FIGURE 1.3**(c)**.

The description of SSMF for the Mott transition captures the Brinkman-Rice picture, see FIGURE 1.7**(b)** [4, 5]. The quasiparticle weights evolve from the weakly correlated metal, where all $Z_m \approx 0.8 - 1$, to the Mott insulating state where all $Z_m = 0$. When adding the orbital degree of freedom, the strongly correlated metal state where all $Z_m \sim 0.1 - 0.5$ can be also found, as in the case of a single-orbital system (see **Section 1.3**). But then, new additional cases can appear, where weakly ($0.7 < Z_m \leq 1$), moderately ($0.3 < Z_n \lesssim 0.7$) and strongly ($0 < Z_p \lesssim 0.3$) correlated orbitals coexist at the same time. For example, when some $Z_m = 0$ but others are $Z_{n\neq m} \neq 0$, the system is in the so called orbital selective Mott phase (OSMP) [6, 38–41]. I will comment later on that iron-based superconductors (FeSCs) can be seen as systems where weakly, moderately and strongly correlated orbitals coexist [5, 9, 15, 36, 37].

The band energy is renormalized by these Z_m factors (or equivalently, the orbital mass enhancements $(m^*/m_0)_m$), until the bands dissappear at the Mott transition, see FIGURE 1.7**(b)**. Thus, once the Mott insulator is reached, SSMF cannot provide further information. As already mentioned, this technique will allow for a faster treatment of local correlations effects, where hundreds of points can be obtained without increasing too much

[1] During this chapter and the next ones, we will focus in this picture, as already pointed out in **Chapter 1**.

the time spent by the calculations. At $T = 0\,K$ and for equivalent orbitals systems, SSMF gives good results when comparing with other more sofisticated techniques, such as Dynamical Mean-Field theory (DMFT) (see comparison in FIGURE 2.3) [35]. In the case of real materials, like FeSCs, SSMF gives also good predictions when comparing with the experimental results [9, 34, 42–44].

In **Section 2.2**, I will study the most important features of multiorbital systems by exploring the equivalent orbitals systems when varying U, J_H, n_e and N [5, 15, 35]. I will explain in detail the Hund metal phenomenology, as well as its relation with Mott insulator physics. I will briefly review the orbital selective Mott transition (OSMT) for non-equivalent orbitals systems [38, 39]. In **Section 2.3**, I will focus on the theoretical and experimental results obtained in FeSCs [9, 33, 34, 42–44]. I will show that FeSCs can be seen as multiorbital systems in which weakly, moderately and strongly correlated orbitals coexist at the same time. In **Section 2.4**, a brief summary of the chapter is given.

2.2 Equivalent orbitals systems

Local correlations effects are robust from one lattice to another, and the details of the dispersion relations (like the lattice symmetry or the number of hoppings included) are not very important when studying this phenomenology in a first approximation. The parameters which control the effects of local correlations are the total bandwidth W, the interaction energy scales U and J_H, the number of electrons per atom n_e and the number of orbitals per atom N. Thus, the results obtained for simple toy models, as the ones presented here, can be used to give a first approximation for the phenomenology present in many real materials, such as FeSCs. In this section, I will review the results on equivalent orbitals systems (see next paragraph) and the local correlations phenomenology when varying U, J_H, n_e and N.

In a system of N equivalent orbitals, these orbitals have the same dispersion relation and zero crystal field splittings. Except otherwise indicated, I will consider a 2D square lattice symmetry, in which only intraorbital nearest neighbor hoppings t are included, then only intraorbital dispersion relations will be non-zero $\varepsilon_{km} = -2t(\cos k_x + \cos k_y)$. All the results are presented in units of t or $W = 8t$ (or equivalently, half-bandwidth $D = W/2$). In some cases (as in FIGURE 2.3), Bethe lattice is considered, which is an infinite-dimensional lattice with $\varepsilon_{km} = -2t\sum_{d=1}^{\infty}\cos k_d$ and a semicircular DOS ($W = 4t$). For equivalent orbitals, all the Z_m are reduced to the same Z value. I will restrict the discussion to $T = 0\,K$.

For a multiorbital system, the kinetic energy gain $\widetilde{W}$ when the electrons hop through the system is not simply the total bandwidth W, as in the single-orbital case. Due to the N-orbital degeneracy, there will be N degenerated bands. Thus, the electrons have N degenerated channels to hop through the system. Then, the kinetic energy gain $\widetilde{W}$ will increase with N and W [109]. We will see later on that, a finite J_H will promote the breaking of the ground state degeneracy, and hence an effective reduction of $\widetilde{W}$ to $\sim W$.

In terms of the total filling $x = n_e/2N$, the interaction energy cost of a hopping process is defined as the atomic gap Δ^x, see Eq. (2.1).

$$\Delta^x = E(n_e + 1) - E(n_e - 1) - 2E(n_e) \tag{2.1}$$

where $E(n_e)$ is the energy of an atom for a certain number of electrons per atom n_e. Δ^x depends on U, J_H, N and integer n_e values. The atomic gap is a stability energy, i.e. it states how stable an electronic configuration of electrons in a atom is in the large-U limit ($t \approx 0$).

For $J_H = 0$, $\Delta^x = U$ for any N and any integer filling n_e. Then, the Mott insulating state does not only appear for half-filling ($n_e = N$), but also for other integer fillings $n_e = 1, 2, \ldots N$.

The critical interaction for the Mott transition U_c^x at a certain filling x will depend on the competition between this interaction energy cost Δ^x and the kinetic energy gain $\widetilde{W}$. Thus, for multiorbital systems, the local electronic correlations effects are controlled by the ratio $\Delta^x/\widetilde{W}$, which reduces to U/W in the single-orbital situation. When Δ^x increases, U_c^x decreases (due to the enhancement of the ratio $\Delta^x/\widetilde{W}$). U_c^x will increase if N increases when including the effect of $\widetilde{W}$. In [110], the authors demonstrated that, at half-filling, U_c increases linearly with N:

$$U_c = 8|\sum_k \varepsilon_k < f_k^\dagger f_k > |N \tag{2.2}$$

In FIGURE 2.1, I show the SSMF calculations for Z in terms of the ratio U/W for the square lattice and various N-equivalent orbitals cases. The U_c versus N behavior of Eq. (2.2) can be seen clearly in the INSET of the figure.

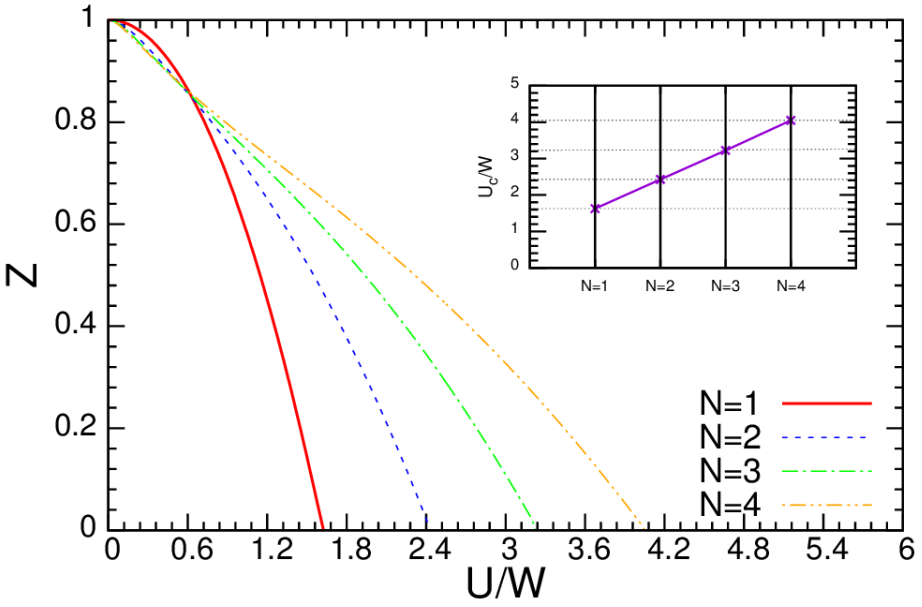

FIGURE 2.1: SSMF calculations of Z versus U/W for different systems with N equivalent orbitals at half-filling and $J_H = 0$. INSET: U_c/W for different N values (extracted from Z vs. U/W curves). U_c increases linearly with N, as expected from Eq. (2.2). Adapted from [38].

2.2.1 The effect of the Hund's coupling

Now, I will consider $J_H \neq 0$ and study its effects on $\Delta^x(J_H)$. In Eq. (2.3), the interaction energy cost $\Delta^x(J_H > 0)$ is estimated, where Mott insulating states can appear, not only for half-filled systems, but also for any integer filling $n_e = 1, 2, \ldots, N-1$, same as in the $J_H = 0$ situation.

$$\Delta^x\left(J_H > 0\right) = \begin{cases} = U + (N-1)J_H & n_e = N \\ = U - 3J_H & other\ integer\ n_e \end{cases} \tag{2.3}$$

J_H favors the Mott insulator for half-filled systems, whether disfavors it for other integer filling systems. In FIGURE 2.2, U_c in terms of J_H is presented, for various integer fillings n_e and $N = 2$ and $N = 3$ equivalent orbitals systems. For half-filling ($n_e = N$) and one-electron systems ($n_e = 1$), the behavior of U_c in terms of J_H is well captured by Eq. (2.3), except for small J_H (see previous section). For $n_e = 1$, U_c increases if J_H also increases (Mott insulator is disfavored by J_H), and for $n_e = N$, U_c decreases if J_H increases (Mott insulator is favored by J_H).

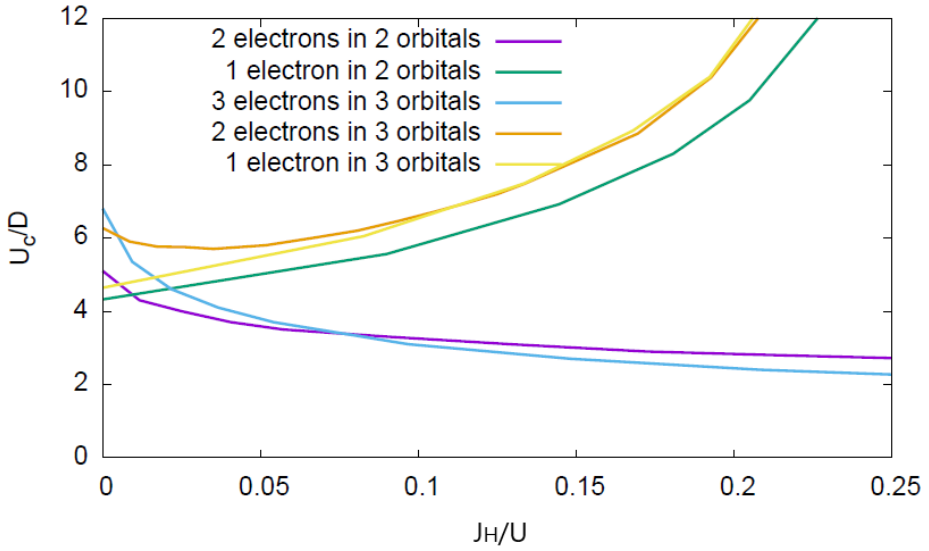

FIGURE 2.2: SSMF calculations of U_c/D (where $D = W/2$ is the half-bandwidth) in terms of J_H/U for various integer fillings n_e and $N = 2, 3$. At half-filling (blue and purple lines in the plot), U_c becomes smaller when J_H increases, following Eq. (2.3). At $n_e = 1$ (green and yellow lines), U_c trend in terms of J_H also follows Eq. (2.3), where U_c increases when J_H increases. See main text for the discussion of the case $N = 3$ and $n_e = 2$ (orange line). Taken from [15].

However, for $N = 3$ in $n_e = 2$ (orange line in FIGURE 2.2), the behavior of the system is controled by $\Delta^x(J_H > 0)$ only at large J_H, where Hund's coupling disfavors Mott insulating behavior. As shown in FIGURE 2.3 (for DMFT and SSMF calculations[2] in a Bethe lattice), for small J_H, Hund's coupling favors the Mott insulator. This non-monotonic behavior is general to all the other cases for $1 < n_e < N$ and $N > 2$.

[2] As anticipated, a very good agreement between DMFT and SSMF can be seen, specially for $n_e = 1$ and $n_e = 3$ situations, with Z being slightly overstimated in SSMF due to its Brinkman-Rice character (larger Z is translated into an understimation of U effects). At $n_e = 2$, the differences are more evident, where Z suppression is weaker in SSMF than in DMFT. In any case, the behavior is well captured by SSMF when compared with DMFT

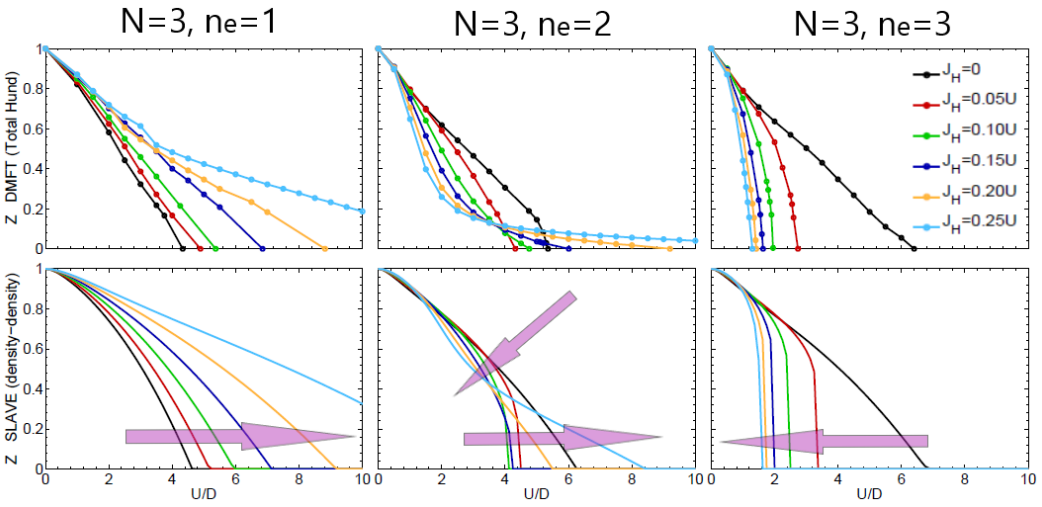

FIGURE 2.3: Z in terms of U/D for different integer fillings and different J_H/U values, in the Bethe lattice for $N = 3$. DMFT (upper row) and SSMF (lower row) calculations are presented. DMFT calculations are done using the full hamiltonian of Eq. (1.22), with the pair-hopping and spin-flip terms included, while in SSMF those terms are neglected. Each column stands for different integer fillings $n_e = 1, 2, 3$. Big violet arrows are marked in order to follow the increasing J_H/U, where for $n_e = 1$ when J_H increases, U_c increases and for $n_e = N = 3$ when J_H increases, U_c decreases. For $n_e = 2$, there is a non-monotonic behavior, where for increasing J_H, first U_c decreases, and then it starts to increase. Taken from and adapted from [35].

In FIGURE 2.4, the Z color map for J_H/U versus U/W is presented for $N = 3$. Here, the non-monotonic behavior can be more easily identified in FIGURE 2.4**(d)** for $n_e = 2$ (i.e. the purple region surrounded by a green dashed square). It can be seen that this correlated metallic state (with low Z values) follows the same dependence on the interaction energy scales U and J_H as the Mott insulator. In **Section 2.2.3**, I will show that this correlated metallic state and the Mott insulator follows the same dependence with the total filling n_e. This correlated metal is what is known as the **Hund metal** [31]. The Hund metal can also appear for other situations between single-electron and half-filling systems ($1 < n_e < N$) with $N > 2$. Note that other purple regions are not necessarily describing the Hund metal regime, due to the additional properties that I will discuss in the next section.

In FIGURE 2.5, dZ/dJ_H values for the plane J_H/U versus U/W and **(a)** $N = 5$, $n_e = 6$ and **(b)** $N = 3$, $n_e = 2$ are shown. Depending on the value of the parameters (U, J_H, n_e), Z can increase or decrease with J_H. In FIGURE 2.5**(a)** and **(b)**, this is signaled by the positive (yellow regions) or negative (blue region) sign of the slope dZ/dJ_H.

Between the weakly correlated metal and the Hund metal, there is a crossover. Its width depends on the lattice, U, J_H and n_e/N. In [35], the authors identified the crossover by a characteristic J_H^* value. This crossover between the weakly correlated metal and the Hund metal was located around the most prominent suppression of Z with J_H ($dZ/dJ_H < 0$). In FIGURE 2.5**(c)**, several J_H^*/W are presented for different n_e/N situations. J_H^*/U decreases if x decreases, except when comparing the cases $n_e/N = 2/3$ ($x \sim 0.33$) and $n_e/N = 3/5$ ($x = 0.3$).

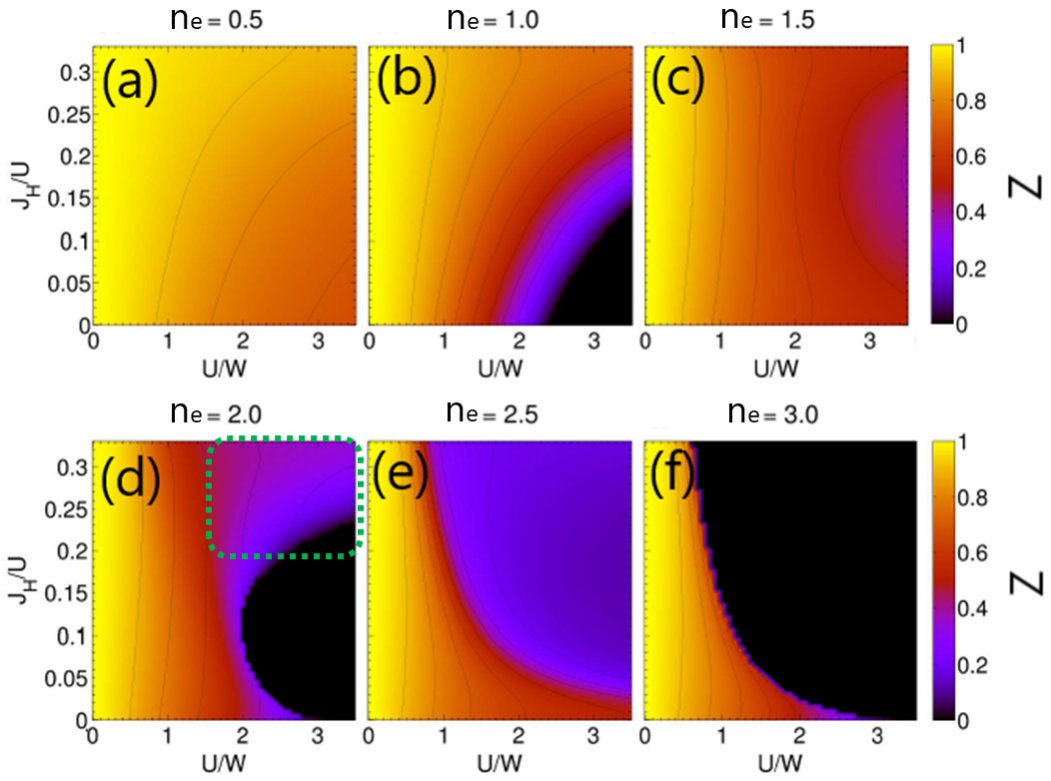

FIGURE 2.4: SSMF calculations of Z color map for the J_H/U versus U/W phase diagram, for $N = 3$ at different fillings n_e. Integer and non-integer fillings are included, in order to show that the appearance of the Mott insulator (black region) is restricted to integer fillings. Colored areas follow the next scheme: yellow region for the weakly correlated metal ($Z \sim 0.8 - 1$), purple region for the strongly correlated metal ($Z \sim 0.1 - 0.5$) and black region for the Mott insulator ($Z = 0$). Dark red regions describe the moderately correlated metal ($Z \sim 0.6 - 0.7$). Purple region surrounded by a green dashed square for **(d)** $n_e = 2$ can be identified as the Hund metallic state. Other purple regions are not necessarily describing a Hund metal, see **Section 2.2.2**. This correlated metal state follow the same dependence as the Mott insulator with U and J_H. Taken and adapted from [35].

2.2.2 Local spin and charge correlations

In the previous section, I have pointed out that there is a region of the (U, J_H) space in which a specific correlated metallic state, the Hund metal, can be found [5, 9, 15, 26–37]. In this section, I will review the origin and properties of the Hund metal by following the discussion in [35].

The local spin C_S correlations can be defined as:

$$C_S =< S^2 > - < S >^2 \tag{2.4}$$

where $S = \sum_m (\hat{n}_{m\uparrow} - \hat{n}_{m\downarrow})$, and $\hat{n}_{m\sigma} = d^\dagger_{m\sigma} d_{m\sigma}$ are the orbital and spin occupation number operators. For a spin-degenerate system, $< S >= 0$ and $< \hat{n}_{m\uparrow} >=< \hat{n}_{m\downarrow} >\equiv< \hat{n}_m >$, and for equivalent orbitals $< \hat{n}_m >= n_e/2N = x$ for all m.

C_S refers to the local interorbital spin correlations. The ratio C_S/C_S^0 (where C_S^0 is the non-interacting value) describes the fluctuations around the spin configuration in each atom,

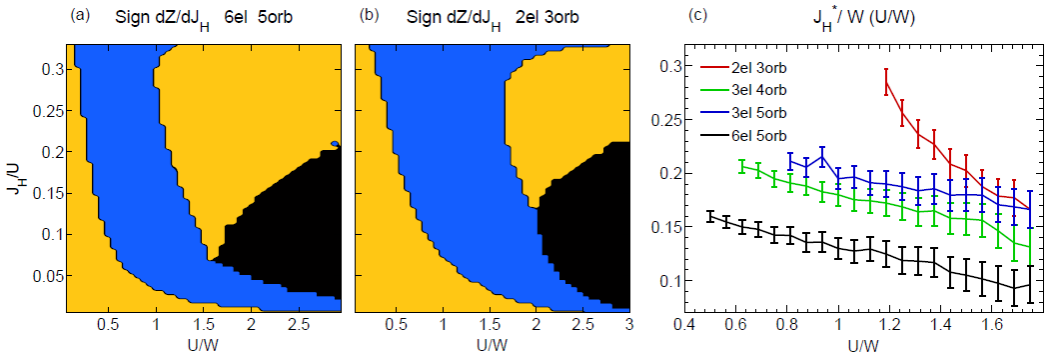

FIGURE 2.5: SSMF calculations of dZ/dJ_H maps for **(a)** $N = 5$, $n_e = 6$ and **(b)** $N = 3$, $n_e = 2$. Blue area marks $dZ/dJ_H < 0$, yellow areas mark the metallic states with $dZ/dJ_H \geq 0$ and black area marks the Mott insulating phase. Note that the blue region below the Mott insulating phase is just a signal of a decreasing Z value, and does not signal the crosssover to the Hund metal regime. **(c)** J_H^*/W curves for different n_e/N cases. J_H^*/W is smaller if x is smaller, except when comparing $n_e/N = 2/3$ and $n_e/N = 3/5$. Taken from [35].

hence it is directly related with the local moment in each atom. Then, if C_S/C_S^0 is in a low value, the spins are aligned anti-parallel in each orbital, while if it is in a large value, the spins are aligned parallel in each orbital. In FIGURE 2.6, I have plotted both Z and C_S/C_S^0 when varying J_H/U. The figure is obtained for $N = 5$ orbitals at $n_e = 6$ and $U/W = 1.5$. The U/W value is selected in order to see the crossover J_H^* (dashed line) and the Hund metal regime $J_H > J_H^*$. The blue shaded region marks $dZ/dJ_H < 0$, same as in FIGURE 2.5.

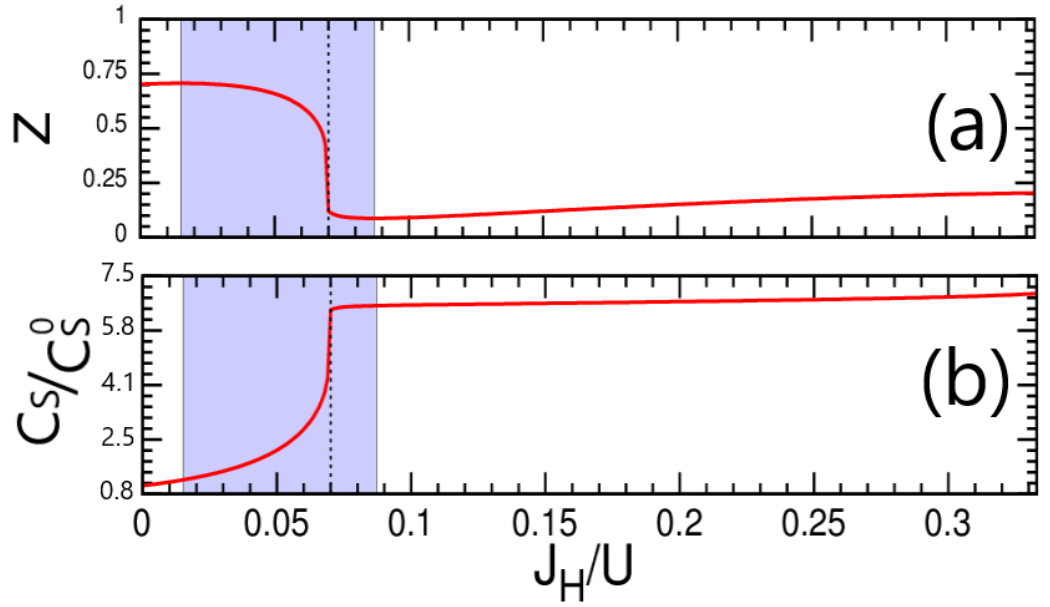

FIGURE 2.6: SSMF calculations of **(a)** Z and **(b)** local spin correlations C_S/C_S^0 in terms of J_H/U for $N = 5$ and $n_e = 6$ at $U/W = 1.5$. Blue shaded area marks the negative slope $dZ/dJ_H < 0$ region, and dashed line marks the crossover $J_H^*/U = 0.07$. At J_H^*, Z drops to a finite value and C_S/C_S^0 get enhanced. Once the system enters in the Hund metal regime ($J_H > J_H^*$), Z increases slightly and C_S/C_S^0 saturates to the local moment in the atom ($\approx 6 - 7$). There is a clear relation between the drop of Z and the enhancement of C_S/C_S^0 at the Hund metal crossover.

At J_H^*, Z suffers a large drop, while C_S get enhanced. Once the system is in the Hund metal regime $J_H > J_H^*$, Z has an almost constant value while C_S saturates to a high value. Deep in the Hund metal $J_H \gg J_H^*$, Z increases slighly. The saturation of C_S indicates that the atoms are in a local high-spin configuration (the spins in different orbitals will be parallel to each other). This is nothing but the Hund's rules being satisfied locally in each atom. Like the spins have to be parallel, correlations are induced between electrons, so that Z decays.

Another aspect of the Hund metal is related with the local total charge correlations C_{n_T}, which can be defined as:

$$C_{n_T} =< n_T^2 > - < n_T >^2 \tag{2.5}$$

where $n_T = \sum_m (\hat{n}_{m\uparrow} + \hat{n}_{m\downarrow})$. C_{n_T} describes how delocalized is the charge, then for a low value, the charge is localized, while for a large value, the charge becomes more delocalized through the system. For a spin- and orbital-degenerated systems, C_{n_T} can be alternatively written as:

$$C_{n_T} = N(C_n^{intra} + (N-1)C_n^{inter}) \tag{2.6}$$

where $C_n^{intra} =< \hat{n}_m^2 > - < \hat{n}_m >^2$ is the intraorbital charge correlations (fluctuations around the average charge in a given orbital) and $C_n^{inter} =< \hat{n}_m \hat{n}_n > - < \hat{n}_m >< \hat{n}_n >$ is the interorbital charge correlations (fluctuations around the non-correlated value for the charge between two different orbitals, m and n). C_n^{intra} is related with the double occupancy in a given orbital, while C_n^{inter} states how correlated are two different orbitals. C_n^{intra} is zero or positive (in the non-correlated limit has a finite value), while C_n^{inter} is zero or negative (in the non-correlated limit goes to zero). Thus, both of them contribute with different sign to C_{n_T}. In the Mott insulator, C_{n_T} vanishes, because C_n^{intra} and C_n^{inter} cancel each other. We can also define the orbital coupling $C_O = C_n^{inter}/C_n^{intra}$ as the correlation of an electron when it jumps between different orbitals. In the case of $C_O = 0$, the orbitals are decoupled of each other. In FIGURE 2.7, I show these correlations in terms of J_H/U for the same system as in FIGURE 2.6.

At J_H^*, C_{n_T} gets suppressed, and then it is enhanced in the Hund metal regime ($J_H > J_H^*$). This enhancement signals an increase of metallicity in the system. However, this is done in spite of a low Z value (see FIGURE 2.6**(a)**). This situation is totally different from single-orbital systems, in which the low Z value implies charge localization in each atom (i.e. low C_{n_T} value). Thus, for systems with sizable electronic correlations and Hund metal phenomenology, the system shows an increased metallic behavior. The different behavior between Z and C_{n_T} can be seen in FIGURE 2.8**(a)** for $n_e/N = 2/3$ and $6/5$, and $U/W = 1.5$ and 1, respectively. Then, a low Z value does not necessarily imply charge localization for a multiorbital system.

C_n^{intra} and C_n^{inter} compete to give the behavior of C_{n_T}, with both being suppressed with J_H. C_n^{intra} mainly contributes to the initial drop in C_{n_T} at J_H^*. C_n^{inter} governs the enhancement of C_{n_T} in the Hund metal regime ($J_H > J_H^*$).

The orbital coupling C_O follows the opposite tendency of C_{n_T} with J_H. Thus, at J_H^* there is a small enhancement of the orbital coupling, and in the Hund metal regime ($J_H > J_H^*$), C_O tends to 0, signaling an orbital decoupled behavior. This orbital decoupling is driven by the suppression of C_n^{inter} in the Hund metal regime.

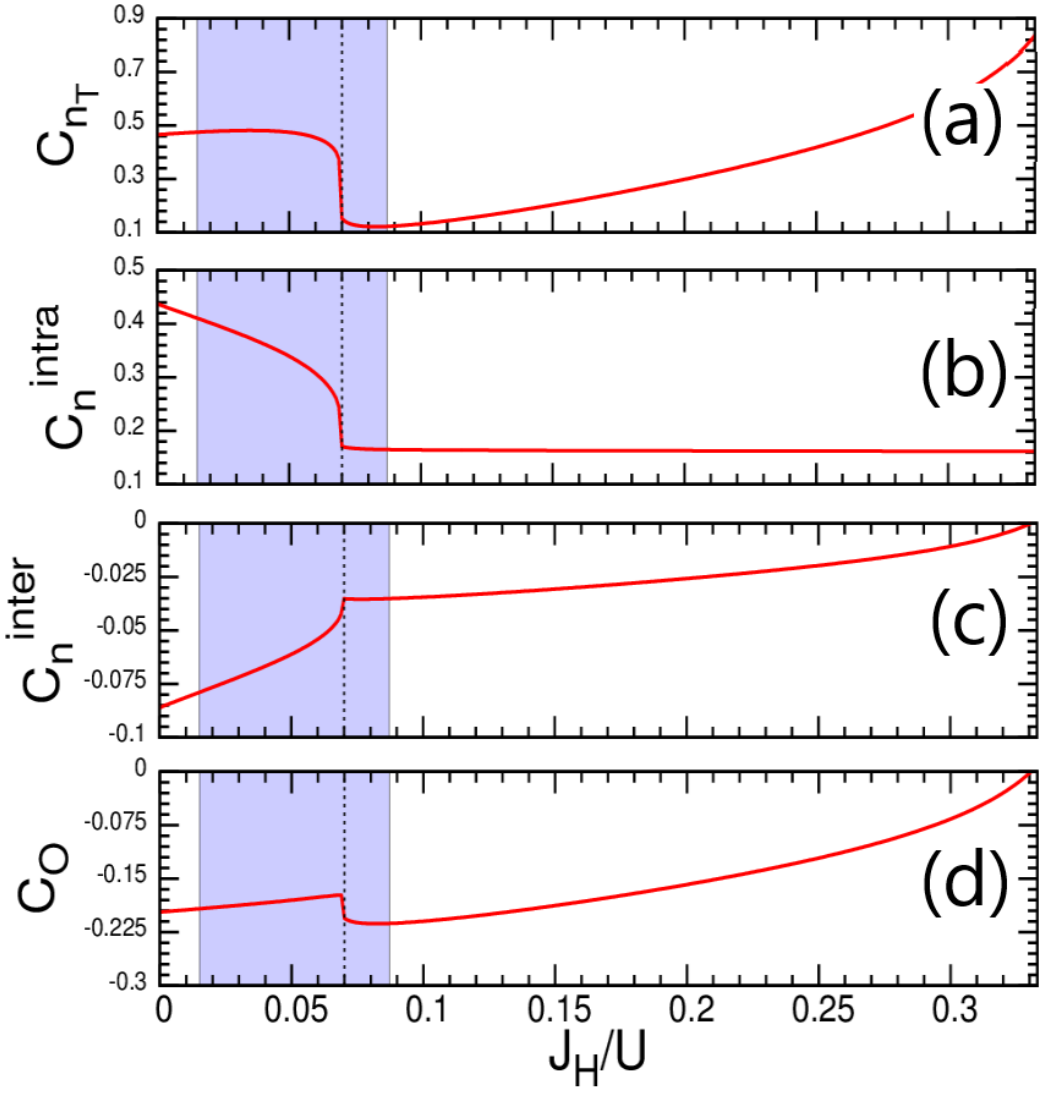

FIGURE 2.7: SSMF calculations of **(a)** local total charge correlations C_{n_T}, **(b)** intraorbital charge correlations C_n^{intra}, **(c)** interorbital charge correlations C_n^{inter} and **(d)** orbital coupling C_O in terms of J_H/U for $N = 5$ and $n_e = 6$ at $U/W = 1.5$. Blue shaded area marks the negative slope $dZ/dJ_H < 0$ region, and dashed line marks the crossover $J_H^*/U = 0.07$. At J_H^*, C_{n_T} suffers a drop due to the effect of C_n^{intra} (whether the contribution from C_n^{inter} is not important in this point). Once the system enters in the Hund metal regime ($J_H > J_H^*$), C_{n_T} increases due to the contribution from C_n^{inter}. In this regime, C_n^{intra} saturates and C_n^{inter} gets strongly suppressed. C_O approaching 0 signals the orbital decoupling.

For $N = 3$ and $n_e = 2$, total charge correlations C_{n_T} does not show the initial drop, as appeared in other cases, as shown in FIGURE 2.8**(a)** for $U/W = 1.5$ (red lines). This indicates that in such situations, C_n^{inter} dominates the behavior of the charge correlations for all J_H, while C_n^{intra} gives a smaller contribution to the J_H-dependence. I will discuss this situation in the next paragraphs.

The enhancement of total charge correlations is suppressed when the system approaches to half-filling. In FIGURE 2.8**(b)**, the evolution of $C_{n_T}/C_{n_T}^0$ (where $C_{n_T}^0$ is the $U = J_H = 0$ value) in terms of the filling can be seen, for $U/W = 1$ and when approaching $n_e = N = 5$.

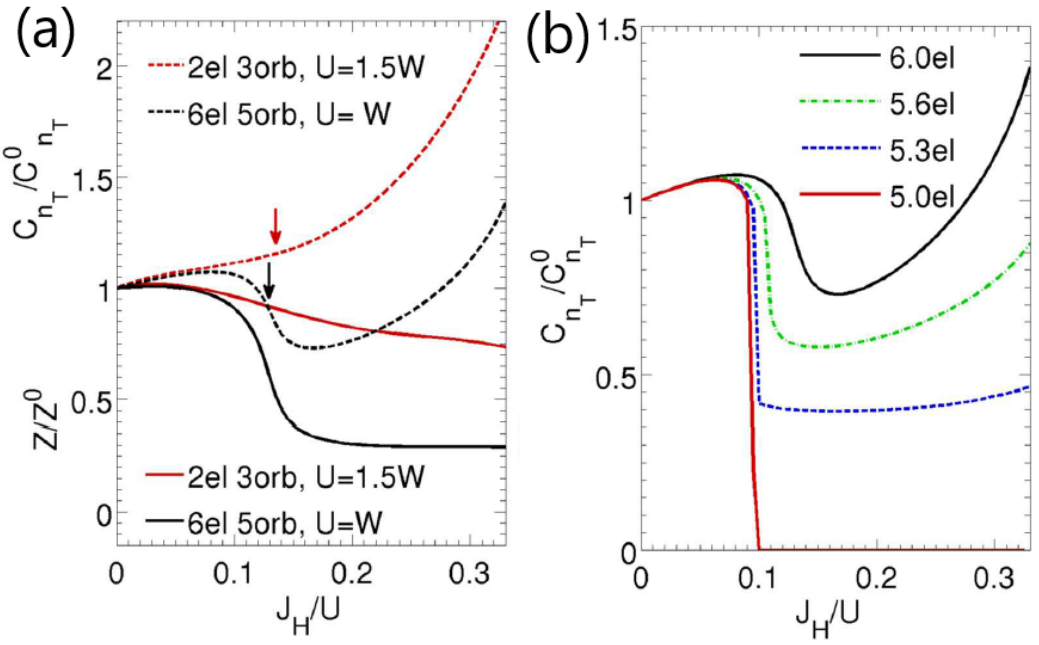

FIGURE 2.8: **(a)** $C_{n_T}/C^0_{n_T}$ (dotted lines) and Z/Z^0 (continuos lines) versus J_H/U comparison between $n_e/N = 2/3$ (red lines) and 5/6 (black lines) cases. Note that for $n_e/N = 2/3$, there is no suppression at the entrance of the Hund metal regime (arrows mark J^*_H/U). This is due to the fact that C^{inter}_n dominates over the whole interaction parameters. For $n_e/N = 5/6$ there is a suppression, due to the competition between C^{intra}_n and C^{inter}_n. A clear independent behavior can be seen between Z and C_{n_T}. **(b)** $C_{n_T}/C^0_{n_T}$ versus J_H/U for $N = 5$ and various n_e values. When the system approaches half-filling, the suppression of the local charge correlations becomes more prominent, until it wins when the Mott insulator is realised at half-filling. Taken from [35].

Now, I will discuss the fact that the local spin polarization given by C_S (FIGURE 2.6**(b)**) is responsible of the Hund metal phenomenology, hence driving the drop in Z and the orbital decoupling behavior. I will follow the energetic arguments discussed in [35].

Let's consider two sites with N orbitals and $n_e \leq N$ (particle-hole symmetry is assumed, so similar arguments can be applied to $n_e > N$) and the large-U limit. In the correlated metallic state, each atom is spin polarized due to J_H, so the possible virtual hopping processes are: (A) both atoms have the same spin alignement, and one electron jumps to an empty orbital ($\Delta_{\uparrow\uparrow}$), (B) both atoms have the opposite spin alignement, and one electron jumps to an empty orbital ($\Delta^{inter}_{\uparrow\downarrow}$) and (C) both atoms have the opposite spin alignement, and one electron jumps to an occupied orbital ($\Delta^{intra}_{\uparrow\downarrow}$). Δ gives the interaction cost for these virtual hopping processes. These virtual hopping processes are depicted in FIGURE 2.9.

$$\begin{cases} Process\,(A) \rightarrow \Delta_{\uparrow\uparrow} = U - 3J_H \\ Process\,(B) \rightarrow \Delta^{inter}_{\uparrow\downarrow} = U - (n_e - 3)J_H \\ Process\,(C) \rightarrow \Delta^{intra}_{\uparrow\downarrow} = U - (n_e - 1)J_H \end{cases} \tag{2.7}$$

At half-filling ($n_e = N$) there is one electron per orbital, so processes (A) and (B) are blocked, hence (C) controls U_c behavior (J_H promotes Mott insulating behavior). When $n_e < N$ (for $N < 7$) and J_H is large, process (A) has the lowest energy, so it controls

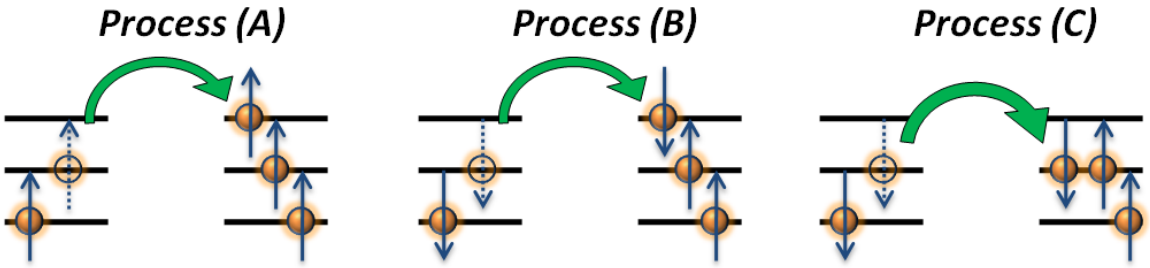

FIGURE 2.9: Virtual hopping processes for a $N = 3$ system with finite Hund's coupling J_H around the Hund metal regime. **(A)** both sites have all the orbitals with parallel spin alignement, and one electron jumps to an empty orbital, **(B)** both sites have all the orbitals with anti-parallel spin alignement, and one electron jumps to an empty orbital, and **(C)** both sites have all the orbitals with anti-parallel spin alignement, and one electron jumps to an occupied orbital.

the Mott transition, hence J_H disfavors Mott insulating behavior (see FIGURE 2.2 for large J_H/U values at $n_e \neq N$). Process (A) is promoted by J_H, and enhances metallicity.

At J_H^*, the entrance in the Hund metal regime emerges to avoid the process (C). Process (C) is suppressed by J_H for $n_e > 1$. As shown in Eq. (2.3), suppression of process (C) is related with the Mott insulating phase at half-filling ($n_e = N$), and this suppression strongly reduces C_n^{intra}. Process (B) is suppressed by J_H for $n_e > 3$ and promoted for $n_e < 3$. Then, systems with $n_e = 2$ will behave differently than $n_e > 2$ ones (note the absence of the drop for C_{n_T} at J_H^*/U in FIGURE 2.8**(a)**). In this $n_e = 2$ situation, C_n^{inter} dominates the behavior of C_{n_T} for all J_H/U (and not only for large $J_H > J_H^*$ values).

At J_H^*, the suppression of process (C) (which is accompanied by a large reduction of C_n^{intra}) indirectly suppress the process (B) (reducing C_n^{inter}). In the Hubbard-Kanamori hamiltonian of Eq. (1.22), local anti-parallel or parallel configurations in different orbitals of the same atom will have an effective interaction cost $U - 2J_H$ and $U - 3J_H$, respectively. Then, at finite J_H, anti-parallel configurations in each atom will cost more energy, so they become less frequent, enhancing C_S, and then reducing C_n^{inter}.

This mechanism is behind the orbital decoupling promoted by Hund's coupling (due to the reduction of C_n^{inter} when (B) is suppressed). If J_H further increases ($J_H > J_H^*$), the orbital decoupling is enhanced (the orbital coupling C_O is reduced). At the maximum value $J_H/U = 1/3$, $C_n^{inter} = 0$, hence the orbitals are totally decoupled ($C_O = 0$).

Then, at J_H^*, the reduction of C_n^{intra}, and the indirect reduction of C_n^{inter}, comes from an effective reduction of local anti-parallel configurations. So the enhancement of C_S drives the low Z values and the orbital decoupling mechanism in the Hund metal regime.

In summary, in the Hund metal, the atoms are in a high spin state due to the Hund's coupling J_H, and hopping processes (C) involving intraorbital double occupancy are suppressed. Such suppression reduces Z. However, because the hopping processes with parallel spin to an empty orbital are promoted by J_H, the system is metallic.

2.2.3 Relation between Mott insulators and Hund metals

In the previous section, I have discussed the fact that the enhancement of the local spin polarization in the Hund metal, reduces the intraorbital double occupancy (C_n^{intra}), and

indirectly reduces C_n^{inter}. The suppression of the intraorbital double occupancy is directly related with the Mott transition at half-filling.

In FIGURE 2.10, Z color map for the J_H/U versus n_e phase diagram of $N = 5$ for $U/W = 1$ is presented. There is a clear relation between the Mott insulator at half-filling and the correlated metallic region (Hund metal). This relation can be more easily identified by looking at the $Z = 0.1, 0.2, \ldots$ lines included in the figure, taken for each 0.1 step. When approaching the half-filled Mott insulator, the strength of correlations increase.

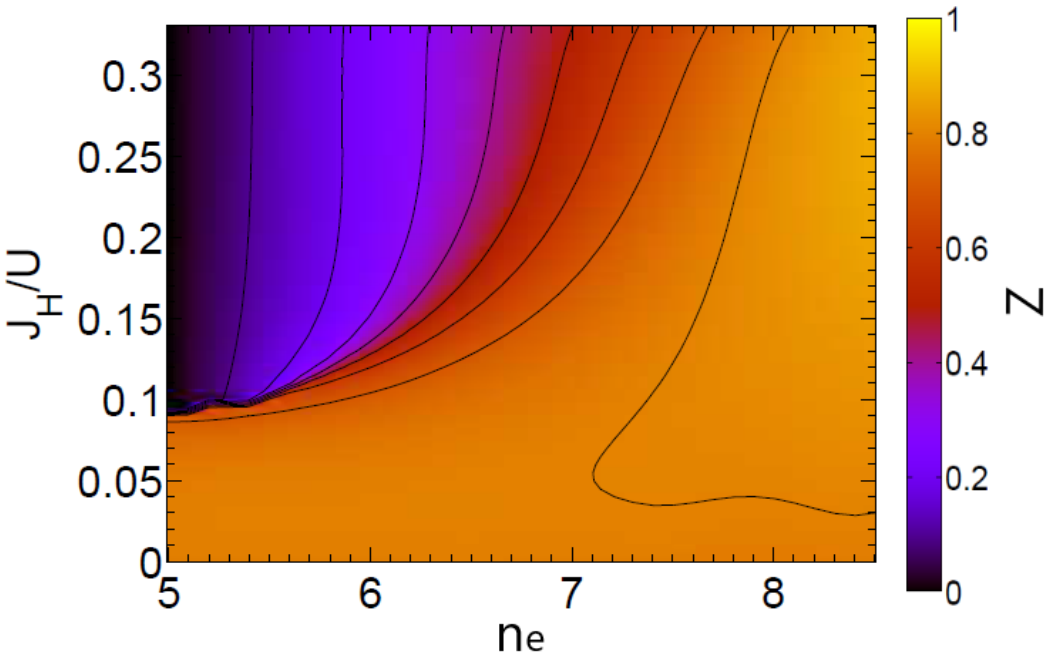

FIGURE 2.10: Z color map for the phase diagram J_H/U versus number of electrons per atom n_e for $N = 5$ at $U/W = 1$. A clear relation can be seen between Mott insulator at half-filling and the correlated metallic regions. This can be more easily identified by following the $Z = 0.1, 0.2, \ldots$ lines included in the phase diagram. Taken from [35].

In general, for any n_e/N and almost all $J_H \neq 0$ (larger than a certan threshold), the system becomes more correlated when approaching half-filling [9, 28, 29, 32, 34, 100–104, 111, 112]. For $J_H = 0$, the situation is different, as seen in FIGURE 2.2. In this situation, the orbital fluctuations stabilize the metallic state at half-filling [46, 113], disfavoring the Mott insulator. Then, at $J_H = 0$ and half-filling, U_c will increase. In **Chapter 5**, I will discuss more in detail this situation for $N = 2$ orbitals system.

The relation between the Hund metal and the Mott insulator is at the heart of the ideas that I will discuss in the following sections and, specially in **Chapter 3**, where I will use this link between both Mott insulator physics and Hund metal physics to propose a new high-T_c superconducting family.

2.2.4 Hund's coupling and orbital-selective Mott transition (OSMT)

In this section, I will briefly review an important consquence of the Hund's coupling related with the orbital decoupling. This is the already mentioned orbital-selective Mott transition (OSMT) [6, 38–41].

Due to the Hund's coupling J_H, an orbital decoupling behavior is promoted (see **Section 2.2.2**). For a system with non-equivalent orbitals, this behavior can lead to the OSMT, i.e. some of the $Z_m = 0$ while others $Z_{n\neq m}$ remain finite [6, 38–41]. When orbital degeneracy is broken and orbital decoupling behavior is acting on the system, each non-degenerated Z_m will behave differently in terms of U, J_H and n_e. This property is called orbital differentiation. The equivalence between different orbitals can be broken in three distinct manners: (1) by changing the hopping parameters for different orbitals, hence there will be different dispersion relations for each orbital ε_{km} [38], (2) by introducing a crystal field splitting, so there will be different ϵ_m parameters for each orbital [39], or (3) by considering orbital-dependent interacting parameters. I discuss the first two cases below. The third case goes along similar lines. Note that I will only consider intraorbital hoppings t^{ij}_{mm} and neglect interorbital ones t^{ij}_{mn}.

The first case can be equivalently recognised with an orbital-dependent bandwidth W_m. In FIGURE 2.11**(a)**, the phase diagram U/D_1 versus D_2/D_1 (where $D_m = W_m/2$) for $N = 2$ at half-filling and different J_H/U values is presented. For $J_H = 0$, a really large $D_2/D_1 \approx 0.2$ is needed to obtain a OSMP, whether if J_H/U (and hence the orbital decoupling) is increased, this OSMP widens. Here, the orbital which takes $Z_m = 0$ is the one with the lowest W_m.

In FIGURE 2.11**(b)**, the phase diagram J_H/D versus U/D for $N = 3$ at $n_e = 4$ is shown, when one of the orbitals has a finite crystal field splitting Δ with respect to the other two. The orbital filling per spin was fixed to $n_{3\sigma} = 0.5$ and $n_{1\sigma} = n_{2\sigma} = 0.75$. As appreciated, this phase diagram looks really similar to the one in FIGURE 2.4**(d)**, showing the important role played by Hund's coupling in this area. Here, the orbital which takes $Z_m = 0$ is the one with an orbital filling $n_{m\sigma}$ closer to half-filling.

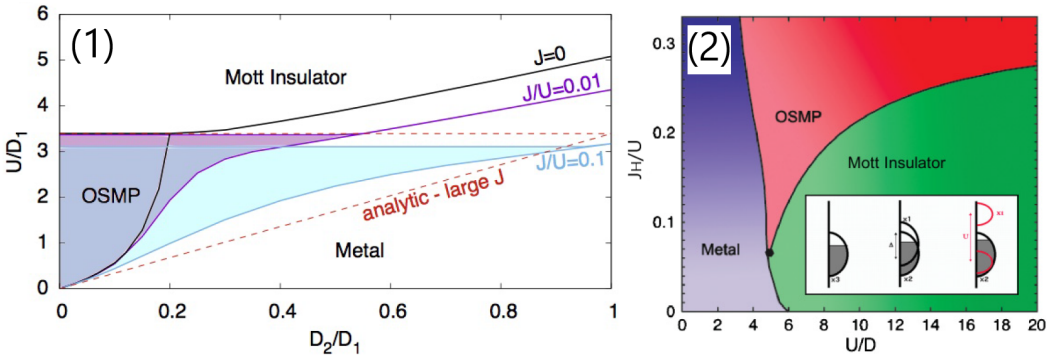

FIGURE 2.11: **(1)** U/D_1 versus D_2/D_1 phase diagram for $N = 2$ at half-filling, where metallic, OSMP and Mott insulator phases are shown. Various $J_H/U = 0, 0.01$ and 0.1 values are presented. Once J_H/U increases, OSMP enlarges, due to the promotion by J_H of the orbital decoupling mechanism. Large-J_H/U limit included as a dashed red line. Taken from [38]. **(2)** J_H/U versus U/D phase diagram for $n_e/N = 4/3$, where one of the orbitals has a finite crystal field different to the other two orbitals. The orbital filling per spin is fixed to $n_{3\sigma} = 0.5$ and $n_{1\sigma} = n_{2\sigma} = 0.75$. INSET: Sketch for the OSMT, where black bands refer to the two equivalent orbitals, whether red band is the one splitted by a finite crystal field $\epsilon_3 \neq \epsilon_1 = \epsilon_2$. Taken from [39].

As a summary, Hund's coupling J_H promotes a local spin polarization, which results in an orbital decoupling behavior. For non-equivalent orbitals, J_H can drive the system into an OSMT. Any hybridization between orbitals, like an interorbital hopping t^{ij}_{mn}, will act against the appearance of a OSMT. In this situation, any finite interorbital hybridization will turn (depending on the strength of the orbital differentiation, i.e. different Z_m values)

the OSMT into a state with weakly ($0.7 < Z_m \leq 1$), moderately ($0.3 < Z_n \lesssim 0.7$) and strongly ($0 < Z_p \lesssim 0.3$) correlated orbitals coexisting at the same time [5, 9, 15, 36, 37].

The most correlated orbitals will be determined by the smaller W_m (due to an increase of the ratio Δ^x/W_m) and the closeness to half-filling of the orbital filling per spin $n_{m\sigma}$.

2.3 Hund metals and FeSCs

In **Chapter 1**, the discussion about the strength of electronic correlations in FeSCs was presented, arguing about a weakly [2, 77–79] or a strongly [55, 80] correlated approach to study FeSCs. In this section, I will show that in FeSCs, weakly, moderately and strongly correlated electrons coexist at the same time, with the Hund metal phenomenology playing a major role.

FeSCs are multiorbital systems for which the parent compound (i.e. the system without doping or external perturbations) has $n_e = 6$ electrons in 5 d orbitals in a tetragonal symmetry. Non-zero interorbital hoppings t^{ij}_{mn} will turn a possible OSMT into a metallic state with weakly ($Z_m \sim 0.8 - 1$), moderately ($Z_n \sim 0.6 - 0.7$) and strongly ($Z_p \sim 0.1 - 0.5$) correlated orbitals.

In this section, I present a review on the role of local correlations in real materials, specifically on FeSCs [9, 33, 34, 42–44]. First, I will briefly review the theoretical calculations for various FeSCs, such as $LaFeAsO$, $BaFe_2As_2$ and $FeSe$. Then, in **Section 2.3.1**, I will present the experimental evidences which support that FeSCs are close to or in the Hund metal regime.

In Figure 2.12**(a)**, a table with the orbital-averaged interactions for various FeSCs calculated using constrained random phase approximation (cRPA) [24] is shown. The authors obtained $U \approx 2.5 - 4\,eV$ and $J_H \approx 0.35 - 0.5\,eV$, with 1111 ($LaFePnO$ with $Pn = P, As$) and 122 ($BaFe_2As_2$) families being the less correlated and 11 ($FeCh$ with $Ch = Se, Te$) and 111 ($LiFeAs$) the most correlated ones. The differences between the orbital-averaged (U and J_H) and the orbital-dependent interactions (U_{mm} and $J_{H\,mn}$) oscillate between 1% and 35%, so that U and J_H can be seen as a good approximation. The relation $U' = U - 2J_H$ is approximately satisfied, where the differences with respect to its orbital-dependent values U'_{mn} are $\approx 5\%$.

In Figure 2.12**(b)**, the SSMF $U(1)$ phase diagram obtained for undoped ($n_e = 6$) $LaFeAsO$ in the unfolded Brillouin zone (BZ), i.e. in a 5 d orbitals tight-binding model, is shown [9, 25]. Note that SSMF formalism tends to underestimate the effects of the real interaction values, so that the U and J_H are not straighforwardly extracted from Figure 2.12**(a)**, and they should be a bit larger in SSMF. Shaded circle marks an estimated region where most of the FeSCs can be localized. This shaded area is obtained when comparing Z_m values from theoretical with experimental results from orbital-resolved band structure measurements, such as ARPES and quantum oscillations (QOs) [42]. Both experimental techniques are sensible to the real band structure, and when comparing with DFT band structure calculations, Z_m can be obtained. Here, FeSCs are located around the Hund metal crossover and in the Hund metal regime, so it is expected that they show the properties explained in **Section 2.2**.

In Figure 2.13, DFT + Gutzwiller approximation (GA) calculation (see **Section 1.4.1**) in a 5 d orbitals tight-binding model for undoped ($n_e = 6$) $FeSe$ at $J_H/U = 0.224$ is presented [33]. As shown, all the features mentioned in **Section 2.2** are well reproduced in this

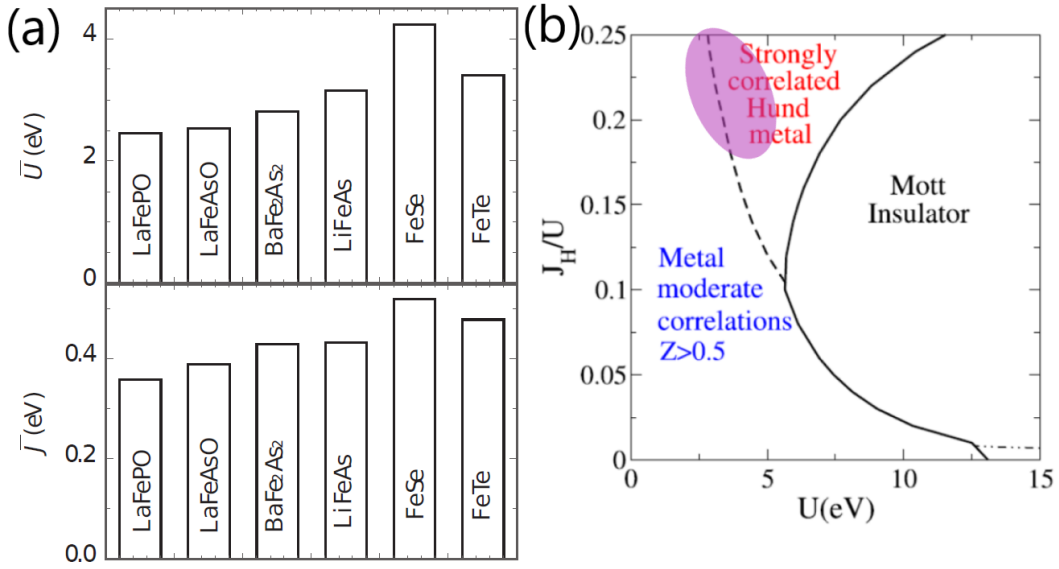

FIGURE 2.12: **(a)** Orbital-averaged interaction parameters for various FeSCs. U ranges from 2.5 to 4 eV and J_H from 0.35 to 0.5 eV. Relation $U' = U - 2J_H$ is approximately satisfied. Taken and adapted from [24]. **(b)** SSMF $U(1)$ J_H/U versus U phase diagram for $LaFeAsO$ at $n_e = 6$ electrons. Shaded circle marks an approximate region for locating FeSCs, where the area is estimated when comparing SSMF calculations with experimental Z_m values from ARPES and QOs. Taken and adapted from [9, 25].

system. The most correlated orbital (i.e., with the lowest Z_m) is xy, followed by xz (which is degenerated with yz) and z^2, and the less correlated orbital is $x^2 - y^2$. In the Hund metal regime ($U > 3\,eV$), this trend follows the closeness to half-filling of each orbital filling per spin $n_{m\sigma}$, plotted in FIGURE 2.13**(c)**, rather than depend on the total filling ($n_e = 6$), which signals an orbital decoupling behavior. It can be seen that, even for a large $U = 7\,eV$, the system is not yet in the Mott insulating state, due to the effect of $J_H/U = 0.224$, disfavoring the appearance of the Mott insulator. The enhancement of spin correlations C_S and orbital decoupling (with the interorbital charge correlations C_{mn} approaching 0) can be clearly seen in FIGURE 2.13**(b)** and **(d)**, except for interorbital correlations $C_{x^2-y^2,z^2}$, due to their less correlated behavior in which the considered J_H was not able to produce an orbital decoupling.

In FIGURE 2.14, SSMF Z_2 calculations for $BaFe_2As_2$ at $U = 2.7\,eV$ and $J_H/U = 0.25$ when varying the filling n_e of the system, are shown [34]. The 0 in the x-axis represents the undoped $BaFe_2As_2$ with $n_e = 6$. Negative x represents hole doping, while positive represents electron doping. As far as KFe_2As_2 (with $n_e = 5.5$) is approached with hole doping, the strength of correlations increases, giving larger mass enhancement factors $(m^*/m_0)_m$ (i.e. lower Z_m values) due to the influence of the Mott insulator at half-filling $n_e = 5$, as discussed in **Section 2.2.3**. Colored squares mark the solution for a tight-binding model for KFe_2As_2, instead of using the one for $BaFe_2As_2$ and doped it up to $n_e = 5.5$. This is done in order to reproduce the real band structure of KFe_2As_2. Differences in the scale of the strength of local correlations are found, but the increase of the strength towards half-filling is still present.

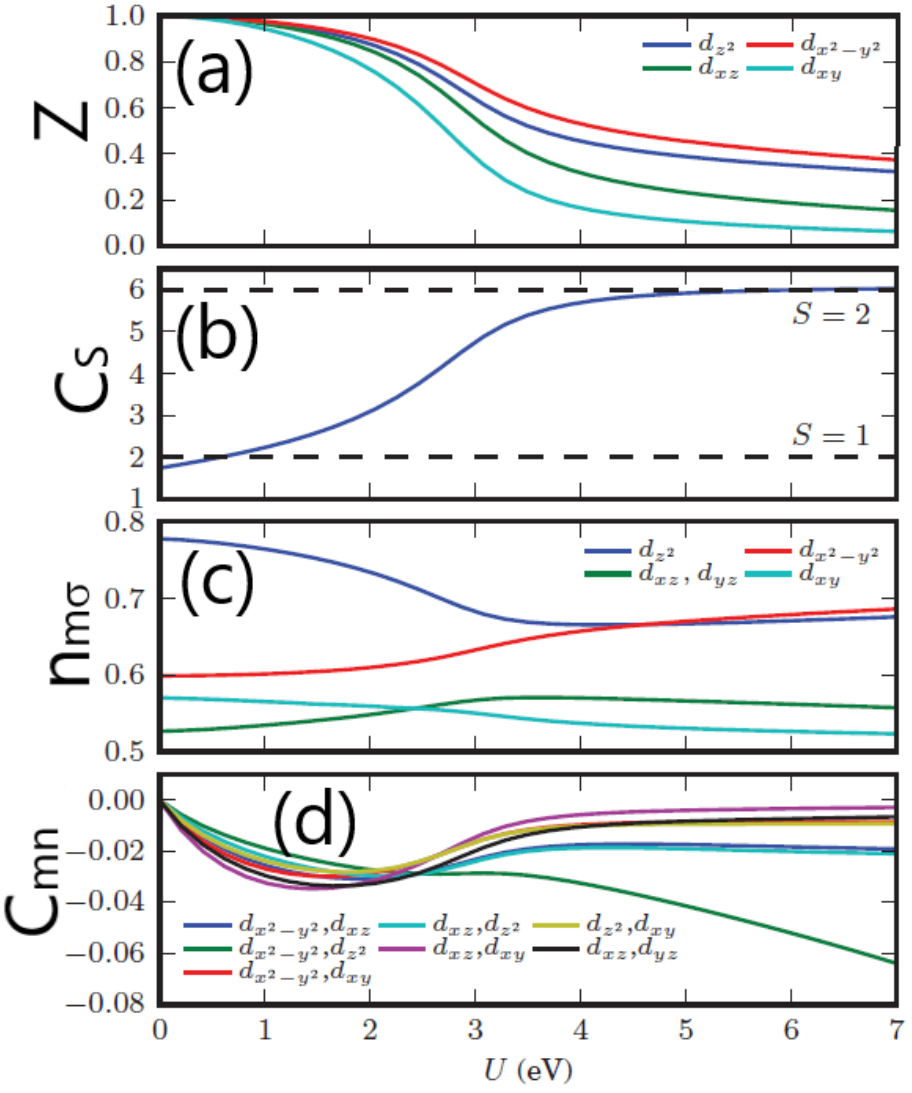

FIGURE 2.13: DFT + Gutzwiller approximation calculations for $FeSe$ in a 5 d orbitals tight-binding model at $n_e = 6$ and $J_H/U = 0.224$. **(a)** Orbital quasiparticle weights Z_m, **(b)** total spin correlations C_S, **(c)** orbital fillings per spin $n_{m\sigma}$ and **(d)** interorbital charge correlations $C_{mn} \equiv C_n^{inter}$. The strength of local correlations for each orbital is stated by the closeness to half-filling ($n_{m\sigma} = 1/2$) of the orbital fillings $n_{m\sigma}$. Spin correlations are enhanced and interorbital charge correlations are suppressed (except for $C_{x^2-y^2,z^2}$, due to their less correlated behavior). Taken and adapted from [33].

2.3.1 Experimental evidences for Hund metal behavior in FeSCs

Now, I will comment the experimental evidences which support that the FeSCs are indeed in a Hund metal regime (or at least, in the crossover) due to local correlations [9, 15, 33, 34, 42–44].

In FIGURE 2.15**(a)**, the experimental Sommerfeld coefficient γ (i.e. the linear term of the low-T specific heat $C(T) \sim \gamma T^2$) for various 122 FeSCs (from $n_e = 6$ to $n_e = 5.5$ and $n_e = 6.25$) and the comparison with DFT calculations are shown. SSMF Z_2 (labeled with DFT + Slave-spin in the legend) calculations are also shown [15, 37, 104]. The Sommerfeld

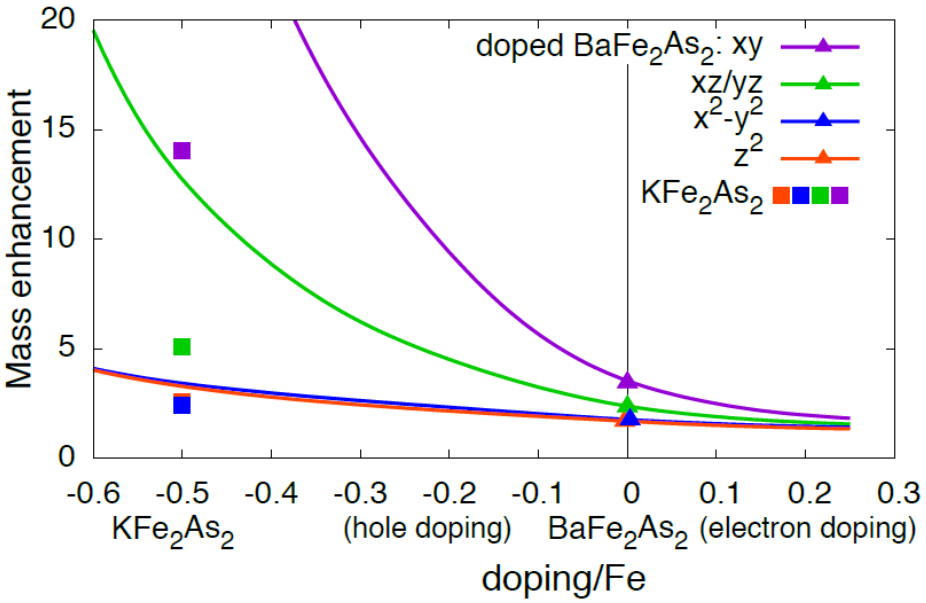

FIGURE 2.14: SSMF Z_2 calculations of a 5 d orbitals tight-binding model for $BaFe_2As_2$ and hole-doped $Ba_{1-x}K_xFe_2As_2$. Correlations increase when half-filling is approached. Each orbital behaves differently in terms of the filling, as an indication of the orbital selectivity of local correlations. Colored squares describe a tight-binding model for KFe_2As_2 (instead of using the one for $BaFe_2As_2$ and doped it to $n_e = 5.5$). Taken and adapted from [34].

coefficient was already introduced in Eq. (1.15), and depends on the mass enhancements $(m^*/m_0)_m$ for a multiorbital system as:

$$\gamma^* = \frac{\pi^2 k_B^2 N^*(\mu)}{3} \rightarrow \frac{\gamma^*}{\gamma_0} = \sum_m (\frac{m^*}{m_0})_m = \sum_m \frac{1}{Z_m} \tag{2.8}$$

where $N^*(\mu)$ is the DOS at the chemical potential for the correlated system which is proportional to the mass enhancements in the multiorbital system $(m^*/m_0)_m = 1/Z_m$, and γ_0 is the Sommerfeld coefficient in the non-correlated limit. When comparing experiments and theoretical results, the deviation with respect to DFT calculations to see the effect of local correlations is used, as for example γ^*/γ_0. The strength of correlations increases when approaching and decreases when moving away from half-filling. A good agreement can be seen between SSMF and experimental results, signaling the importance of local correlations in these systems.

γ will be mainly controled by the most correlated orbitals, i.e. those with the largest mass enhancement factors $(m^*/m_0)_m$ (lowest Z_m values). On the other hand, other measurements are sensible to the less correlated orbitals, such as the Drude weight D obtained from optical conductivity measurements ($D/D_0 = \sum_m (m_0/m^*)_m$, where D_0 is the non-correlated Drude weight), or the renormalization of the whole bandstructure measured by ARPES (labeled as ARPES whole in FIGURE 2.15**(b)**). Finally, ARPES and QOs are orbital-resolved measurements, so they are sensible to $(m^*/m_0)_m$ for each orbital. FIGURE 2.15**(b)** shows a compendium of the different experimental probes in the 122 FeSCs $BaFe_2As_2$ family [15, 34]. In the background, an sketch of the phase diagram for $BaFe_2As_2$ can be seen, to locate the different phases in this material. The strength of correlations clearly increases when approaching half-filling (left side of the x axis in the figure), as expected from SSMF calculations

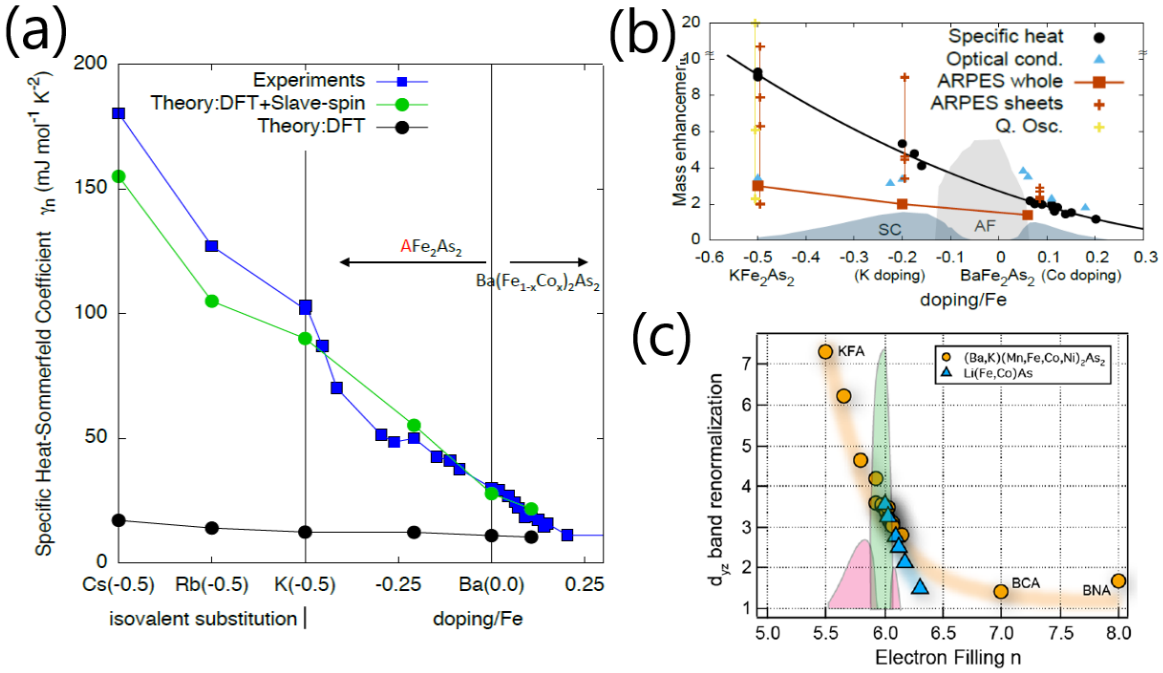

FIGURE 2.15: **(a)** Low-T specific-heat in terms of the total filling, where the Sommerfeld coefficient γ is shown for various 122 FeSCs. A comparison with DFT and SSMF Z_2 calculations is shown. A really good agreement can be seen between SSMF and experimental results. Taken from [15, 37, 104]. **(b)** Mass enhancement factors $(m^*/m_0)_m$ for different experimental probes when varying the total filling for various 122 FeSCs. Each experimental probe is sensible to different orbitals with respect to their behavior with local correlations. Specific heat is sensible to the most strongly correlated orbitals. Optical conductivity and ARPES whole are sensible to weakly correlated orbitals. ARPES and QO are orbital-resolved measurements. In the background, the phase diagram for $BaFe_2As_2$ is shown as a eyeguide to locate the different phases of this FeSC. The strength of correlations clearly increases when doping with holes, i.e. when approaching half-filling (left side of the x axis in the figure), and decreases with electron doping. Taken and adapted from [15, 34]. **(c)** ARPES measurements for the renormalization of the d_{yz} orbital in terms of the electronic filling n_e of the 122 FeSCs, $BaFe_2As_2$. KFA, BCA and BNA labels stand for the isostructural compounds, KFe_2As_2 (with $n_e = 5.5$), $BaCo_2As_2$ (with $n_e = 7$) and $BaNi_2As_2$ (with $n_e = 8$), respectively. Taken from [114].

(see FIGURE 2.14). In FIGURE 2.15**(c)**, I show the ARPES measurements for the renormalization of the d_{yz} orbital in terms of the electronic filling n_e of the 122 FeSCs, $BaFe_2As_2$ [114]. KFA, BCA and BNA labels stand for the isostructural compounds, KFe_2As_2 (with $n_e = 5.5$), $BaCo_2As_2$ (with $n_e = 7$) and $BaNi_2As_2$ (with $n_e = 8$), respectively.

An important consequence can be extracted from these experimental results [9, 15]: different experimental probes will be sensible to different weakly or strongly correlated orbitals. All the measurements together show that both weakly and strongly correlated orbitals coexist at the same time. This can be more clearly seen in orbital-resolved measurements, such as ARPES or QOs [114, 115].

FIGURE 2.16 shows the experimental results for X-ray emission spectroscopy (XES) in hole-doped $Ba_{1-x}K_xFe_2As_2$ systems [15, 43, 44]. This experimental probe is sensible to the local magnetic moment (XES IAD value is proportional to the local moment) in a system which is not necessarily ordered. INSET shows the total spin correlations C_S calculated with SSMF for $BaFe_2As_2$ ($n_e = 6$) and KFe_2As_2 ($n_e = 5$) in terms of U. In the weakly correlated

regime ($U \leq 1\,eV$), local spin correlations are the same for both compounds as shown in the INSET, totally different to what happens in the experimental results, where local moment increases when approaching half-filling. Experiment agrees well with theory for $U \geq 2.5\,eV$, where a different magnitude of local spin correlations for both fillings can be found. This indicates that the compounds are in (or at least in the crossover to) the Hund metal.

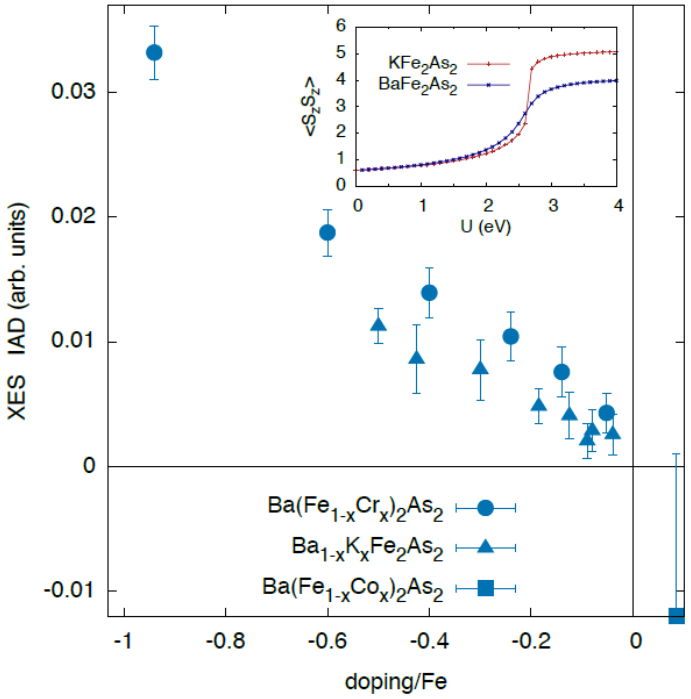

FIGURE 2.16: XES IAD values for $Ba_{1-x}K_xFe_2As_2$. XES IAD values are proportional the local moment, i.e. to the local spin correlations, in a non-ordered system. INSET: local spin correlations for $BaFe_2As_2$ and KFe_2As_2 systems calculated using SSMF Z_2. No difference is seen for the weakly correlated regime ($U \leq 1\,eV$), and only being in deep in the Hund metal regime ($U \geq 2.5\,eV$) would reconcile the experimental results with the theoretical expectations. Taken from [15].

All of these measurements sustain the idea that FeSCs are close to or in the Hund metal regime with the phenomenology explained in **Section 2.2**. The ideas explained here can be used for other materials and establish a basis to check whether local correlations are playing an important role in the system under study.

2.4 Conclusions

Along this chapter, I have presented the phenomenology for multiorbital systems and the role of local correlations [5, 9, 15, 26–37, 100–104].

In a multiorbital system, the Mott insulating state will appear, not only at half-filling, but also for any integer fillings $n_e = 1, 2, \ldots N-1$ [15, 35]. The critical interaction for the Mott transition U_c^x and its behavior with J_H depend on the filling n_e. For single-occupied systems ($n_e = 1$), U_c increases when J_H increases, while the opposite happens for half-filled systems ($n_e = N$).

A new correlated metallic state, the Hund metal [5, 9, 15, 26–37] is found for a certain filling region $1 < n_e < N$. This Hund metal regime shows a correlated metallic behavior which is promoted for large J_H values, so that the Mott insulating state is disfavored when J_H increases (similar to what happens in $n_e = 1$ systems).

In the Hund metal regime, the atoms are highly spin polarized (Hund's rule is satisfied). As a consequence, Z_m are in a low value and there is an orbital decoupling behavior [9, 15, 35]. Between the weakly correlated metal and the Hund metal there is a crossover defined by a characteristic J_H^*, whose value depends on the lattice symmetry and n_e/N.

The enhancement of local spin correlations in the Hund metal regime drives also an orbital decoupling behavior [9, 35]. This comes from the fact that there is an effective reduction of local anti-parallel spin configurations, while parallel configurations are promoted. The reduction of anti-parallel spin configurations results in a reduction of C_n^{intra}, and an indirect reduction of C_n^{inter}, which translates in the orbital decoupling.

The suppression of C_n^{intra} is directly related with the Mott transition at half-filling, hence providing a link between the Hund metal regime at $1 < n_e < N$ and the Mott insulating state at half-filling $n_e = N$ [9, 28, 29, 32, 34, 100–104, 111, 112]. .

In the case of non-equivalent orbitals, the orbital decoupling promoted by J_H can lead to an OSMT [6, 38–41]. For any finite interorbital hopping t_{mn}, this OSMT is suppressed, and the system has weakly, moderately and strongly correlated orbitals coexisting at the same time. Different orbitals will have different correlation strengths (orbital differentiation).

In this framework, various theoretical and experimental results for FeSCs (low-T specific heat, ARPES renormalized band structure, XES for the local moment, etc.) [9, 33, 34, 42–44] sustain the idea that these systems can be seen as being close to or in the Hund metal regime.

Chapter 3

Strong correlations and the search for high-T_c superconductivity in chromium pnictides and chalcogenides[1]

In **Chapter 2**, I have mentioned a connection between the Mott insulating state at half-filling and the Hund metal regime for multiorbital systems. This connection could serve as a link between the two most well-known families of high-T_c superconductors, the cuprates, in which the undoped system (with one d orbital at half-filling) is a Mott insulator, and the iron-based superconductors (FeSCs), in which the system (where the total number of electrons per Fe atom is $n_e = 6$ in 5 d orbitals) is close to or in the Hund metal regime. Both the Mott insulator and Hund metal phenomenology appear due to local correlations. In 2010, *Ishida and Liebsch* [29] showed that FeSCs can be seen as electron-doped systems from the Mott insulator at half-filling ($n_e = 5$ in 5 d orbitals), instead of being a completely different family when compared with the cuprates. In this chapter, we explore more deeply this idea by going into the other side of the Mott insulator at half-filling, i.e. by studying the hole-doped Mott insulator systems.

Here, we propose to search for high-T_c superconductivity in a new material family based on chromium instead of iron. We expect that the strength of electronic correlations evolves in the hole-doped side ($n_e < 5$) in a similar way as in the electron-doped side ($n_e > 5$). Then, we assume that an optimal degree of the electronic correlations is needed in order to obtain high-T_c superconductivity, and focus on the holpe doping level at which the strength of correlations is closest to the one found in FeSCs. We will assume that this superconducting phase is driven by AFM fluctuations, as it seems to occurr in most FeSCs, and discuss the superconducting instability. As an example, we study the 1111 $LaCrAsO$ chromium pnictide, the analogue of the iron superconductor $LaFeAsO$. $LaCrAsO$ [116] has the same crystal structure as its iron counterpart (see FIGURE 1.16), with Cr atoms forming a 2D square lattice and tetrahedrally coordinated by As atoms. $LaCrAsO$ shows a DFT band structure similar to other 1111 transition metal pnictides, like $LaFeAsO$, with all the 5 d orbitals of Cr mainly contributing to the bands around the Fermi level, with a total bandwidth $W \sim 4\,eV$ (in $LaFeAsO$ is $W \sim 4.5 - 5\,eV$). Experimentally, this compound shows an antiferromagnetic (AFM) phase with (π, π) ordering (checkerboard AFM), which can be suppressed by doping [116]. The main difference in undoped $LaCrAsO$ with respect to undoped $LaFeAsO$ is the number of electrons per site, which is $n_e = 4$ in $LaCrAsO$, while $n_e = 6$ in $LaFeAsO$.

[1] Results presented in this Chapter published in [96]

In this chapter, I will first check if a generic 5 d orbitals model for FeSCs (in particular for $LaFeAsO$) follows the idea of increasing the strength of local correlations when approaching half-filling $n_e = 5$ from both sides, i.e. I will study the mass enhancement factors $m^*_m/m_0 \sim 1/Z_m$ when varying n_e from 4 and from 6 to $n_e = 5$.

After demonstrating that the strength of local correlations increases (i.e. m^*_m/m_0 increases) when moving towards half-filling from the electron- and the hole-doped part, I will study the case of chromium systems, using $LaCrAsO$ as an example. I will present the results obtained by my co-workers to calculate the DFT band structure for the undoped $LaCrAsO$ ($n_e = 4$), and the 5 d orbitals tight-binding model using the same Slater-Koster fitting procedure as in the case of $LaFeAsO$. Then, I will calculate the mass enhancement factors m^*_m/m_0 for $LaCrAsO$ when varying the total filling from $n_e = 4$ to $n_e = 5$, i.e. when approaching half-filling. I found that the strength of local correlations is similar to the undoped $LaFeAsO$ for $LaCrAsO$ at $n_e = 4.5$. We expect that this behavior will hold for any other Cr pnictide or chalcogenide.

To study the strength of local correlations, I will use the SSMF Z_2 formalism. U and J_H will be fixed for both $LaFeAsO$ and $LaCrAsO$. In the case of $LaFeAsO$, $U = 3\,eV$ and $J_H/U = 0.25$ are the values for which the mass enhancement factors m^*_m/m_0 obtained by SSMF equal the ones observed experimentally in angle-resolved photoemission spectroscopy (ARPES) and quantum oscillations (QOs). For $LaCrAsO$, we will assume that, due to the equivalency of both systems, U and J_H will take the same values as in $LaFeAsO$.

$LaCrAsO$ shows a metallic behavior, as well as $LaFeAsO$, for realistic interaction parameters U and J_H. Then, we assumed that the spin fluctuation theory to study the superconducting instability is applicable, but instead of using the weakly correlated DFT band structure, we used the renormalized one as a better approach for the real band structure. First, my co-workers calculated the spin susceptibility by means of multiorbital random phase approximation (RPA) in the renormalized band structure. They obtained that the AFM with nesting vector $\vec{Q} = (\pi, \pi)$ (checkerboard-like) is the ground state of $LaCrAsO$, as expected from experiments [116]. A secondary peak at $\vec{Q}_2 = (\pi/2, 0)$ (and $(0, \pi/2)$ due to the fact that the system is in the tetragonal phase) is found. At $n_e = 4.5$, my co-workers also found that the superconducting instability is driven by this secondary peak $(\pi/2, 0)$, rather than by the nesting vector responsible of the AFM order. They argued that this enhanced response at $\vec{Q}_2$ is due to the nearness of a Lifshitz transition. Finally, they found that the superconducting order parameter symmetry is d_{xy}.

We conclude by stating that it seems plausible to find a new family of high-T_c superconductors in the chromium analogue of $LaFeAsO$, $LaCrAsO$. If this behavior is found in such a system, it will open a new route to search for new high-T_c superconductors based on the Mott doped scenario.

3.1 Introduction & Motivation

In previous chapters, I have summarized several important properties present in high-T_c cuprates superconductors and FeSCs, as well as explained the phenomenology of local correlations in single- and multiorbital systems, which results in the emergence of Mott insulator and Hund metal behaviors.

As shown in **Chapter 1**, in most cuprates and FeSCs, and other unconventional superconductors, the parent compound shows a magnetic phase, usually AFM. Once the system is doped with electrons or holes (or pressure is applied in some cases), the AFM phase is suppressed and the unconventional superconducting dome emerges. This behavior is quite robust in unconventional superconductors. It is believed that the magnetic phase suppression is a key ingredient to find unconventional superconductivity

Nevertheless, there is an important difference between cuprates and FeSCs. The parent magnetic phase of the cuprates is Mott insulating. There has been an intense debate about the role of the Mott physics in high-T_c superconductivity. On the other hand, the parent magnetic phase of FeSCs is metallic. This led to the quastion whether Mott insulator physics was necessary for obtaining high-T_c superconductivity.

A new point of view came out in 2010, when *Ishida and Liebsch* [29] found, by using DMFT, that that the strength of correlations in FeSCs are stronger when moving from the undoped $LaFeAsO$, with $n_e = 6$ in 5 d orbitals, towards half-filling $n_e = 5$. Based on these results, they proposed to see FeSCs as electron-doped Mott insulators, making a possible connection between cuprates and FeSCs. Interestingly, $n_e = 6$ corresponds to 1.2 electrons per orbital on average, close to the filling of the single relevant orbital at optimal doping (~ 1.16) in the cuprates [117]. A lot of experiments [100–104] and theoretical [28, 34, 111, 112, 118, 119] results have confirmed this Mott doped scenario, see **Chapter 2**, and for a review [9]. This suggests that not only a magnetic phase suppression is needed as a prelude of the high-T_c superconducting dome, but also an optimal degree of electronic correlations.

By taking into account the optimal degree of electronic correlations and their increase when approaching half-filled systems, we propose to search for a new family of high-T_c superconductors similar to FeSCs [96]. Considering that FeSCs can be seen as electron-doped Mott insulators, we looked into the other side of the half-filled Mott insulator, i.e. for the hole-doped Mott systems. By considering a similar system as the FeSCs, we propose to search for unconventional superconductivity in the Cr pnictides and chalcogenides. For the same crystal structure of quasi-2D FeSCs, only the total number of electrons per atom in the d orbitals will vary when changing Fe atoms by Cr ones, where for FeSCs is $n_e = 6$ in the 5 d orbitals, while for Cr systems is $n_e = 4$ (in this situation, the half-filled systems are the Mn pnictides and chalcogenides, where $n_e = 5$ in 5 d orbitals). If unconventional superconductivity is found in these chromium-based systems[2], the connection between cuprates and FeSCs, and the role of the electronic correlations would became clear. This could open a new route to search for new high-T_c superconductors.

In the doped Mott scenario previously described, there is an explanation of why other transition metal (TM) pnictides and chalcogenides have failed when searching for high-T_c superconductivity. For $TM = Ni$, Pd or Pt the system has $n_e/N = 8/5$, while for Co, Ir or Rh it has $n_e/N = 7/5$. In these situations, the distance from the Mott insulator at

[2]Note that I will not talk about the quasi-1D Cr_3As_3 systems [120], but rather focus on the quasi-2D chromium pnictides, with crystal structures equivalent to the ones for FeSCs.

$n_e = N = 5$ is too large, and hence, the strength of correlations is too small to host high-T_c superconductivity.

In the next section, I will give a brief summary of the current experiments and theoretical calculations for Mn and Cr pnictides and chalcogenides to give a context in the actual status on the study of such systems.

3.1.1 Preliminary results in Mn and Cr pnictides and chalcogenides

In this section, I summarize the available results obtained in the literature for Mn- and Cr-based compounds. I will conclude by arriving to the sketch of a proposed unified phase diagram for $LaTMAsO$, where $TM = Fe$, Mn and Cr, FIGURE 3.1.

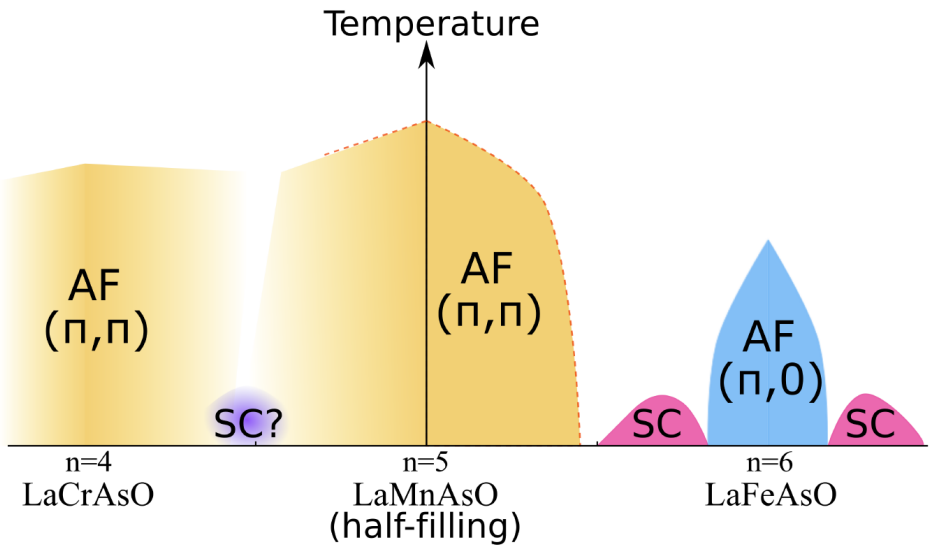

FIGURE 3.1: Sketch of the proposed unifying phase diagram for $LaTMAsO$ and related compounds, with $TM = Fe$ ($n_e = 6$), Mn ($n_e = 5$) and Cr ($n_e = 4$). The different phases are reproduced from the existing literature. By comparing with cuprates and FeSCs, AFM phase in $LaCrAsO$ has to be suppress around $n_e = 4.5$ in order to the superconducting dome to appear. If high-T_c superconductivity is found in chromium pnictides or chalcogenides, the connection between high-T_c cuprates and FeSCs will be made. This could open a route to discover new high-T_c superconductors based on the Mott doped scenario.

As a brief reminder of the previous chapters, the undoped FeSCs are AFM $(\pi, 0)$ (stripe AFM ordering, with spins in x direction aligned parallel, while antiparallel in the y direction) metals with magnetic moments $\mu \sim 0.5 - 1\,\mu_B/Fe$ and Néel temperatures $T_N \sim 100 - 150\,K$. The AFM phase can be suppressed with doping or pressure, and unconventional superconducting domes emerge, with high critical temperatures $T_c \sim 20 - 50\,K$, see FIGURE 1.12**(c)** for the electron-doped phase diagram of $BaFe_2As_2$. From the theoretical point of view, FeSCs are multiorbital systems [70, 71], where the usual tight-binding models have 5 d orbitals coming from the Fe atoms in the unfolded Brillouin zone (BZ), which it is identified as the $1Fe$ atom unit cell, see **Section 1.5.2** [72–74]. The undoped compound has $n_e = 6$ electrons per Fe atom. In **Chapter 2**, I have shown that FeSCs present sizable electronic correlations.

Mn pnictides and chalcogenides have been extensively studied and no-superconducting dome has been found up to date [121–139]. These systems are AFM insulators, with large values for $\mu \sim 3-4\,\mu_B/Mn$ and $T_N \sim 300-600\,K$. The AFM phase is checkerboard inplane (π, π),

and it may vary between C- (FM order of Mn layers in the z direction) or G-type (AFM order of Mn layers in the z direction). In the case of $LaMnPO$ [122], when pressure is applied, the system first undergoes an insulator-to-metal transition (at around $15-20\,GPa$), and then a second transition where AFM is suppressed (at around $25-30\,GPa$). In $BaMn_2As_2$ [122], an insulator-to-metal transition can be driven when it is doped with holes (with K) at $x \approx 0.016$, while the AFM is not suppressed, so it is robust against doping. We assume that the electronic correlations are too large to make Mn pnictides and chalcogenides able to host unconventional superconductivity.

Different Cr pnictides and chalcogenides have been studied, with only few articles coming out during the last decade [116, 140–146]. There are studies on $BaCr_2As_2$ [140], $EuCr_2As_2$ [145], $LNCrAsO$ (with $LN = La$, Ce, Pr and Nd) [116], $Sr_2Cr_3As_2O_2$ [146] and $CrSe$ [141], and also mixed systems with layers of $CrFe$ [142–144]. Here, I briefly review the most important features in these compounds.

$BaCr_2As_2$ [140] is an AFM (π,π) metal. There is no signal for the magnetic ordering temperature T_N (up to $200\,K$) in the specific heat and the resistivity, so there is no data available for T_N or other transitions. In [140], the authors performed DFT calculations for the magnetic ground state, obtaining C-type AFM (π,π) with $\mu = 2.01\,\mu_B/Cr$.

$LNCrAsO$ with $LN = La$, Ce, Pr and Nd [116] are AFM (π,π) metals up to $300\,K$. No data for T_N is available. From DFT calculations, it was concluded that the C-type AFM (π,π) is the most stable order. The computed magnetic moment is $\mu \sim 2.6\,\mu_B/Cr$. In [116], the authors doped $LaCrAsO$ with F (holes) and Mn (electrons), obtaining an increase/decrease of the resistitivy for F/Mn-doped compounds, with a metal-to-insulator transition found at $LaCr_{0.8}Mn_{0.2}AsO$. $LaCrAsO$ doped with F/Mn corresponds to a hole/electron doping, respectively.

$CrSe$ [141] has not be synthesized yet, but it is expected that it will be stable and crystallize in the same crystal structure as $FeSe$. In [141], the authors performed DFT calculations and show that both $CrSe$ and $MnSe$ present an itinerant FM ground state.

As an example, later in this chapter, we will pick $LaCrAsO$ as our system to study the effects of electronic correlations in Cr pnictides and chalcogenides. Due to the robustness of the local correlations effects, the results explained here can be applied for any other similar Cr pnictides and chalcogenides. Using $LaCrAsO$ will be also useful when making a direct analogy with the 1111 FeSCs, $LaFeAsO$.

3.2 Results & Discussion

Here, I present the results that I have obtained and published in [96], altogether with the ones obtained by my co-workers. In **Section 3.2.1**, I use a 5 d Slater-Koster tight-binding model proposed for FeSCs, in particular for $LaFeAsO$ [74], to demonstrate that the increase of the strength of local correlations when approaching half-filling is a robust feature from both the electron- ($n_e > 5$) and the hole-doped ($n_e < 5$) part. However, the applicability to a real material of this tight-binding model in regions where n_e is much different from $n_e = 6$ is not realistic. So in **Section 3.2.2**, I show the DFT band structure calculation performed by my co-workers for $LaCrAsO$, and the tight-binding model obtained by performing a similar Slater-Koster fitting procedure as it was made for $LaFeAsO$ [74]. In **Section 3.2.3**, I calculate the mass enhancement factors $m^*_m/m_0 \sim 1/Z_m$ for $LaCrAsO$ when varying the

filling $4 < n_e < 5$, showing that the phenomenology of strength of correlations getting increase towards half-filling is maintained. Local correlations calculations are done both in **Section 3.2.1** and **Section 3.2.3** using SSMF Z_2 formalism. Finally, in **Section 3.2.4**, I show the calculations done by my co-workers on the spin susceptibility and the superconducting order parameter in the renormalized band structure. Multiorbital RPA is used with focus on singlet solutions, due to the expected AFM order as the ground state for $LaCrAsO$. We conclude by proposing that this system could host high-T_c superconductivity in a similar fashion than occurrs in FeSCs.

3.2.1 Electronic correlations for FeSCs around half-filling

In this section, I will use the Slater-Koster tight-binding model proposed for $LaFeAsO$ in [74] to study the strength of local correlations when the total filling varies and approaches half-filling from $n_e = 6$ and $n_e = 4$. In the Slater-Koster framework [147], the fitting to the DFT band structure using a tight-binding model is done in the $FeAs$ 2D layer by writting each hopping parameter t^{ij}_{mn} as functions of various overlap integrals and the angle α. α is defined as the angle between the As atoms and the Fe plane, where for a regular tetrahedron $\alpha = 35.3\,°$. The overlap integrals describe the direct overlap between d orbitals in neighbor Fe atoms (denoted by $(dd\sigma)_i$, $(dd\pi)_i$ and $(dd\delta)_i$ where $i = 1, 2$ are the first and second neighbors, respectively) and the indirect overlap between Fe d and As p orbitals (denoted by $pd\sigma$ and $pd\pi$).

The t^{ij}_{mn} expressions in terms of these indirect overlaps are computed in second order perturbation theory, neglecting the crystal field splitting in between Fe and As orbitals and in between the different As orbitals. The matrix elements t^{ij}_{mn} depend on the difference $|\epsilon_p - \epsilon_d|$. As an example, the intraorbital first neighbor hopping for xy in the X direction is written as:

$$t^{x}_{xy,xy} = \underbrace{\frac{1}{|\epsilon_p - \epsilon_d|}\left(-\frac{3}{2}pd\sigma^2 - 2pd\pi^2 + 2\sqrt{3}pd\sigma pd\pi\right)}_{indirect\,overlap}\underbrace{\cos^4\alpha \sin^2\alpha}_{angle\,term} + \underbrace{(dd\pi)_1}_{direct\,overlap} \tag{3.1}$$

Similar expressions can be obtained for all the other first and second neighbor hoppings t^{ij}_{mn}.

The hopping matrix elements in the tight-binding model depend on the direct and indirect overlaps, and on the angle α. A crystal field splitting term ϵ_m between the Fe d orbitals is also included in the model. These parameters can be tuned to give a similar band structure to the one obtained in DFT calculations. The d orbitals are defined in the unfolded BZ, with zx and yz being degenerated. In FIGURE 3.2**(a)**,**(b)**, the Slater-Koster tight-binding band structure and the DOS, with the orbital character included can be seen (color code in the caption of the figure). Overlap integrals and crystal field splittings are those considered in [74]. This Slater-Koster model compares well with the DFT band structure (see FIGURE 1.17), giving a good description of the band energies and orbital content. This model was previously used in the context of FeSCs to study their magnetic properties, the optical conductivity, the Raman spectra and the anisotropy present in the FeSCs [9].

All the d orbitals contribute for the band structure around the Fermi level. The total bandwidth is $W \sim 5.3\,eV$, while the individual orbital bandwidths are approximately $W_{zx,yz} \approx$

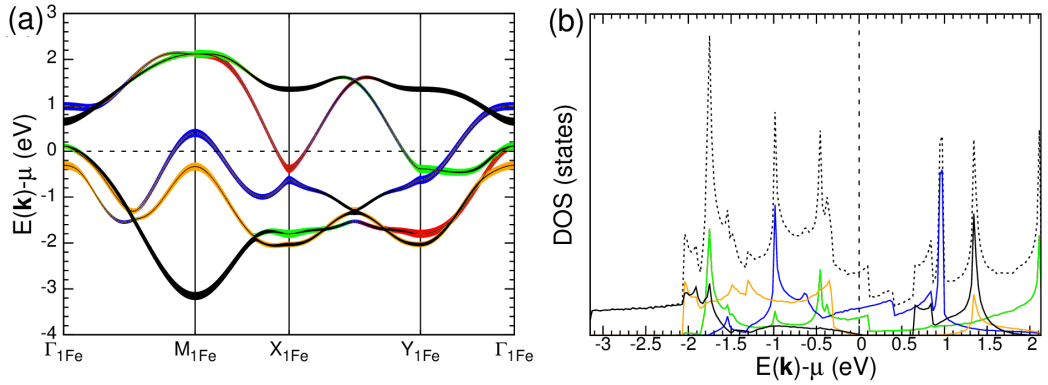

FIGURE 3.2: Slater-Koster tight-binding model for $LaFeAsO$ with $n_e = 6$ and $\alpha = 35.3\,^\circ$ in the unfolded BZ, where **(a)** shows the band structure with the orbital character included and **(b)** the total DOS (dotted line) and the orbital-resolved DOS. Color code for the orbitals: red for yz, green for zx, blue for xy, orange for $3z^2 - r^2$ and black for $x^2 - y^2$. Figures obtained from the Slater-Koster tight-binding model of [74].

$3.75\,eV$, $W_{xy} \approx 2\,eV$, $W_{3z^2-r^2} \approx 3.5\,eV$ and $W_{x^2-y^2} \approx 4.5\,eV$. The smallest orbital bandwidth is W_{xy}, whether the largest is the one of $x^2 - y^2$. A more extense discussion about this Slater-Koster tight-binding model can be found in [74].

I now apply the SSMF Z_2 formalism to obtain the mass enhancement factors $m_m^*/m_0 = 1/Z_m$ in terms of the number of electrons per Fe atom n_e, keeping $U = 3\,eV$ and $J_H/U = 0.25$ as constants. These are the interaction values for which the mass enhancement factors m_m^*/m_0 obtained by SSMF equal the ones observed experimentally in ARPES and QOs for undoped $LaFeAsO$ [42]. I will vary the total filling $4 < n_e < 6$. The enhancement of m_m^*/m_0 signals the increase on the strength of correlations. In FIGURE 3.3, I present the mass enhancement factors m_m^*/m_0 and the orbital filligns n_m in terms of the number of electrons n_e. The orbital fillings are defined as $n_m = 2n_{m\sigma}$ where $n_{m\sigma}$ is the orbital filling per spin, hence $n_m \in [0, 2]$ with $n_m = 1$ defined as half-filling.

The strength of correlations of all orbitals increases when approaching half-filling $n_e = 5$ from both sides, as expected from the Mott doped scenario. The most correlated orbitals, i.e. larger m_m^*/m_0, are xy and zx/yz , while $3z^2 - r^2$ and $x^2 - y^2$ are the less correlated ones. Interestingly, in the hole-doped part (around $n_e = 4$), the orbitals closer to half-filling ($n_m = 1$) are not the most correlated ones, due to the effect of the effective kinetic energies given by the orbital bandwidths W_m, see **Chapter 2**.

The situation when comparing $3z^2 - r^2$ and zx/yz might be troublesome when looking to the lowest W_m and the closeness to half-filling of each n_m. In this case, the most correlated orbitals are xz/yz, even if they have a larger W_m and they are further away from half-filling. This is due to the fact that at the considered interaction values U and J_H, the system is in the crossover to the Hund metal regime, and the orbitals are still coupled. For larger U, the system will show an orbital decoupling behavior, and hence the strength of correlations will follow the lowest W_m and the closest to half-filling n_m expectations, as explained in **Chapter 2**.

In FIGURE 3.4, I have plotted the Z_m and n_m evolution for $n_e = 4$ and $J_H/U = 0.25$ in terms of U. Once the system is deep in the Hund metal regime ($U > 4.5\,eV$), Z_m follows the expectations for the lowest W_m and the closest to half-filling behavior. Above $U > 4\,eV$,

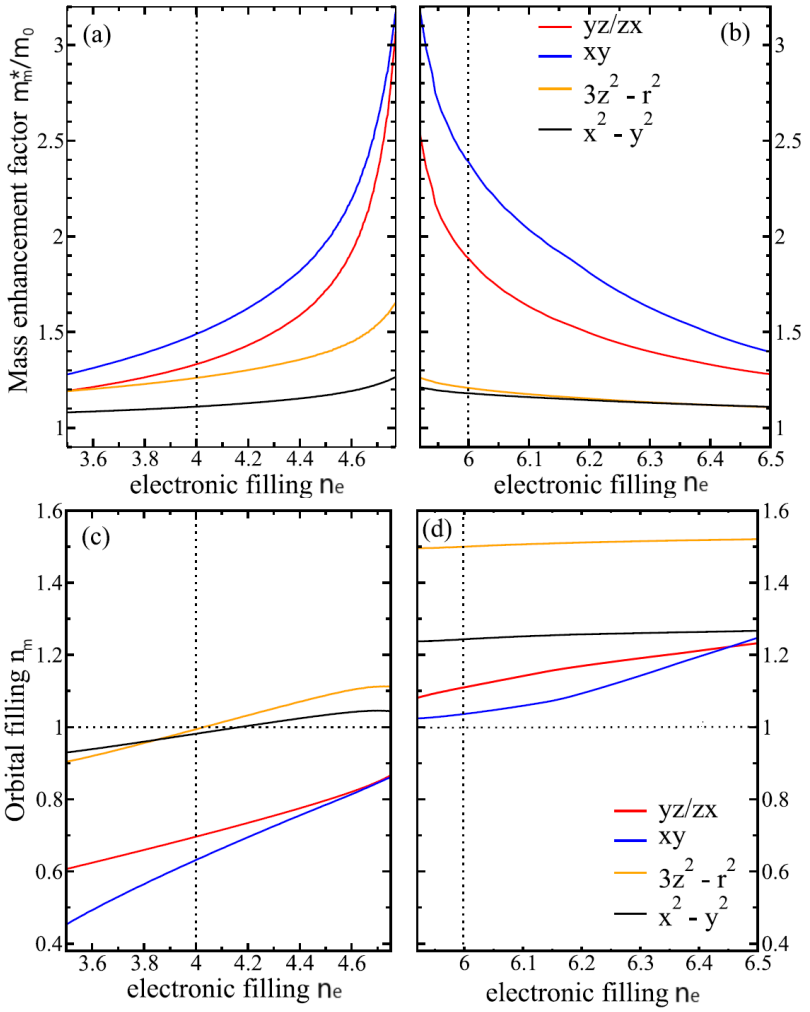

FIGURE 3.3: **(a)**, **(b)** Orbital mass enhancement factors m_m^*/m_0 and **(c)**,**(d)** orbital fillings n_m for the Slater-Koster model of $LaFeAsO$ in terms of n_e and at $U = 3\,eV$ and $J_H/U = 0.25$. Dotted line marks the undoped $n_e = 4$ or $n_e = 6$ compound, and the half-filling line ($n_m = 1$). Color code for the orbitals: red for $yz \equiv zx$, blue for xy, orange for $3z^2 - r^2$ and black for $x^2 - y^2$.

$3z^2 - r^2$ is more correlated than zx, yz, and for $U > 4.5\,eV$, $3z^2 - r^2$ becomes the most correlated orbital, due to its closeness to half-filling.

Thus, I have demonstrated that the Mott doped scenario is valid when approaching from both sides of half-filling for a generic tight-binding model for FeSCs. However, the applicability of this tight-binding model for $n_e = 4$ is not realistic. Then, in the next section I will present the DFT band structure and the Slater-Koster tight-binding model for Cr-based systems, specifically for $LaCrAsO$.

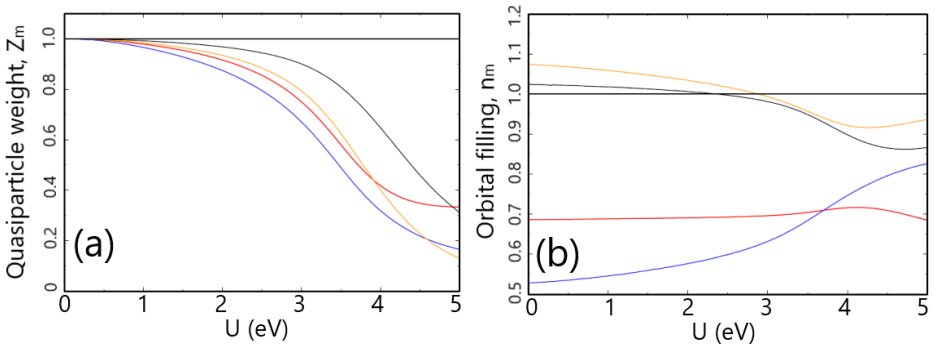

FIGURE 3.4: **(a)** Orbital quasiparticle weights Z_m and **(b)** orbital fillings n_m for the Slater-Koster model of $LaFeAsO$ in terms of U and at $n_e = 4$ and $J_H/U = 0.25$. Deep in the Hund metal regime ($U > 4\,eV$), Z_m evolution follows the lowest W_m and the closeness to half-filling behavior. Same color code as in FIGURE 3.3.

3.2.2 DFT band structure and tight-binding model for $LaCrAsO$

In this section, I will show the DFT band structure calculations done by my co-workers, using the Vienna ab-initio Simulation Package (VASP), with the GGA exchange-correlation potential, see **Appendix A**. The crystal structure of $LaCrAsO$ is tetragonal (space group $P4/nmm$), same as in $LaFeAsO$, see FIGURE 1.16, with crystal parameters fixed at the experimental values ($a = b = 4.0412\,$Å, $c = 8.9863\,$Å). The DFT band structure is given in the folded BZ, i.e. in the $2Cr$ atoms unit cell. In FIGURE 3.5, I show the DFT band structure, the DOS with the atomic character included and the Fermi surfaces at $k_z = 0$ and $k_z = \pi$.

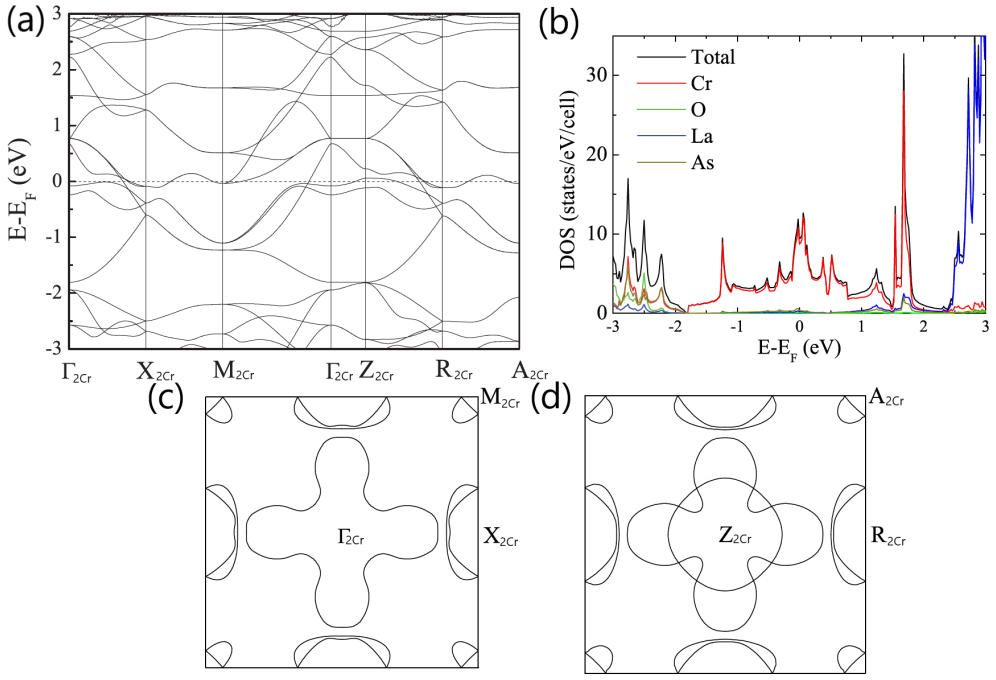

FIGURE 3.5: DFT calculations obtained by VASP code for tetragonal $P4/nmm$ $LaCrAsO$, where the crystal structure is fixed to the experimental parameters ($a = b = 4.0412\,$Å, $c = 8.9863\,$Å). **(a)** Band structure, **(b)** DOS with the atomic character included and **(c)** $k_z = 0$and **(d)** $k_z = \pi$ Fermi surfaces. Figures given in the folded BZ. See main text for the discussion.

The band structure for Cr atoms extends between $-2\,eV$ and $2.5\,eV$ ($W \approx 4.5\,eV$), with Cr d orbitals mostly contributing in this energy window (and a negligible contribution from La presents around $\sim 1.5\,eV$). The band structure is quite similar to those obtained for Mn and Fe isostructural compounds. The Fermi surface is quasi-2D. Thus, $LaCrAsO$ can be modeled as a quasi-2D system where $CrAs$ layers control the physics in it. The Fermi surface is composed of a flower-shaped hole pocket at Γ_{2Cr}, electron pockets at X_{2Cr}/Y_{2Cr} and shallow electron pockets at M_{2Cr}. Note that this topology will change when the unfolding of the BZ is performed (see **Section 1.5.2**). The folded and unfolded BZ will be identified with the subscript $2Cr$ and $1Cr$, as a reference to the number of atoms per unit cell.

For the tight-binding model, the same 2D Slater-Koster fitting than for $LaFeAsO$ [74] was used, with some changes. $\alpha = 35.26\,°$, the crystal fields splittings are set to $\epsilon_{zx,yz} = 0$, $\epsilon_{xy} = -0.3$, $\epsilon_{3z^2-r^2} = -0.9$ and $\epsilon_{x^2-y^2} = -0.48$, the overlap integrals are set to $pd\sigma = 1.12$, $pd\pi = -0.79$, $dd\sigma_1 = -0.42$, $dd\pi_1 = 0.36$, $dd\delta_1 = -0.12$ and $dd\sigma_2 = -0.024$, and $\epsilon_d - \epsilon_p = 3$, all in eV units. The quantity 0.2 is substracted from the first-nearest neighbor hoppings $t^{i,i+1}_{yz,yz}$ and symmetry-related ones. The tight-binding band structure and the Fermi surface are well reproduced, see FIGURE 3.6. Note that these calculations are done in the unfolded BZ.

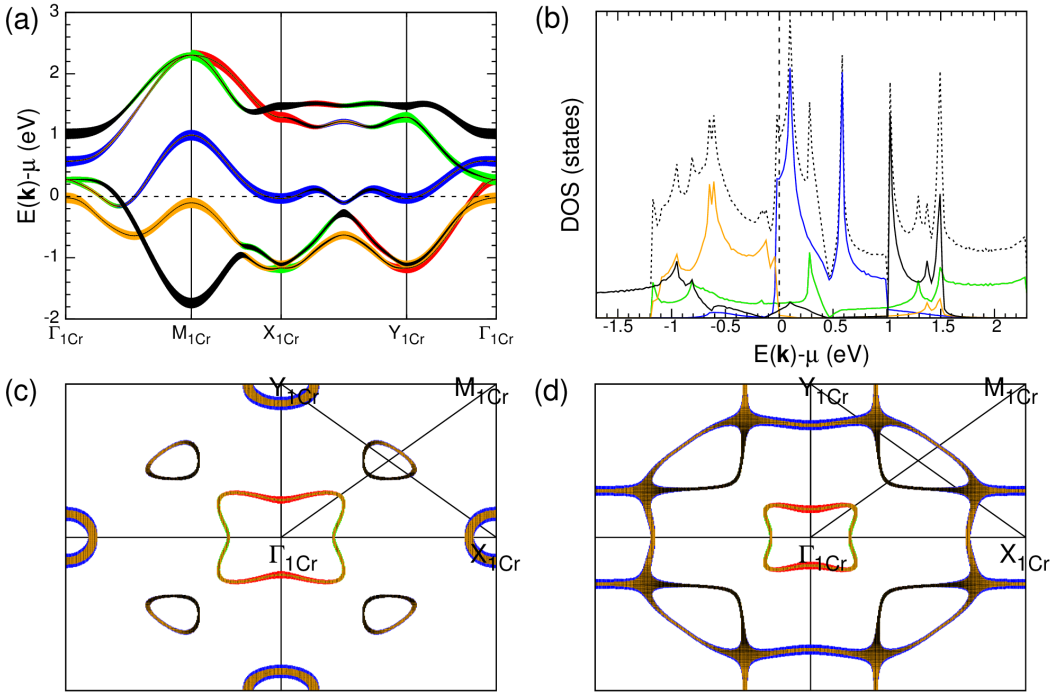

FIGURE 3.6: Slater-Koster tight-binding model for $LaCrAsO$ with $\alpha = 35.3\,°$ in the unfolded BZ, where **(a)** shows the band structure with the orbital character included and **(b)** the total DOS (dotted line) and the orbital-resolved DOS, and **(c)** $n_e = 4$ and **(d)** $n_e = 4.5$ show the Fermi surfaces with orbital character included. At $n_e = 4.5$, there is a Lifshitz transition between the electron pockets at X_{1Cr}/Y_{1Cr} and $(\pi/2, \pi/2)$. Color code for the orbitals: red for yz, green for zx, blue for xy, orange for $3z^2 - r^2$ and black for $x^2 - y^2$.

The Slater-Koster tight-binding model for $LaCrAsO$ has a total bandwidth $W \approx 4\,eV$, where the most striking feature is that xy is much more concentrated in a smaller energy window than in $LaFeAsO$ (see FIGURE 3.2). The orbital bandwidths can be estimated as $W_{zx,yz} \approx 3.5\,eV$, $W_{xy} \approx 2\,eV$, $W_{3z^2-r^2} \approx 2.5\,eV$ and $W_{3z^2-r^2} \approx 3\,eV$. In FIGURE 3.6**(c)** and **(d)**, I show the Fermi surfaces for $n_e = 4$ and $n_e = 4.5$, respectively. For $n_e = 4$, a

central Γ_{1Cr} hole-pocket (a bit distorted flower-shaped) with mainly zx and yz character, and electron pockets at X_{1Cr} and Y_{1Cr} with mainly xy character and other electron pockets centered at $\approx (\pi/2, \pi/2)$ with $3z^2 - r^2$ and $x^2 - y^2$ character are obtained. Both the DFT and the Slater-Koster model calculations compares reasonably well.

3.2.3 Electronic correlations in *LaCrAsO*

Once the tight-binding is obtained, I can calculate the mass enhancement factors m^*_m/m_0 in *LaCrAsO* when varying n_e. I apply the SSMF Z_2 formalism [38, 47] fixing U and J_H/U values, see **Appendix B**. There are not available experimental results for Z_m to compare with and obtain U and J_H values. Thus, I will use the same $U = 3\,eV$ and $J_H/U = 0.25$ values as in *LaFeAsO* [9], by considering the similarities between both compounds. I will vary n_e from 3.5 to 4.5 to obtain m^*_m/m_0, and I will also calculate the renormalized band structures and Fermi surfaces.

FIGURE 3.7 shows the mass enhancement factors m^*_m/m_0 and orbital fillings n_m for *LaCrAsO* when varying n_e. I obtained the similar trend as in *LaFeAsO* (FIGURE 3.3). *LaCrAsO* at $n_e = 4$ is less correlated than *LaFeAsO* at $n_e = 6$, but at larger filling, the correlations get of the order of undoped *LaFeAsO*. For $n_e \sim 4.5$, the strength of correlations in *LaCrAsO* is similar to those of undoped ($n_e = 6$) *LaFeAsO*. xy is the most correlated orbital, due to its reduced bandwidth W_{xy}. In *LaCrAsO* the order between different orbitals for the strength of correlations changes when compared with *LaFeAsO*. This reorganization will come from the different tight-binding model used (hence the different W_m and n_m values).

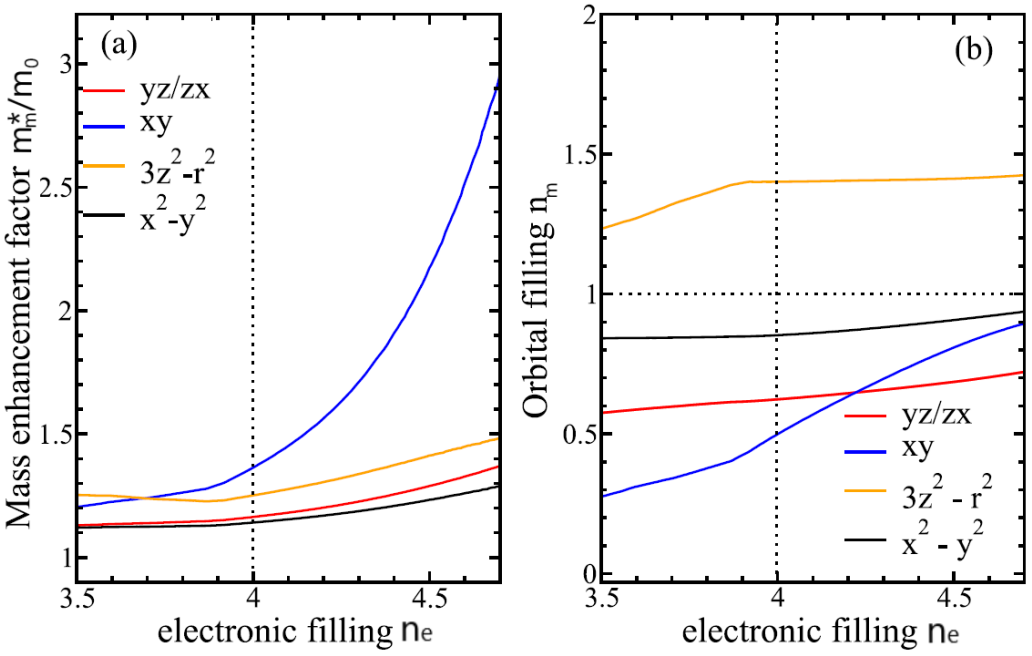

FIGURE 3.7: **(a)** Orbital mass enhancement factors m^*_m/m_0 and **(b)** orbital fillings n_m in terms of n_e for the tight-binding model for *LaCrAsO* explained in **Section 3.2.2**, and $U = 3\,eV$ and $J_H/U = 0.25$. Color code included in the legend of the figure.

The dependence of the strength of correlations when doping *LaCrAsO* towards half-filling is similar to the one found in FeSCs, so it behaves as a hole-doped Mott insulator with an increase of the strength of electronic correlations when approaching half-filling. Even if xy

orbital filling is the furthest away from half-filling at $n_e = 4$, it is the most correlated orbital due to its very small W_{xy}.

Local correlations will alter the Fermi surface topology in a non-negligible way. Γ_{1Cr} hole pocket becomes square-like for all the fillings $4 < n_e < 4.5$, while X_{1Cr}/Y_{1Cr} electron pockets become really shallow for $n_e < 4.3$ (see next section). In the next section, I will explain my co-workers calculations for the spin susceptibility χ^{RPA}_{spin} and the superconducting order parameter $g(\vec{k})$, by means of multiorbital RPA [73, 148, 149] in the spin fluctuation framerwork [56, 76]. Like in FeSCs, the applicability of the spin fluctuation theory is still under a debate [9], as discussed in **Chapter 1**. In these calculations, the band structure and Fermi surface used to calculate the spin fluctuations is renormalized using the values calculated in FIGURE 3.7, as a better approach to the real band structure and Fermi surfaces of $LaCrAsO$.

Due to the strength of electronic correlations, we expect that the superconducting dome is found in the range $n_e \sim 4.4-4.7$. In the next section, we considered that the superconducting emerges around $n_e = 4.5$, and study the magnetic and superconducting instability at this filling (as well as around it).

3.2.4 Spin susceptibility and superconducting order parameter for $LaCrAsO$

To search for the magnetic and superconducting instabilities, the system is considered a metal with a renormalized band structure. In this situation, spin fluctuation theory [56, 76] (i.e. superconductivity driven by spin fluctuations) can be applied for the renormalized band structure, as it will be a better approximation for the real band structure and Fermi surfaces for $LaCrAsO$. In this section, I will show the calculations done by my co-workers when applying multiorbital RPA [73, 148, 149] to calculate the spin susceptibility χ^{RPA}_{spin} and the superconducting order parameter $g(\vec{k})$.

Only singlet solutions are considered, due to the expected AFM (π, π) ground state for $LaCrAsO$ [116]. The magnetic ground state will be recognised by a divergence in the spin susceptibility χ^{RPA}_{spin}. The interaction parameter U assumed in RPA is not the same as in other techniques, such as in SSMF or DMFT, due to the weakly correlated character of RPA (see FIGURE 2.12). The interaction values in RPA are labeled as U_{RPA}. As explained in **Chapter 1**, the correct symmetry for the superconducting order parameter is given by the largest eigenvalue of the pairing interaction vertex $\Gamma_{\nu\mu}(\vec{k}, \vec{k}')$, with Γ being the scattering matrix between two k points in the BZ and for bands ν and μ. Thus, the largest eigenvalue will give the most important scattering process for the pairing instability. The pairing vertex $\Gamma_{\nu\mu}$ is a matrix which depends on the interaction parameters, and on the spin and charge susceptibilities.

FIGURE 3.8 shows the $n_e \geq 4.2$ evolution of the spin susceptibility χ^{RPA}_{spin} in the unfolded BZ for the renormalized band structure. Red color marks a peak in χ^{RPA}_{spin}. Figures are taken for U_{RPA} slightly smaller than the critical interaction U^c_{RPA} at which χ^{RPA}_{spin} diverges. The relative height of the peaks depends on n_e and U_{RPA}. χ^{RPA}_{spin} diverges for $\vec{Q} = (\pm\pi, \pm\pi)$ at U^c_{RPA}, signaling a checkerboard AFM ground state, as obtained in experiments. The electron pockets at X_{1Cr}/Y_{1Cr} play a major role in the formation of this AFM (π, π) ground state for $LaCrAsO$.

In electron-doped $LaCrAsO$, there are secondary peaks appearing at $\vec{Q}_2 \approx (\pm\pi/2, 0)$ (and $(0, \pm\pi/2)$) for $n_e \geq 4.4$, where FIGURE 3.9 at $n_e = 4.5$ shows this scattering vector $\vec{Q}_2$. The

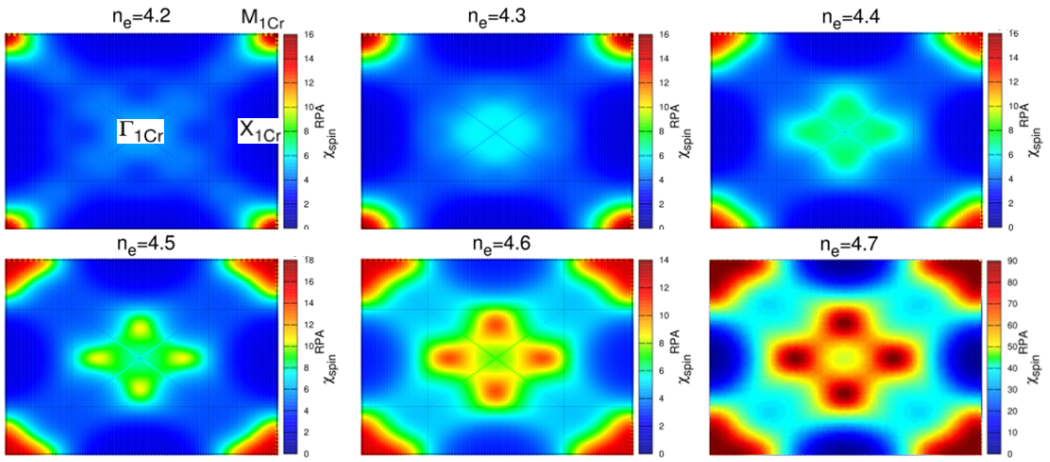

FIGURE 3.8: Spin susceptibility χ^{RPA}_{spin} calculated by multiorbital RPA in doped $LaCrAsO$ at various n_e. χ^{RPA}_{spin} peaks are colored by red, while negligible $\chi^{RPA}_{spin} \sim 0$ regions are shown in blue. Figures taken for $U_{RPA} < U^c_{RPA}$. χ^{RPA}_{spin} diverges at U^c_{RPA} for $\vec{Q} = (\pm\pi, \pm\pi)$, signaling a AFM (π, π) ground state, as expected from experiments. For $n_e > 4.4$, secondary peaks at $\vec{Q}_2 = (\pm\pi/2, 0)$ (and $(0, \pm\pi/2)$) appear. At $n_e = 4$, χ^{RPA}_{spin} peaks at $\vec{Q}' \approx (\pm 3\pi/4, 0)$ (and $(0, \pm 3\pi/4)$). The electron pockets at X_{1Cr}/Y_{1Cr} play a major role in the formation of the AFM (π, π) ground state for $LaCrAsO$.

presence of these secondary peaks signal the competing magnetic instabilities. Note that a Lifshitz transition happens between electron pockets at $X_{1Cr}/Y1Cr$ and at $(\pm\pi/2, \pm\pi/2)$ occurs at $n_e \sim 4.5 - 4.6$, see FIGURE 3.9.

In FIGURE 3.9, I show the superconducing order parameter $g(\vec{k})$ for the same n_e values in the renormalized Fermi surface as in FIGURE 3.8 and interaction parameters U_{RPA}. Red and blue colors marks the different sign of $g(\vec{k})$.

$g(\vec{k})$ shows a complex evolution with n_e. For interactions $U_{RPA} < U^c_{RPA}$, the largest eigenvalue has a d_{xy} symmetry ($g(\vec{k})$ changes sign at the x and y axis), where the maximum amplitude of $g(\vec{k})$ is found in the tips of the X_{1Cr} and Y_{1Cr} electron pockets. Suprisingly, the leading nesting vector for the superconducting instability is given by $\vec{Q}_2$, and not $\vec{Q}$, at which χ^{RPA}_{spin} diverges for U^c_{RPA} (it was expected to give a major contribution). The enhanced response at $\vec{Q}_2$ originates between the tips of the electron pockets at X_{1Cr} and Y_{1Cr} (I signaled $\vec{Q}_2$ in FIGURE 3.9 at $n_e = 4.5$ for clarification purposes), due to the proximity of the Lifshitz transition.

The discussion above for χ^{RPA}_{spin} and $g(\vec{k})$ was made for the renormalized Fermi surfaces, which show really shallow electron pockets at X_{1Cr} and Y_{1Cr}. For other fittings, other interaction parameters U and J_H (and then, different renormalizations m^*_m/m_0) and possibly other Cr related compounds, the preferred superconducting symmetry might vary, but it will most probably be d-wave due to the peak in χ^{RPA}_{spin} at $\vec{Q}$. Finding the superconducting instability due to spin fluctuations is possible in these systems, and the details will only vary the specific d-wave superconducting order parameter symmetry, but not the possibility of finding a solution for $g(\vec{k})$.

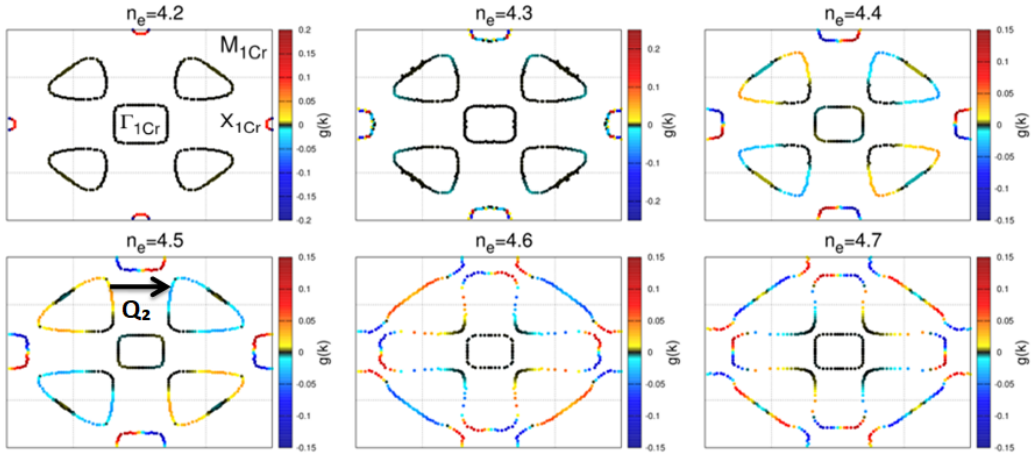

FIGURE 3.9: Superconducting order parameter $g(\vec{k})$ calculated by multiorbital RPA in the renormalized Fermi surface of $LaCrAsO$ at various n_e. Local correlations modified the Fermi surface, with Γ_{1Cr} hole pocket becoming square-like for all the fillings $n_e < 5$, and X_{1Cr}/Y_{1Cr} electron pockets becoming really shallow for $n_e < 4.3$. Except for $n_e < 4.3$, the maximum values of $g(\vec{k})$ occur in the tips of X_{1Cr} and Y_{1Cr} electron pockets. $\vec{Q}_2$ (and not $\vec{Q}$) is the responsible of the leading superconducting order parameter symmetry. This occur due to an enhanced scattering response for the tips of X_{1Cr}/Y_{1Cr} electron pockets which are close to the Lifshitz transition. At $n_e = 4.5$, the superconducting order parameter symmetry is d_{xy}.

3.3 Summary

I conclude this chapter by making a summary of the obtained results:

- Considering the Mott doped scenario [29], we proposed to search for a new family of unconventional superconductors, based on chromium instead of iron. For the same crystal structure, only the total number of electrons per atom in the d orbitals will vary when changing Fe atoms by Cr ones, where for FeSCs is $n_e = 6$ in the 5 d orbitals, while for Cr systems is $n_e = 4$ (in this situation, the half-filled systems are the Mn pnictides and chalcogenides, where $n_e = 5$ in 5 d orbitals). As an example, we have chosen $LaCrAsO$ to study the evolution of the strength of local correlations, and also the leading AFM and superconducting order. We expect that the results obtained here could be applied in any Cr related pnictide or chalcogenide. $LaCrAsO$ is an isostructural compound of $LaFeAsO$ [116], so the crystal structure and crystal parameters are similar, and the main difference relies in the total filling n_e, with Cr-based compounds describing the hole-doped Mott insulating part.

- In **Section 3.2.1**, I demonstrated that the strength of correlations increases when approaching to half-filling from both electron- and hole-doped Mott insulators. I used a Slater-Koster tight-binding model proposed for FeSCs, in particular for $LaFeAsO$ [74], keeping $U = 3\,eV$ and $J_H/U = 0.25$ as constants. These are the interaction values for which the mass enhancement factors m^*_m/m_0 obtained by SSMF equal the ones observed experimentally in ARPES and QOs for undoped $LaFeAsO$ [42]. I varied $4 < n_e < 6$. I demonstrated that the Mott doped scenario still holds for the hole-doped part.

- However, using a tight-binding model for $LaFeAsO$ in the $n_e = 4$ region does not seem too realistic, then a realistic tight-binding model to describe $LaCrAsO$ is needed. In **Section 3.2.2**, my co-workers calculated the ab-initio DFT band structure and the Slater-Koster tight-binding model for $LaCrAsO$. The band structure is quite similar to $LaFeAsO$ (with $W_{LaCrAsO} \leq W_{LaFeAsO}$), but the topology of the Fermi surface has changed. In $LaCrAsO$, the xy is concentrated in a smaller energy window ($W_{xy} \approx 2\,eV$). The Fermi surface consists in a hole-pocket centered at Γ_{1Cr} and electron pockets centered at X_{1Cr}/Y_{1Cr} and $\approx (\pm\pi/2, \pm\pi/2)$. The electron pockets X_{1Cr}/Y_{1Cr} and $(\pm\pi/2, \pm\pi/2)$ are near of a Lifshitz transition at $n_e \sim 4.5$.

- In **Section 3.2.3**, I calculated the evolution of the strength of correlations with the total filling for $LaCrAsO$ in $3.5 < n_e < 4.5$. The values m^*_m/m_0 show a similar trend as in $LaFeAsO$ when approaching half-filling. The strength of correlations is smaller in electron-doped $LaCrAsO$ at $n_e < 5$ than for hole-doped $LaFeAsO$ at $n_e > 5$. Around $n_e \sim 4.5$, $LaCrAsO$ has similar values for m^*_m/m_0 as for undoped $LaFeAsO$. Due to this similarity, we assumed that this would be the doping at which superconductivity is more likely to appear.

- In **Section 3.2.4**, my co-workers calculated the spin susceptibility and the superconducting order parameter using multiorbital RPA, in the framework of the spin fluctuation theory. They used the renormalized band structure as a better approximation for the real band structure. For U^c_{RPA}, the peaks at $\vec{Q}$ diverge, signaling the (π, π) AFM ground state as found in experiments [116]. Other AFM instabilities are present, like $\vec{Q}_2 = (\pi/2, 0)$ and $(0, \pi/2)$. These peaks at $\vec{Q}$ and $\vec{Q}_2$ are interaction and filling dependent. My co-workers argued that X_{1Cr}/Y_{1Cr} electron pockets are controlling the magnetic and superconducting instabilities.

- Interestingly, for $U_{RPA} < U^c_{RPA}$ at $n_e = 4.5$, the largest eigenvalue for the superconducting order parameter is given by $\vec{Q}_2$ (and not by the AFM nesting vector $\vec{Q}$) and it has a d_{xy} symmetry. This enhanced response at $\vec{Q}_2$ originates between the tips of the electron pockets at X_{1Cr} and Y_{1Cr}. This enhancement appears due to the proximity of the Lifshitz transition at $n_e \sim 4.5 - 4.6$. The symmetry d_{xy} found for $LaCrAsO$ might vary for a different tight-binding model or a different choice of interacting parameters U and J_H (hence the renormalized Fermi surface will change). However, we expect that a solution for the superconducting order parameter can be still found for $n_e \sim 4.4 - 4.7$, maintaining the d-wave character due to the peak in χ^{RPA}_{spin} at $\vec{Q}$.

I would like to conclude by giving a few comments on other related articles that came out after the publication in arXiv of the present work [150–154]. Simultaneously, another article [150] proposing $BaCr_2As_2$ as a new high-T_c superconductor was published on arXiv. This article motivates the search by following the same ideas that we proposed, and the results presented in it are consistent with ours. They focused on the idea that an enhancement of the electronic compressibility (defined by $\kappa_{el} = dn/d\mu$) will drive a charge instability, hence a possible superconducting instability. A few experimental [151–153] and theoretical [154] articles about $BaCr_2As_2$ have been published afterwards. They pointed out a remarkable reduction of the effect of local correlations in this compound, due to the influence of the larger hybridization of Cr d orbitals with As p orbitals, as compared with $BaFe_2As_2$. We have also found the same trend.

Chapter 4

Strong electronic correlations and Fermi surface reconstruction in the quasi-one dimensional iron superconductor $BaFe_2S_3$[1]

In **Chapter 1**, I have emphasized that iron-based superconductors (FeSCs) are usually metals, in contrast with cuprates which are Mott insulators. Recently, in 2015, a new family of FeSCs was discovered, showing insulating behavior which persists for $T > T_N$, i.e. for T larger than the antiferromagnetic (AFM) ordering temperature T_N. By applying pressure, there is an insulator-to-metal transition, the AFM order is suppressed and superconductivity emerges, all around the same pressure. These systems are the 123 two-leg ladder family of iron chalcogenides. The peculiarity of these 123 FeSCs is that the crystal structure is similar to other FeSCs (see FIGURE 1.16), but with every third column of Fe atoms in the Fe layer is absent, showing a quasi-1D crystal structure. $BaFe_2S_3$ shows a $T_c^{max} \sim 24\,K$ for $P_c \sim 11\,GPa$ [155, 156] and $BaFe_2Se_3$ shows a $T_c^{max} \sim 11\,K$ for $P_c \sim 12.7\,GPa$ [157]. It was argued by some authors [155, 156] that these systems are Mott insulators.

In the 123 FeSCs, the filling per Fe atom is the same as in other FeSCs families, i.e. $n_e = 6$ electrons per Fe atom. Then, by following the arguments of previous chapters, we expect that the system is a metal, rather than a Mott insulator (Hund's coupling tends to disfavor the appearance of the Mott insulating state). Here, I will calculate the effect of local correlations at $T = 0\,K$ for $BaFe_2S_3$ to clarify the origin of the insulating state. I will consider the 5 d orbitals tight-binding model, proposed by [98] using Wannier parametrization of the Density Functional Theory (DFT) band structure obtained for two pressures, $0\,GPa$ and $12.4\,GPa$, where at the latter pressure, the system is superconducting. I will apply the slave-spin mean-field (SSMF) $U(1)$ formalism for both pressures. I will show that, for realistic U and J_H, the system is still metallic at both pressures for $T = 0\,K$. At $0\,GPa$, the strength of correlations for the orbitals which mostly contribute to the band structure around the Fermi level is very strong, so that we will argue that the insulating behavior in a local correlations picture could come from temperature effects (see FIGURE 1.11**(b)**). At $12.4\,GPa$, the strength of correlations shows similar values as in other FeSCs, as shown in **Chapter 2**. The Fermi surfaces suffer a huge reconstruction due to local correlations effects, contrary to what happens in other quasi-2D FeSCs.

In this chapter, I will first briefly review the tight-binding model presented for $BaFe_2S_3$ at $0\,GPa$ and $12.4\,GPa$ [98]. I will show that the band structures around the Fermi level and Fermi surfaces for

[1] Results presented in this Chapter published in [97]

both pressures show a 3D character, in contrast with the quasi-1D structure and with other FeSCs which show a quasi-2D behavior. Due to the substraction of every third column of Fe atoms, there is a breaking of degeneracy of the x and y directions, hence d_{zx} and d_{yz} are not degenerated anymore. All 5 d non-degenerated orbitals contribute to the band structure. In $BaFe_2S_3$, the unit cell has 4 equivalent Fe atoms, hence the tight-binding hamiltonian in the k-space is a 20×20 matrix ($5\,d$ orbitals $\times$ $4\,Fe$ atoms), substantially increasing the complexity of the problem. I have checked the impossibility of performing an unfolding of the Brillouin zone (BZ) in these systems (while it was possible for other quasi-2D FeSCs, see **Section 1.5.2**), due to various off-plane hoppings which are not negligible.

In the 4 Fe atoms unit cell, there are non-zero off-diagonal crystal field energies ϵ_{mn} with $m \neq n$. In order to simplify the SSMF calculations, we rewrite the tight binding hamiltonian to retain only diagonal crystal field splittings ϵ_m, see **Appendix B**. The original tight-binding model is written in a new orbital basis (labeled by w_m with $m = zx, yz, xy, x^2 - y^2$ and $3z^2 - r^2$), in which only diagonal crystal field energies persist. I will comment the effects of writing the tight-binding hamiltonian in this new orbital basis. The main effect is that w_{zx} and w_{yz} orbitals mostly contribute to the bands around the Fermi level, hence highly reducing the orbital bandwidths W_{w_m} for these two orbitals.

Then, I will calculate Z_{w_m} in the new orbital basis by using SSMF $U(1)$ formalism, setting $n_e = 6$ and discussing the correct U and J_H values for $BaFe_2S_3$ at both pressures [9, 98]. I obtained finite quasiparticle weights $Z_{w_m} \neq 0$ for all orbitals, at both pressures and for realistic values of U and J_H. These values range between $Z_{w_m} \sim 0.03 - 0.06$, so the system is a correlated metal at $T = 0\,K$. However, $Z_{w_{zx}}$ and $Z_{w_{yz}}$ at $0\,GPa$ are very small, and we will argue that the system can be driven to an insulating behavior by a finite T. Applying pressure will increase the total bandwidth, hence the system is expected to be less correlated (due to the increase of the kinetic energy gain $\widetilde{W}$) at $12.4\,GPa$. For $12.4\,GPa$, the strength of correlations, in fact, decreases and becomes similar to other FeSCs. This finding may help to link the optimal degree of correlations plus an AFM order being suppresed with the appearance of high-T_c superconductivity, an idea pointed out in previous chapters.

Finally, I will calculate the renormalized band structure for both pressures. I will show that there is a non-negligible Fermi surface reconstruction for both pressures, in contrast with other FeSCs, in which the Fermi surface is almost unaffected by local correlations. This reconstruction will alter the results extracted from Fermi surface-based theories for magnetic and superconducting instabilities.

4.1 Introduction & Motivation

Recently, in 2015 [155, 156], and later in 2017 [157], a new family of FeSCs has been discovered in the 123 iron chalcogenides, for $BaFe_2S_3$ and $BaFe_2Se_3$, respectively. The undoped compounds at ambient pressure are AFM insulators, and the insulating behavior persist for $T > T_N$, with $T_N \sim 240 - 255\,K$, $\mu \sim 2.8\,\mu_B/Fe$ for $BaFe_2Se_3$ [158–160] and $T_N \sim 100 - 120\,K$, $\mu \sim 1.20\,\mu_B/Fe$ for $BaFe_2S_3$ [155, 156, 161, 162]. $BaFe_2S_3$ shows closer T_N and μ values to other quasi-2D FeSCs, see **Section 1.5.2**. The AFM ordering is different in both compounds, see next paragraphs.

123 FeSCs have a different crystal structure than other quasi-2D FeSCs. 123 FeSCs are formed by two-leg ladders of iron atoms, where Fe atoms are tetrahedrally coordinated with the chalcogen atoms Se or S (like in quasi-2D FeSCs). This can be identified as a quasi-1D crystal structure. The two-leg ladders structure is similar to the quasi-2D layers of Fe, but substracting every third column of Fe atoms, then effectively reducing the dimensionality, see FIGURE 4.1 for $BaFe_2S_3$.

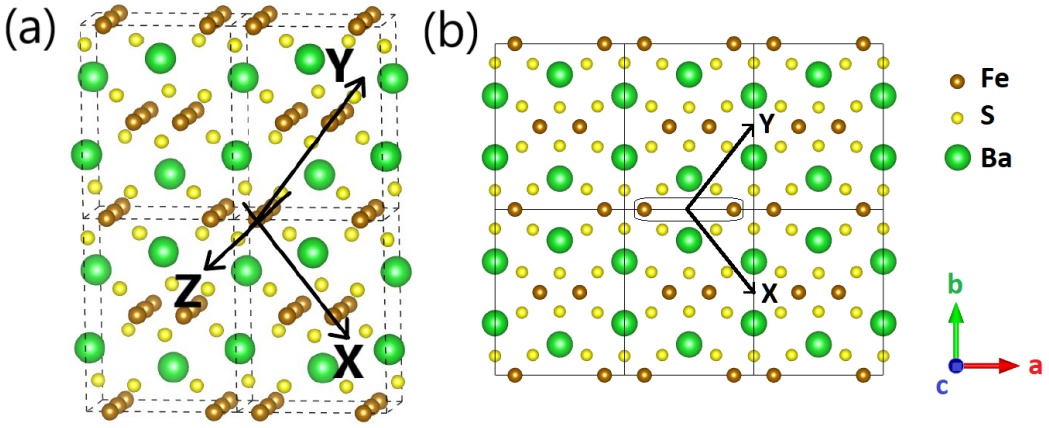

FIGURE 4.1: **(a)** General view and **(b)** perpendicular to the ladder view of the crystal structure $CmCm$ for $BaFe_2S_3$. Two-leg ladders can be visualized like the square Fe layers of quasi-2D FeSCs, but substracting every third column of Fe atoms. Real space axes X, Y and Z and crystallographic axes a, b and c are marked, where Z and c coincides, and XY and ab run in different directions. When obtaining the tight-binding model, the orbitals will be oriented along the crystallographic axes abc, while the hopping amplitudes are written in the real space axes XYZ. Note also the difference with quasi-2D FeSCs, where the Fe layer is in the ab plane, while here it is in the ac plane.

In FIGURE 4.2, I compare the two different crystal structures present in 123 FeSCs. $BaFe_2Se_3$ has $Pnma$ crystal structure symmetry, while $BaFe_2S_3$ has $CmCm$ crystal structure symmetry. The difference relies in the tilting of the two-leg ladders.

The AFM order is different in both compounds. $BaFe_2Se_3$ shows a Block AFM order, where the spins are parallel for each 2×2 arrange of Fe atoms in the two-leg ladder, and they oriented out-of-plane of the two-leg ladders. In $BaFe_2S_3$, the AFM order is the typical stripe AFM, present in other FeSCs (see **Section 1.5.2**), with spins oriented parallel in the a direction of the two-leg ladder and antiparallel in the c direction [155, 164]. In $BaFe_2Se_3$, there is a sizable magnetoelastic coupling (i.e. the crystal structure parameters are sensible to changes in the magnetism) [157, 158, 165, 166], which is believed to be related with the formation of the Block AFM order.

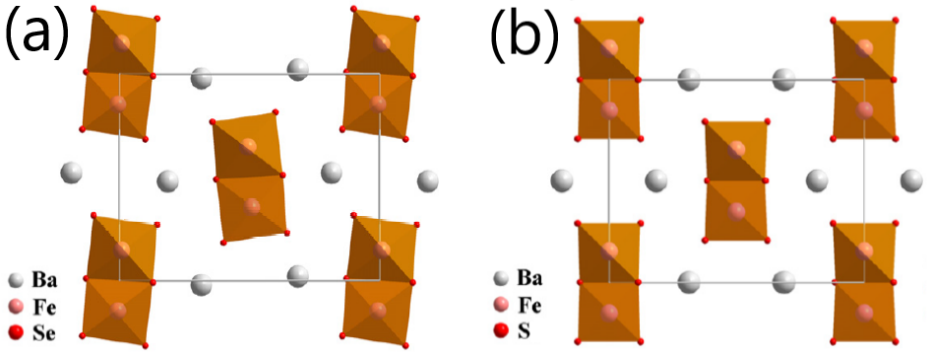

FIGURE 4.2: Crystal structures for **(a)** $BaFe_2Se_3$ ($Pnma$) and **(b)** $BaFe_2S_3$ ($CmCm$). The two-leg ladders run perpendicular to the paper. The difference between both structures is the tilting of the two-leg ladders for the $Pnma$ crystal structure, which is also believed to be related with the magnetoelastic coupling in $BaFe_2Se_3$ and the different AFM ordering in both crystal structure symmetries. Taken and adapted from [163].

Different dopings on $BaFe_2Se_3$ and $BaFe_2S_3$ have been studied [166, 167], see FIGURE 4.3. For hole-doped $Ba_{1-x}K_xFe_2Se_3$ [166], the Block AFM phase gets suppressed, and there are structural (from $Pnma$ to $CmCm$) and magnetic (from Block AFM to stripe AFM) transitions when approaching KFe_2Se_3 ($n_e = 5.5$ per Fe atom). For hole-doped $Ba_{1-x}K_xFe_2S_3$, CX-AFM order (spins aligned parallel along the x axis, and antiparallel along the y axis, see FIGURE 4.3**(a)**) gets suppressed. For electron-doped $BaFe_{2-y}Co_yS_3$ [167], stripe AFM phase is more robust and no sign of suppression is seen up to $y \sim 0.2$. A resistivity anomaly at $\approx 200\,K$ have been seing for $BaFe_{2-y}Co_yS_3$ [167]. The authors argued about a possible orbital ordering (OO) as the origin of this anomaly, but yet it is not fully established and further studied would be required. No superconducting transition have been found when doping these systems.

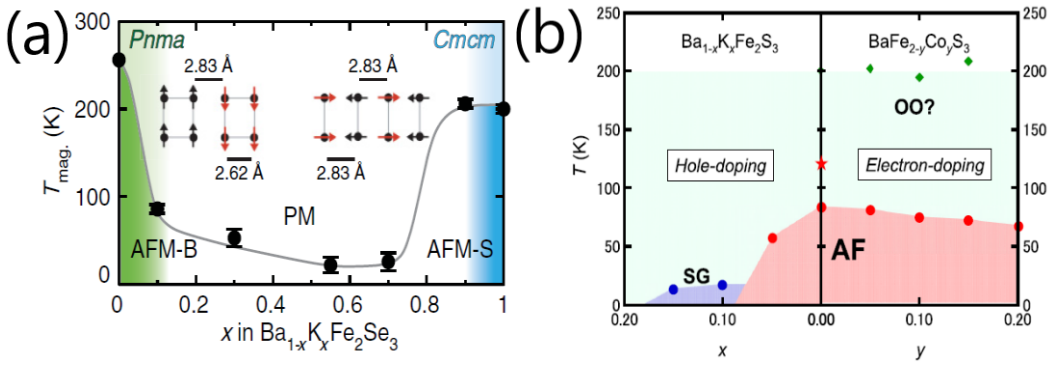

FIGURE 4.3: Doping phase diagrams for **(a)** $Ba_{1-x}K_xFe_2Se_3$ (hole-doped) and **(b)** $Ba_{1-x}K_xFe_{2-y}Co_yS_3$ (both hole- and electron-doped). For $BaFe_2Se_3$, the Block AFM order and the $Pnma$ crystal structure symmetry is progresively replaced by the stripe AFM order and the $CmCm$ crystal structure symmetry when KFe_2Se_3 is reached. For $BaFe_2S_3$, the stripe AFM order is suppressed for the hole-doped part, while it remains robust for the electron-doped part. A spin-glass phase appears at $x \sim 0.1$. The authors [167] argued about a possible orbital ordering at T_{OO} as the origin of a kink in the resistivity for $BaFe_{2-y}Co_yS_3$, but yet it is not fully established and further studied would be required. Taken and adapted from [166, 167].

When pressure is applied for both $BaFe_2Se_3$ and $BaFe_2S_3$ [155–157], the AFM phase is suppressed, there is an insulator-to-metal transition and superconductivity emerges, all around

the same P_c, see FIGURE 4.4. $BaFe_2Se_3$ shows a $T_c^{max} \sim 11\,K$ for $P_c \sim 12.7\,GPa$, and $BaFe_2S_3$ shows a $T_c^{max} \sim 24\,K$ for $P_c \sim 11\,GPa$. Interestingly, the insulating behavior for ambient pressure 123 FeSCs, persists for $T > T_N$ [155–157, 165, 168].

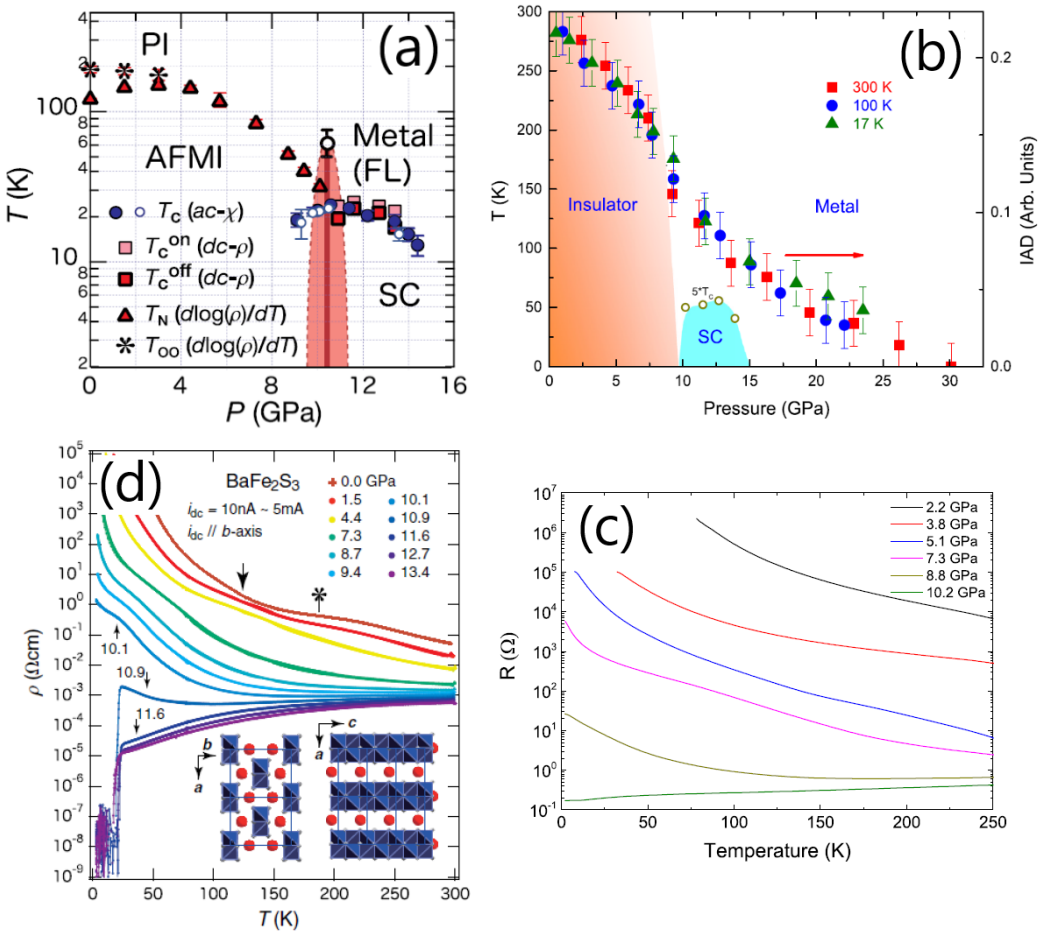

FIGURE 4.4: Pressure phase diagram for **(a)** $BaFe_2S_3$ and **(b)** $BaFe_2Se_3$, where the insulating (both AFM and paramagnetic, PI), the metallic and superconducting phases are marked. $BaFe_2Se_3$ shows a $T_c^{max} \sim 11\,K$ for $P_c \sim 12.7\,GPa$, and $BaFe_2S_3$ shows a $T_c^{max} \sim 24\,K$ for $P_c \sim 11\,GPa$. Stars in the phase diagram of $BaFe_2S_3$ signal a kink in the resistivity. **(c)**, **(d)** Resistivity versus temperature curves for $BaFe_2S_3$ and $BaFe_2Se_3$ at various pressures. The insulating behavior persist for $T > T_N$ ($\rho(T)$ decreases with T) in both systems. Taken from [156, 157].

Fe two-leg ladders control the band structure around the Fermi level, with a total number of electrons per Fe atom $n_e = 6$, like in other FeSCs. The reduced dimensionality will decrease the kinetic energy gain $\widetilde{W}$ of the electrons, hence increasing the ratio $\Delta^x/\widetilde{W}$, see **Section 2.2**, and increasing the electronic correlations effects. This has led to some authors [155, 156] to claim that these systems are Mott insulators, like high-T_c cuprates superconductors. Nevertheless, in previous chapters, I have shown that in Hund metals (thus in FeSCs) the Mott insulating behavior is disfavored by J_H, so $\Delta^x/\tilde{W}$ should be strongly reduced, by the effective reduction of the dimensionality, in order to be able to drive the system into a Mott insulating state, see FIGURE 2.12**(b)**. This situation does not seem plausible according to the band structure calculations (see next paragraph).

In [98], the band structure and tight-binding models were calculated for $BaFe_2S_3$, finding that all 5 d orbitals of Fe atoms mainly contribute to the band structure around the Fermi

level with a total bandwidth $W \sim 4\,eV$ (see **Section 4.2.1**). Also in [98], constraint random phase approximation (cRPA) calculations showed that the realistic U and J_H values for $BaFe_2S_3$ are similar to $LiFeAs$, i.e. larger than in $BaFe_2As_2$ and smaller than in $FeSe$, therefore, we expect that $BaFe_2S_3$ is close to or in the Hund metal regime (see violet shaded area in FIGURE 2.12**(b)**).

DFT calculations can reproduce the correct AFM but with a larger magnetic moment $\mu_{DFT} \sim 2.1\,\mu_B/Fe$ [164, 169], as occurs in other FeSCs, see **Section 1.5.2**. From the experimental point of view, in $BaFe_2S_3$, the magnetic moment is $\sim 1.20\,\mu_B/Fe$, much smaller than in a Mott insulator where the saturation gives $4\,\mu_B/Fe$ [161], see **Section 1.5.2**. Photoemission and X-ray experiments in $BaFe_2S_3$ suggest the coexistance of local and itinerant electrons at the same time in this system [170, 171].

So far, the theoretical analysis in 123 FeSCs on the role of electronic correlations have used models with two or three Fe d orbitals [160, 172, 173]. Due to the hybridization between the 5 d orbitals, the orbital bandwidths and fillings depend highly on the number of orbitals included in the initial model. Thus, the two and three orbitals models cannot properly address the strength of the electronic correlations for each orbital. Furthermore, in the case of two orbitals models [160, 172], no Hund metal physics is found (see **Chapter 2**). The three orbital model [173] cannot reproduce neither the correct band structure nor the correct quasiparticle weights for each orbital in the 123 FeSCs (see next sections). Another important failure of these two and three orbitals models is that the authors assumed a 1D two leg ladder to reproduce the band structure. In $BaFe_2S_3$, the band structure shows a non-negligible 3D dispersion [98], hence questioning the validity of these previous works. To address the strength of electronic correlations in this family, a suitable technique for a model containing the 5 Fe d orbitals is required.

All of these results point to the importance of electronic correlations for a 5 d orbitals model of 123 FeSCs, and also to the need of clarification about the insulating phase in these multiorbital systems. From the perspective worked on previous chapters, it does not seem plausible to find a Mott insulator at $T = 0\,K$, as assumed by other authors.

4.2 Results & Discussion

Now, I will present the results that I have obtained and published in [97]. In **Section 4.2.1**, I will briefly review the tight-binding model obtained by [98] for $BaFe_2S_3$ at two different pressures $0\,GPa$ and $12.4\,GPa$. Fe d orbitals are mainly contributing to the band structure around the Fermi level, with $n_e = 6$ in each Fe atom. I will discuss the results of this model in the folded BZ, i.e. with 4 Fe atoms in the unit cell. Then, I performed a change of basis from the non-diagonal crystal field original orbitals to a new orbital basis with diagonal crystal field energies (labeled by w_m). This change of basis is done in order to simplify the local correlations calculations, see **Appendix B**. In **Section 4.2.2**, I calculated Z_{w_m} using SSMF $U(1)$ formalism at $T = 0\,K$. We have estimated U and J_H for the different pressure values, according to the comments made in [98] when using cRPA, and taking into account the cRPA and SSMF comparison, as discussed in FIGURE 2.12. I will show that the system at $T = 0\,K$ and both pressures is still in the Hund metal regime, and no Mott (or even orbital-selective Mott transition) is found. However, at $0\,GPa$, the quasiparticle weights Z_{w_m} of the orbitals mostly contributing to the band structure around the Fermi level are very small, $\sim 0.03 - 0.06$. Thus, we argue that a finite T (see FIGURE 1.11**(b)**) the incoherence of the

system increases, hence the insulating nature of $BaFe_2S_3$ could be reconciled with the local correlations picture. Finally, in **Section 4.2.3**, I calculate the renormalized band structure, showing the sizable reconstruction suffered by the Fermi surfaces at both pressures. The consequences of this reconstruction for Fermi surface instability theories are discussed. The Fermi surface reconstruction will change the expectations for Fermi surface-based magnetic and superconducting instabilities.

4.2.1 Tight-binding model for $BaFe_2S_3$ at $0\,GPa$ and $12.4\,GPa$

Here, I reproduce the tight-binding model derived by [98] for $BaFe_2S_3$ at $0\,GPa$ and $12.4\,GPa$. This tight-binding model is obtained by doing a Wannier parametrization for the Fe d orbitals. For $12.4\,GPa$, crystal structural parameters shrinks around $92-96\,\%$ of those at $0\,GPa$.

In $BaFe_2S_3$, the unit cell has 4 Fe atoms. Thus, the total number of orbitals in the unit cell is $N_{orb}=20$ ($5\,d$ orbitals $\times$ $4\,Fe$ atoms). In the unit cell there is only 1 inequivalent Fe atom, so there are 5 d fourly-degenerated orbitals. I have checked that the unfolding of the BZ (as done in other FeSCs) is not possible in this system. Thus, we have to work in the folded BZ, with 4 Fe atoms in the unit cell, hence with all the 20 d-like bands.

The real (and k-) space axes X, Y and Z are oriented as shown in FIGURE 4.1, and the hopping parameters are written using these axes. On the other hand, d orbitals are oriented along the crystalographic axes a, b and c. The crystalographic axes (shown in FIGURE 4.1**(b)**) are chosen differently from other FeSCs, where 2D square of Fe atoms is in the ab plane and c is the offplane axis. In $BaFe_2S_3$, the two-leg ladder is oriented along c, in the plane ac, whether b stands for the offplane axis. Then, the d orbitals are not defined in the same way as in $BaFe_2S_3$ as in other quasi-2D FeSCs[2]. Due to the breaking of the degeneracy of x and y directions in the two-leg ladder plane, xz and yz orbitals are not degenerate in 123 FeSCs. Also, it can be seen that $(0,0,k_z)\rightarrow(\pi,0,k_z)$ and $(0,0,k_z)\rightarrow(0,\pi,k_z)$ directions are equivalent, while $(0,0,k_z)\rightarrow(\pi,\pi,k_z)$ and $(0,0,k_z)\rightarrow(\pi,-\pi,k_z)$ are not, where $k_z\in[-\pi,\pi]$.

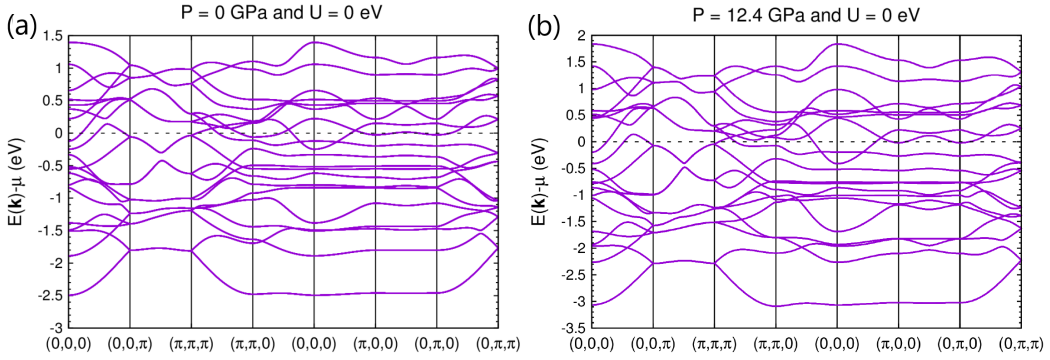

FIGURE 4.5: Band structures for **(a)** $0\,GPa$ and **(b)** $12.4\,GPa$ in the non-interacting limit ($U=0\,eV$). Bandwidth is of the order of other quasi-2D FeSCs, with $W^{0\,GPa}\sim 4\,eV$ and $W^{12.4\,GPa}\sim 5\,eV$. The band structure close to the Fermi level shows a marked 3D character, besides the system shows a quasi-1D crystal structure. Reproduced from [97] using the parameters proposed in [98].

[2]For example, in $BaFe_2S_3$, zx orbital will be equivalent to xy orbital in other quasi-2D FeSCs.

FIGURE 4.5**(a)** and **(b)** show the band structure for both pressures, where the total bandwidth is $W^{0\,GPa} \sim 4\,eV$ and $W^{12.4\,GPa} \sim 5\,eV$. Close to the Fermi level, the band structure have a singular 3D character (see the non-negligible dispersion when varying k_x or k_y), on spite of the quasi-1D crystal structure.

In FIGURE 4.6, I present the Fermi surfaces for both pressures and undoped ($n_e = 6$) $BaFe_2S_3$, in the reduced BZ (the full BZ is just the repetition of this one-quarter reduced BZ). The top row refers to $0\,GPa$ and the bottom row to $12.4\,GPa$. I included the Fermi surface **(a.2)**, **(b.2)** cuts along k_z-$(k_x - k_y)$ plane, and **(a.3)**, **(b.3)** cuts along kz-$(k_x + k_y)$ plane, both in the full BZ. The Fermi surfaces consist on several pockets with a 3D character. At $0\,GPa$, the Fermi surface has an electron pocket α at Γ, surrounded by a large electron pocket β, and a couple of hole pockets γ around $(0, 0, \pm 3\pi/4)$ and directed along $(k_x, -k_x, \pm 3\pi/4)$. With pressure, the size of the pockets change, specially for the electron pocket β which shrinks significatively, dissappearing around the corners $(\pm\pi, \pm\pi, 0)$).

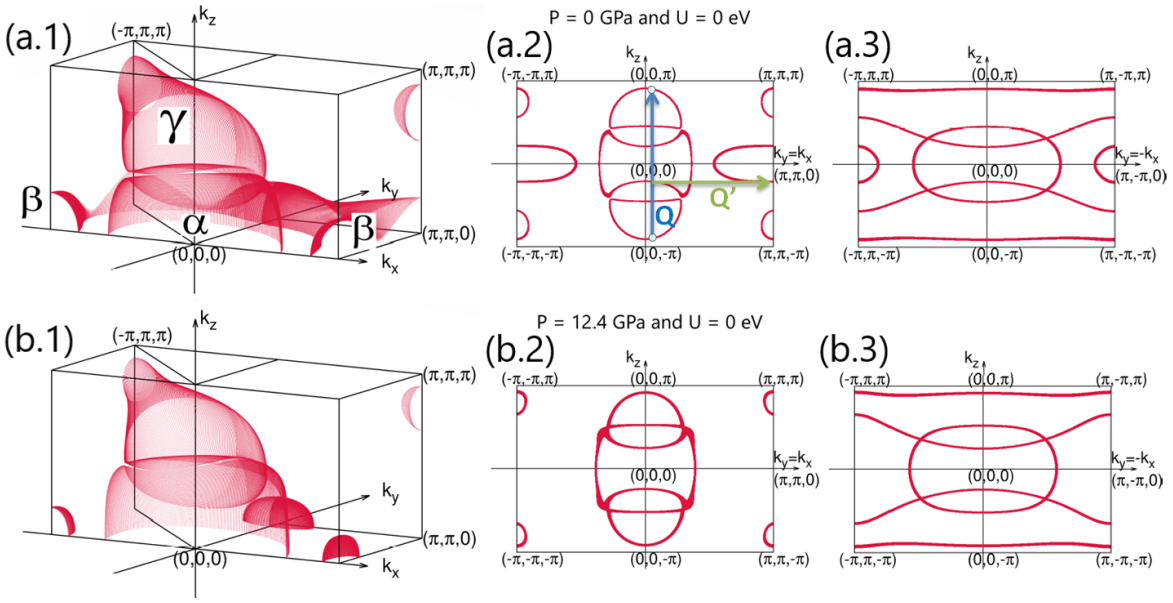

FIGURE 4.6: **(a.1)** $0\,GPa$ and **(b.1)** $12.4\,GPa$ 3D Fermi surfaces in the reduced BZ. The Fermi surfaces consist on different pockets, which can be identified as α, β and γ (see main text). **(a.2)** $0\,GPa$ and **(b.2)** $12.4\,GPa$ Fermi surface cuts along k_z-$k_x - k_y$ plane, and **(a.3)** $0\,GPa$ and **(b.3)** $12.4\,GPa$ Fermi surface cuts along k_z-$k_x + k_y$ plane, in the full BZ. Figures taken at $n_e = 6$ and for the non-interacting limit. $\vec{Q}$ intra-ladder AFM nesting vector [164] connects the top and bottom γ pockets, while $\vec{Q}'$ inter-ladder AFM nesting vector connects α and β pockets. $\vec{Q}$ and $\vec{Q}'$ included as blue and green lines, respectively.

From a weakly correlated picture of magnetism, the nesting vector appears around a slightly incommensurate $\vec{Q} \sim (0, 0, 2\pi)$ (see blue vector in FIGURE 4.6**(a.2)** and **(b.2)**), and it could give some contribution (see below) for the intra-ladder stripe AFM order [164] (in the unfolded BZ, $\vec{Q}$ would transform into $\vec{Q}^* \sim (0, 0, \pi)$). The nesting vector which would produce the inter-ladder stripe AFM order is given by $\vec{Q}' = (\pm\pi, \pm\pi, k_z)$ (see green vector in FIGURE 4.6**(a.2)** and **(b.2)**). $\vec{Q}$ would not be suppressed by pressure, but $\vec{Q}'$ will, so the experimental suppression of AFM when applying pressure could by explained as a decrease of the inter-ladder scattering. Nevertheless, at $0\,GPa$, the system is an insulator, and I will show later on that the orbitals controlling the Fermi surface are very strongly correlated, so weakly correlated theories are highly in doubt to be applicable for the ambient pressure compound.

The tight-binding model of [98] is written in the non-diagonal (crystal field energies) orbitals basis, hence there exist non-zero $\epsilon_{m\neq n}$, i.e. different orbitals have onsite mixing terms. To simplify the SSMF $U(1)$ calculations (see **Appendix B**), the tight-binding hamiltonian is rewritten in a new basis in which the onsite terms are diagonal. This is done by taking the matrix of crystal field energies, diagonalizing it, and rewriting H_0 (where H_0 is the tight-binding hamiltonian, see Eq. (1.4)) in the new orbital basis (defined by the eigenvectors obtained in the crystal field energies matrix diagonalization).

The new orbitals are labeled as w_m with $m = zx, yz, xy, 3z^2 - r^2$ and $x^2 - y^2$, and they are a linear combination of the old orbitals. The subscripts stand for the largest contribution to these new orbitals from the old ones. FIGURE 4.7 show the tables for $0\,GPa$ and $12.4\,GPa$, with the contributions of each original orbital for the new orbitals, as well as the new crystal field splittings ϵ_{w_m}, the orbital filllings per spin $n_{w_m\sigma}$ ($n_{w_m\sigma} = 0.5$ is defined as half-filling) and the estimated orbital bandwidths W_{w_m}. ϵ_{w_m} are of the same order, so all new orbitals are playing an important role in the band structure. Applying pressure does not vary significantly the orbital filling, but it increases W_{w_m}. Then, we expect that the strength of local correlations will be reduced by pressure for all the orbitals, due to an increase of the kinetic energy gain.

(a) P = 0 GPa

	zx	yz	xy	x^2-y^2	$3z^2-r^2$	ϵ_{w_m} (eV)	$n_{w_m\sigma}$	W_{w_m} (eV)
w_{zx}	0.8252	–	0.1748	–	–	0	0.473	~2.25
w_{yz}	–	0.8705	–	0.1250	0.0045	0.083	0.611	~2.00
w_{xy}	0.1748	–	0.8252	–	–	−0.066	0.572	~2.50
$w_{x^2-y^2}$	–	0.1027	–	0.8119	0.0854	−0.354	0.738	~2.50
$w_{3z^2-r^2}$	–	0.0268	–	0.0268	0.9101	−0.591	0.606	~3.00

(b) P = 12.4 GPa

	zx	yz	xy	x^2-y^2	$3z^2-r^2$	ϵ_{w_m} (eV)	$n_{w_m\sigma}$	W_{w_m} (eV)
w_{zx}	0.9262	–	0.0738	–	–	0	0.478	~2.75
w_{yz}	–	0.8537	–	0.1387	0.0077	0.035	0.638	~2.50
w_{xy}	0.0738	–	0.9262	–	–	−0.156	0.567	~3.25
$w_{x^2-y^2}$	–	0.0972	–	0.7491	0.1537	−0.445	0.724	~3.50
$w_{3z^2-r^2}$	–	0.0492	–	0.1122	0.8386	−0.705	0.593	~3.50

FIGURE 4.7: Table for the basis change from the old orbital basis to the new one for **(a)** $0\,GPa$ and **(b)** $12.4\,GPa$, and values of the new crystal field splittings, orbital fillings per spin and orbital bandwidths. The name of the new orbitals is given by looking at the largest contribution of the old ones when changing the basis.

FIGURE 4.8**(a)** and **(b)** show zooms of the band structure around the Fermi level for $0\,GPa$ and $12.4\,GPa$, with the majority orbital (in the new orbital basis) contribution included. Red and green colors refer to the contribution of w_{yz} and w_{zx} orbitals, respectively. As it can be seen, both orbitals dominate the band structure around the Fermi level, hence they also dominate the Fermi surfaces.

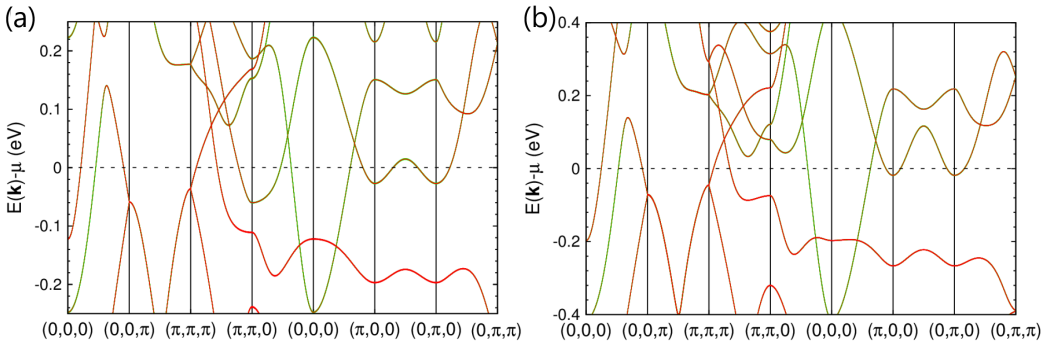

FIGURE 4.8: Zooms of the non-interacting band structure around the Fermi level for **(c)** $0\,GPa$ and **(d)** $12.4\,GPa$. New orbitals w_m (see main text) majority contribution included, where w_{zx} (green) and w_{yz} (red) contribute to the band structure around the Fermi level.

4.2.2 Local electronic correlations in $BaFe_2S_3$

Now, I apply the SSMF $U(1)$ formalism to calculate the local correlations for $n_e = 6$ in the new orbital basis w_m. In the local correlations approach, each Fe site of the unit cell is equivalent to other sites, hence the interacting hamiltonian H^{PS}_{dens} of Eq. (1.23) only affects 5 w_m orbitals, and only 5 different quasiparticle weights Z_{w_m} have to be calculated. Note that I considered H^{PS}_{dens} written in the new orbital basis, and not in the old one. If H^{PS}_{dens} would have been written in the old orbital basis, and then change to the new one, some non-density-density terms would have appeared (similar to the pair-hopping and spin-flip H_{add} terms). Nevertheless, these terms would have been neglected in the SSMF $U(1)$ formulation, because, as mentioned in previous chapters, it is not known how to treat non-density-density terms.

In [98], the authors calculated U and J_H interaction parameters by means of cRPA in $BaFe_2S_3$, locating it (at $0\,GPa$) close to $LiFeAs$, i.e. between $BaFe_2As_2$ and $FeSe$. For these compounds, SSMF gives good results when comparing with angle-resolved photoemission spectroscopy (ARPES) experiments [9] for $J_H/U = 0.25$, $U_{BaFe_2As_2} = 2.7\,eV$ [34] and $U_{FeSe} = 3\,eV$ [174]. I will fix $J_H/U = 0.25$ and vary U. In **Section 4.2.3** when calculating the renormalized band structure, we will assume that $U^{0\,GPa}_{BaFe_2S_3} = 2.9\,eV$. Also in [98], the authors mentioned that the interaction parameters are reduced by a $6-7\%$ when applying pressure. Thus, we will also consider $U^{12.4\,GPa}_{BaFe_2S_3} = 2.75\,eV$.

FIGURE 4.9 shows the results for Z_{w_m} and n_{w_m} for both pressures, when U varies at $n_e = 6$ and $J_H/U = 0.25$. Dotted line marks the U^P estimated in the previous paragraph for $0\,GPa$ and $12.4\,GPa$. The crossover from the weakly correlated to the Hund metal is located around $U^*_{0\,GPa} \sim 2.1\,eV$ and $U^*_{12.4\,GPa} \sim 2.6-2.7\,eV$, so the system at $0\,GPa$ is located in the Hund metal regime and the system at $12.4\,GPa$ in the crossover. As anticipated, at $12.4\,GPa$, there is a decrease of the strength of local correlations when comparing with $0\,GPa$, so the Hund metal regime moves to larger U values. For both cases, w_{zx} and w_{yz} are the most correlated orbitals, followed by w_{xy} and $w_{x^2-y^2}$, and finally the less correlated orbital is $w_{3z^2-r^2}$. This behavior can be traced down to the lowest W_{w_m} and the closeness to half-filling of each orbital filling n_{w_m} (note that $n_{w_m} = 1$ is defined as half-filling), as already pointed out in previous chapters.

From our calculations at $T = 0\,K$, no Mott insulating (or even orbital-selective Mott insulating) behavior is found, so the system is still metallic at both pressures. At $0\,GPa$, the

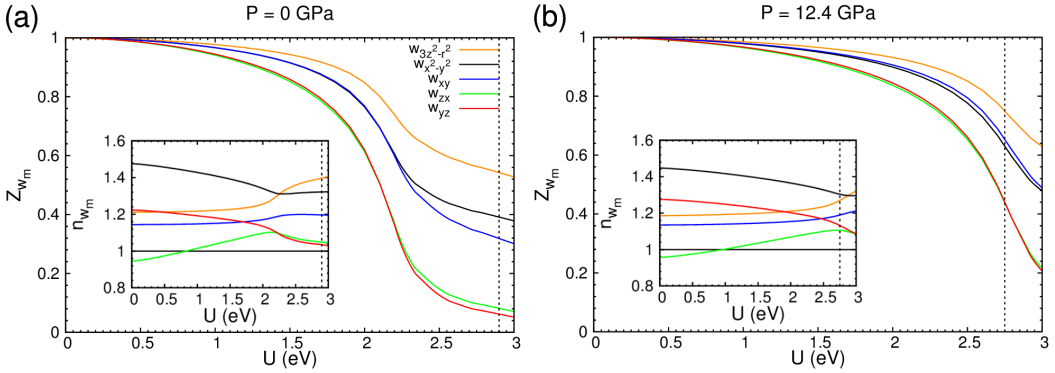

FIGURE 4.9: Z_{w_m} in terms of U at **(a)** $0\,GPa$ and **(b)** $12.4\,GPa$, using SSMF $U(1)$ formalism at $n_e = 6$ and $J_H/U = 0.25$. INSET: same evolution for the orbital fillings n_{w_m} in terms of U, where half-filling ($n_{w_m} = 1$) is marked as a straight black line. Dotted lines mark the estimated interaction U^P for $BaFe_2S_3$ at both pressures, $U^{0\,GPa} = 2.9\,eV$ and $U^{12.4\,GPa} = 2.75\,eV$. For both pressures, the strength of correlations of different orbitals is related with the lowest W_{w_m} and the closeness to half-filling. $12.4\,GPa$ shows a less correlated behavior (as anticipated), and while the $0\,GPa$ compound is in the Hund metal regime, $12.4\,GPa$ is located in the crossover region. The crossover region is found at $U^*_{0\,GPa} \sim 2.1\,eV$ and $U^*_{12.4\,GPa} \sim 2.6-2.7\,eV$. For the estimated U^P, the system is still metallic at both pressures. The color code for each orbital is included in the legend.

strength of correlations is considerably larger for w_{zx} and w_{yz} (with $Z_{w_m} < 0.1$), while it is more similar to quasi-2D FeSCs for other orbitals (with $Z_{w_m} \sim 0.3 - 0.6$). The strongest correlated orbitals (w_{zx} and w_{yz}) are those contributing to the band structure around the Fermi level. This would have important implications when studying the magnetic and superconducting instabilities (see below). Interestingly, at $12.4\,GPa$, the strength of correlations becomes similar to those found in quasi-2D FeSCs for all the orbitals, in accordance with the ideas of needing an optimal degree of electronic correlations to host unconventional superconductivity (see **Chapter 3**).

Note that the SSMF $U(1)$ calculations are performed for $T = 0\,K$. As shown in **Section 1.3.3** for the local correlations behavior with temperature, when T increases, incoherence also increases, hence reducing Z , and promoting an insulating behavior. Due to the extremely low values of the quasiparticle weights for w_{zx} and w_{yz} ($Z_{w_m} \sim 0.03 - 0.06$), we expect that T could lead to the disappearance of the quasiparticle peak and the opening of a gap at the Fermi level. Thus, we expect that calculations for finite T at $0\,GPa$ would be able to drive the system to an insulating state.

4.2.3 Band renormalization and Fermi surface reconstruction by local correlations

In other quasi-2D FeSCs, local correlations do not almost change the Fermi surface because different pockets renormalize in a similar way. Thus, a weakly correlated picture of magnetism in quasi-2D FeSCs will be mostly unaffected by including local correlations for the Fermi surface. In some cases (like in 111 FeSCs), local correlations will mainly alter the pockets with xy character (yz and zx ones are renormalized without nematicity), see for example [114], hence the expectations from a weakly correlated picture of magnetism and superconductivity will vary.

In FIGURE 4.10, I show the renormalized band structure for both pressures, as well as the zoom around the Fermi level. The interactions reduce the total bandwidth around $\sim 50\%$ for $0\,GPa$ and $\sim 30\%$ for $12.4\,GPa$, to $W^{0\,GPa} \sim 2\,eV$ and $W^{12.4\,GPa} \sim 3.5\,eV$.

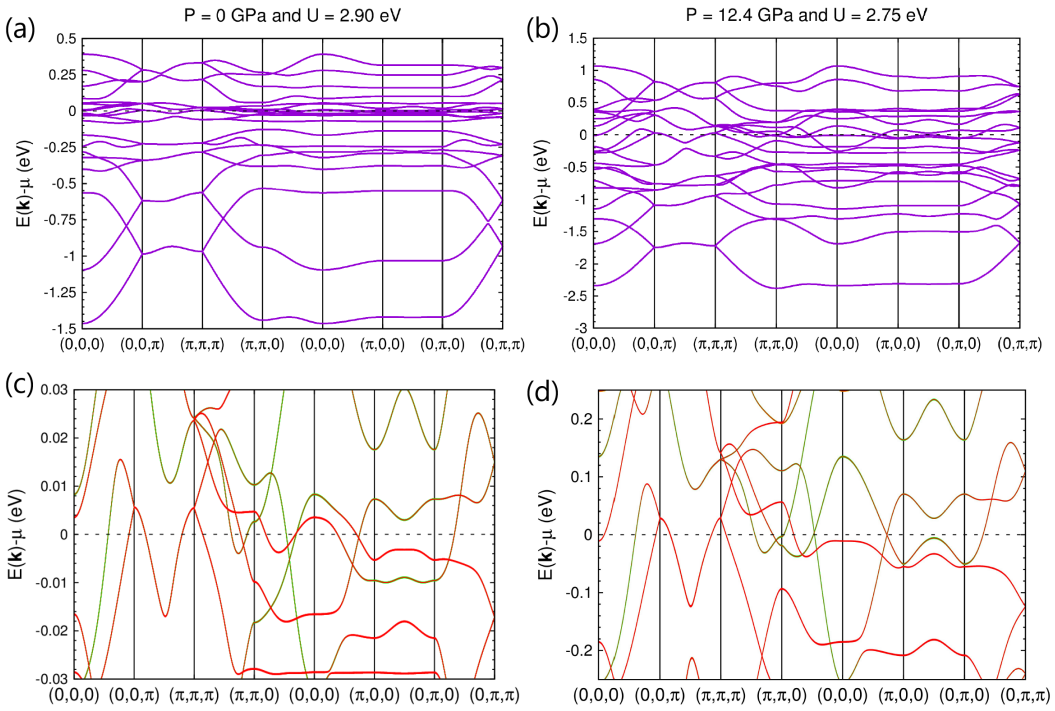

FIGURE 4.10: Band structures for **(a)** $0\,GPa$ at $U = 2.9\,eV$ and **(b)** $12.4\,GPa$ at $U = 2.75\,eV$, with $J_H/U = 0.25$. Bandwidths are reduced with respect to their non-interacting value (see FIGURE 4.5) due to the local correlations effect, $W^{0\,GPa} \sim 2\,eV$ and $W^{12.4\,GPa} \sim 3.5\,eV$. The color code is the same as in previous figures. Around the Fermi level, the bands suffer a considerable change, which can be traced back to a upwards shift for w_{yz}-like bands and a downwards shift for w_{zx}-like bands. This large reconstruction appears due to the fact that w_{zx} and w_{yz} are the most correlated orbitals.

Interestingly, the most strongly correlated orbitals w_{zx} and w_{yz} (with $Z_{w_m} \sim 0.03 - 0.06$) are those who mainly contribute to the band structure around the Fermi level, in a range of a few dozens and hundreds of meV. Local correlations alter the bands, where the most striking feature is the upwards/downwards shift of the w_{yz}/w_{zx}-like bands. Thus, there is a sizable Fermi surface reconstruction in $BaFe_2S_3$ due to local correlations. This can be more clearly seen in FIGURE 4.11, where I present the Fermi surfaces (as well as the same cuts as in FIGURE 4.6) for $0\,GPa$, $U = 2.9\,eV$ and $12.4\,GPa$, $U = 2.75\,eV$.

When including the effect of local correlations, the γ hole pockets change their shape and cut the border $k_z = \pm\pi$, and the β electron pocket grows and new smaller hole pockets appear close to $(\pm\pi, \pm\pi, 0)$. At $0\,GPa$, the α electron pocket dissapears and evolves in triangular-shaped electron pockets around $(\pm\pi/2, \pm\pi/2, 0)$. At $12.4\,GPa$, the α electron pocket evolves into a H-shaped electron pocket. Some of these pockets (for example, those around $(\pi, \pi, 0)$) are extremely shallow, specially for $0\,GPa$, where a small change on the Fermi level will make these pockets dissappear, see FIGURE 4.10**(c)** and **(d)**.

An important consequence of the Fermi surface reconstruction is how the nesting changes. When interactions are turned on, there is an enhancement of the scattering with the intra-ladder AFM nesting vector $\vec{Q} = (0, 0, 2\pi)$ (marked in FIGURE 4.11**(a.2)** and **(a.3)**) between the γ hole pockets with respect to the non-interacting case, see FIGURE 4.6. This is due to

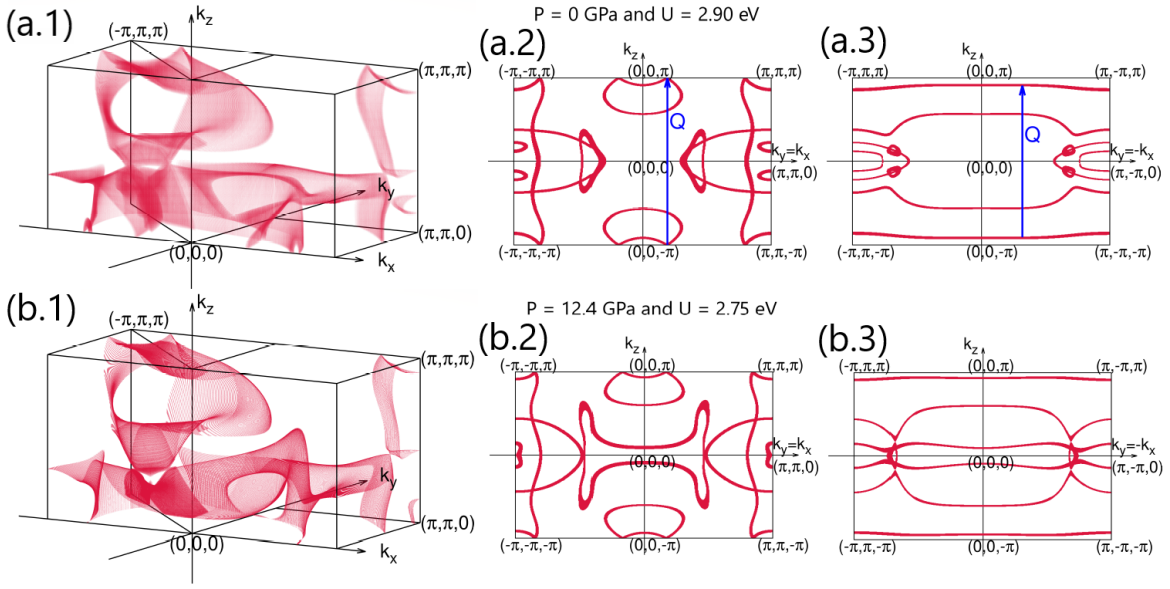

FIGURE 4.11: **(a.1)** $0\,GPa$ and **(b.1)** $12.4\,GPa$ 3D Fermi surfaces in the reduced BZ. The Fermi surfaces evolve, with some pockets dissapearing and new ones appearing (see main text). **(a.2)** $0\,GPa$ and **(b.2)** $12.4\,GPa$ Fermi surface cuts along k_z-k_x-k_y plane, and **(a.3)** $0\,GPa$ and **(b.3)** $12.4\,GPa$ Fermi surface cuts along k_z-k_x+k_y plane. Figures taken at $n_e = 6$ and $U = 2.9\,eV$ for $0\,GPa$ and at $U = 2.75\,eV$ for $12.4\,GPa$. The Fermi surfaces suffer a sizable reconstruction, which will affect the predictions for Fermi surface instability based theories. Intra-ladder AFM nesting vector $\vec{Q}$ included, where the scattering gets enhanced by the cut of the γ pockets with the k_z axis, which is not present in the $U = 0\,eV$ case.

the fact that in the interacting case, γ hole pockets cut the $k_z = \pm\pi$ border, while in the non-interacting case, they do not.

Thus, in a Fermi surface-based magnetic instability, this intra-ladder AFM susceptibility will be enhanced. Nevertheless, at $0\,GPa$, the strength of correlations for the orbitals controlling the Fermi surface (w_{zx} and w_{yz}) is very strong, and a weakly correlated picture of AFM does not seem a good starting point. In the case of $12.4\,GPa$, where correlations are of the order of quasi-2D FeSCs, a weakly correlated picture to study the superconducting instability could maybe be applied. An interesting issue which requires further work is whether this weakly correlated picture for superconductivity is invalidated by the non-weakly correlated picture of magnetism or not. If so, the Fermi surface reconstruction will affect the superconducting instability calculation.

4.3 Summary

I conclude this chapter by making a summary of the obtained results:

- In 2015 and 2017, high-T_c superconductivity was found in a new family of FeSCs, the 123 iron chalcogenides [155–157]. Superconductivity in these systems appears when applying pressure. The undoped at ambient pressure compound is an insulator with an AFM order. The insulating behavior persists for $T > T_N$. There is an insulator-to-metal transition around the pressure at which superconductivity emerges and AFM is suppressed. 123 FeSCs form quasi-1D structures of two-leg ladders of Fe atoms, which

are tetrahedrally coordinated with the chalcogen atoms. Part of the community claim that these systems are Mott insulators [155, 156].

- In **Section 4.2.1**, I have reproduced the tight-binding model developed in [98] for $BaFe_2S_3$ at two pressures, $0\,GPa$ and $12.4\,GPa$. The tight-binding model is given for 4 Fe atoms in the unit cell, and considering the 5 d orbitals of each Fe atom, which are controlling the band structure around the Fermi level. As expected, pressure increases W, so it will promote metallic behavior in the presence of electronic correlations. Even if the system shows a quasi-1D crystal structure, the bands and the Fermi surfaces have a non-negligible 3D character. I rewrote the tight-binding hamiltonian in the diagonal onsite energy basis, where the new orbitals are labeled by w_m. In this new orbital basis, w_{zx} and w_{yz} are concentrated around the Fermi level, giving the largest contribution for the Fermi surfaces.

- In **Section 4.2.2**, I calculated Z_{w_m} and n_{w_m} for both pressures and varying U, using SSMF $U(1)$ formalism at $n_e = 6$. We use $J_H/U = 0.25$, and $U^{0\,GPa} = 2.9\,eV$ and $U^{12.4\,GPa} = 2.75\,eV$. When pressure is applied, the strength of correlations decreases for all the orbitals, as anticipated. For both pressures, the system is still metallic. At $0\,GPa$, compound is located in the Hund metal regime, whether at $12.4\,GPa$, it is in the crossover region, defined by $U^*_{0\,GPa} \sim 2.1\,eV$ and $U^*_{12.4\,GPa} \sim 2.6 - 2.7\,eV$. At $0\,GPa$, w_{zx} and w_{yz} are very strongly correlated, with $Z_{w_m} \sim 0.03 - 0.06$, while the other 3 orbitals are moderately and strongly correlated, with $Z_{w_m} \sim 0.3 - 0.6$. At $12.4\,GPa$, all the orbitals w_m are moderately and strongly correlated, with $Z_{w_m} \sim 0.2 - 0.6$, similar to other quasi-2D FeSCs.

- The system is metallic at both pressures. However, SSMF $U(1)$ calculations are made at $T = 0\,K$. Including T effects in the local correlations picture increases the incoherence, hence promoting an insulating behavior. Thus, at $0\,GPa$), we conclude by stating that the insulating phase in 123 FeSCs could be driven by T due to the low values of Z_{w_m} for the orbitals which control the band structure around the Fermi level.

- In **Section 4.2.3**, I calculated the effect of local correlations in the band structure and the Fermi surfaces at $0\,GPa$ and $12.4\,GPa$. The total bandwidths are reduced $\sim$ %50 for $0\,GPa$ and $\sim$ %30 for $12.4\,GPa$. Fermi surfaces suffer a sizable reconstruction, which can be traced back to the shift downwards/upwards of the w_{zx}/w_{yz}-like bands. γ hole pockets change their shape and cut $k_z = \pm\pi$. When including local correlations, there is an enhancement of the intra-ladder AFM nesting vector $\vec{Q} = (0, 0, 2\pi)$ with respect to the non-interacting case. This enhancement is due to the cut of γ pockets with $k_z = \pm\pi$. Nevertheless, at $0\,GPa$, the Fermi surface will be absent (due to the insulating nature), and any explanation of the AFM in terms of a weakly correlated picture is highly in doubt. At $12.4\,GPa$, the strength of correlations becomes similar to other FeSCs. An interesting issue which requires further work is whether the weakly correlated picture for superconductivity is invalidated by the non-weakly correlated picture of magnetism or not. The Fermi surface reconstruction will be important and will affect the possible instabilities, opposite to what usually happens in most quasi-2D FeSCs.

Chapter 5

The nature of correlations in the insulating states of twisted bilayer graphene[1]

During the APS Meeting 2018, Pablo Jarillo-Herrero presented the recent results of his group in the magic-angle twisted bilayer graphene (MA-TBG) [175]. The results were published in two articles in Nature [84, 85]. The authors have mainly discovered that: (1) electron- and hole-doped MA-TBG show an unexpected insulating behavior for a certain commensurate fillings [85] and (2) around the insulating state of the hole-doped MA-TBG, a couple of superconducting domes emerge with $T_c \sim 1-2\,K$ [84]. These results open a new area for studying unconventional superconductivity, where the possibilities of creating magic-angle twisted systems and unveling the origin of unconventional superconductivity in a non-invasive and sistematic way are enormous.

In **Section 1.6.1**, I have already introduced the phenomenology previously known for MA-TBG [86–92]. In twisted bilayer graphene (TBG), a moiré pattern emerges, as shown in FIGURE 1.22. In the moiré pattern, or alternatively called the superlattice, AA and AB/BA regions form triangular and hexagonal patterns, respectively. For $\theta < 2^\circ$ and due to the interlayer hybridization $w(\theta)$, at a certain (magic) angles the bands around the Fermi level become very flat, with theoretically obtained bandwidths $W \sim 10\,meV$ (see FIGURE 1.24 for the low-energy continuum model results), with Dirac points at K and K' [89]. Between the flat bands and the next bands, there are two superlattice gaps $\sim 40\,meV$, obtained by transport measurements [84, 85, 90, 176]. Around these K points, the electronic density is mostly located in AA regions [91].

In MA-TBG, there are a total of four spin-degenerated flat bands, in which there is a valley degeneracy, see **Section 1.6.1** [87, 89, 177–179]. In 2D systems, doping can be induced in a non-invasive way via an external gate voltage [84, 85, 90, 176]. The unexpected insulating states in MA-TBG appear at a doping of 2 electrons and 2 holes with respect to the charge neutrality point (CNP), which is defined as zero filling. Alternatively to this notation, here I will define half-filling of the flat bands at the CNP. At the CNP, the system shows the typical Dirac points of the graphene hexagonal lattice, with no gap opening and a semimetallic behavior seen in transport experiments. Due to the fact that in MA-TBG the bandwidth is strongly reduced for the flat bands (hence, U/W ratio will largely increase), as well as that these unexpected insulating states appear at commensurate fillings, the authors [84, 85] argued that the insulating states in MA-TBG are, indeed, Mott insulating states.

During the next months, there has been a lot of activity in the scientific community to model and discuss the phenomenology of MA-TBG. Here, I present the results that we have published [99] about

[1] Results presented in this Chapter published in [99]

our analysis of the nature of the insulating states in electron- and hole-doped MA-TBG. Our goal is to check whether the insulating states in MA-TBG are compatible with Mott physics. We will assume that the electronic interaction in MA-TBG is short-ranged due to the screening effect of the external gate voltage, hence we will be able to use an effective Hubbard model for the flat bands. We will focus on the analysis of three experimental results which will not be explained when only local correlations, i.e. correlations between electrons in the same lattice site (see **Chapter 1**) are considered: (i) the insulating behavior disappears when temperature increases, (ii) the insulating behavior also dissapears when the magnetic field increases and (iii) the gap size ($\sim 0.3\,meV$) is two orders of magnitude smaller than the expected gap $U - W \sim 15 - 25\,meV$. We will conclude by proposing that the Mott physics can explain the insulating states of MA-TBG where non-local correlations (correlations between electrons in different lattice sites) are playing a major role in MA-TBG, rather than be an effect of the local correlations.

In this chapter, I first discuss the tight-binding model used for MA-TBG. I will introduce the triangular and hexagonal symmetries discussed when modeling MA-TBG [93, 177–180]. We chose the hexagonal moiré superlattice as the best initial approximation for MA-TBG. We consider 2 equivalent orbitals, and only nearest neighbor intraorbital hoppings $t \approx 2\,meV$ (in a hexagonal lattice, the total bandwidth is $W = 6t \approx 12\,meV$). In this model, the A and B sites of the hexagonal lattice represent the AB and BA regions of MA-TBG. I write all the energy scales in units of the hopping t

I will calculate the critical interaction for the Mott transition by using the SSMF $U(1)$ formalism for $N = 2$ equivalent orbitals in a honeycomb lattice. Similar results were already studied for other models in [46, 113, 177, 181, 182]. For multiorbital systems, Mott insulating states appear at certain commensurate fillings, which in the case of $N = 2$ is for a number of electrons per site $n_e = 1$ (quarter filling), $n_e = N = 2$ (half-filling) and $n_e = 3$ (three-quarter filling). In order to reproduce the experimental findings, i.e. at half-filling (the CNP of MA-TBG where the Dirac points are located) the system shows a metallic behavior, and at quarter and three-quarter filling of the flat bands the system is an insulator, I will show that J_H should be small, so I will take $J_H = 0$ as an initial guess for its value in MA-TBG.

Then, I will calculate the effect of a Zeeman field in the Mott transition in the SSMF $U(1)$ formalism by including a spin-dependent onsite energy shift, to study the insulating states of MA-TBG response with the magnetic field. Breaking spin-degeneracy is a novel implementation in SSMF techniques. I will show that the opposite tendency with respect to the experiments is found: when the Zeeman magnetic field increases, the system becomes more insulating (and not metallic). I will argue that the metallic state promoted by temperature T is also at odds with the theoretical results in local correlations, as shown in **Section 1.3.3** for single and multiorbital systems in which insulating behavior is promoted when T increases [8, 17, 20]. For $N = 2$ orbitals, this phenomenology holds [113]. Also, the small size of the gap could not be explained when considering only local correlations [17, 183, 184], in which the gap ($\sim U - W$) is expected to be two orders of magnitude smaller than the one obtained in transport measurements ($\sim 0.3\,meV$), see **Section 1.3.1**.

Thus, assuming that the Mott physics is at the heart of the insulating states in MA-TBG, we will show that by only considering local correlations the experimental results cannot be explained, and hence it is necessary to go beyond local correlations, and consider non-local correlations effects. Based on previous results in other lattices [19, 21, 185–199], we argued that the experimental results could be explained by including these non-local phenomenology. Nevertheless, further calculations are needed to study the insulating states in MA-TBG. For non-local correlations, the tight-binding model details are important, and hence these calculations would required a good enough tight-binding model for MA-TBG, something which is yet not available

5.1 Introduction & Motivation

On March 2018, Pablo Jarillo's group reported [85] that MA-TBG shows unexpected insulating states at a certain commensurate electron and hole dopings for the moiré superlattice (and not for the lattice of C atoms, see below). Pablo Jarillo's group also discovered [84] that, around the insulating state for hole-doped MA-TBG, two superconducting domes with $T_c \sim 1-2\,K$ emerge, in a similar fashion as in high-T_c cuprates superconductors, see **Section 1.5**. Since then, a lot of scientific effort has been put by the community to understand the physics playing a role in MA-TBG. The emergence of insulating states at commensurate fillings suggests the possibility to describe the system using an effective tight-binding model for the moiré superlattice. However, this tight-binding model for the moiré superlattice is still difficult to establish [93, 177–179]. In this section, I am going to explain various important results from Pablo Jarillo's group [84, 85], as well as giving a brief summary of the works done after these discoveries about the tight-binding model for the moiré superlattice [93, 177–180]. At the end of this chapter, I summarize the results presented in this work, as well as making a brief comment of the recent work and discussion about the tight-binding model in MA-TBG [200].

In **Section 1.6.1**, I have explained the basic phenomenology known about TBG [86–92] before Pablo Jarillo's group discoveries. In TBG, a moiré pattern appears for a twisting angle θ, see FIGURE 1.22. The size of this moiré pattern λ varies with θ and takes values of the order of $10-20\,nm$ for $\theta \sim 1-1.5\,^\circ$. In the moiré pattern, or alternatively the superlattice, AA regions form a triangular superlattice, while AB and BA form a hexagonal superlattice. This notation is used to refer to the alignement between bottom and top sublattice of the graphene layers. For $\theta < 2\,^\circ$ and due to the interlayer hybridization $w(\theta) \propto \sin\theta$, at a certain (magic) angles the bands around the Fermi level become very flat (see FIGURE 1.24), with Dirac points at K and K'. The set of angles at which the bands around the CNP become very flat appears due to a vanishing Fermi velocity $v_F = 0$, hence v_F is a cyclic function of θ, as shown in FIGURE 1.23**(d)**. The flat bands disperse between the maxima and minima located at Γ, and between them and the next bands, there are a couple of superlattice gaps which appear due to the hybridization of the two graphene layers [89, 90, 93], and also due to corrugation effects in the interface of the two graphene layers [93] (see **Section 1.6.1** and discussion about $w \neq w'$). Around the K points, the electronic density is located in the AA regions [91].

In [85], Pablo Jarillo's group have discovered that two gaps ($\approx 0.3\,meV$) open at a certain commensurate fillings per moiré unit cell, 2 electrons and 2 holes with respect to the CNP. Here, I will use an alternative notation for the moiré superlattice (see below), they appear at $n_e^{moire} = 2$ and 6 electrons with respect to the bottom of the flat bands, see FIGURE 5.1 for the conductance curves at $\theta_1^{magic} = 1.08\,^\circ$ (these two insulating states are marked by a darker red and blue regions, with the label $\pm n_s/2$). The superlattice gaps ($\approx 40\,meV$), i.e. the gaps associated to the total emptying ($n_e^{moire} = 0$) and total filling ($n_e^{moire} = 8$) of the flat bands, can be also seen in FIGURE 5.1 (marked by light red and blue regions and labeled as $\pm n_s$).

According to a hexagonal symmetry, I will alternatively use the number of electrons per moiré site ($n_e = n_e^{moire}/2$), where $n_e = 2$ is half-filling (and the total filling per site, spin and orbital is $x = n_e/2N = 1/2$), $n_e = 1$ is quarter filling ($x = 1/4$) and $n_e = 3$ is three-quarter filling ($x = 3/4$). Due to the small value $W \sim 10\,meV$ (U/W ratio largely increases), the authors [84, 85] argued that these unexpected insulating states in MA-TBG are in fact Mott insulating states. Interestingly, at half-filling (CNP of MA-TBG where the Dirac points are

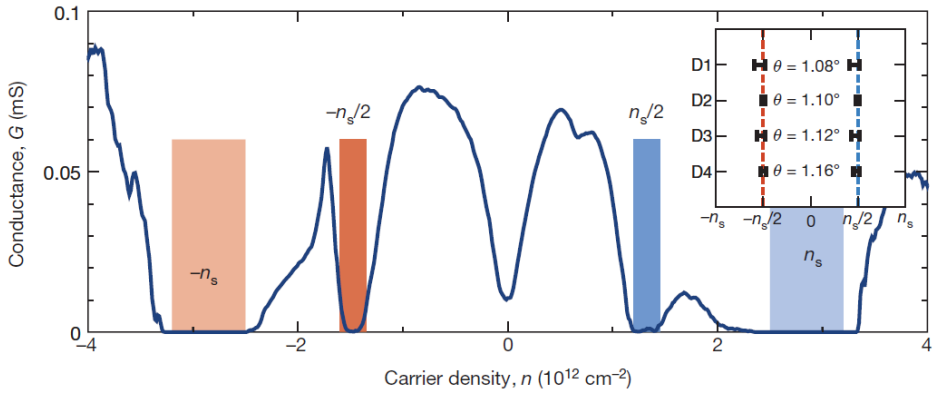

FIGURE 5.1: Conductance versus external gate voltage induced doping for MA-TBG with $\theta = 1.08\,^\circ$ measured at $T = 0.3\,K$. Flat bands develop between $\pm n_s \approx 2.7 \times 10^{12}\,cm^{-2}$, which are identified as the superlattice gaps $\approx 40\,meV$. At half-filling ($n_s = 0$) a V-shaped conductance is found, typical for Dirac points. Insulating states are found at $\pm n_s/2$. During this chapter, I will use the alternative notation in which superlattice gaps develop at $x = 0$ (light red area) and $x = 1$ (light blue area), half-filling is $x = 1/2$ (V-shaped conductance), and insulating states appear at commensurate fillings $x = 1/4$ (dark red area) and $x = 3/4$ (dark blue area). INSET: Locations of the unexpected insulating states for several rotation angles θ. Taken from [85].

located) there is no insulating behavior, and a V-shaped conductance typical for semimetals is seen [85].

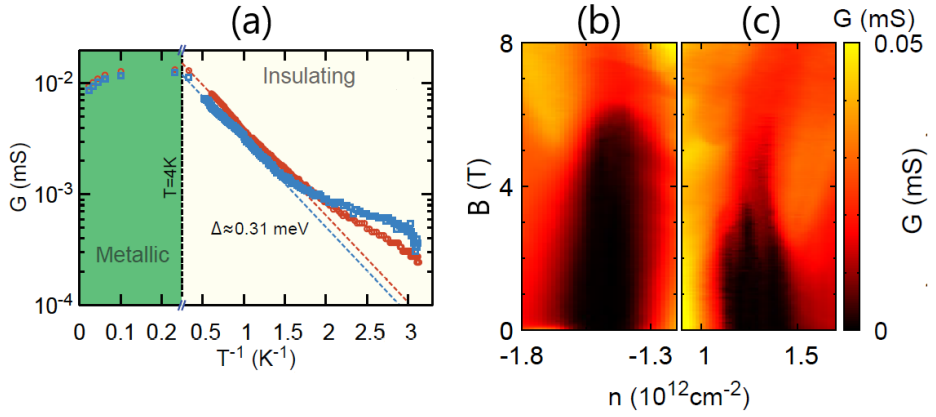

FIGURE 5.2: Insulator-to-metal transition for the unexpected insulating states (see dark red and dark blue regions in FIGURE 5.1) at quarter (red line) and three-quarter (blue line) fillings when **(a)** increasing T and increasing Zeeman magnetic field B for **(b)** quarter and **(c)** three-quarter filling in MA-TBG. Both transitions appear when the thermal ($k_B T$) and magnetic ($\mu_B B$) excitation energies are of the same order of the *gap* $\sim 0.3\,meV$. Taken and adapted from [85].

The insulating states at quarter and three-quarter filling behave similarly with respect to T and with respect to an external magnetic field B, see below [85]. The magnetic field behavior is the same for both perpendicular and parallel (with respect to the superlattice) directions, hence in [85], the authors concluded that it comes from a Zeeman magnetic field effect. In both cases, there is an insulator-to-metal transition at $T \approx 4\,K$ ($\sim 0.3\,meV$) and $B \approx 5 - 6\,T$ ($\sim 0.3\,meV$). These excitation energies are of the same order of the gap size $\sim 0.3\,meV$, which is determined by thermal-activated fitting to transport measurements. In FIGURE 5.2, both experimental results are shown. I will argue in **Section 5.2** that the T

and B behaviors signal a major role played by non-local correlations, rather than being a local correlations effect, as usually expected for a Mott insulator.

Pablo Jarillo's group [84] also found that, around the quarter filling insulating state, a couple of superconducting domes emerge, see FIGURE 5.3 for two different twisting angles θ around θ_1^{magic}. Around the same carrier density at which superconductivity emerges, there is an insulator-to-metal transition. This behavior resembles the one obtained in cuprates and other unconventional superconductors, see **Section 1.5**. MA-TBG superconducting domes show a record low carrier densities (previously held by interfaces $LaAlO_3/SrTiO_3$ with $1.5 \times 10^{13}\, cm^{-2}$ [201]), with $T_c^{max} \approx 1.7\, K$ at $\approx -1.5 \times 10^{12} cm^{-2}$.

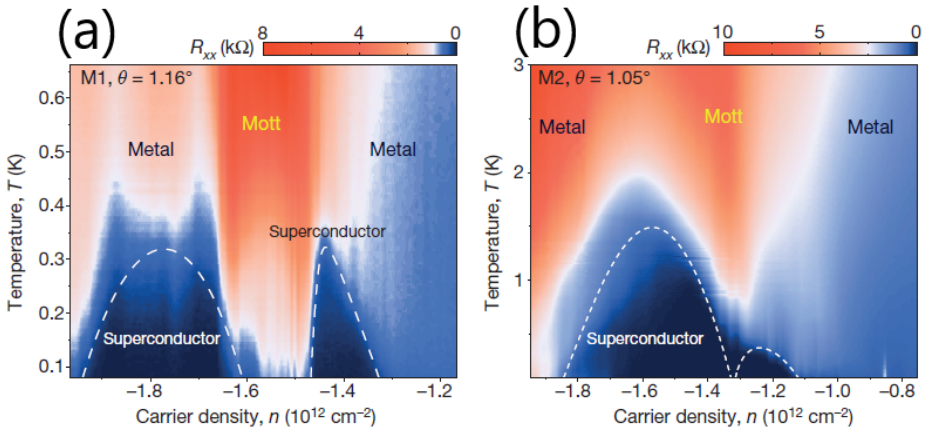

FIGURE 5.3: Color map of the resistance for the temperature phase diagram and hole-doped MA-TBG in terms of external gate voltage induced doping at **(a)** $\theta = 1.16\,^\circ$ and **(b)** $1.05\,^\circ$. The insulating phase is colored in red, superconductivity is colored in dark blue. The metallic states are marked in light blue and light red. Superconductivity appears around the insulating state, similar to cuprates and other unconventional superconductors. It appears at a record carrier density, with $T_c^{max} \approx 1.7\, K$ at $\approx -1.5 \times 10^{12} cm^{-2}$. Taken from [84].

Superconductivity is supressed by a perpendicular magnetic field $B_\perp \approx 70\, mT$ ($\approx 4\, \mu eV$) [84]. FIGURE 5.4 shows the schematic evolution of the phase diagram in terms of the perpendicular magnetic field. As mentioned, there is a first suppression of the superconducting domes at $70\, mT$, and then an insulator-to-metal transition at $6\, T$.

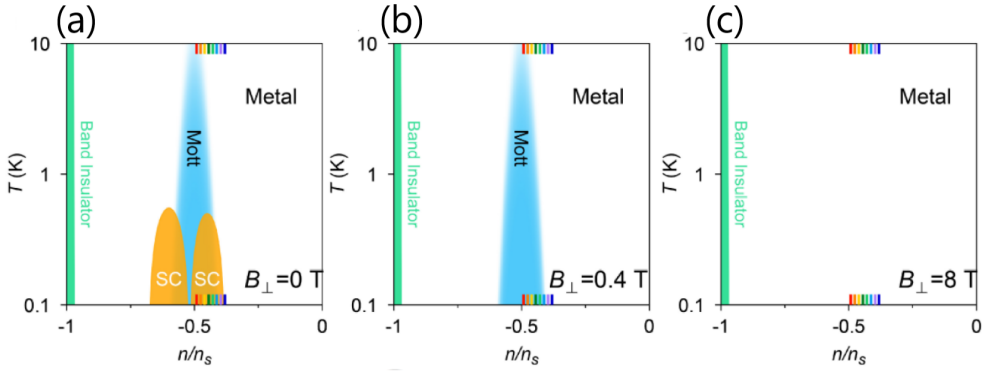

FIGURE 5.4: **(a)-(c)** Sketch of the phase diagram for hole-doped MA-TBG in terms of perpendicular magnetic field. At $B_\perp = 0$, the insulating state appears at $x = 1/4$, and also a couple of unconventional superconducting domes around it. At $B_\perp = 0.4\, T$ ($\approx 20\, \mu eV$), superconductivity is suppressed, and at $B_\perp = 8\, T$ ($\approx 0.4\, meV$), the insulating state dissappears. Taken from [84].

5.1.1 Works published after *Y. Cao et al.* discoveries

During the months after the discovery of Pablo Jarillo's group presentation and publications [84, 85, 175], a lot of works have been published in arXiv about studying MA-TBG. Here, I will briefly review the ones related with the initial tight-binding model for MA-TBG, focusing in the works [93, 177–179]. These works were uploaded to arXiv prior or simultaneously to our work.

In **Section 1.6.1**, I have discussed the low-energy continuum model [87, 89, 93], in which the flat bands around the Fermi level compare well with calculations from tight-binding models in the lattice of C atoms. Each layer will contribute with its own dispersions h^l, where $l = 1, 2$ is the layer index, and for $\theta < 6\,^\circ$, it can be shown that there is an interlayer hybridization $w(\theta)$ contribution. In the mini-BZ of MA-TBG, there are four bands, with two Dirac points located at K and K' for each valley $\xi = \pm$ [89], see **Section 1.6.1**. The low-energy continuum hamiltonian is block diagonal, where each non-zero diagonal block is a 4×4 (including the layer and spin degree of freedom) matrix H_ξ, see Eq. (1.24). Then, the flat bands consist on two bands per spin and valley (eight bands if we take into account explicitly the spin and valley degrees of freedom).

Due to corrugation effects [93], superlattice gaps open between the flat bands and the higher-in-energy bands, see FIGURE 1.24**(b)**. In order to be able to study the effects of electronic correlations, a correct and minimal tight-binding model is needed for the moiré superlattice of MA-TBG. Due to the opening of superlattice gaps, it is reasonable to try to obtain the tight-binding model describing only the flat bands. The number of orbitals N which has to be taken to describe the flat bands coincides with the number of bands per spin and per valley (note the valley and spin degeneracy), hence flat bands are described by $N = 2$ orbitals per spin and valley [93, 177–179].

Two different tight-binding models were proposed for the moiré superlattice: the first one consider s- and off-plane p-like orbitals centered at each AA site of the triangular superlattice [202–204], while the second one consider two in-plane p-like orbitals centered at AB and BA sites of the hexagonal superlattice [93, 177–179]. Due to the fact that the electronic density is mainly located in AA regions around K points [91], it seems reasonable to start from a triangular superlattice model. However, according to the symmetry analysis done in [93, 177–179], the two orbitals should be centered at the AB and BA regions, forming a hexagonal superlattice. The basic idea of these arguments is that the flat bands have to fulfill certain symmetries at the principal points of the mini-BZ, Γ, K and M. It turns out that the triangular superlattice model does not correctly capture the symmetries of the flat bands, like for example, it cannot reproduce the Dirac points at K and K'. Then, it was proposed that the initial tight-binding model for the flat bands have to be written in a hexagonal superlattice with $N = 2$ in-plane p-like orbitals.

When obtaining the Wannier parametrization in the hexagonal superlattice model, the maximum amplitude of the in-plane p-like orbitals is located in the AA regions, as shown in FIGURE 5.5**(a)**. This result agrees with the fact that the electronic density is located at AA regions around the K points. The resulting tight-binding model, as well as the density of the states (DOS) of the flat bands in the low-energy continuum model [93] are shown in FIGURE 5.5**(b)** and **(c)**. Up to five neighbor hoppings are included in this tight-binding model. Note that in this hexagonal superlattice model, first neighbor hopping refers to an interorbital hopping, second neighbor hopping to an intraorbital one, etc. The total bandwidth is $W \sim 8\,meV$. A very good agreement can be seen between the $N = 2$ p-like orbitals

tight-binding model (marked as a black dashed line) and the low-energy continuum model (green continuous line) for the flat bands. The total DOS shows the typical Dirac point at the CNP, and also two very large van-Hove singularities emerge because of the M saddle point. The quarter and three-quarter fillings are located at a larger energy than the location of this van-Hove peaks [93]. The low-energy continuum model shows particle-hole symmetry, while in the real material this symmetry is broken [205].

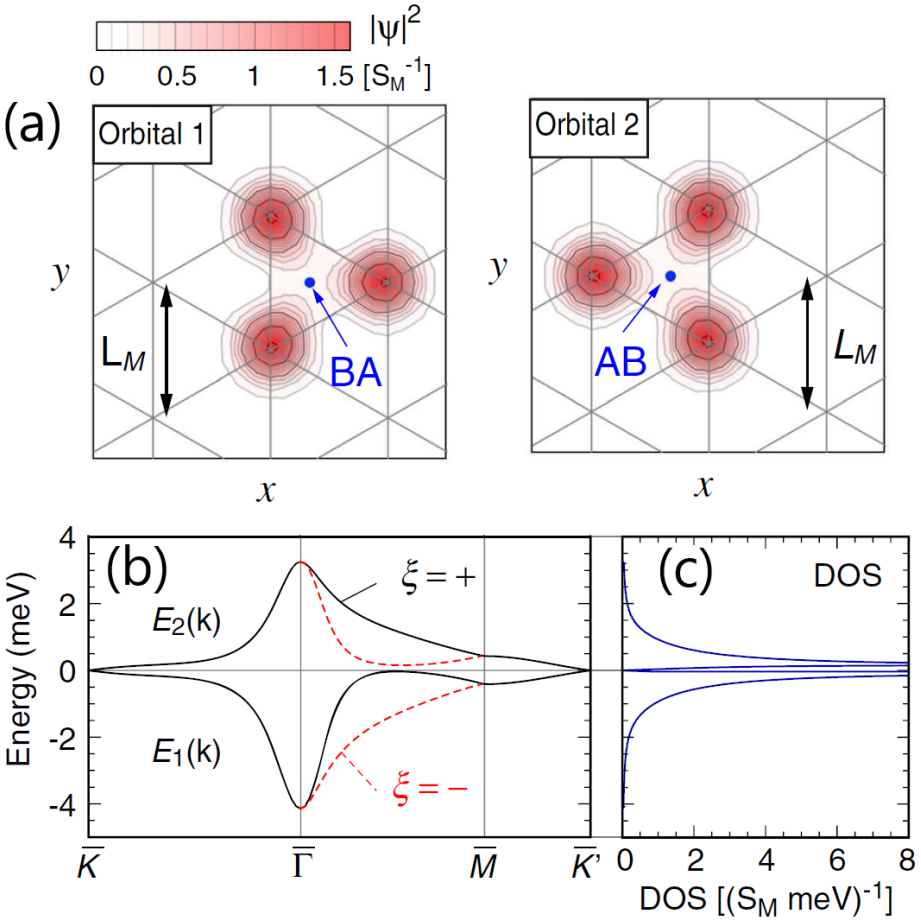

FIGURE 5.5: **(a)** Squared amplitudes $|\psi|^2$ for the two p orbitals (labeled as 1 and 2), centered in the hexagonal superlattice formed by AB/BA regions. The maximum amplitude is located at the AA regions. **(b)** Tight-binding model obtained from the fitting (black dashed line) using five neighbor hoppings for the two in-plane p-like orbitals hexagonal superlattice model, where there is a good enough agreement with the low-energy continuum model flat bands (green continuous line). **(c)** Total DOS for the low-energy continuum model of MA-TBG, which shows the typical Dirac point at the CNP, and also two very large van-Hove singularities emerge because of the M saddle point. The quarter and three-quarter fillings are located at a larger energy than the location of this van-Hove peaks. Taken and adapted from [93].

5.2 Results & Discussion

Now, I will present the results that we have obtained and published in [99]. In **Section 5.2.1**, I will first discuss the tight-binding model that we have used. We chose $N = 2$ equivalent orbitals per site in a hexagonal lattice with only intraorbital hoppings $t \sim 2\,meV$ ($W = 6t \sim$

$12\,meV$) model. We have assumed that long-range interactions are screened in MA-TBG due to the external gate voltage (which induces the doping in MA-TBG) in the experiments of Pablo Jarillo's group [84, 85]. This is because the metallic gate is placed at a distance similar to the moiré superlattice constant. Then, I will present the local correlations calculations in this $N = 2$ equivalent orbitals model [46, 113, 177, 181, 182], using the SSMF $U(1)$ formalism at half-filling $n_e = N = 2$ ($x = 1/2$) and quarter filling $n_e = 1$ ($x = 1/4$). I will study the critical interactions for the Mott transition U_c/t in terms of J_H/U. I will show that, in order to reproduce the experimental findings (at quarter filling, the system behaves as an insulator, while at half-filling, it shows metallic behavior), a small J_H value has to be considered. I will consider then $J_H = 0$ as a first approximation for the real J_H value in MA-TBG. In **Section 5.2.2**, I implement the Zeeman effect in the SSMF $U(1)$ formalism. I will also show that the evolution of the insulating states in a magnetic field H as observed experimentally (H promotes metallic behavior) cannot be explained if only local correlations are considered. I will also remind that, when only onsite correlations are taken into account, T promotes an insulating behavior [8, 17, 20, 113] and the gap should be of the order of $\sim U - W$ (where estimations give $U \sim 20 - 25\,meV$ and $W \sim 10\,meV$) [17, 183, 184], also at odds with the experimental results. Assuming that the Mott physics still plays a major role in the insulating states of MA-TBG, these theoretical results point to a non-local correlations origin of these insulating states. In **Section 5.2.3**, I will briefly review the results obtained for non-local correlations in various single- and two-orbital systems [19, 21, 185–199]. Then, we conclude by proposing that the nature of the insulating states in MA-TBG could be explained by Mott physics if non-local correlations are explictly taken into account.

5.2.1 Local correlations in 2-orbital tight-binding model for hexagonal symmetry MA-TBG

In order to study the effects of local correlations in MA-TBG, we have used a tight-binding model by considering $N = 2$ equivalent orbitals in a hexagonal lattice with only intraorbital hoppings $t \approx 2\,meV$ included, aimed to qualitatively reproduce the flat bands of MA-TBG. As mentioned in **Chapter 1**, the details of the tight-binding model will not affect the local correlations physics (like for example, the behavior of the critical interaction for the Mott transition U_c in terms of J_H), and only the energy scales at which the effects occurr will change slightly with the inclusion of further neighbor hoppings. In this hexagonal lattice model, A and B sites represent the AB and BA regions in MA-TBG, and the two orbitals are located in each A and B site in order to reproduce the valley degree of freedom of the four flat bands. The total bandwidth W is $6t \approx 12\,meV$. For simplicity, I will usually write all the energy scales in units of t.

The tight-binding hamiltonian H_0 (note that the dispersion relations are 2×2 matrices which are the same for both degenerated orbitals) for a hexagonal lattice with intraorbital nearest neighbor hoppings t (in the hexagonal first Brillouin zone) is:

$$H_0 \begin{pmatrix} 0 & \varepsilon_k^{AB} \\ \left(\varepsilon_k^{AB}\right)^\dagger & 0 \end{pmatrix} \rightarrow \varepsilon_k^{AB} = -t - 2t\cos\left(\frac{k_x}{2}\right)e^{i\sqrt{3}k_y/2}\begin{pmatrix} 1 & 0 \\ 0 & 1 \end{pmatrix} \tag{5.1}$$

where the electrons jump between A and B sites of the hexagonal lattice and between the same orbitals. In FIGURE 5.6, I have plotted the DOS in terms of the number of electrons

per site n_e and the filling per orbital, spin and site $x = n_e/2N$. This model shows a particle-hole symmetry around the CNP, but we expect that the results when including only onsite correlations will not change qualitatively. The Dirac points are located at half-filling, and the van-Hove singularities are located in the middle point of quarter (and three-quarter) and half-filling. Compared with the low-energy continuum model of [93], our model would be at least qualitatively similar, where also the van-Hove peaks are located in between quarter and three-quarter filling and the CNP.

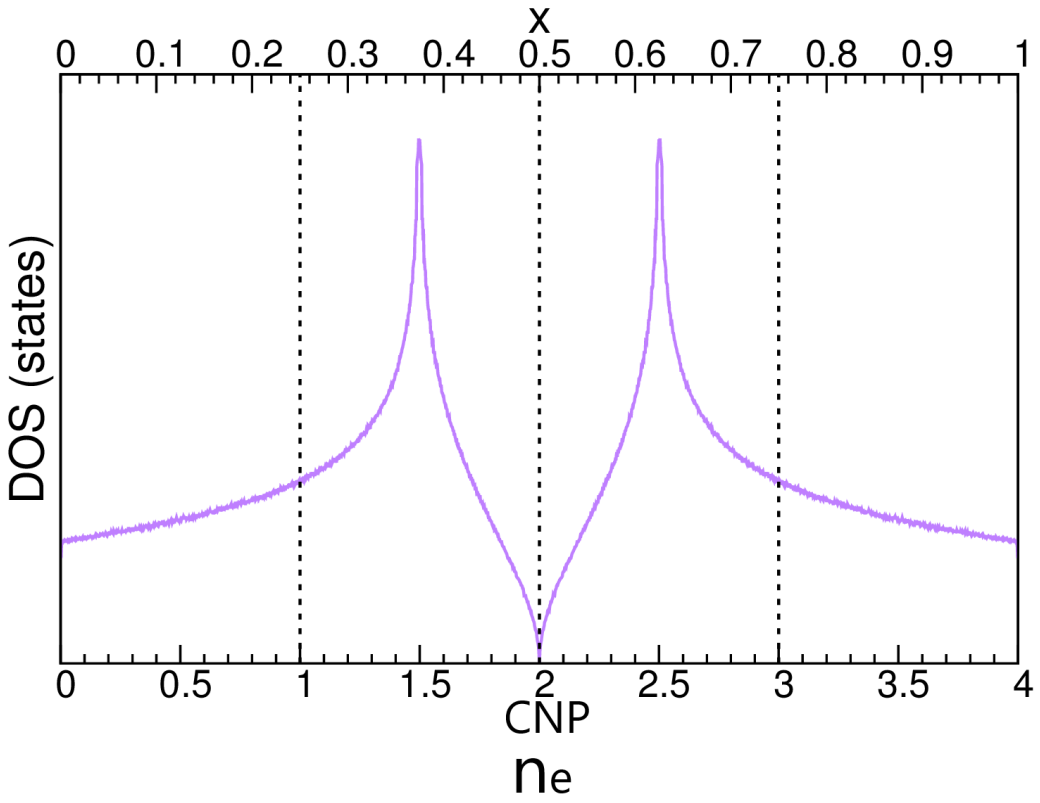

FIGURE 5.6: DOS for the $N = 2$ equivalent orbitals hexagonal lattice with only nearest neighbor hoppings included, as described in Eq. (5.1). Our model is particle-hole symmetric with respect to half-filling $n_e = 2$ ($x = 1/2$). Vanishing DOS can be seen at the CNP, as expected for Dirac points. The van-Hove singularities are located $n_e \sim 1.5$ and ~ 2.5, in between quarter (and three-quarter) filling and half-filling, quantitatively similar to the low-energy continuum model [93].

In principle, due to the 2D character of MA-TBG, long-range interactions will become more important because of the reduced screening, see **Section 1.6**. In Pablo Jarillo's group experiments [84, 85], MA-TBG is sandwiched between hexagonal boron-nitride (hBN), whose thichness is $\approx 10-30\,nm$, of the order of the superlattice size ($\lambda \sim 13\,nm$) for MA-TBG. The doping is induced by an external gate voltage, and due to the similar thickness of the hBN layers with respect to the superlattice distance, we believe that this external electric field is effectively screening the long-range character of the Coulomb interaction, hence disminishing the long-range interaction effects, in a first approximation. We then assume that the interaction effects will be restricted to electrons which are in the same superlattice site. I will use the SSMF $U(1)$ formalism to calculate the effect of local correlations, see **Appendix B**.

In FIGURE 5.7, I reproduce the critical interaction for the Mott transition U_c/t versus J_H/U [46, 113, 177, 181, 182], by using SSMF $U(1)$ formalism at $x = 1/2$ (red line) and $x = 1/4$ (black line).

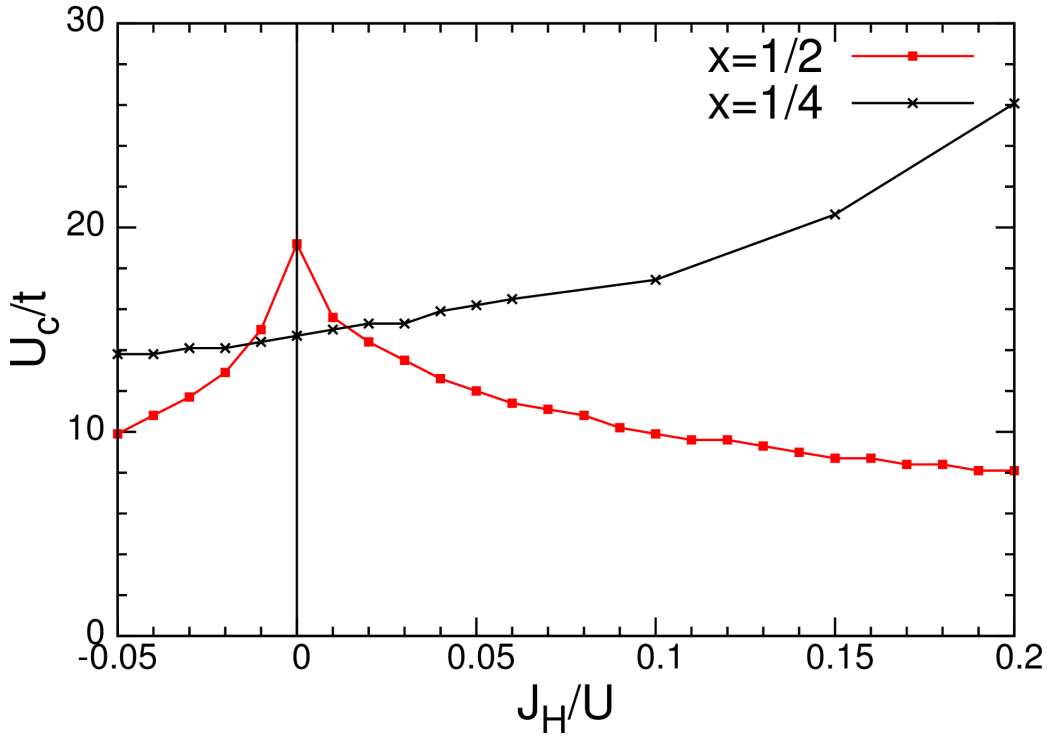

FIGURE 5.7: U_c/t versus J_H/U for $x = 1/2$ (red line) and $x = 1/4$ (black line) in the hexagonal tight-binding model proposed Eq. (5.1). U_c behavior follows Eq. (2.3) and Eq. (5.2). We found that metallicity at $x = 1/2$ and a Mott insulating state at $x = 1/4$ occurr in a small range $-0.01 < J_H/U < 0.01$.

For $J_H \leq 0$, U_c behavior follows the evolution already explained in **Chapter 2**. The region $J_H/U < 0$ is included because some authors [206] argued that, once the effect of phonons (with frequencies $\omega \sim 200\,meV$) is included in MA-TBG, J_H may take an effective small negative value. This region might be of interest when applying non-local correlations techniques. For $J_H < 0$, the interaction energy cost Δ^x can be obtained as done in Eq. (2.3) for $J_H > 0$, so in the large-U limit:

$$\Delta^x\,(J_H < 0) = \begin{cases} = U + 5J_H & n_e = N \\ = U & other\ integer\ n_e \end{cases} \tag{5.2}$$

In a multiorbital system, the ratio between the interaction energy cost and the kinetic energy gain is given by $\Delta^x/\widetilde{W}$, see **Chapter 2**, and this ratio controls the critical interaction U_c^x at a given filling x. So, when Δ^x increases, U_c^x will decrease. Then, for the $J_H < 0$ region, at half-filling $n_e = N = 2$, U_c decreases if $|J_H|$ increases (Mott insulating behavior promoted), and at quarter filling $n_e = 1$, U_c is unaffected by $J_H < 0$.

As seen in FIGURE 5.7, there is a small region of J_H/U in which a Mott insulating state can be obtained for $x = 1/4$ and a metallic state for $x = 1/2$ (same as in the experimental results, see FIGURE 5.1), i.e. $U_c^{x=1/2} > U_c^{x=1/4}$. This region occurs in the small range $-0.01 < J_H/U < 0.01$. This region appears due to the promotion of metallic behavior in the case of $x = 1/2$ (thus, increasing U_c^x), but not for $x = 1/4$ [46, 113, 177, 181, 182]. I will consider from now on $J_H = 0$ as an approximation of its value in MA-TBG. In the case of the hexagonal lattice at $J_H = 0$, $U_c^{x=1/4} = 14.7t$ ($\sim 30\,meV$) and $U_c^{x=1/2} = 19.2t$

($\sim 40\,meV$), and also $U_c^{x=1/2}/U_c^{x=1/4} \sim 1.28$. In other lattices, such as the square lattice, $U_c^{x=1/2}/U_c^{x=1/4} \sim 1.13$ [46, 113, 182]. This difference emerges due to the vanishing DOS in the hexagonal lattice at half-filling, in contrast with the van-Hove peak in the square lattice at half-filling. The relation $U_c^{x=1/2}/U_c^{x=1/4} > 1$ at zero J_H holds for any lattice symmetry in the local correlations case for $J_H = 0$.

In FIGURE 5.8, I show Z versus n_e and $x = n_e/2N$ for different U values at $J_H = 0$ [46, 113, 177, 181, 182]. Due to the particle-hole symmetry, Z is symmetric with respect to half-filling $n_e = 2$. For interactions $U_c^{x=1/4} < U < U_c^{x=1/2}$, there is a finite Z value (i.e. metallic behavior) at $x = 1/2$ and $Z = 0$ (Mott insulator behavior) at $x = 1/4$. Nevertheless, correlations are sizable at all dopings, specially at half-filling (where $Z \leq 0.3$), which would produce a sizable effect in the renormalization of the Fermi velocity v_F of MA-TBG. The strength of correlations is asymmetric with respect to the insulating state at $x = 1/4$, due to the asymmetry of the DOS around this filling, and also due to the proximity of the Mott insulating state at $x = 1/2$ (see **Chapter 2**). The van-Hove singularity at $x = 0.375$ does not have a significant effect.

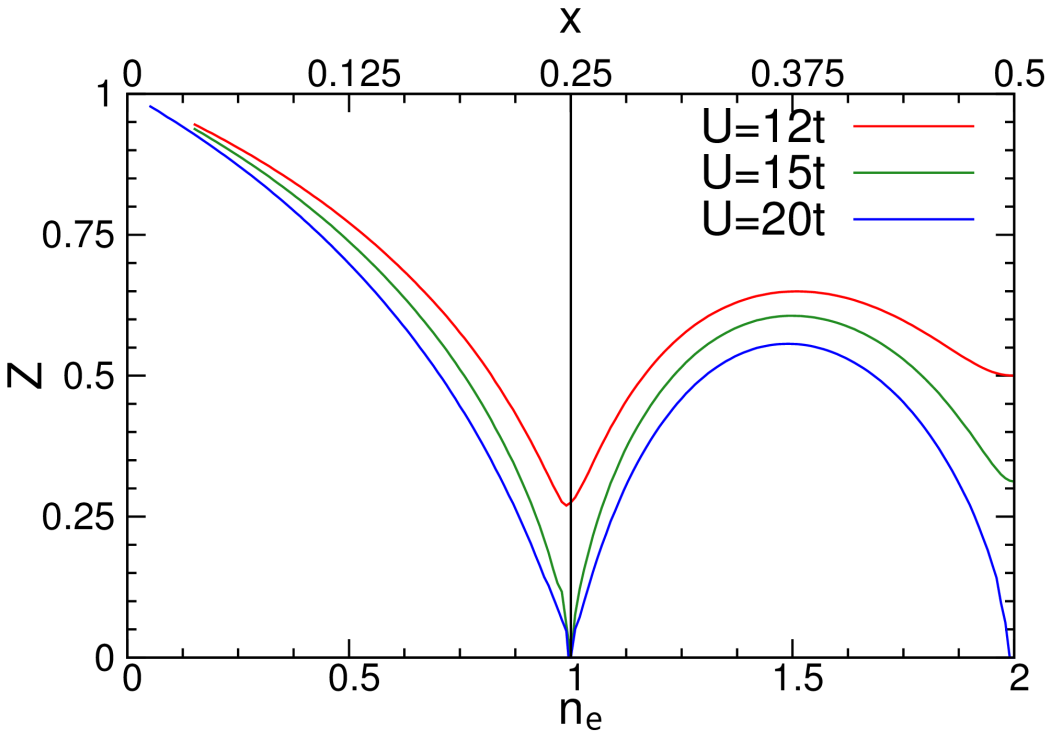

FIGURE 5.8: Z versus filling curves for $U = 12t$ (red line), $15t$ (green line) and $20t$ (blue line), and for $J_H = 0$. The experimental results are consistent for $U_c^{x=1/4} < U < U_c^{x=1/2}$, where $U_c^{x=1/4} = 14.7t$ and $U_c^{x=1/2} = 19.2t$. Correlations are sizable at all dopings, specially at half-filling (where $Z \leq 0.3$), which would produce a sizable effect in the renormalization of the Fermi velocity v_F of MA-TBG. The strength of correlations is asymmetric with respect to the insulating state at $x = 1/4$, due to the asymmetry of the DOS around this filling, and also due to the proximity of the Mott insulating state at $x = 1/2$ (see **Chapter 2**). The van-Hove singularity at $x = 0.375$ does not have a significant effect.

5.2.2 Local correlations and Zeeman effect in MA-TBG

I will now study the effect that a Zeeman magnetic field has on the insulating states at quarter filling ($x = 1/4$). In order to do the calculations, I have implemented the Zeeman field term in the SSMF $U(1)$ formalism, as detailed in **Appendix C**, by adding the following term to the Hubbard-Kanamori hamiltonian of Eq. (1.22):

$$H_{Zeeman} = H \sum_{im} (\hat{n}^d_{im\uparrow} - \hat{n}^d_{im\downarrow}) \tag{5.3}$$

where $\hat{n}^d_{im\sigma} = d^\dagger_{im\sigma} d_{im\sigma}$. Through this section, I will check how the critical interaction for the Mott transition U_c evolves in terms of the Zeeman field H.

The Zeeman field H breaks the spin degeneracy. Here the majority spin band is labeled with $\downarrow$ and the minority spin with $\uparrow$. This term is a spin-dependent onsite energy shift, so the majority spin band will move downwards, being progresively filled when H increases, and the minority spin band will move upwards, being emptied when H increases. When the minority spin band is empty, its quasiparticle weight $Z_\uparrow$ cannot be defined anymore[2]. Then, H will produce a spin polarization which is enhanced by increasing interactions. This enhancement appears when the majority spin band progresively approaches half-filling, thus following the ideas pointed out in previous chapters. Then, the filling per spin $n_{m\sigma}$ of the majority spin band evolves from $n_{m\downarrow} = 0.25$ (quarter filling) to 0.5, and the minority spin band is emptied.

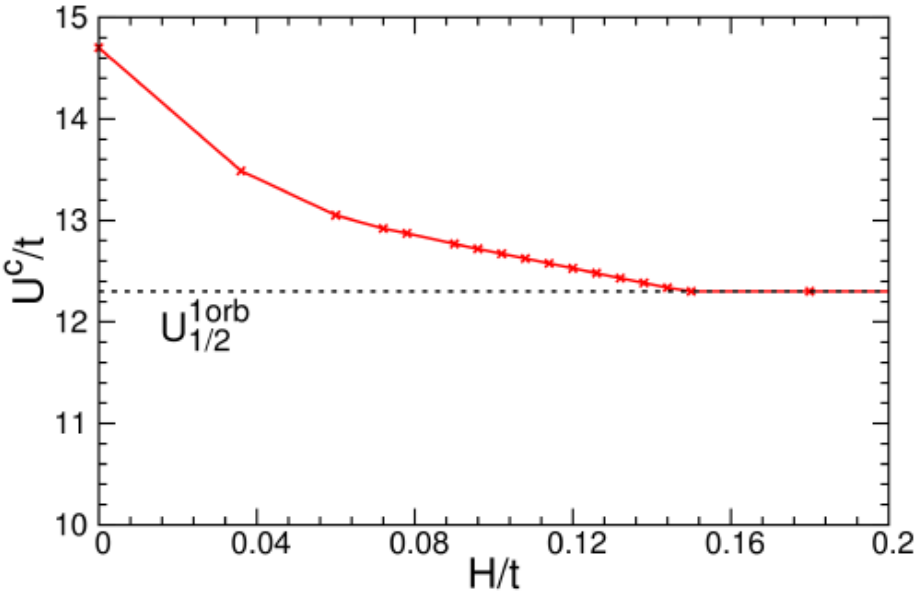

FIGURE 5.9: **(a)** Critical interaction for the Mott transition U_c/t versus Zeeman field H/t for the honeycomb lattice model at quarter filling $x = 1/4$. At $H_c \sim 0.15t$, the system fully polarizes, saturating to an effective single-orbital at half-filling system, in which the critical interaction is given by $U^{1orb}_{1/2}$.

H promotes insulating behavior (when H increases, $\Delta^{x=1/4}$ decreases, and hence $U_c^{x=1/4}$ increases), rather than promoting metallicity as expected from the experiments [85]. At

[2]Note that the condition to define the quasiparticles in the Fermi liquid theory (FLT) is that the corresponding bands are crossed by the Fermi level, see **Section 1.2.2**.

$J_H = 0$, H reduces the degeneracy of the ground state, hence it reduces the effective kinetic energy $\tilde{W}$, see **Section 2.2.2**. Then, $U_c^{x=1/4}$ will be reduced with respect to its zero Zeeman field value $U_c^{x=1/4}(H=0)$. In FIGURE 5.9, I show the results for U_c/t in terms of the Zeeman field H/t at quarter filling $x = 1/4$.

Once the orbitals are completely spin polarized (i.e. $n_{m\downarrow} = 0.5$ and $n_{m\uparrow} = 0$), I have found that the system becomes equivalent to a single-orbital model at half-filling with a critical interaction $U_{1/2}^{1orb} < U_c^{x=1/4}(H=0)$. Two regimes can be distinguished depending on the H/t value: weak Zeeman field $H \leq 0.15t$ and strong Zeeman field $H > 0.15t$. As shown in FIGURE 5.10, in the strong Zeeman field regime, the system saturates to $U_{1/2}^{1orb}$, following the Z evolution of the single-orbital system at half-filling down to the Mott insulating phase. In the weak Zeeman field regime, once the system fully polarizes, it jumps into the Mott insulator at $U > U_{1/2}^{1orb}$.

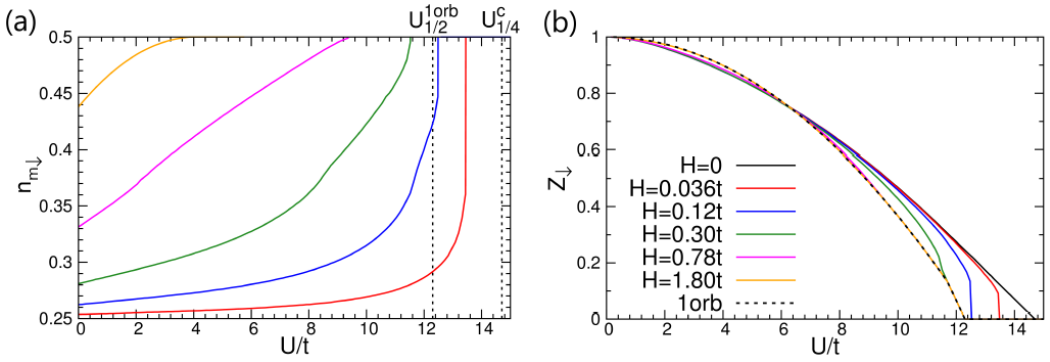

FIGURE 5.10: **(a)** Majority spin filling $n_{m\downarrow}$ and **(b)** quasiparticle weight $Z_\downarrow$ curves versus U/t at various Zeeman field H/t values. H/t values included in the legend. I included the Z evolution in terms of U/t for the single-orbital system at half-filling (labeled by "1orb"). The system fully polarizes at a $H \sim 0.15t$ ($\sim 0.3\,meV$). For weak Zeeman field, $H \leq 0.15t$, the system jumps into the Mott insulator at $U_c > U_{1/2}^{1orb}$, while for strong Zeeman field, $H > 0.15t$, it follows the single-orbital at half-filling behavior.

Then, I have shown that the Zeeman field at quarter filling in the local correlations picture will promote insulating behavior ($U_c^{x=1/4}$ decreases when H increases) as it reduces the degeneracy of the ground state. This is precisely the opposite behavior than the one found in the experiments [85].

Besides ours, other works [183, 184] also remarked the fact that the gap ($\approx 0.3\,meV$) of the Mott insulating phases is in contradiction with the expected gap from a Mott insulator in the local correlations picture. In a single-orbital at half-filling system [17], the Mott transition takes place at $U_c \sim 1.5 - 2W$ and the gap is $\sim U - W \sim 15 - 25\,meV$. In multiorbital systems, the gap is of the same order of magnitude [183, 184].

In **Section 1.3.3**, I have shown that in local correlations for a single-orbital at half-fillling system, the temperature T promotes an insulating behavior [8, 17, 20], rather than metallicity (see FIGURE 1.11**(b)**). In multiorbital systems the trend is similar [113]. Then, when including only local correlations, the experimental behaviors for the Mott insulating states observed at quarter and three-quarter fillings in MA-TBG [85] cannot be explained (a metallic state is promoted when increasing T). In next section, we will argue that these insulating states could be theoretically explained by Mott physics if non-local correlations are taken into account explicitly.

5.2.3 Non-local correlations as a possible explanation

When non-local correlations are included in the description, correlations between different adjacent sites are also taken into account [19, 21, 185–199]. Note that the interactions in a non-local correlations picture are still between electrons in the same lattice site. Inter-site magnetic correlations will promote a short-range ordering of the spins at different lattice sites. Inter-site orbital correlations will promote the location of electrons in specific orbitals from one lattice site to another. These inter-site correlations can produce long-range order. However, even if there is not long-range order, the short-range correlations which are established (e.g. spin singlets if the correlations have antiferromagnetic character) can result in a Mott-like insulating behavior.

Including the effect of non-local correlations could explain the experimental behaviors of the unexpected insulating states in MA-TBG. In contrast with local correlations physics, in which the details of the tight-binding model are not too important when studying the physical trends, for the non-local correlations effects, the specific tight-binding model will influence the behavior of the system. In MA-TBG, the tight-binding model is not yet fully established and understood [93, 177–179, 200]. Nevertheless, there are qualitative conclusions which are expected to be valid regardless of the model.

Here, I will briefly review the effect that including non-local correlations has on the basis of known results in other lattice models, mainly the 2D square lattice [19, 21, 188, 191, 192]. These results were obtained by means of cellular dynamical mean-field theory (cellDMF), dynamical cluster approximation (DCA), variational cluster approximation (VCA) and dynamical vertex approximation (DΓA). Due to the computational cost of these techniques, and specially for multiorbital systems, only a few results are available. Up to date, there is not available any study for the $N = 2$ orbitals hexagonal lattice in the existing literature. This section would prepare the path for a future calculation in MA-TBG.

In **Chapter 1** and for the single-orbital 2D square lattice at half-filling, I have explained that there are two critical interactions U_{c1} and U_{c2} (with $U_{c1} < U_{c2}$), where the first interaction U_{c1} is related with the formation of the Hubbard bands and the emergence of a gap between them, and the second U_{c2} is related with the dissapearance of the quasiparticle peak [17], see FIGURE 1.9**(a)**. For a finite T, the Mott transition U_c is defined in between this two critical interaction values, see **Section 1.3.3**.

In the presence of non-local correlations, both U_{c1} and U_{c2} are shifted towards smaller interaction values, maintaining the relation $U_{c1} < U_{c2}$ [19, 21, 188, 191, 192]. At $T = 0\,K$, U_c^{local} coincides with U_{c2}, while for non-local correlations, $U_c^{nonlocal}$ coincides with U_{c1} [19, 21]. In FIGURE 5.11, I show an unified sketch of the phase diagrams presented in FIGURE 1.11 and obtained using the results in [8, 17, 19–21], as well as the results obtained in this chapter.

Thus, non-local correlations will shift the Mott transition to a smaller $U_c^{nonlocal} < U_c^{local}$ for all n_e fillings and N orbitals [19, 21, 188, 191, 192]. This is due to the interplay between local charge correlations C_{n_T} and inter-site magnetic and orbital correlations, see **Section 1.3.2** for the case of inter-site magnetic correlations in the single-orbital 2D square lattice at half-filling. As seen in FIGURE 5.11, at large T and U, local correlations results are recovered, and the system is not sensible to the non-local correlations effects. Close to $U_c^{nonlocal}$ (orange shaded region in FIGURE 5.11), the Zeeman field behavior, the temperature behavior [19, 21] and the gap size [19] will be controlled by the inter-site correlations.

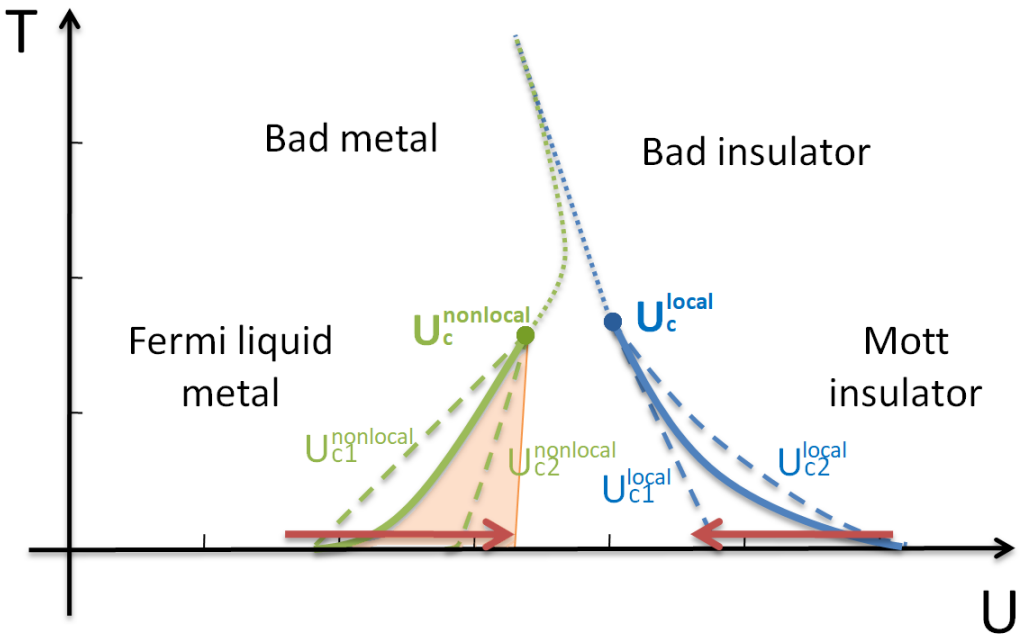

FIGURE 5.11: Sketch of the phase diagram T vs U for a single-orbital 2D square lattice at half-filling, including local (blue lines) and non-local (green lines) correlations results. U_c^{local} and $U_c^{nonlocal}$ are plotted as continuous lines, while $U_{c\,1}$ (Hubbard bands start to form and gap opens) and $U_{c\,2}$ (quasiparticle peak dissapears) for both cases as dashed lines. For $U < U_c$, a metallic behavior is found, while for $U > U_c$ the system is a Mott insulator. These lines end in a critical point marked by a filled circle. The dotted lines mark the crossover between a bad metal and bad insulating behavior at larger T. At large T and U, local correlations give good results. The orange shaded region marks the area in which a small gap is opened (lower than the expectation for local correlations $\sim U-W$). For $J_H \leq 0$, Zeeman field H will shift the Mott transition to lower (larger) U values for local (non-local) correlations, see red arrows. Sketch made by using the results in [8, 17, 19–21, 99].

For multiorbital systems, depending on J_H value, AFM or FM inter-site correlations are promoted. For $J_H > 0$, inter-site FM and antiferro-orbital (i.e. electrons will sit in different orbitals with parallel spins from one site to another) correlations are promoted. For $J_H \leq 0$, inter-site AFM and ferro-orbital (i.e. electrons will sit in the same orbital with antiparallel spins from one site to another) correlations are promoted [188, 193]. A sufficiently large Zeeman magnetic field could suppress the AFM inter-site correlations and promote metallicity, as obtained in the experiment. I signaled the increasing Zeeman magnetic field H with red arrows in FIGURE 5.11. At $J_H = 0$, when H increases, U_c^{local} is pushed to lower values (insulating behavior is promoted), as shown in **Section 5.2.2**, and $U_c^{nonlocal}$ is pushed to larger values (metallicity is promoted) if $J_H \leq 0$.

This behavior will qualitatively hold for a tight-binding model without magnetic frustration. For frustrated lattices, the non-local critical interaction $U_c^{nonlocal}$ approaches the local one, hence the effects of the non-local correlations will be reduced. In the limit of an infinite dimensional lattice (Bethe lattice) completely frustrated, the local correlations limit is recovered. For the non-frustrated honeycomb model used in this work, we expect that the phenomenology explained here will qualitatively hold.

Due to the experimental behavior found in MA-TBG with respect to the Zeeman field and temperature, we expect that the system shows the phenomenology described above for $J_H \leq 0$, so that inter-site AFM correlations will be controlling the behavior of this system.

I have already commented the resulting T behavior in a single-orbital 2D square lattice at half-filling [8, 17, 19–21], see **Section 1.3.3**. Inter-site AFM correlations are suppressed when increasing T in square and hexagonal single-orbital lattices at half-filling [19, 21]. Close to $U_c^{nonlocal}$ (orange shaded region in FIGURE 5.11), at low T the system is insulating and at larger T is metallic, opposite to what happens in local correlations. The suppression of the inter-site AFM correlations when increasing T have been also obtained for $N = 2$ orbitals 2D square lattice at quarter filling $x = 1/4$ and $J_H = 0$ [188]. Then, we expect that the experimental T behavior could be also explained by non-local correlations physics.

The small gap found in experiments might be also reconciled with the one in a Mott insulator if non-local correlations are included. For non-local correlations, a small gap opens in the quasiparticle peak close to $U_c^{nonlocal}$ [19], which is signaled by an orange shaded area. For larger $U \gg U_c^{nonlocal}$, the gap size will converge to the local correlation expected one $\sim U - W \sim 15 - 25\,meV$ [17, 183, 184]. The evolution of the spectral function at $(\pi, 0)$ obtained by cellDMFT can be seen in FIGURE 5.12 for various points of the phase diagram of FIGURE 5.11, for the metallic state ($U < U_{c1}^{nonlocal}$), for the coexistance region ($U_{c1}^{nonlocal} < U < U_{c2}^{nonlocal}$) and for the insulating state ($U > U_{c2}^{nonlocal}$) for $U < U_{c1}^{local}$. At the metallic state ($U < U_{c1}^{nonlocal}$), the spectral function shows the typical quasiparticle peak at the Fermi level ($\omega = 0$). In the coexistance region ($U_{c1}^{nonlocal} < U < U_{c2}^{nonlocal}$), a small gap starts to develop, and the quasiparticle peak shows a reduced weight. At the insulating state ($U > U_{c2}^{nonlocal}$), but for $U < U_{c1}^{local}$, a small gap ($\sim 0.2t$) is found

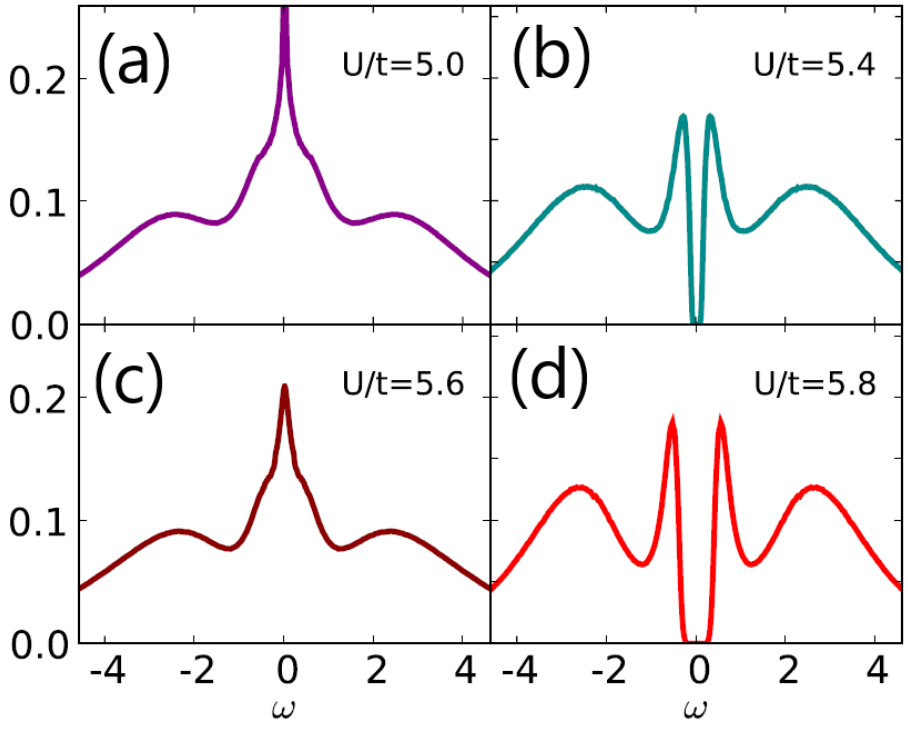

FIGURE 5.12: CellDMFT spectral functions at $(\pi, 0)$ and $T = 0.01t$ (well below the end critical point in FIGURE 5.11) for the 2D square lattice at half-filling and various interactions around the non-local critical interaction for the Mott transition. **(a)** At the metallic state ($U < U_{c1}^{nonlocal}$), the spectral function shows the typical quasiparticle peak at the Fermi level ($\omega = 0$) with a sizable renormalization $Z \sim 0.4$. In the coexistance region ($U_{c1}^{nonlocal} < U < U_{c2}^{nonlocal}$), a **(b)** small gap starts to develop and **(c)** the quasiparticle peak shows a reduced weight $Z < 0.4$. **(d)** At the insulating state ($U > U_{c2}^{nonlocal}$), but for $U < U_{c1}^{local}$, a small gap ($\sim 0.2t$) is found. Taken and adapted from [19].

Finally, another important effect of non-local correlations is that the ratio $U_c^{x=1/2}/U_c^{x=1/4}$ for multiorbital systems will be altered [188, 189]. In order to reproduce the experimental results, the ratio $U_c^{x=1/2}/U_c^{x=1/4}$ has to be larger than 1. Specific calculations should address whether the inequality $U_c^{x=1/2,nonlocal}/U_c^{x=1/4,nonlocal} < 1$ is obtained for $J_H \leq 0$ in MA-TBG in order to reproduce the experimental behavior [85].

Note that these results are obtained for different tight-binding models that the one which would describe MA-TBG. However, it is interesting to note that non-local correlations could reconcile the experimental results with the theoretical expectations. In FIGURE 5.11, I point to the possible location of MA-TBG in the orange shaded area. In this region, a metallic behavior promoted by T and the Zeeman magnetic field H, as well as the small gap size are obtained.

5.3 Summary

I conclude this chapter by making a summary of the obtained results:

- On April 2018, unexpected insulating states at commensurate fillings of the moiré superlattice [85], and superconducting domes around the insulating state for the hole-doped MA-TBG [84] were found, with $T_c^{max} \approx 1.7\,K$ at $\approx -1.5 \times 10^{12} cm^{-2}$. In this system, the band structure around the Fermi level is formed by four degenerated flat bands, with the total bandwidth $W \sim 10\,meV$ [87, 89, 177–179]. The flattening of the bands around the Fermi level comes from the hybridization between the twisted graphene layers. The insulating states of MA-TBG show an interesting behavior: the gap is $\sim 0.3\,meV$, two orders of magnitude smaller than W, and they are suppressed by T and by a Zeeman magnetic field H, at the same energy scales as the size of the gap.

- The correct tight-binding model for MA-TBG is still under discussion [93, 177–179, 202–204]. At the time when we made this work, there was a consensus about the fact that the correct lattice symmetry should show the Dirac points at K and K', and that two in-plane p-like orbitals should be centered at the AB and BA regions [93, 177–179]. These orbitals show a maximum amplitude centered at AA regions, in agreement with the previously known fact that the electronic density around K is mainly located in AA regions [91]. Then, we have adopted a simple hexagonal lattice tight-binding model with only intraorbital nearest neighbor hoppings $t \approx 2\,meV$ (then, $W = 6t \approx 12\,meV$) in order to mimic the correct tight-binding model for MA-TBG. Our aim is studying local correlations effects in MA-TBG. In local correlations picture, the tight-binding model details are not too important, hence the trends that I have obtained will be robust and applicable to MA-TBG.

- We argued that the external gate voltage responsible for the induced doping, also screens the long-range character of the Coulomb interaction. Hence, we concluded that onsite interactions physics are playing a major role in MA-TBG. Whether local or non-local correlations are responsible of these effects is something that we explored in this work. We clarified that local correlations cannot explain the experiments that are found in MA-TBG, but non-local correlations could in principle reconcile experimental and theoretical results.

- In **Section 5.2.1**, I have reviewed the results obtained in $N = 2$ orbital systems [46, 113, 177, 181, 182]. I solved the hexagonal lattice tight-binding model with SSMF $U(1)$ formalism. I extended the U_c versus J_H curves to include a negative $J_H < 0$ region, which may appear due to the effect of phonons with $\omega \sim 200\,meV$ [206]. I found that, in order to obtain a Mott insulator at $x = 1/4$ and a metal at $x = 1/2$ like in the experiment (i.e. $U_c^{x=1/4} = 14.7t \sim 30\,meV < U_c^{x=1/2} = 19.2t \sim 40\,meV$), J_H should lie between $-0.01 < J_H/U < 0.01$. In the following, we assumed $J_H = 0$ as a good approximation for the real J_H value in MA-TBG. I found that $U_c^{x=1/2}/U_c^{x=1/4} \sim 1.28$ (the experimental behavior is reproduced if $U_c^{x=1/2}/U_c^{x=1/4} > 1$). Even if the system at $x = 1/2$ is not a Mott insulator, the electronic correlations are sizable, giving $Z \approx 0.3$.

- In **Section 5.2.2**, I studied the Zeeman effect for the same $N = 2$ orbitals hexagonal lattice model. I implemented it in SSMF $U(1)$ via a spin-dependent onsite energy. I considered $J_H = 0$ and $x = 1/4$. By estimating $\Delta^{x=1/4}$, I found that the Zeeman field H does not promote metallicity. In contrast, $U_c^{x=1/4}$ will be reduced with respect to $U_c^{x=1/4}(H = 0)$, and Mott insulating behavior is promoted by the Zeeman field H. This behavior is opposite to the one observed in the experiments.

- For strong Zeeman field ($H > 0.15t$), the system will be fully spin-polarized (i.e. $n_\downarrow = 0.5$ and $n_\uparrow = 0$) at $U < U_{1/2}^{1orb}$, and at larger interactions, it will effectively behave as a single-orbital at half-filling system. $U_c^{x=1/4}$ saturates to $U_{1/2}^{1orb}$ at 0.15. For weak Zeeman field ($0 < H < 0.15t$), the system jumps to the Mott insulating state at $U_c > U_{1/2}^{1orb}$, value at which the system fully polarizes.

- In the local correlations picture, when T increases, the Mott insulating state is promoted [8, 17, 20, 113], see **Section 1.3.3**, opposite to what occurs in the experiment. The expected gap for local correlations is $gap \sim U - W \sim 15 - 25\,meV$ [17, 183, 184], much larger than the obtained experimentally. All of these behaviors suggest that local correlations cannot explain the phenomenology of MA-TBG. Then, in **Section 5.2.3**, we proposed to go beyond local correlations, by including the effects of non-local correlations in order to explain the phenomenology of MA-TBG.

- I made a brief review on the present results for non-local correlations in single- and multiorbital systems [19, 21, 185–199]. When non-local correlations are included, all the critical interactions U_c, are pushed to lower values [19, 21, 188, 191, 192], due to the interplay between local charge correlations C_{n_T} and inter-site magnetic and orbital correlations. At large T and U, local correlations will control the physics of the system [8, 17, 19–21]. Close to $U_c^{nonlocal}$ and for $J_H \leq 0$, AFM and ferro-orbital inter-site correlations are promoted [188, 193]. In this case, a Zeeman field will suppress AFM inter-site correlations. Also, T [19, 21] and the small gap [19] results can be reconcile with the experiment in this region. On the other hand, the needed relation $U_c^{x=1/2}/U_c^{x=1/4} > 1$ is not known [188, 189]. But non-local correlations results are sensible to the correct tight-binding model, and hence for MA-TBG this factor may change.

Now, I would like to mention the current status of the discussion about the tight-binding model for MA-TBG. In **Section 1.6.1** and **Section 5.1.1**, I have mentioned that there is a ξ valley degeneracy, due to the fact that the Dirac points are uncoupled, which results in four flat bands per spin. Around K, the electronic density is mainly located at the AA regions. In order to fit the flat bands, MA-TBG was modeled as a $N = 2$ orbitals system. Due to

symmetry arguments [177–179], the two orbitals have an in-plane p-like character and they are centered at the AB and BA regions, forming a hexagonal superlattice. The maximum amplitude of these orbitals is centered at AA regions at K.

However, there is still a debate about the applicability of this model. It was discussed that this model suffers a topological obstruction [178] (related with the valley symmetry at K_ξ^l Dirac points) when trying to construct a minimal model only for the flat bands. Some authors [179] have argued that such topological obstruction can be overcomed by considering that both valleys are not perfectly uncoupled, and hence there is not a perfect valley degeneracy.

These two problems point to the necessity of including more than only the four flat bands to model MA-TBG. Ten and six bands models (valley degeneracy considered) were proposed in [200]. The ten bands model fits the two flat bands and the four bands above and below. There are different orbitals centered at different regions of the superlattice. In this model, there are three p-like orbitals centered at the AA regions forming a triangular superlattice, four p-like orbitals centered at the AB and BA regions forming a hexagonal superlattice and one s-like orbital centered at the middle point between AB and BA regions, forming a Kagome superlattice. In total, there are 10 orbitals (3 p $\times$ 1 site+ 4 p $\times$ 2 sites + 1 s $\times$ 3 sites) which will reproduce the 10 bands. The simplified six bands model fits the two flat bands and the four bands below the,, where only the 3 p-like orbitals in the triangular superlattice and the s-like orbital in the Kagome superlattice are retained. These models looks promising, but yet there is not a consensus in the community about them.

Chapter 6

Wannier tight-binding model for the single-layer Fe_3GeTe_2

Very recently, few layers of an iron-based material, Fe_3GeTe_2 (FGT), were obtained (by exfoliating the bulk FGT), reaching the monolayer limit. FGT is the first metallic ferromagnet which has been isolated in the monolayer form [207, 208], and it is free of rare-earth elements. In this material, the ferromagnetic temperature in the bulk is $T_F \sim 220\,K$. When exfoliating the bulk system, T_F decreases until $T_F \sim 20\,K$ in monolayer FGT. This critical temperature T_F can be tuned with doping via an external voltage, reaching room temperature ferromagnetism for the trilayer FGT at an electron carrier density doping of $\sim 10^{14}\,cm^{-2}$.

Bulk FGT was already experimentally and theoretically studied [209–213]. On the other hand, few layer FGT is theoretically less known.

ARPES and low-T specific heat measurements in bulk FGT [213] reported the presence of sizable electronic correlations. Here, we want to study the possible similarities between bulk and monolayer FGT, and other iron chalcogenides, with an special focus on the possible role of the Hund's coupling in FGT. In order to do this, the first step is to calculate the band structure and Wannier tight-binding model of FGT.

In this chapter, I will present the calculations that I have performed to calculate the DFT band structure and the Wannier tight-binding model for FGT. I will study both the bulk and the monolayer FGT. Lastly, I will give some final comments. This chapter could serve as a first step to the study the ferromagnetism and other electronic properties in FGT.

6.1 Introduction & Motivation

FGT is a van der Waals crystal, so it can be easily exfoliated to obtain atomically thin layers. It was recently discovered that monolayer FGT is the first monolayer metallic ferromagnetic system [207, 208], and it is free of rare-earth elements. When exfoliating FGT, the critical temperature of the itinerant ferromagnetic phase T_F evolves from $T_F \sim 220\,K$ in the bulk to $T_F \sim 20\,K$ in the monolayer, as shown in FIGURE 6.1**(a)**. A large intrinsic magnetocrystalline anisotropy in the monolayer FGT lifts out the restriction imposed by the Mermin-Wagner theorem[1], hence the 2D long-range ferromagnetic order can be formed. When applying an external ionic voltage which effectively dopes with electrons the system, T_F changes non-monotonously, and it can reach room temperature ($T_F \sim 300\,K$) in the case of trilayer FGT for an electron carrier density $\sim 10^{14}\,cm^{-2}$ [207], see FIGURE 6.1**(b)**.

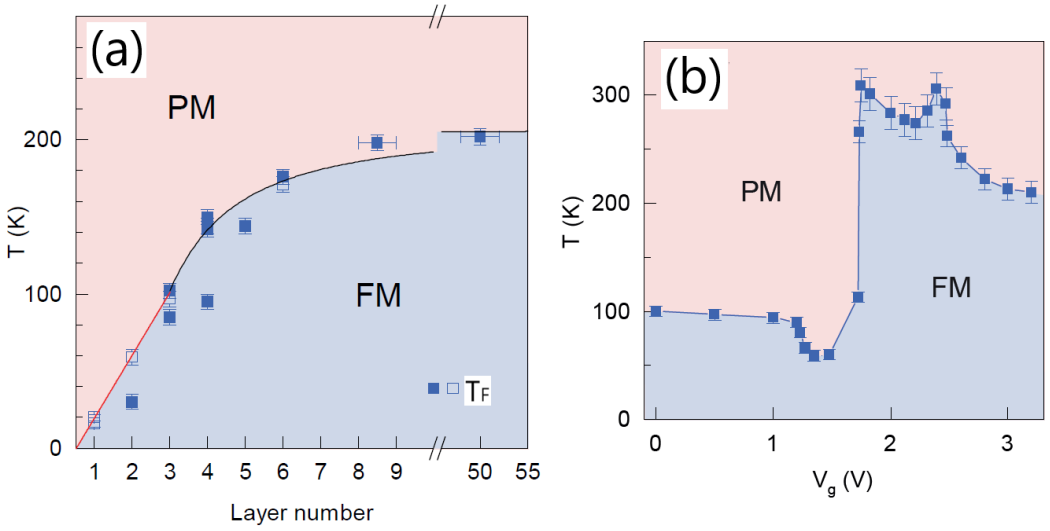

FIGURE 6.1: **(a)** Temperature T versus layer number phase diagram, where T_F evolves from $\sim 220\,K$ in the bulk FGT (identified as $50-55$ layers) down to $\sim 20\,K$ in monolayer FGT. **(b)** T versus ionic external voltage V_g (which acts as an effective electron doping) phase diagram for trilayer FGT. Due to the itinerant character of FGT, it is expected that this phase diagram follows the evolution of the total DOS of FGT. Taken and adapted from [207].

Fe_3GeTe_2 has a hexagonal symmetry (space group $P63/mmc$), see FIGURE 6.2. The crystal structure parameter along the c axis is quite large ($c = 16.333$Å) when compared with the in-plane parameters ($a = b = 3.991$Å), hence indicating a quasi-2D crystal structure. In the unit cell, 2 Fe atoms are equivalent (labeled by $Fe1$), while the third one (labeled by $Fe3$) is not. $Fe1$ atoms form a triangular lattice which sandwiches the $Fe3$ and Ge atoms forming an hexagonal lattice, see FIGURE 6.2**(b)**. 2 Te spacers atoms are located between adjacent $Fe1-Fe3-Ge$ layers. A single stack of $2Fe1$, $Fe3-Ge$ and $2Te$ atoms forms the monolayer.

Due to the itinerant character of FGT, a weakly correlated Stoner criteria [8] could be possible applied. In the Stoner criteria for ferromagnetism, the peaks in the total density of states (DOS) give the tendency towards ferromagnetism. Hence, the total DOS for FGT should give the same evolution as the one shown in FIGURE 6.1**(b)** when doping with electrons. On

[1] This theorem [214] states that in an isotropic system with dimensions lower than three, thermal fluctuations suppress any possible long-range order.

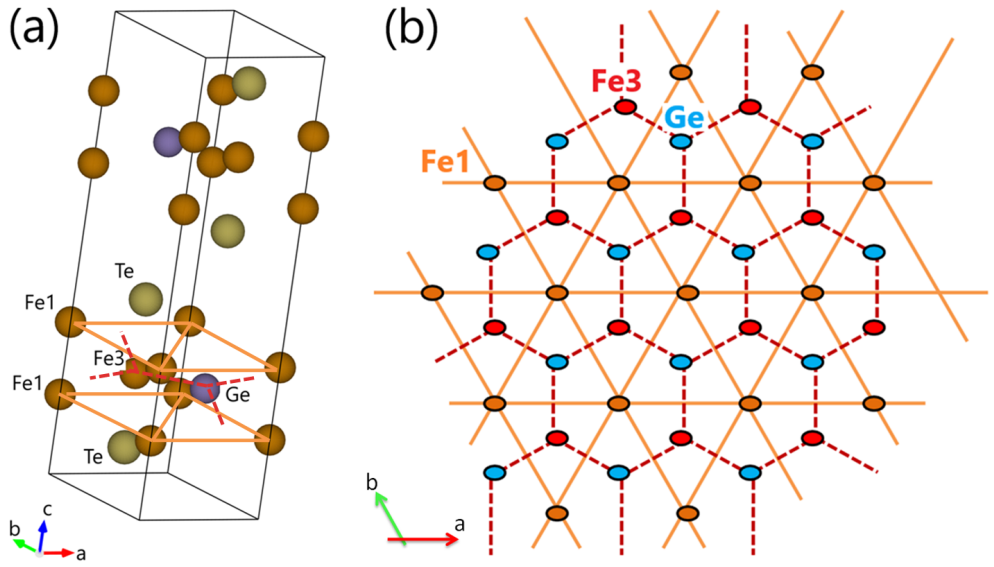

FIGURE 6.2: **(a)** Hexagonal crystal structure (space group $P63/mmc$) of bulk FGT where the different atomic species are recognised, and $Fe1$ and $Fe3 + Ge$ planes are marked. c axis directed along adjancent layers of FGT. **(b)** Perpendicular view of FGT, along the ab plane. $Fe1$ atoms form a triangular lattice which sandwiches the hexagonal lattice formed by $Fe3$ and Ge.

the other hand, ARPES and low-T specific heat measurements [213] signaled the presence of strong correlations, by measuring large mass enhancement factors.

So far, only calculations for bulk FGT have been performed [211–213]. These calculations show that the band structure around the Fermi level consists on several flat bands of mainly Fe d orbitals character. It urges to clarify the nature of this itinerant ferromagnetic phase, as well as its relation with the number of layers reduction, by studying the band structure of low dimensional FGT in the non-magnetic state. It is also interesting to study the possible similarities with other Fe-based materials, such as $FeSe$ [215] or $FeGe$ [216], and clarify the role of the Hund's coupling in FGT.

In this chapter, I calculate the band structure, DOS and Fermi surfaces for bulk and monolayer FGT, as well as the Wannier parametrization for monolayer FGT. I will also compare with experimental expectations. This chapter could serve as an initial step to study the origin of ferromagnetism and other electronic properties in FGT and related systems.

6.2 Results & Discussion

In this section, I will present the calculations that I have performed on bulk and monolayer FGT. I will calculate the band structure, DOS and Fermi surfaces for both situations, and the Wannier tight-binding model for monolayer FGT by using the DFT WIEN2K and WANNIER90 codes, as explained in **Appendix A**. In **Section 6.2.1**, I obtain the band structure for bulk and monolayer FGT, and the DOS and Fermi surface for monolayer FGT. In **Section 6.2.2**, I calculate a Wannier tight-binding model for the monolayer FGT.

6.2.1 Band structure, DOS and Fermi surfaces of Fe_3GeTe_2

In this section, I will show the DFT WIEN2K calculations for bulk and monolayer Fe_3GeTe_2. The calculations were run with a k-mesh of $28 \times 28 \times 2$ for bulk FGT and $23 \times 23 \times 1$ for monolayer FGT, where this notation refers to the grid in the $k_x \times k_y \times k_z$ directions of the Brillouin zone (BZ).

I calculate the total number of electrons per atom for the electronic shells in bulk and monolayer FGT for those shells which will mainly contribute to the band structure around the Fermi level, i.e. the valence electronic shells. In both cases, $Fe1$ and $Fe3$ atoms have a total number of electrons per atom in the d electronic shells of $n_e^{Fe1} \approx 6.07$ and $n_e^{Fe3} \approx 6.12$. Thus, FGT shows the same number of electrons per Fe atom as in the case of iron-based superconductors (FeSCs), see **Section 1.5.2**, which could be important when calculating the effects of the electronic correlations. In the remaining atoms, the p shells have a total number of electrons per atom of $n_e^{Ge} \approx 0.95$ and $n_e^{Te} \approx 1.99$.

In FIGURE 6.3, I show the band structure for both bulk and monolayer FGT.

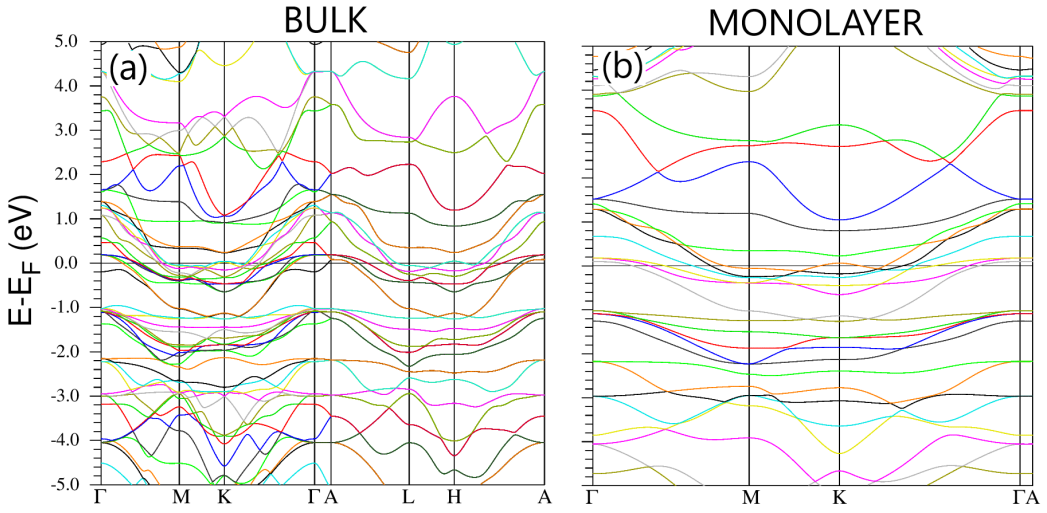

FIGURE 6.3: DFT band structure of **(a)** bulk and **(b)** monolayer FGT. Flat bands with a predominant $Fe1$ and $Fe3$ d orbitals character dominate the band structure around the Fermi level. In the case of bulk FGT, a doubling in the number of bands appears due to the folded BZ considered in the calculations. The principal directions Γ, M and K for $k_z = 0$ (while A, L and H for $k_z = \pi$) are defined in the hexagonal BZ.

As already mentioned, a set of weakly dispersive bands dominate the band structure around the Fermi level. The number of bands in bulk FGT for $k_z = 0$ is doubled with respect to monolayer FGT, due to the presence of two monolayers in the unit cell, see FIGURE 6.2**(a)**. Except for the doubling of bands, the band structure is very similar in both cases, with some differences, apart from the folded/unfolded character of the BZ for bulk/monolayer FGT. This result remarks the quasi-2D character that bulk FGT already has. 6 hole pockets can be seen surrounding Γ, and small electron pockets around K points. I plotted the Fermi surfaces for monolayer FGT (in bulk FGT, twice the Fermi surfaces appear) in FIGURE 6.4, where the mentioned hole and electron pockets can be seen.

The band structure extends between -6 and $4\,eV$. The bands around the Fermi level between -4 and $3\,eV$ have mostly $Fe1$ and $Fe3$ d orbitals character, as shown in the DOS plot of FIGURE 6.5, for both bulk and monolayer FGT. The bulk FGT DOS compares very well

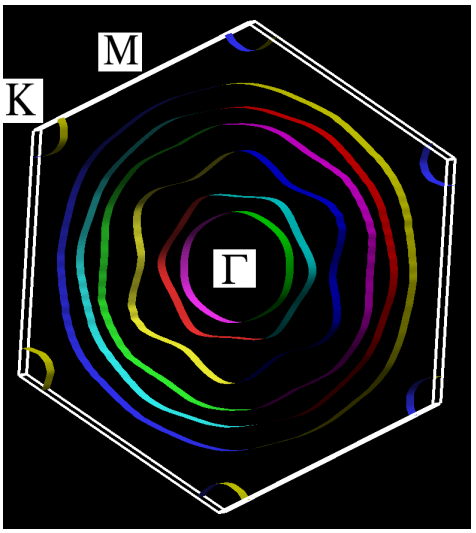

FIGURE 6.4: Fermi surfaces of monolayer FGT in the hexagonal BZ. 6 hole pockets surround the Γ point, with different shapes, while small electron pockets are located in the K points.

with previous calculations [211]. The most important feature in both bulk and monolayer FGT is the very large DOS at and close to the Fermi level. The bandwidth for $Fe1$ and $Fe3$ d orbitals is $W \sim 3 - 4\,eV$. $Fe1$ d orbitals mostly contribute to the flat bands around the Fermi level, while the major contribution from $Fe3$ d appears around -2 and $0\,eV$. An important contribution from Ge p orbitals appear around $2.5 - 3\,eV$, while Te p orbitals contribute around $-2.5\,eV$ and $-3\,eV$. In the case of monolayer FGT, two depletions can be seen around $-0.7\,eV$ and $-1.6\,eV$, whether in bulk FGT the first depletion appears, while the second one does not. In monolayer FGT, there is an splitting of the DOS around $1\,eV$.

For the chosen non-orthogonal orbital axis a and b, see FIGURE 6.2, d_{xz} and d_{yz} are equivalent, as well as a $d_{x^2-y^2}$ and d_{xy}[2]. This holds for both $Fe1$ and $Fe3$ atoms. In FIGURE 6.6, I plot the orbital resolved DOS for $Fe1$ and $Fe3$ d orbitals in the monolayer FGT. In the next section, I will calculate that, in order to obtain a Wannier tight-binding model for monolayer FGT, it is also necessary to include the p orbitals coming from Ge and Te, due to their sizable hybridization with Fe d orbitals, which results in a non-negligible contribution to the bands around $\pm 2.5\,eV$.

[2]Note that the orbitals in FGT are defined differently than in FeSCs. Here, the lobes of the d orbitals form $120\,^\circ$, while in FeSCs these lobes are orthogonal.

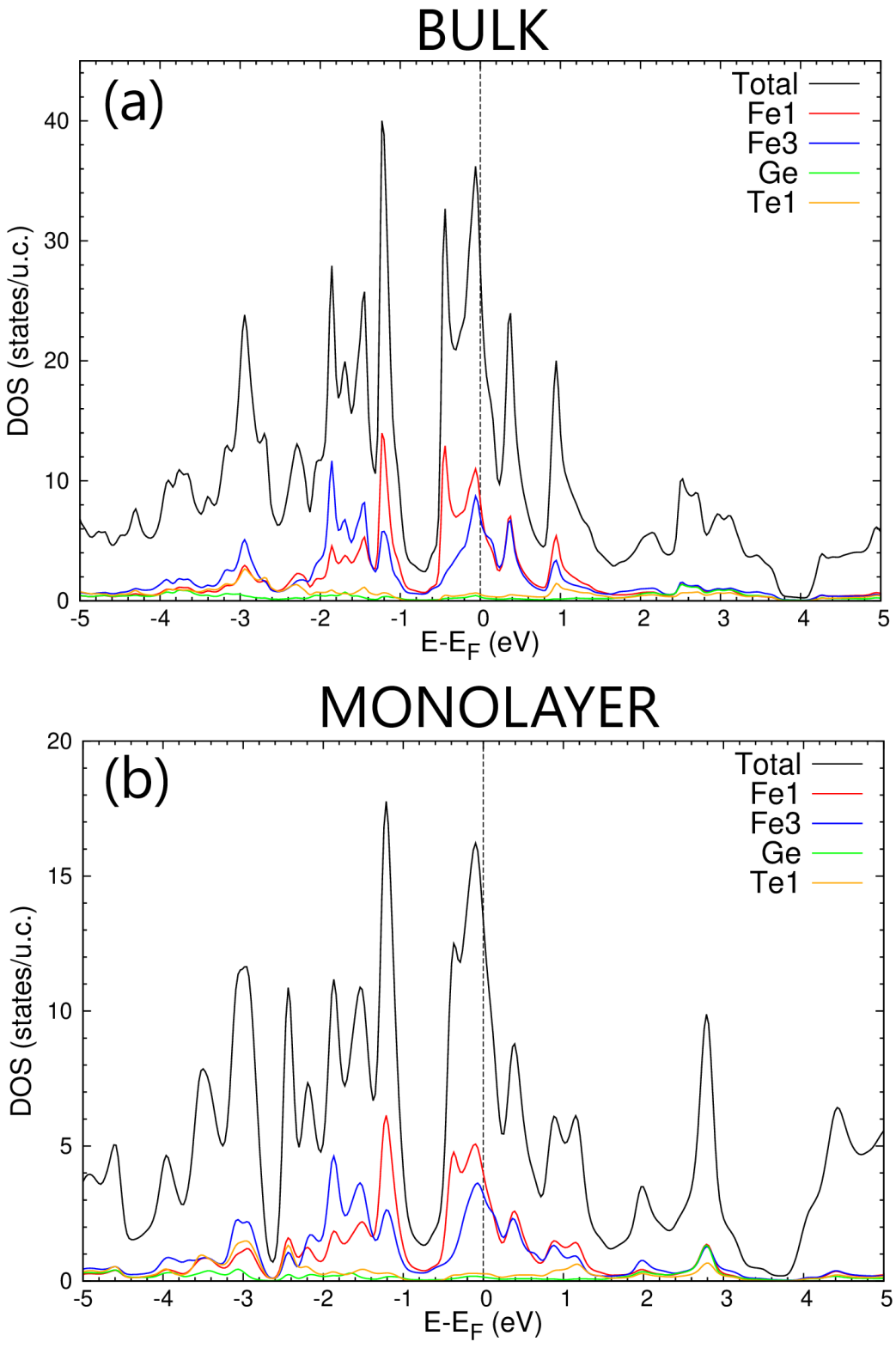

FIGURE 6.5: Total (black lines) and contributions from each atom (color lines) DOS for **(a)** bulk and **(b)** monolayer FGT. Note that I have not included the contribution from $Fe2$ and $Te2$ due to their degeneracy with $Fe1$ and $Te1$, respectively. $Fe1$ and $Fe3$ d orbitals contribute to the band structure around the Fermi level between -2 and $2\,eV$. $Fe1$ d orbitals mostly contribute to the flat bands around the Fermi level, while the major contribution from $Fe3$ d orbitals appear around -2 and $0\,eV$. Ge p orbitals mostly contribute around $2.5-3\,eV$. Te p orbitals mostly contribute around -2.5 and $-3\,eV$.

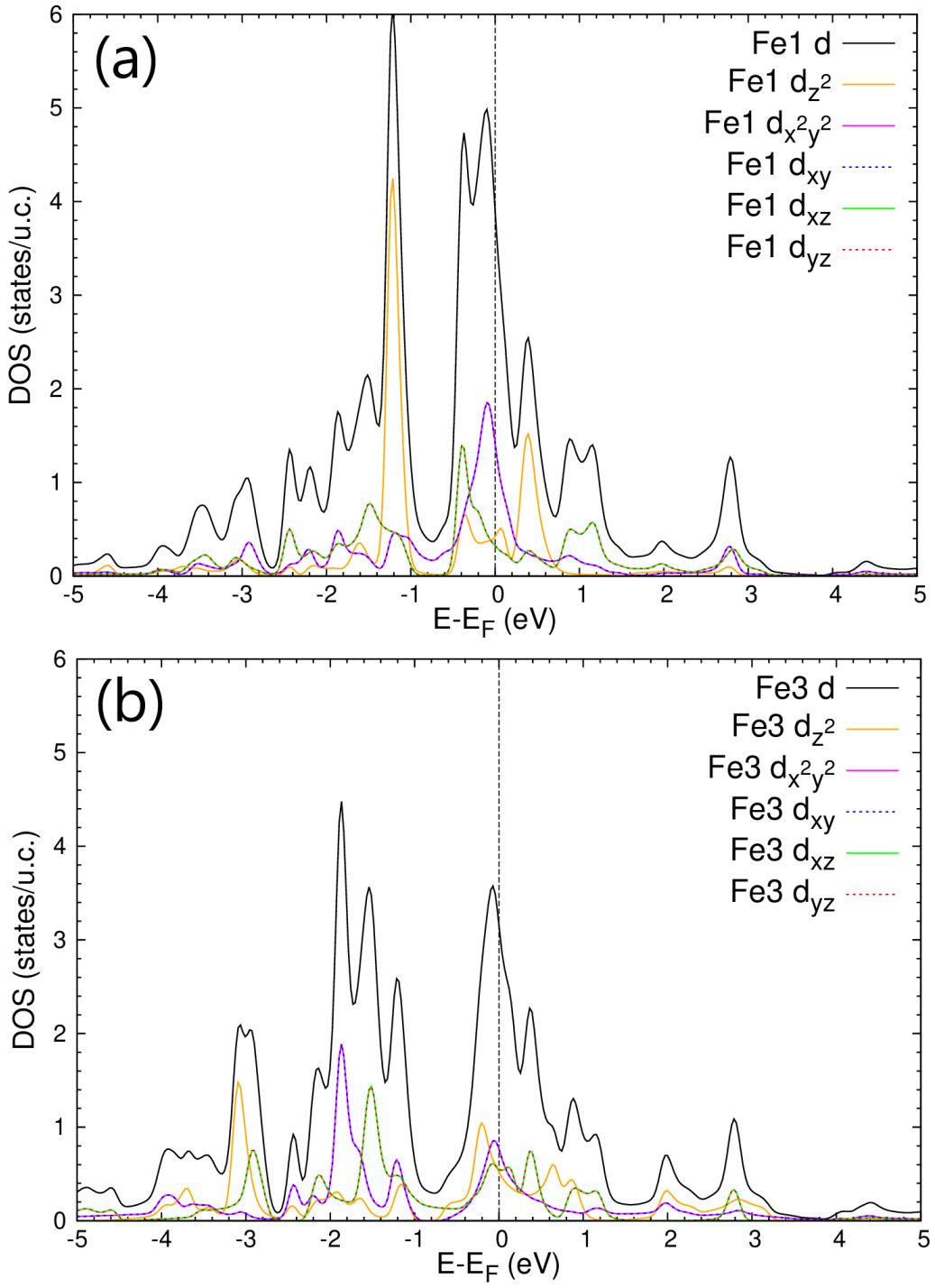

FIGURE 6.6: Orbital DOS for monolayer FGT for **(a)** $Fe1$ and **(b)** $Fe3$ d orbitals around the Fermi level. All the d orbitals contribute to the band structure around the Fermi level. d_{xy} (blue dashed line) and $d_{x^2-y^2}$ (magenta line) are degenerated, as well as d_{xz} (green line) and d_{yz} (red dashed line).

6.2.2 Wannier tight-binding model for monolayer Fe_3GeTe_2

In order to fit the previous band structure, a tight-binding model is proposed here considering the $Fe1$ d, $Fe3$ d, Ge p and Te p orbitals, as well as a minimal one using only $Fe1$ and $Fe3$ d orbitals. The Wannier fitting was done using the projector method explained in **Appendix A**, as implemented in the WANNIER90 code. The energy window to obtain the *ddpp* is selected between -6 and $4\,eV$, with a total of 24 bands being fitted. For the *dd* model, the energy window is between -3 and $1.5\,eV$.

Due to the entanglement present between the bands with mainly Fe d orbitals character and with Ge and Te p orbitals character, the tight-binding will include all of them. I will call this tight-binding the *ddpp* model. In FIGURE 6.7**(a)**, I show the band structure (red line) obtained by the Wannier tight-binding *ddpp* model as compared with the DFT band structure (purple crosses). The Wannier fitting shows a very good agreement with the DFT band structure. I tried to reduce the number of orbitals needed for the tight-binding model. In the case of a Wannier parametrization using only $Fe1$ and $Fe3$ d orbitals (called *dd* model), the fitting shows very large deviations from the original band structure, see FIGURE 6.7**(b)** for the comparison between both *dd* and *ddpp* model.

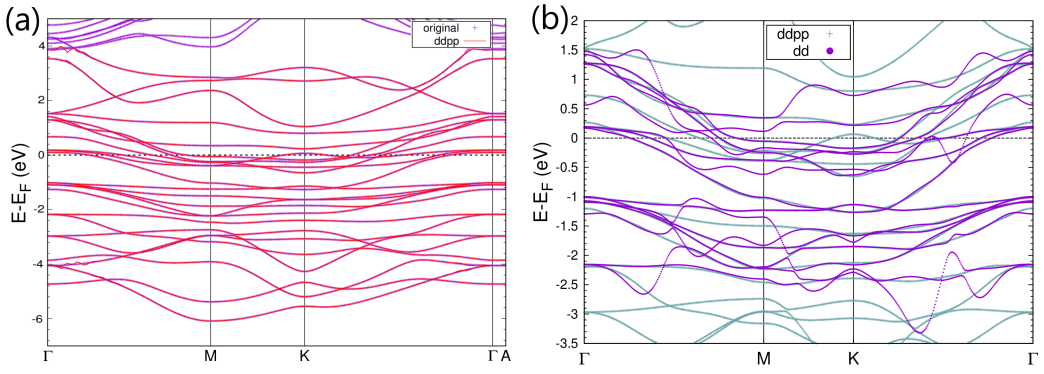

FIGURE 6.7: **(a)** DFT band structure (purple crosses) and *ddpp* model (red line) for monolayer FGT. The agreement between both cases is very good. **(b)** Wannier *ddpp* (green crosses) and *dd* (purple points) tight-binding model comparison. The *dd* model shows large deviations from the original band structure (here represented by the *ddpp* model), specially for the bands close to -2 and $1.5\,eV$. Calculations done using the projector method as explained in the WANNIER90 code, see **Appendix A**.

Due to the similar values of the bandwidth of the Fe d orbitals $\sim 3-4\,eV$ and the filling per Fe atom ($n_e^{Fe} \approx 6$) for FGT with respect to other FeSCs, we expect that Hund metal phenomenology might play a role in this system. It seems natural to think that Hund's coupling and atomic spin polarization could play a major role in the ferromagnetic phase of FGT. However, for FGT, the crystal symmetry and band structure differs from other quasi-2D FeSCs, see previous chapters. In FGT, the hybridization between Fe d and p orbitals is larger than in most of the FeSCs. The study of electronic correlations will be very complicated when using the *ddpp* model. A more appealing model will only include Ge p orbitals (due to the fact that the minimal *dd* model do not correctly reproduce the band structure), in what I will call the *ddp* model. Yet further work is needed along this path.

6.3 Summary

I conclude this chapter by making a summary of the obtained results:

- Very recently, the rare-earth free compound Fe_3GeTe_2 was exfoliated and became the first monolayer itinerant ferromagnet [207, 208]. When the number of layers is reduced, the critical temperature T_F evolves from $\sim 220\,K$ in the bulk FGT to $\sim 20\,K$ in monolayer FGT. T_F can be further tuned by effectively doping with electrons via an external voltage [207, 208]. In trilayer FGT, T_F rises up to room temperature ($\sim 300\,K$). The study of the band structure for FGT is an important first step to be done. I calculated here the band structure, DOS, Fermi surfaces and a minimal Wannier tight-binding model for the monolayer FGT by using DFT WIEN2K and WANNIER90 codes.

- In **Section 6.2.1**, I presented the DFT calculations on the band structure, DOS and Fermi surfaces for bulk and monolayer FGT. The number of electrons per Fe atom is the same as in the FeSCs ($n_e \approx 6$) studied in previous chapters. A set of flat bands dominate the band structure around the Fermi level with mainly $Fe1$ and $Fe3$ d orbitals character. The band structure of bulk and monolayer FGT is quite similar, signaling the quasi-2D character of bulk FGT. The bandwidth for $Fe1$ and $Fe3$ d orbitals is $W \sim 3 - 4\,eV$. $Fe1$ d orbitals mostly contribute to the flat bands around the Fermi level, while the major contribution from $Fe3$ d appears around -2 and $0\,eV$. An important contribution from Ge p orbitals appear around $2.5 - 3\,eV$, while Te p orbitals contribute around $-2.5\,eV$ and $-3\,eV$. An interesting difference between bulk and monolayer FGT is a splitting that emerges around $1\,eV$ in the DOS.

- In **Section 6.2.2**, I obtained the Wannier tight-binding model for monolayer FGT. I derived the *dd* (only $Fe1$ and $Fe3$ d orbitals included) and the *ddpp* model for monolayer FGT. Even though $Fe1$ and $Fe3$ d orbitals dominate the bands around the Fermi level, the entanglement with Ge and Te p orbitals is very important, hence the *dd* model shows large discrepancies with respect to the original DFT band structure. The *ddpp* model is fitted for an energy window between -6 and $4\,eV$, and it shows a good agreement with the DFT band structure.

This brief chapter was a summary of my recent work on FGT. Some calculations and analysis have to be performed yet, meanwhile I have shown here the actual status of this work.

Chapter 7

Conclusions

During this thesis, I have studied the effects of electronic correlations in various systems. I have focused on studying the local correlations effects in multiorbital systems, and the phenomenology that appears in such multiorbital systems in contrast with single-orbital systems when including the orbital degrees of freedom. I have studied these effects in real materials, specially in iron-based superconductors (FeSCs) and related materials, such as $LaCrAsO$, see **Chapter 3**, and $BaFe_2S_3$, see **Chapter 4**, and in 2D materials, specifically on magic-angle twisted bilayer graphene (MA-TBG), see **Chapter 5**. I have also obtained the DFT band structure and Wannier tight-binding model for the 2D material Fe_3GeTe_2 (FGT), see **Chapter 6**. Understanding the band structure serves as a first step to study the electronic correlations.

After reviewing some generic concepts of correlations in **Chapter 1**, in **Chapter 2** I have introduced the phenomenology of local correlations in multiorbital systems. In multiorbital systems, the ratio between the interaction energy cost Δ^x and the kinetic energy gain $\widetilde{W}$ depends on the number of orbitals per atom N, the number of electrons per atom n_e and the Hund's coupling J_H. The Mott insulator is not restricted to half-filled systems ($n_e = N$), but it can also happen at other integer fillings ($n_e = 1, 2, \ldots, N-1$). When J_H increases, the critical interaction for the Mott transition U_c decreases (increases) for half-filling $n_e = N$ (single-electron $n_e = 1$) systems. For $N > 2$, $1 < n_e < N$ and intermediate to large J_H, a correlated metallic state emerges, called the Hund metal. In the Hund metal regime, the strength of local correlations is large, the atoms are highly and locally spin polarized, and there is orbital decoupling. The Hund metal phenomenology is driven by the enhancement of local spin correlations, which occurs due to a decrease of anti-parallel spin configurations in each atom. Then, there is a atomic spin polarization promoted by J_H. The suppression of the anti-parallel spin configurations is related with the Mott insulator at half-filling, hence a link exists between the Mott insulator physics and the Hund metal physics, besides the difference of being in an insulating or metallic state. In the case of non-equivalent orbitals systems, J_H promotes orbital differentiation, hence an orbital selective Mott transition (OSMT) might occur. Various theoretical and experimental results for FeSCs (low-T specific heat, angle-resolved photoemission spectroscopy (ARPES) renormalized band structure, X-ray emission spectroscopy (XES) for the local moment, etc.) sustain the idea that these systems can be seen as being close to or in the Hund metal regime.

The main results of the thesis can be summarized as follows:

- In **Chapter 3** [96], we have proposed to search for a new family of high-T_c superconductors similar to the FeSCs, but based on chromium instead of iron. Our argument is based on the idea of having an optimal degree of electronic correlations, as it occurrs in most of the unconventional superconductors. We proposed that Cr pnictides and chalcogenides could host high-T_c superconductivity, similar to FeSCs. The main difference between Cr-based systems and FeSCs is the total number of electrons per atom, which is $n_e = 4$ for Cr-based materials and $n_e = 6$ for FeSCs. The strength of local correlations increases when approaching half-filling ($n_e = 5$) from $n_e = 6$ for FeSCs, then it has been argued that FeSCs can be seen as electron-doped Mott insulators, hence linking both high-T_c cuprates and FeSCs physics. I have shown that the similar trend is obtained when moving from the hole-doped Mott part $n_e = 4$ towards half-filling. We have chosen $LaCrAsO$ as an example to study the evolution of local correlations, and to study the magnetic and superconducting instabilities in a Fermi surface instability picture. I have shown that the strength of correlations in $LaCrAsO$ is similar to FeSCs when $n_e = 4.5$, hence we proposed to search for unconventional superconductivity in this region. My co-workers showed that the most plausible superconducting order parameter has a d-wave symmetry. In the band structure studied, d_{xy} is favored. Nevertheless, we have pointed out that the electron pockets responsible for the superconductivity are shallow, and the expectations may change if these shallow pockets are not present, to other symmetry, most probably $d_{x^2-y^2}$.

- In **Chapter 4** [97], I have studied the strength of correlations in the quasi-1D two-leg ladder FeSC, $BaFe_2S_3$. At ambient pressure, the undoped $BaFe_2S_3$ shows an insulating behavior which persists for $T > T_N$. Various authors have argued that these systems are Mott insulators. When considering only local correlations in multiorbital systems, in the Hund metal regime (in which $BaFe_2S_3$ seems to lie, see below), this statement does not seem very plausible, see FIGURE 2.12. The aim of this work was to clarify the nature of the insulating states in these materials. I have used the tight-binding model proposed by *Arita et al.* [98] for two pressures $0\,GPa$ and $12.4\,GPa$, which considers all the 5 Fe d orbitals on each of the 4 Fe atoms of the unit cell. In this model, the band structure of $BaFe_2S_3$ shows a 3D dispersion, even if the system is initially seen as a quasi-1D material. I have studied the strength of correlations for both pressures at $T = 0\,K$. I have obtained a metallic behavior for both pressures. We have argued that temperature T could reconcile the local correlations picture with the experimental behavior, due to the fact that T favors a more incoherent system, hence it promotes an insulating behavior. I have also shown that, at $12.4\,GPa$ (which is the pressure at which superconductivity emerges), the strength of correlations is similar to other FeSCs. I have obtained a remarkable reconstruction of the Fermi surface, which can modify the expectations from Fermi surface-based instability theories. We argued that due to this reconstruction, the intra-ladder AFM scattering vector is enhanced. At $0\,GPa$, the system shows an insulating behavior, and hence it does not have Fermi surface, so any Fermi surface-based instability picture is highly in doubt to be applicable. At $12.4\,GPa$, the Fermi surface modifications will be important when elucidating the Fermi surface instabilities, such as the superconductivity order parameter.

- In **Chapter 5** [99], I studied the nature of the insulating states found by Pablo Jarillo's group in MA-TBG [84, 85]. In MA-TBG, unexpected insulating states appear when the charge neutrality point (CNP) is doped with 2 electrons or 2 holes. Various authors have argued that these insulating behaviors are Mott insulating states, but the insulating

nature is still unknown. We assumed that MA-TBG can be describe by an effective model for the moiré superlattice, and that flat bands are responsible for its correlated behavior. We also assumed that the interactions are Hubbard-like, and studied three experimental features of these insulating states to check whether local correlations could explain their behavior: when increasing an external magnetic field or the temperature T, there is a transition to a metallic state, and the gap size ($\sim 0.3\,meV$) of these insulating states is two orders of magnitude smaller than the expected bandwidth ($W \sim 10\,meV$). I have shown that all these behaviors cannot be explained by considering only local correlations. We then considered the change in the phenomenology which appears in Mott states when non-local correlations are important. Based on the phenomenology driven by non-local correlations in related models, we argued that if these non-local correlations are included, the experimental observations could be reconciled with the expectations for Mott-like insulating states.

- In **Chapter 6**, I have presented a DFT calculation and the Wannier tight-binding model for the rare-earth free 2D material FGT. This system shows an itinerant ferromagnetic (FM) phase which persists down to the monolayer FGT. The critical temperature T_F can be tuned by effective electron doping via an external voltage. Trilayer FGT shows room temperature itinerant ferromagnetism at an density electron doping of $\sim 10^{14}\,cm^{-2}$. Due to the itinerant character of the FM phase, a peak in the density of states (DOS) could explain the origin of this phase (following a Stoner criteria). On the other hand, ARPES and low-T specific heat measurements pointed to the existance of strong correlations. Similarities between FGT and FeSCs (like the total filling per Fe atom, or the bandwidth of the Fe d orbitals) suggest that the Hund's coupling could be playing a role in the ferromagnetic phase of FGT. As a fisrt step to study the electronic correlations, I calculated via DFT Wien2k and Wannier90 codes the band structure, DOS and Fermi surfaces for bulk and monolayer FGT, as well as the tight-binding model for monolayer FGT. I showed that the most important feature of the DOS for bulk and monolayer FGT is the very large peaks at and around the Fermi level. I also showed that the contribution from Ge and Te p orbitals is not negligible. I calculated the so called *ddpp* model, as well as a minimal version including only Fe d orbitals, the so called *dd* model. However, the *dd* model shows large discrepancies with respect to the original band structure. Yet, further work is needed to elucidate the origin of this ferromagnetic phase and the role of electronic correlations in few layers FGT.

I expect that the local correlations in multiorbital systems phenomenology explained in this thesis may serve as a background for future theoretical calculations and the interpretation of experimental results in real materials. I believe that having an optimal degree of electronic correlations is an important ingredient to find new unconventional superconductors, and hence understanding the phenomenology of such electronic correlations is essential to understand the unconventional superconductivity.

Chapter 8

Conclusiones

A lo largo de esta tesis, he estudiado los efectos de las correlaciones electrónicas en varios sistemas. Me he centrado en estudiar los efectos de las correlaciones locales en sistemas multi-orbitales, y en la fenomenología que aparecer en dichos sistemas multi-orbitales en comparación con sistemas de un solo orbital cuando se incluyen los grados de libertad orbitales. He estudiado estos efectos en materiales reales, especialmente en superconductores basados en hierro (FeSCs) y materiales relacionados, tales como $LaCrAsO$, ver **Capítulo 3**, y $BaFe_2S_3$, ver **Capítulo 4**, y en materiales 2D, específicamente en el grafeno bicapa rotado en ángulo mágico (MA-TBG), ver **Capítulo 5**. También he obtenido la estructura de bandas DFT y el modelo de enlaces-fuertes Wannier para el material 2D Fe_3GeTe_2 (FGT), ver **Capítulo 6**. Entender la estructura de bandas sirve como primer paso para estudiar las correlaciones electrónicas.

Después de revisar algunos conceptos genéricos de las correlaciones en el **Capítulo 1**, en el **Capítulo 2** he introducido la fenomenología de las correlaciones locales en sistemas multi-orbitales. En los sistemas multi-orbitales, el ratio entre el coste de energía de interacción Δ^x y la ganancia de energía cinética $\widetilde{W}$ depende del número de orbitales por átomo N, el número de electrones por átomo n_e y el acoplo Hund J_H. El aislante de Mott no está restringido a sistemas a llenado mitad ($n_e = N$), si no que también puede aparecer a otros llenados enteros ($n_e = 1, 2, \ldots, N-1$). Cuando J_H aumenta, la interacción crítica para la transición de Mott U_c disminuye (aumenta) para sistemas a llenado mitad $n_e = N$ (a llenado de un solo electrón $n_e = 1$). Para $N > 2$, $1 < n_e < N$ y valores intermedios y largos de J_H, un estado metálico correlacionado surge, llamado metal de Hund. En el régimen del metal de Hund, la fuerza de las correlaciones locales es grande, los átomos están localmente en un estado de espín grande, y hay un desacople orbital. La fenomenología del metal de Hund es manejada por el aumento de las correlaciones de espín locales, que ocurre debido a la disminución de las configuraciones de espín anti-paralelas en cada átomo. Por tanto, hay una polarización atómica de espín promovida por J_H. La supresión de las configuraciones de espín anti-paralelas está relacionada con el aislante de Mott a llenado mitad, por lo tanto, esto marca un enlace entre la física del aislante de Mott y la del metal de Hund, a pesar de la diferencia de ser un estado aislante o metálico. En el caso de sistemas de orbitales no equivalentes, J_H promueve la diferenciación orbital, por lo que una transición de Mott selectiva en orbitales puede ocurrir. Varios resultados teóricos y experimentales para los FeSCs (calor específico a baja T, espectroscopía de fotoemisión resuelta en ángulo (ARPES) para la estructura de bandas renormalizada, espectroscopía de emisión de rayos X (XES) para el momento local,

etc.) sostienen la idea de que estos sistemas pueden verse como estando cerca o en el régimen del metal de Hund.

Los principales resultados de esta tesis pueden resumirse como sigue:

- En el **Capítulo 3** [96], hemos propuesto buscar una nueva familia de superconductores de alta T_c similar a los FeSCs pero basados en cromo en vez de en hierro. Nuestro argumento está basado en la idea de necesitar un grado óptimo de correlaciones electrónicas, tal y como ocurre en la mayorá de superconductores no-convencionales. Hemos propuesto que los pnicturos y calcogenuros de Cr podrían alojar superconductividad de alta T_c, similar a los FeSCs. La diferencia más importante entre los sistemas basados en Cr y los FeSCs es el número total de electrones por átomo, el cual es $n_e = 4$ en los materiales basados en Cr y $n_e = 6$ en los FeSCs. La fuerza de las correlaciones locales aumenta cuando nos acercamos al llenado mitad ($n_e = 5$) desde $n_e = 6$ para los FeSCs, por lo que se argumentó que los FeSCs pueden verse como aislantes de Mott dopados con electrones, así enlazando la física de los cupratos de alta T_c y de los FeSCs. He demostrado que una tendencia similar se obtiene cuando nos movemos desde el aislante de Mott dopado con huecos $n_e = 4$ hacia llenado mitad. Hemos elegido $LaCrAsO$ como ejemplo para estudiar la evolución de las correlaciones locales, y para estudiar las inestabilidades magnéticas y superconductoras en una descripción basada en inestabilidades de la superficie de Fermi. He demostrado que la fuerza de las correlaciones en $LaCrAsO$ es similar a los FeSCs cuando $n_e = 4.5$, por lo que hemos propuesto buscar superconductividad no-convencional en esta región. Mis colaboradores demostraron que el parámetro de orden superconductor más probable tiene simetría de onda d. Para la estructura de bandas estudiada, d_{xy} se favorece. No obstante, hemos señalado que los *pockets* de electrones responsables de la superconductividad son poco profundos, y las expectativas pueden cambiar si estos *pockets* de electrones no están presentes, dando lugar a otra simetría, la más probable $d_{x^2-y^2}$.

- En el **Capítulo 4** [97], he estudiado la fuerza de las correlaciones electrónicas en el FeSCs quasi-1D en escalera de dos patas, $BaFe_2S_4$. A presión ambiente, el $BaFe_2S_3$ no dopado muestra un comportamiento aislante, el cual persiste para $T > T_N$. Varios autores han argumentado que estos sistemas son aislantes de Mott. Cuando se consideran únicamente las correlaciones locales en sistemas multi-orbitales, en el régimen de Hund (en el cual $BaFe_2S_3$ parece estar situado, ver más abajo), esta afirmación no parece muy acertada, ver FIGURA 2.12. El objetivo de este trabajo fue clarificar la naturaleza de los estados aislantes en estos materiales. He usado el modelo de enlaces-fuertes propuesto por *Arita et al.* [98] para dos presiones $0\,GPa$ y $12.4\,GPa$, el cual considera los 5 orbitales d del Fe en cada uno de los 4 átomos de Fe de la celda unidad. En este modelo, la estructura de bandas del $BaFe_2S_3$ muestra una dispersión 3D, incluso aunque el sistema fuera inicialmente visto como un material quasi-1D. He estudiado la fuerza de las correlaciones para ambas presiones a $T = 0\,K$. He obtenido un comportamiento metálico para ambas presiones. Hemos argumentado que el efecto de la temperatura T podría reconciliar las expectativas de las correlaciones locales con el comportamiento experimental, debido al hecho de que T favorece un sistema más incoherente, por lo que promueve el comportamiento aislante. También he mostrado que, a $12.4\,GPa$ (que es la presión a la que la superconductividad surge), la fuerza de las correlaciones es similar a otros FeSCs. He obtenido una reconstrucción notable de la superficie de Fermi, lo cual puede cambiar las expectativas de teorías basadas en inestabilidades de la superficie de Fermi. Hemos argumentado que debido a esta

reconstrucción, el vector de dispersión AFM entre escaleras se ve aumentado. A $0\,GPa$, el sistema muestra un estado aislante, por lo que no tiene superficie de Fermi, así que cualquier descripción basada en inestabilidades de la superficie de Fermi está altamente en duda de ser aplicable. A $12.4\,GPa$, las modificaciones en la superficie de Fermi serán importante a la hora de estudiar las inestabilidades de la superficie de Fermi, tales como el parámetro de orden superconductor.

- En el **Capítulo 5** [99], he estudiado la naturaleza de los estados aislantes encontrados en el MA-TBG por el grupo de Pablo Jarillo [84, 85]. En el MA-TBG, unos estados aislantes inesperados aparecen cuando el punto de carga neutral (CNP) es dopado con 2 electrones o 2 huecos. Varios autores argumentaron que estos comportamientos aislantes corresponden a estados aislantes de Mott, pero la naturaleza de dichos estados es todavía desconocida. Hemos asumido que el MA-TBG puede describirse con un modelo efectivo para la superred de moiré, y que las bandas planas son responsables de su comportamiento correlacionado. También, hemos asumido que las interacciones son de tipo Hubbard, y hemos estudiado tres resultados experimentales de estos estados aislantes para comprobar si las correlaciones locales podrían explicarlos: cuando un campo magnético externo o la temperatura T aumentan, hay una transición a un estado metálico, y el tamaño del gap ($\sim 0.3\,meV$) de estos estados aislantes es dos órdenes de magnitud más pequeño que la anchura de banda esperada ($W \sim 10\,meV$). He demostrado que todos estos comportamientos no pueden explicarse considerando únicamente las correlaciones locales. Consideramos más tarde el cambio en la fenomenología que aparece en los estados de Mott cuando las correlaciones no-locales son importantes. Basados en la fenomenología debida a las correlaciones no-locales en modelos relacionados, hemos argumentado que si estas correlaciones no-locales son incluidas, las observaciones experimentales podrían reconciliarse con las expectativas para los estados aislantes de tipo Mott.

- En el **Capítulo 6**, he presentado los cálculos DFT y el modelo de enlaces-fuertes Wannier para el material 2D libre de tierras raras FGT. Este sistema muestra una fase ferromagnética (FM) itinerante que persiste hasta el sistema monocapa FGT. La temperatura crítica T_F puede modificarse por el dopaje efectivo de electrones via un voltaje externo. La tricapa FGT muestra ferromagnetismo itinerante a temperatura ambiente a un dopaje de densidad de electrones de $\sim 10^{14}\,cm^{-2}$. Debido al carácter itinerante de la fase FM, los picos en la densidad de estados (DOS) podrían explicar el origen de esta fase (siguiendo el criterio de Stoner). Por otro lado, medidas ARPES y de calor específico a baja T señalan la existencia de correlaciones fuertes. Similitudes entre FGT y los FeSCs (como el llenado total por átomo de Fe, o la anchura de banda de los orbitales d del Fe) sugieren que el acoplo Hund podría estar jugando un papel en la fase ferromagnética del FGT. Como un primer paso para estudiar las correlaciones electrónicas, he calculado via los códigos de DFT Wien2k y Wannier90, la estructura de bandas, DOS y las superficies de Fermi del material en volumen y monocapa FGT, así como el modelo de enlaces-fuertes para la monocapa FGT. He mostrado que la propiedad más importante en el material en volumen y monocapa FGT es la aparición de grandes picos en la DOS alrededor del nivel de Fermi. También he mostrado que la contribución de los orbitales p del Ge y Te no son despreciables. He calculado el modelo *ddpp*, así como una versión más sencilla incluyendo solo los orbitales d del Fe, el modelo *dd*. Sin embargo, el modelo *dd* muestra grandes discrepancias con respecto a la estructura de bandas original. No obstante, se necesita más trabajo para elucidar el origen de la fase ferromagnética y el papel de las correlaciones electrónicas en pocas capas de FGT.

Espero que la fenomenología sobre las correlaciones locales en sistemas multi-orbitales explicada en esta tesis pueda servir como antecedente para futuros estudios teóricos y la interpretación de resultados experimentales en materiales reales. Creo que tener un grado óptimo de correlaciones electrónicas es un ingrediente importante para encontrar nuevos superconductores no-convencionales, por lo que entender la fenomenología de dichas correlaciones electrónicas es esencial para entender la superconductividad no-convencional.

Appendices

Appendix A

Density Functional Theory and Wannier parametrization

In this appendix, I will briefly present the Density Functional Theory (DFT) for band structure calculations, following the overview given in [11, 13], and the Wannier parametrization in order to calculate the hopping integrals t^{ij}_{mn} and crystal field splittings ϵ_m for any given material, by following the manual of WANNIER90 code [217].

DFT and Wannier parametrization calculations were used through all this thesis. Personally, I used them in **Chapter 6** when calculating the DFT band structure and the Wannier tight-binding model for Fe_3GeTe_2 (FGT).

A.1 DFT framework

DFT was originally developed by Hohenberg, Kohn and Sham in 1964 and 1965 [218, 219]. This theory has become very useful in these days to calculate the electronic properties of solids, like band structure, band-gaps, optical responses, etc. It is based on two main theorems called the Hohenberg-Kohn theorems [218], which state:

1. The ground state properties of a system of particles are uniquely determined by the electronic density $\rho(\vec{r})$. This means that the energy is a functional of the electronic density $E[\rho(\vec{r})]$.
2. The correct ground state electronic density minimizes the energy functional, so the ground state energy is $E_0 = E[\rho_0(\vec{r})] \leq E[\rho(\vec{r})]$

Then, DFT uses the electronic density instead of the wavefunctions to determine the ground state properties. In this situation, the original Schrödinger problem of Eq. (1.1) for solving N differential equations greatly reduces to solve the equation for the electronic density in terms of $\vec{r}$. Due to the fact that DFT calculates the ground state properties, it tends to have problems with excitation properties, such as the band gap of semiconductors.

In the Born-Oppenheimer approximation (where ions will sit motionless in each lattice site because they are more massive than electrons, $M \ll m$), the equation to be solved for $E[\rho(\vec{r})]$ is given by Eq. (A.1).

$$E[\rho] = T[\rho] + V[\rho] + U[\rho] \tag{A.1}$$

where $V[\rho]$ is a material-dependent (and known) quantity. In this equation, T refers to the kinetic energy of electrons, V to the potential created by the ions in which the electrons are moving and U to the electron-electron interaction (see also Eq. (1.2)). $U[\rho]$ can be written as a Hartree potential $U_H[\rho]$ plus an exchange-like interaction term $E_X[\rho]$:

$$U[\rho] \approx \underbrace{\frac{1}{2}\int \frac{\rho(\vec{r})\rho(\vec{r}')}{|\vec{r}-\vec{r}'|} d^3\vec{r} d^3\vec{r}'}_{U_H[\rho]} + E_X[\rho] \tag{A.2}$$

A.1.1 Kohn-Sham equations

The form of $T[\rho]$ will depend on further approximations. In most DFT approximations, the single-particle states approximation is used, $\rho(\vec{r}) = \sum_{i=1}^{N} f_i |\psi_i(\vec{r})|^2$ where f_i is the occupation number, $\psi_i(\vec{r})$ are the so called Kohn-Sham orbitals and N is the number of these Kohn-Sham orbitals. Thus, $T[\rho] \approx T_{hom}[\rho] + E_C[\rho]$, where $T_{hom}[\rho]$ is the kinetic energy of the non-correlated homogeneous electron gas (a well-known quantity) and $E_C[\rho]$ is the kinetic correlation energy left out when ρ is approximated by an expression in terms of single-particle states [220, 221].

After these considerations, Eq. (A.1) can be rewritten as:

$$E[\rho(\vec{r})] = T_{hom}[\rho(\vec{r})] + \int v_{ext}(\vec{r})\rho(\vec{r}) d^3\vec{r} + \frac{1}{2}\int \frac{\rho(\vec{r})\rho(\vec{r}')}{|\vec{r}-\vec{r}'|} d^3\vec{r} d^3\vec{r}' + E_{XC}[\rho(\vec{r})] \tag{A.3}$$

with $E_{XC}[\rho] = E_X[\rho] + E_C[\rho]$. The form of $E_{XC}[\rho]$ is given by the different approximations used, as in local density approximation (LDA), generalized gradient approximation (GGA), etc. The exchange-correlation potential is $V_{XC}(\vec{r}) = \delta E_{XC}[\rho(\vec{r})]/\delta\rho(\vec{r})$. In LDA V_{XC} is approximated as a local potential. It only depends on the electronic density, which is a constant function of $\vec{r}$, hence $V_{XC}^{LDA}(\rho)$. In GGA [222], V_{XC} further depends on the first derivative of ρ with respect to $\vec{r}$, hence $V_{XC}^{LDA}(\rho, \nabla\rho)$.

With the aid of the Kohn-Sham orbitals, the Kohn-Sham equation can be derived:

$$\left[-\frac{1}{2}\nabla^2 + v_{ext} + U_H + V_{XC}\right]\psi_i = \varepsilon_i \psi_i \tag{A.4}$$

Note that this equation is not equivalent to the original many-body hamiltonian of Eq. (1.2). Only in the ideal case that V_{XC} is exactly treated (which is not solvable), the full correlations and interactions effects will be included. In the most widely used approximations, LDA and GGA, these correlations and interactions are almost neglected, and further models are needed to solve the problem.

A.1.2 Obtaining the band structure using DFT

In order to obtain the band structure of a given material, Kohn-Sham orbitals have to be expanded in a suitable basis of functions $\{\phi_{k\nu}\}$, then $\psi_i = \sum_\nu c^i_{k\nu}\phi_{k\nu}$. There are different approximations to calculate this basis, like using augmented plane waves (APW) or linearized augmented plane waves (LAPW). The difference between APW and LAPW lies in the expansion used to write $\phi_{k\nu}$. In the case of LAPW, both the energy dependence of the radial part and its derivative are considered, while for APW only the energy dependence for the radial part is considered (see below). These approximations exploit the fact that close to the atomic nuclei, the ionic potential in a solid is similar to the one of an isolated atom, whether far from the nuclei, the potential varies weakly and electrons move freely. This is the so called muffin-tin spheres (MTS) approximation. Inside an sphere around the atom, the electron has atomic-like functions (radial and spherical harmonics functions), whereas in the interstitial region is described by free plane waves-like functions.

These basis are useful for valence states, while core and semi-core states are not so well treated. This problem can be improved by using the LAPW,LO basis. In this basis, band energies $\varepsilon_{k\nu}$ and Bloch states $\phi_{k\nu}(\vec{r})$ are calculated using Eq. (A.5) (note that $\vec{r}$ is defined inside the MTS).

$$\phi^{LAPW,LO}_{lm\,\alpha}(\vec{r}) = \left[A^{\alpha,\,LO}_{l\,m} u^\alpha_l(r, E^\alpha_{1,l}) + B^{\alpha,\,LO}_{l\,m} \dot{u}^\alpha_l(r, E^\alpha_{1,l}) + C^{\alpha,\,LO}_{l\,m} u^\alpha_l(r, E^\alpha_{2,l})\right] Y^m_l(\theta, \varphi) \quad \text{(A.5)}$$

where α is the atom index, l and m are the angular quantum numbers associated with the angular solution $Y^m_l(\theta, \varphi)$ of Eq. (A.4), A, B and C are expansion coefficients to be determined self-consisenly, u^α_l is the radial part solution of each atom and its derivative $\dot{u}^\alpha_l$ with respect to the atomic energy $E^\alpha_{1,l}$. Outside the MTS, $\phi_{lm\,\alpha}$ can be written as free plane waves.

Different codes are available to be used for the calculation of the band structure by means of DFT. In this thesis, I will use the Wien2k codes results.

A.2 Wannier parametrization

The Wannier parametrization is a method in which the hopping integrals t^{ij}_{mn} (as well as crystal field energies ϵ_m) are calculated by fitting a set of specific orbitals to the band structure around the Fermi level. This method is based on the idea that the orbitals which mostly contribute to form the bands around the Fermi level are those which control the physics in the system.

Wannier functions [223] $w^\alpha_m(\vec{r} - \vec{R})$ are localized functions centered at lattice sites $\vec{R}$ can be obtained from Fourier transforming the Bloch states $\phi_{k\nu}(\vec{r})$ (i.e. free plane waves):

$$w^\alpha_m(\vec{r} - \vec{R}) = \sum_k e^{-i\vec{k}\cdot\vec{R}} \sum_{\nu \in W} P^\alpha_{km\nu}\phi_{k\nu}(\vec{r}) \quad \text{(A.6)}$$

where m is the orbital index, ν is the band index and $\nu \in W$ refers to the energy window W taken to fit the band structure to a set of Wannier orbitals. $P^{\alpha}_{km\nu}$ are the projector matrices, which can be obtained from the coefficients A, B and C.

In order to calculate t^{ij}_{mn}, let's consider the DFT hamiltonian H_0 given in Eq. (A.4). This hamiltonian follows the Schrödinger equation $H_0\phi_{k\nu} = E_{k\nu}\phi_{k\nu}$, where $E_{k\nu}$ are the band energies. Then, in the basis of Bloch states $\{\phi_{k\nu}\}$, H_0 is diagonal:

$$\phi^{\dagger}_{k\nu}(\vec{r})H_0\phi_{k\nu}(\vec{r}) = E_{k\nu}\mathbb{I} \tag{A.7}$$

where $\mathbb{I}$ is the identity matrix.

In the Wannier orbital basis $\{w^{\alpha}_{m}(\vec{r})\}$, H_0 is not diagonal and its elements are given by t^{ij}_{mn}, or by the dispersion relations ε_{kmn} if the hoppings are Fourier transformed (FT) into the k-space. In the k-space:

$$w^{\alpha}_{km}(\vec{r}) = \sum_{\nu \in W} P^{\alpha}_{km\nu}\phi_{k\nu}(\vec{r}) \tag{A.8}$$

Then, in the Wannier orbitals basis:

$$w^{\alpha\,\dagger}_{km}(\vec{r})H_0 w^{\alpha}_{km}(\vec{r}) = P^{\alpha\,\dagger}_{km\nu}\left(E_{k\nu}\mathbb{I}\right)P^{\alpha}_{km\nu} \tag{A.9}$$

So that, the hopping integrals t^{ij}_{mn} and crystal field splitting ϵ_m can be numerically obtained as (assuming that Wannier functions are centered at $\vec{R} = \vec{0}$):

$$\begin{cases} t^{ij}_{mn} = \sum\limits_{k} < w_{km}(\vec{i})|H_0|w_{kn}(\vec{j}) > e^{-i\vec{k}\cdot\vec{ij}} \\ \epsilon_m = \sum\limits_{k} < w_{km}(\vec{i})|H_0|w_{km}(\vec{i}) > \end{cases} \tag{A.10}$$

The most widely used code to calculate t^{ij}_{mn} is Wannier90 [217]. Both the projection method explained above and the so called maximally localized Wannier functions (MLWFs) procedure are implemented in this code. MLWFs follows the same scheme as the projection method, but it includes the maximal localization of the Wannier functions $w_{km}(\vec{r})$ [224], hence reducing the spatial spread of the Wannier orbitals in order to ensure the real space localization of these Wannier orbitals.

Appendix B

Slave-Spin Mean Field formalism

In this appendix, an extense discussion about slave-spin mean-field (SSMF) formalisms (both Z_2 and $U(1)$) can be found. I will use the articles where both formalisms were presented [25, 38, 47], as well as my personal notes and mathematical proofs. A comparison between Z_2 and $U(1)$ formulations is also presented. The solving procedure for a SSMF calculation is explained at the end of this appendix.

B.1 SSMF background

SSMF formalism is a framework well suited up to study the effect of local correlations in a multiorbital system via a self-consistent calculation of the quasiparticle weights $Z_{m\sigma}$ for different m orbitals (with $m = 1, 2...N$) and σ spin (with $\sigma = +, -$ or $\sigma = \uparrow, \downarrow$). In the so called single-site approximation, SSMF is constrained to onsite correlations. Usually, the local paramagnetic (PM) solution is obtained, hence Z_m will be spin indepentent. The exception can be seen in **Chapter 5**, where I implemented the calculation of $Z_{m\sigma}$ for the Zeeman effect, in which spin degeneracy is broken by an onsite shift which depends on the Zeeman magnetic field.

SSMF techniques follow the Brinkman-Rice picture for the Mott transition [4, 5, 8], in which Z_m is traced down from $Z_m = 1$ in the non-correlated metal to 0 in the Mott insulator when varying U. Thus, SSMF is expected to slightly understimate the effect of local correlations. For a multiorbital problem, SSMF permits a calculation of Z_m in terms of U, J_H, the number of electrons per atom n_e and the number of orbitals per atom N. Once Mott insulator is reached with all $Z_m = 0$, SSMF cannot provide further information about the system.

Compared with other slave-particle theories, the slave-spin mean field (SSMF) (both in Z_2 and $U(1)$ formulations) allows to treat multiorbital systems in an economical way, using $2N$ *pseudospin*-1/2 variables, while slave-boson technique [45] normally increases its number of variables in an exponential way with N. SSMF formalisms allow a treatment of non-equivalent orbitals system, while slave-rotor technique [46] cannot account for it. Compared with other more sofisticated numerical techniques (such as DMFT [17]), SSMF formalisms are faster and easier to implement, and the results are quite good when comparing with such techniques and with experimental results (see discussion and comparison in **Chapter 2**).

Eq. (1.22) will be the initial hamiltonian to work with. For simplicity, interactions are assumed to be orbital-independent, rotational invariant relations $U' = U - 2J_H$ and $J' = J_H$ are used and H_{add} is neglected. H_{add} is difficult to treat in SSMF, due to the fact that it mixes pseudospin-1/2 and auxiliary fermion operators; in [38], the authors tried to include H_{add} by introducing some operators which actually mix the physical states with the unphysical ones (see text). Later on, the authors realized that such an approximation was not giving good results [225]. Nevertheless, the physics discussed in this thesis is mainly contained in H_{dens}. Thus, we will study the so called Ising hamiltonian $H = H_0 + H_{dens}$, where H_0 describes the tight-binding model and H_{dens} the density-density interaction terms.

SSMF formalisms are, considering the change of representation (Z_2 or $U(1)$), a change of basis from the initial Hilbert space defined by the occupation numbers of the electrons $\mathcal{H}_e \equiv \{|n^d = 0>, |n^d = 1>\}$, with $n^d = d^\dagger d$ (dropping subindices for simplicity) to another expanded Hilbert space in which the occupation number operator n^d is identified by a pseudospin-1/2 operator S^z. This trick is made in order to obtain the pre-factors of the dispersion relations ε_{kmn} which will precisely be the quasiparticle weights Z_m.

Auxiliary fermion operators n^f have to be defined in order to fulfill the anti-commutation rules, so that the new Hilbert space is defined by $\mathcal{H}_{SSMF} \equiv \{|n^f, S^z>\}$. By performing this change of basis, a constraint has to be imposed in order to project out the unphysical states obtained by this basis change, as described in Eq. (B.1).

$$\begin{aligned} physical \rightarrow & \begin{cases} |n^d = 0> = |n^f = 0, S^z = -1/2> \\ |n^d = 1> = |n^f = 1, S^z = +1/2> \end{cases} \\ unphysical \rightarrow & \begin{cases} |\varnothing> = |n^f = 1, S^z = -1/2> \\ |\varnothing> = |n^f = 0, S^z = +1/2> \end{cases} \end{aligned} \tag{B.1}$$

In SSMF, the pseudospin operators carry the charge of the real electrons, while the auxiliary fermions carry the spin. Thus, the metallic phase corresponds to the ordered pseudospins, i.e. with a finite $< O > \neq 0$ value, where O is a pseudospin operator. The constraint has the form:

$$\hat{n}^d = d^\dagger d \equiv \hat{n}^f = f^\dagger f = S^z + \frac{1}{2} \tag{B.2}$$

Generalizing to site i, orbital m and spin σ indices:

$$\hat{n}^d_{im\sigma} = d^\dagger_{im\sigma} d_{im\sigma} \equiv \hat{n}^f_{im\sigma} = f^\dagger_{im\sigma} f_{im\sigma} = S^z_{im\sigma} + \frac{1}{2} \tag{B.3}$$

This constraint is taken into account in $H = H_0 + H_{dens}$ by introducing a set of parameters, the time-dependent Lagrange multipliers $\lambda_{im\sigma}(\tau)$ in the following way:

$$H = H_0 + H_{dens} + \sum_{im\sigma} \lambda_{im\sigma}(\tau) \left(S^z_{im\sigma} + \frac{1}{2} - \hat{n}^f_{im\sigma} \right) \tag{B.4}$$

A set of $2N$ pseudospin-1/2 and auxiliary fermion operators is being introduced in each lattice site i. If the constraint is fully treated as in Eq. (B.4), the solution would be exact.

However, a full treatment is not solvable, and static Lagrange multipliers $\lambda_{im\sigma}$ are imposed by time-averaging the constraint:

$$\lambda_{im\sigma} =< \lambda_{im\sigma}(\tau) >_{time} \tag{B.5}$$

In order to express the non-interacting and the interacting parts of the hamiltonian of Eq. (B.4), an appropriate representation of the operators $d_{im\sigma}$ and $d^{\dagger}_{im\sigma}$ in this new Hilbert space $\mathcal{H}_{SSMF}$ has to be choosen. An initial try could be introducing the pseudospin operators $S^{\pm}$:

$$\begin{cases} d = fS^{-} \\ d^{\dagger} = f^{\dagger}S^{+} \end{cases} \tag{B.6}$$

However, applying further mean-field approximations will end on a $Z \neq 1$ at the non-correlated limit ($U = J_H = 0$), which is an unphysical solution.

I will explain now the Z_2 [38, 47] and the $U(1)$ [25] SSMF formulations, which are able to propose an appropiate representation of $d^{\dagger}_{im\sigma}$ and $d_{im\sigma}$ in the new Hilbert space $\mathcal{H}_{SSMF}$ in order to outcome the $Z \neq 1$ at $U = J_H = 0$ problem.

B.2 SSMF Z_2 formulation

Following the ideas of [38, 47], the change for the electron operators can be chosen to be:

$$\begin{cases} d = fO \\ d^{\dagger} = f^{\dagger}O^{\dagger} \end{cases} \quad where \quad O = \begin{pmatrix} 0 & c \\ 1 & 0 \end{pmatrix} \tag{B.7}$$

where O is a pseudospin operator[1] and c is an arbitrary complex number. Note that $dim\ O_{m\sigma} = 2^{2N}$.

The choice of $c_{im\sigma}$ is a gauge freedom of the Z_2 formalism. It states that different pseudospin operators act in the same way in the physical states but differently in the unphysical ones; if the constraint is treated exactly, the difference of the $c_{im\sigma}$ actuation doesn't affect the problem. Like the full treatment of the constraint is not possible, so the problem has to be approximated by being solved with an appropriate $c_{im\sigma}$.

In the single-site approximation, $c_{m\sigma}$ are real numbers. To recover the non-correlated limit $U = J_H = 0$:

$$c_{m\sigma} = \frac{1}{\sqrt{n_{m\sigma}(1 - n_{m\sigma})}} - 1 \tag{B.8}$$

where $n_{m\sigma}$ is the filling per atom, spin σ and orbital m ($n_{m\sigma} \in [0, 1]$ with $n_{m\sigma} = 0.5$ defined as half-filling). The derivation of this formula can be seen in **Appendix C**.

[1] O is the generalization of the operator $2S^{x}$, which at the beginning of the technique development was constrained to be used only for half-filling systems [38].

Now, H_0 and H_{dens} (see Eq. (B.4)) have to be written in the new Hilbert space $\mathcal{H}_{SSMF}$. H_{dens} is written in terms of pseudospin operators only. Then (note that $H_{dens} = H^{PS}_{dens} - K_{PS}$):

$$H^{PS}_{dens} = \frac{U-U'}{2}\sum_{im}\left(\sum_{\sigma}\tilde{S}^z_{im\sigma}\right)^2 + \frac{U'}{2}\left(\sum_{im\sigma}\tilde{S}^z_{im\sigma}\right)^2 - \frac{J_H}{2}\sum_{i\sigma}\left(\sum_{m}\tilde{S}^z_{im\sigma}\right)^2 \tag{B.9}$$

where the constant K_{PS} is a term which does not affect the mean-field calculations (note that $\widehat{n}_{im\sigma} \equiv S^z_{im\sigma} + \frac{1}{2} = \tilde{S}^z_{im\sigma}$):

$$K_{PS} = \frac{U-J_H}{2}\sum_{im\sigma}\tilde{S}^{z\,2}_{im\sigma} \tag{B.10}$$

To obtain Eq. (B.9), the following expressions have to be considered:

$$\begin{cases} \left(\sum_{m\sigma} S^z_{im\sigma}\right)^2 = \underbrace{\sum_{m\sigma} S^{z\,2}_{im\sigma}}_{constant} + 2\sum_{m} S^z_{im\uparrow}S^z_{im\downarrow} + 2\sum_{\substack{\sigma \\ m<m'}} S^z_{im\sigma}S^z_{im'\bar{\sigma}} + 2\sum_{\substack{\sigma \\ m<m'}} S^z_{im\sigma}S^z_{im'\sigma} \\ \sum_{m}\left(\sum_{\sigma} S^z_{im\sigma}\right)^2 = \underbrace{\sum_{m\sigma} S^{z\,2}_{im\sigma}}_{constant} + 2\sum_{m} S^z_{im\uparrow}S^z_{im\downarrow} \\ \sum_{\sigma}\left(\sum_{m} S^z_{im\sigma}\right)^2 = \underbrace{\sum_{m\sigma} S^{z\,2}_{im\sigma}}_{constant} + 2\sum_{\substack{\sigma \\ m<m'}} S^z_{im\sigma}S^z_{im'\sigma} \end{cases} \tag{B.11}$$

On the other hand, H_0 can be written as:

$$H_0 = \sum_{i\neq j\, mm'\sigma}\left(t^{ij}_{mm'} f^\dagger_{im\sigma} O^\dagger_{im\sigma} f_{jm'\sigma} O_{jm'\sigma} + h.c.\right) + \sum_{im\sigma}\left(\epsilon_m - \mu\right) f^\dagger_{im\sigma} f_{im\sigma} \tag{B.12}$$

In a first mean-field approximation, it is assumed that the auxiliary fermions, which carry the spin, and the pseudospins, which carry the charge, are uncorrelated. Taking into account that $O^\dagger_{im\sigma}$ and $f_{jm'\sigma}$ commute, the tight-binding term can be written as:

$$\begin{aligned} f^\dagger_{im\sigma} f_{jm'\sigma} O^\dagger_{im\sigma} O_{jm'\sigma} \approx & f^\dagger_{im\sigma} f_{jm'\sigma} < O^\dagger_{im\sigma} O_{jm'\sigma} > + O^\dagger_{im\sigma} O_{jm'\sigma} < f^\dagger_{im\sigma} f_{jm'\sigma} > \\ & - < f^\dagger_{im\sigma} f_{jm'\sigma} >< O^\dagger_{im\sigma} O_{jm'\sigma} > \end{aligned} \tag{B.13}$$

Now, a second mean-field approximation will be applied. It assumes that operators in different sites are uncorrelated. This second mean-field gives rise to the single-site approximation. Then, for $i \neq j$:

$$O^\dagger_{im\sigma} O_{jm'\sigma} \approx O^\dagger_{im\sigma} < O_{jm'\sigma} > + O_{jm'\sigma} < O^\dagger_{im\sigma} > - < O^\dagger_{im\sigma} >< O_{jm'\sigma} > \tag{B.14}$$

Using this last expression, it can be shown that the expected value $< O^{\dagger}_{im\sigma} O_{jm'\sigma} >$ factorizes in another quantity $< O_{im\sigma} >< O_{jm'\sigma} >$. In the single-site approximation, the site indices i and j can be dropped out from the pseudospin operators. Then, as shown in **Appendix C**, the quasiparticle weight $Z_{m\sigma}$ is given by:

$$\begin{aligned} Z_{m\sigma} &=< O^{\dagger}_{m\sigma} O_{m\sigma} > \\ &=< O_{m\sigma} >^2 \end{aligned} \tag{B.15}$$

Then, the first mean-field approximation of Eq. (B.13) can be rewritten as:

$$\begin{aligned} f^{\dagger}_{im\sigma} f_{jm'\sigma} O^{\dagger}_{m\sigma} O_{m'\sigma} \approx & \sqrt{Z_{m\sigma}}\sqrt{Z_{m'\sigma}} f^{\dagger}_{im\sigma} f_{jm'\sigma} + < f^{\dagger}_{im\sigma} f_{jm'\sigma} > \left(\sqrt{Z_{m'\sigma}} O^{\dagger}_{m\sigma} + \sqrt{Z_{m\sigma}} O_{m'\sigma} \right) \\ & - \sqrt{Z_{m\sigma}}\sqrt{Z_{m'\sigma}} < f^{\dagger}_{im\sigma} f_{jm'\sigma} > \end{aligned} \tag{B.16}$$

where the last term is a constant which does not affect the mean-field calculations. H_0 can be written as (note that $t^{ij}_{mm'} \equiv t^{ij}_{m'm}$):

$$\begin{aligned} H_0 = & \sum_{ijmm'\sigma} \sqrt{Z_{m\sigma}}\sqrt{Z_{m'\sigma}}\, t^{ij}_{mm'} \left(f^{\dagger}_{im\sigma} f_{jm'\sigma} + h.c. \right) + \sum_{im\sigma} \left(\epsilon_m - \mu \right) f^{\dagger}_{im\sigma} f_{im\sigma} \\ & + \sum_{ijmm'\sigma} t^{ij}_{mm'} \sqrt{Z_{m'\sigma}} \left[O^{\dagger}_{m\sigma} \left(< f^{\dagger}_{im\sigma} f_{jm'\sigma} > + < f^{\dagger}_{jm'\sigma} f_{im\sigma} > \right) + h.c. \right] - K_f \end{aligned} \tag{B.17}$$

where:

$$K_f = \sum_{ijmm'\sigma} t^{ij}_{mm'} \sqrt{Z_{m\sigma}}\sqrt{Z_{m'\sigma}} \left(< f^{\dagger}_{im\sigma} f_{jm'\sigma} > + < f^{\dagger}_{jm'\sigma} f_{im\sigma} > \right) \tag{B.18}$$

Finally, using the Fourier transformation (FT) of the auxiliary fermion operators:

$$f^{\dagger}_{im\sigma} = \sum_{k} e^{-i\vec{k}\vec{i}} f^{\dagger}_{km\sigma} \tag{B.19}$$

And the dispersion relations $\varepsilon_{kmm'}$ are defined as in Eq. (1.5):

$$\sum_{ijmm'\sigma} t^{ij}_{mm'} \left(f^{\dagger}_{im\sigma} f_{jm'\sigma} + h.c. \right) = \sum_{kmm'\sigma} \varepsilon_{kmm'} f^{\dagger}_{km\sigma} f_{km'\sigma} \tag{B.20}$$

The non-correlated hamiltonian H_0 can be written as the sum of 2 terms H^0_{PS} and H_f:

$$\begin{aligned} H_0 = & \underbrace{\sum_{kmm'\sigma} \sqrt{Z_{m\sigma}}\sqrt{Z_{m'\sigma}} \varepsilon_{kmm'} f^{\dagger}_{km\sigma} f_{km'\sigma} + \sum_{km\sigma} \left(\epsilon_m - \mu \right) f^{\dagger}_{km\sigma} f_{km\sigma}}_{H_f} \\ & + \underbrace{\sum_{m\sigma} h_{m\sigma} \left(O^{\dagger}_{m\sigma} + h.c. \right)}_{H^0_{PS}} - K_f \end{aligned} \tag{B.21}$$

where the effective Weiss fields $h_{m\sigma}$ are defined as (note also that $h^{\dagger}_{m\sigma} = h_{m\sigma}$ in the single-site approximation):

$$h_{m\sigma} = \sum_{m'} \sqrt{Z_{m'\sigma}} \sum_{k} \varepsilon_{kmm'} < f^{\dagger}_{km\sigma} f_{km'\sigma} > \tag{B.22}$$

The initial hamiltonian H in the new basis $\mathcal{H}_{SSMF}$ is rewritten as a sum of 2 coupled (via the Lagrange multipliers $\lambda_{m\sigma}$) terms $H = H_f + H_{PS}$, where:

$$\begin{cases} H_f = \sum\limits_{kmm'\sigma} \sqrt{Z_{m\sigma}}\sqrt{Z_{m'\sigma}}\varepsilon_{kmm'} f^{\dagger}_{km\sigma} f_{km'\sigma} + \sum\limits_{km\sigma} \left(\epsilon_m - \mu - \lambda_{m\sigma} + \lambda^0_{m\sigma}\right) f^{\dagger}_{km\sigma} f_{km\sigma} - K_f \\ H_{PS} = \sum\limits_{m\sigma} h_{m\sigma} \left(O^{\dagger}_{m\sigma} + h.c.\right) + \sum\limits_{m\sigma} \lambda_{m\sigma} \left(S^z_{m\sigma} + \dfrac{1}{2}\right) + H^{PS}_{dens} - K_{PS} \end{cases} \tag{B.23}$$

Then, these two hamiltonians Eq. (B.23) have to be solved self-consistenly, taking into account the definitions Eq. (B.15) and Eq. (B.22) and the condition given by averaging the constraint in the single-site approximation:

$$n_{m\sigma} =< S^z_{m\sigma} > + \frac{1}{2} \tag{B.24}$$

In Eq. (B.23), I have added by hand the onsite energies $\lambda^0_{m\sigma}$. In order to recover the tight-binding solution (i.e., when $U = J_H = 0$, all $Z_{m\sigma} = 1$), the noon-zero Lagrange multipliers $\lambda_{m\sigma}$ that are going to appear when the system is out of half-filling have to be removed. The expression for these corrections $\lambda^0_{m\sigma}$ is found to be equal to the non-zero $\lambda_{m\sigma}$ that will appear at $U = J_H = 0$, see **Appendix C**:

$$\lambda^0_{m\sigma} = -2 \frac{n^0_{m\sigma} - 1/2}{n^0_{m\sigma}(1 - n^0_{m\sigma})} h^0_{m\sigma} \tag{B.25}$$

where $n^0_{m\sigma}$ and $h^0_{m\sigma}$ are the non-interacting values of the orbital fillings $n_{m\sigma}$ and the Weiss fields $h_{m\sigma}$.

B.3 SSMF $U(1)$ formulation

Another approach to SSMF is the $U(1)$ formalism, as derived in [25]. The new pseudospin operators $o_{im\sigma}$ (different from the pseudospin operators $O_{im\sigma}$ defined previously) are defined as dressed operators:

$$\begin{cases} d_{im\sigma} = f_{im\sigma} o_{im\sigma} \\ d^{\dagger}_{im\sigma} = f^{\dagger}_{im\sigma} o^{\dagger}_{im\sigma} \end{cases} \quad where \quad o_{im\sigma} = P^{+}_{im\sigma} S^{+}_{im\sigma} P^{-}_{im\sigma} \tag{B.26}$$

$$o^{\dagger}_{im\sigma} = P^{+}_{im\sigma} S^{+}_{im\sigma} P^{-}_{im\sigma} \tag{B.27}$$

where:

$$P^{\pm}_{im\sigma} = \frac{1}{\sqrt{1/2 \pm S^z_{im\sigma}}} \tag{B.28}$$

These operators $o_{im\sigma}$ will play the same role as $O_{im\sigma}$ in the SSMF Z_2 formulation. The same Eq. (B.23)-Eq. (B.24) are obtained by substituting $O_{m\sigma}$ by $o_{m\sigma}$ (note that I have not added any correction $\lambda^0_{m\sigma}$ at this point):

$$\begin{cases} H_f = \sum_{kmm'\sigma} \sqrt{Z_{m\sigma}}\sqrt{Z_{m'\sigma}}\varepsilon_{kmm'} f^{\dagger}_{km\sigma} f_{km'\sigma} + \sum_{km\sigma} \left(\epsilon_m - \mu - \lambda_{m\sigma}\right) f^{\dagger}_{km\sigma} f_{km\sigma} - K_f \\ H_{PS} = \sum_{m\sigma} h_{m\sigma} \left(o^{\dagger}_{m\sigma} + h.c.\right) + \sum_{m\sigma} \lambda_{m\sigma} \left(S^z_{m\sigma} + \frac{1}{2}\right) + H^{PS}_{dens} - K_{PS} \end{cases} \tag{B.29}$$

where:

$$\begin{cases} Z_{m\sigma} = < o_{m\sigma} >^2 \\ h_{m\sigma} = \sum_{m'} < o_{m'\sigma} > \sum_k \varepsilon_{kmm'} < f^{\dagger}_{km\sigma} f_{km'\sigma} > \end{cases} \tag{B.30}$$

Now, as an additional step, a Taylor expansion of o and $o^{\dagger}$ around $\hat{A} - < \hat{A} >$ (where $\hat{A} = S^z, S^+$) can be done, keeping up the linear terms of $\hat{A} - < \hat{A} >$ (see **Appendix C**). This is possible if the system is not close to the fully-filled or fully-emptied situations:

$$o^{\dagger}_{m\sigma} \approx O^{\dagger}_{m\sigma} + < O^{\dagger}_{m\sigma} > \eta_{m\sigma} \left[2S^z_{m\sigma} - \left(2n^f_{m\sigma} - 1\right)\right] \tag{B.31}$$

where (note that $< o_{m\sigma} > = < O_{m\sigma} >$):

$$\begin{cases} O^{\dagger}_{m\sigma} = < P^+_{m\sigma} > S^+_{m\sigma} < P^-_{m\sigma} > \\ \eta_{m\sigma} = \frac{1}{2} \frac{n_{m\sigma} - 1/2}{n_{m\sigma}\left(1 - n_{m\sigma}\right)} \end{cases} \tag{B.32}$$

The operators $O_{m\sigma}$ are named so due to the similarities (see below) with the Z_2 pseudospin operators. This is a remarkable result: the expression for the pseudospin operators $O_{m\sigma}$ in terms of the so called gauge $c_{m\sigma}$ has been recovered:

$$< P^+_{m\sigma} >< P^-_{m\sigma} > = \frac{1}{\sqrt{\left(< S^z_{m\sigma} > + 1/2\right)\left(- < S^z_{m\sigma} > + 1/2\right)}} \tag{B.33}$$

So that, $c_{m\sigma}$ are obtained as:

$$\rightarrow < P^+_{m\sigma} >< P^-_{m\sigma} > = \frac{1}{\sqrt{n_{m\sigma}\left(1 - n_{m\sigma}\right)}} = 1 + c_{m\sigma} \tag{B.34}$$

By doing this Taylor expansion, an expression which resembles the Eq. (B.23) in the SSMF Z_2 formalism is obtained:

$$\begin{cases} H_f = \sum_{kmm'\sigma} \sqrt{Z_{m\sigma}}\sqrt{Z_{m'\sigma}}\varepsilon_{kmm'} f^\dagger_{km\sigma} f_{km'\sigma} + \sum_{km\sigma} \left(\epsilon_m - \mu - \lambda_{m\sigma} + \lambda^0_{m\sigma}\right) f^\dagger_{km\sigma} f_{km\sigma} - K_f \\ H_{PS} = \sum_{m\sigma} h_{m\sigma} \left(O^\dagger_{m\sigma} + h.c.\right) + \sum_{m\sigma} \lambda_{m\sigma} \left(S^z_{m\sigma} + \frac{1}{2}\right) + H^{PS}_{dens} - K_{PS} \end{cases} \tag{B.35}$$

with:

$$\begin{cases} K_f = \sum_{m\sigma} \sqrt{Z_{m\sigma}} h_{m\sigma} \\ K_{PS} = \frac{U - J_H}{2} \sum_{m\sigma} \tilde{S}^{z\ 2}_{m\sigma} + \sum_{m\sigma} \lambda^0_{m\sigma} n_{m\sigma} \end{cases} \tag{B.36}$$

Interestingly, the expression of the correction $\lambda^0_{m\sigma}$ is similar to the Z_2 representation, except for the $\sqrt{Z_{m\sigma}}$ pre-factor which appears in the $U(1)$ formalism:

$$\lambda^0_{m\sigma} = -2\sqrt{Z_{m\sigma}} \frac{n_{m\sigma} - 1/2}{n_{m\sigma}(1 - n_{m\sigma})} h_{m\sigma} \tag{B.37}$$

In this case, $\lambda^{0\ 2}_{m\sigma}$ depends on the interaction via $Z_{m\sigma}$, $n_{m\sigma}$ and $h_{m\sigma}$, opposite to what happens in the SSMF Z_2 formalism.

B.4 Comparison between SSMF Z_2 and $U(1)$ formalisms

As it can be seen when comparing Eq. (B.23) with Eq. (B.35), and Eq. (B.25) with Eq. (B.37), both representations looks really similar.

In fact, in the single-site approximation, both formulations give the same expression for the Weiss term in H_{PS}, $O^\dagger_{m\sigma} + O_{m\sigma}$. Also, both formulations give the same results for equivalent orbitals systems, due to the equivalent parameters Z, λ and λ^0 which vary during the whole process. The gauge parameters $\tilde{c}_{m\sigma} = 1 + c_{m\sigma}$ appear in both formulations inside the pseudospin operators $O_{m\sigma}$. Z_2 gauges are obtained by calculating it in the non-interacting limit $U = J_H = 0$, while for $U(1)$ is obtained for all U values. If $\tilde{c}_{m\sigma}$ are fixed to the value at $U = 0$ in the Z_2 formulation, the system goes to the unphysical $Z > 1$ situation with $U > 0$ (see **Section C.1**). This can be overcomed by varying $\tilde{c}_{m\sigma}$ with U, J_H, FIGURE B.1**(b)**.

The corrections $\lambda^0_{m\sigma}$ are different in both techniques, although the final expressions looks similar. $\lambda^0_{m\sigma}$ arise from a Taylor expansion (far from the cases around full-filled and full-emptied fillings) in the $U(1)$ formalism, while they have to be included by hand in the Z_2 formalism. Also, the pre-factor $Z_{m\sigma}$ and the interaction-dependent Eq. (B.37) for $U(1)$ formalism makes the corrections being renormalized during the whole proccess of varying U

[2] Note that the superindex 0 here is maintained to make a connection with Z_2 SSMF formalism, and not to a fixed $U = 0$ value.

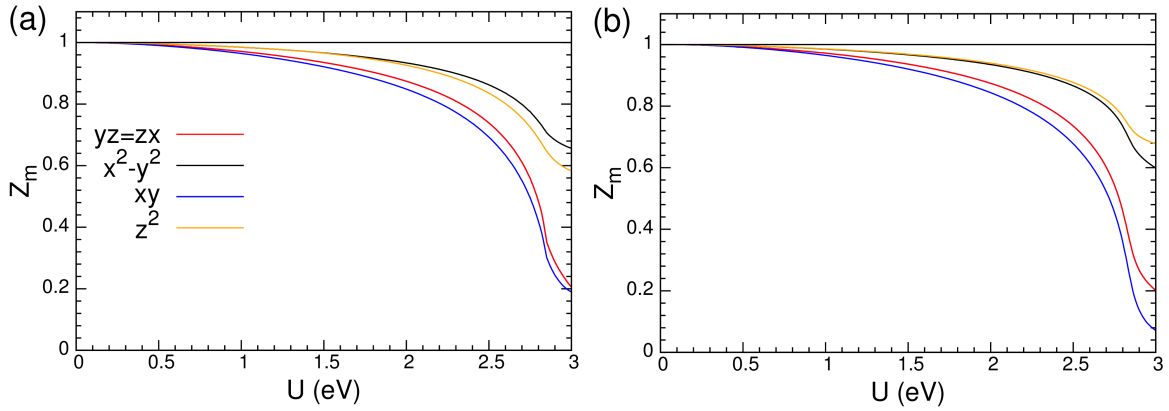

FIGURE B.1: Z_m in terms of U for $J_H = 0.25U$ for the *Graser et al.* [73] 5 d orbitals tight-binding model for $LaFeAsO$, where the filling per atom is $n_e = 6$. **(a)** $U(1)$ formulation calculation and **(b)** Z_2 formulation calculation with $\tilde{c}_m$ varying with U following Eq. (B.8).

and J_H, while the values of Eq. (B.25) have not this pre-factor and they are fixed at the non-interacting value $U = J_H = 0$.

The summary of these conclusions can be seen in the TABLE B.1. In FIGURE B.1, a comparison between different cases can be seen for a 5 d orbitals tight-binding proposed by *Graser et al.* [73] for undoped ($n_e = 6$) $LaFeAsO$ at a fixed $J_H/U = 0.25$. In this case, both formalisms give similar results, except for the order of Z_{z^2} and $Z_{x^2-y^2}$ at $U > 0$. Compared with DMFT results in the same tight-binding model [29], the SSMF $U(1)$ formalism compares better than the SSMF Z_2 one.

Z_2 formalism	$U(1)$ formalism
$O_{m\sigma} = S^-_{m\sigma} + c_{m\sigma} S^+_{m\sigma}$ $O^\dagger_{m\sigma} = c_{m\sigma} S^-_{m\sigma} + S^+_{m\sigma}$	$O_{m\sigma} =< P^+_{m\sigma} > S^-_{m\sigma} < P^-_{m\sigma} >$ $O^\dagger_{m\sigma} =< P^+_{m\sigma} > S^+_{m\sigma} < P^-_{m\sigma} >$
$\tilde{c}_{m\sigma} = 1 + c_{m\sigma} = \frac{1}{\sqrt{n_{m\sigma}(1-n_{m\sigma})}}$	$\tilde{c}_{m\sigma} =< P^+_{m\sigma} >< P^-_{m\sigma} >= \frac{1}{\sqrt{n_{m\sigma}(1-n_{m\sigma})}}$
$\lambda^0_{m\sigma} = -2\lvert h_{m\sigma}\rvert (n_{m\sigma} - \frac{1}{2})\tilde{c}_{m\sigma}$	$\lambda^0_{m\sigma} = -2Z_{m\sigma}\lvert h_{m\sigma}\rvert (n_{m\sigma} - \frac{1}{2})\tilde{c}_{m\sigma}$

TABLE B.1: Comparison between various quantities in the Z_2 and $U(1)$ formulations.

B.5 How to solve the SSMF formalism

In this section, I will briefly explain how to solve both SSMF Z_2 and $U(1)$ formalisms.

The two hamiltonians H_f and H_{PS} (see previous sections) have to be solved self-consistenly by fulfilling the constraint (see Eq. (B.24)), and by self-consistenly calculating the parameters $Z_{m\sigma}$, $\lambda_{m\sigma}$ and, in the case of the $U(1)$ formalism, also $\lambda^0_{m\sigma}$ (see Eq. (B.15), (B.25) or Eq. (B.37)). The SSMF loop procedure can be seen in FIGURE B.2.

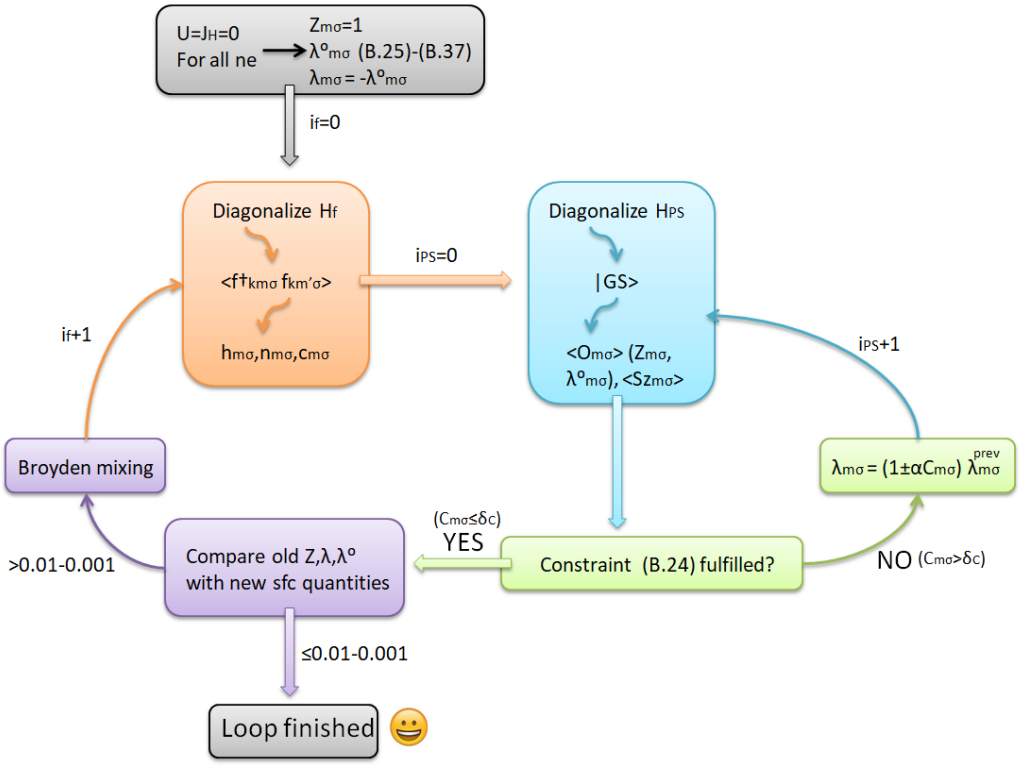

FIGURE B.2: Sketch of the SSMF loop for $U(1)$ formalism (Z_2 formalism is solved by not updating $\lambda^0_{m\sigma}$ in the loop). $C_{m\sigma} = n_{m\sigma} - (< S^z_{m\sigma} > +1/2)$ has to go to 0 in order to fulfill the constraint. δ_C is a dynamical convergence criteria which goes from 10^{-3} down to 10^{-6} according to $\delta_C^{i_f+1} = \delta_C^{i_f}/(i_f+1)$. Apart from the convergence of $Z_{m\sigma}$, $\lambda_{m\sigma}$ and $\lambda^0_{m\sigma}$, the constraint has to be also fulfilled below 10^{-6} at the end of the SSMF loop. See details in main text.

The initial step is done for $U = J_H = 0$, where all $Z_{m\sigma} = 1$, and $\lambda_{m\sigma}$, $c_{m\sigma}$ and $\lambda^0_{m\sigma}$ can be calculated, see previous equations. $\lambda_{m\sigma}$ are set to be the same as $\lambda^0_{m\sigma}$ (Eq. (B.25) or Eq. (B.37)) but with opposite sign. Then, we can proceed with the following steps:

- In the first iteration, $Z_{m\sigma}$, $\lambda_{m\sigma}$ and $\lambda^0_{m\sigma}$ are considered as those obtained for the previous iteration step. When initializing new values of (U, J_H, n_e), the initial $Z_{m\sigma}$, $\lambda_{m\sigma}$ and $\lambda^0_{m\sigma}$ are set to those of the previous (U, J_H, n_e).
- H_f is diagonalized. The orbital fillings per spin $n_{m\sigma}$ and Weiss fields $h_{m\sigma}$ are calculated, see Eq. (B.22) or Eq. (B.30). Using $n_{m\sigma}$, the gauge $c_{m\sigma}$ is also calculated, see Eq. (B.8).
- Then, the hamiltonian H_{PS} is diagonalized, using the obtained $h_{m\sigma}$ and $c_{m\sigma}$. The expected values $< O_{m\sigma} >$ and $< S^z_{m\sigma} >$ are calculated for the ground state $|GS>$ of H_{PS}.
- New values of $Z_{m\sigma}$ (and $\lambda^0_{m\sigma}$ in $U(1)$ formalism) are calculated, see Eq. (B.15).
- Then, the constraint $C_{m\sigma} = n_{m\sigma} - (< S^z_{m\sigma} > +1/2)$ is checked.
- If the constraint is not fulfilled below a certain criteria ($|C_{m\sigma}| > \delta_C$), we have to calculate a new $\lambda_{m\sigma} = (1 \pm \alpha C_{m\sigma})\lambda^{prev}_{m\sigma}$, where $\lambda^{prev}_{m\sigma}$ is the Lagrange multiplier from

the previous iteration and $\alpha = 0.01 - 0.5$ depending on the problem[3]. The sign of α will depend on how the constraint evolves in each iteration step i_{PS} (if $C_{m\sigma}$ grows from the previous iteration, then α changes sign). δ_C is a dynamical quantity which evolves between $\delta_C^{initial} = 10^{-3}$ down to 10^{-6} with the number of iterations i_f, $\delta_C^{i_f+1} = \delta_C^{i_f}/i_f$.

- Then, the new $\lambda_{m\sigma}$ is introduced in H_{PS}. This hamiltonian is diagonalized, and previous step repeats until the constraint is fulfilled.

- If the constraint is fulfilled ($C_{m\sigma} \leq \delta_C$), the initial and the new calculated $Z_{m\sigma}$, $\lambda_{m\sigma}$ and $\lambda^0_{m\sigma}$ are compared. If the differences are below a certain criteria ($|X^{old} - X^{new}| < 0.01 - 0.001$ with $X = Z$, λ and λ^0[4]), and $C_{m\sigma} \leq 10^{-6}$, then the calculation at the corresponding (U, J_H, n_e) is finished. If not, a numerical method, the Broyden scheme [226] is applied to mix the initial and new quantities (this mixing varies between $10 - 50\%$ for the new variable X^{new} depending on the problem). In this case, H_f is diagonalized again, and the previous steps are repeated.

For a given set of parameters (U, J_H, n_e), the run can take from few minutes to various hours. This time will depend on: the number of orbitals and possible degeneracies, the number of k points used to diagonalize H_f, precision criterias for the constraint and the quantities Z, λ and λ^0. Close to the Hund metal crossover or the Mott insulating transition, the run has to be carefully made, with a better precision and lower mixing quantities (e.g. α), hence around this regions the run will take more time to finish.

The biggest system that was treated during this thesis, $BaFe_2S_3$ (where tight-binding model is built on 20 d orbitals), see **Chapter 4**, lasted around three-four weeks to finish. The number of U points taken for fixed J_H and n_e were ≈ 100. For smallest systems, like N equivalent orbitals systems, SSMF can run from a couple of minutes ($N = 1$), up to a few hours ($N = 5$) for ≈ 100 points. For usual 5 d orbitals models in FeSCs, SSMF can take from 2 to 10 days to finish, also for ≈ 100 points.

[3] A smaller α gives a slower evolution, but also smoother, so in situations where the interorbital coupling is important, α should be reduced. The best recipe to chose α is by trying and failing

[4] A relative criteria $|X^{old} - X^{new}|/|X^{old}|$ can be used instead of the absolute error presented in the main text. This can be done to give a better convergence for X, but taking into account that X should not be close enough to 0.

Appendix C

Mathematical proofs

In this appendix, I am going to present some mathematical proofs which have been pointed out in previous chapters and appendices.

C.1 Gauge and correction expressions in SSMF Z_2 formalism

Here, I will proof the expressions Eq. (B.8) and Eq. (B.25) obtained for the gauge $c_{m\sigma}$ and the correction $\lambda^0_{m\sigma}$ in the SSMF Z_2 formalism. I will consider the single-orbital case, for simplicity. I begin by imposing that the non-correlated limit is well reproduced, i.e. when $U = J_H = 0$, $Z = 1$ for any giving filling per atom and spin n.

Taking into account Eq. (B.23) for H_{PS}:

$$H_{PS} = h\left(O^\dagger + h.c.\right) + \lambda\left(S^z + \frac{1}{2}\right) \tag{C.1}$$

where O and S^z are 2×2 spin matrices. Diagonalizing:

$$|H_{PS} - E\mathbb{I}| = \begin{vmatrix} \lambda - E & a \\ a & -E \end{vmatrix} = 0 \tag{C.2}$$

where $a = h(1 + c)$ (see Eq. (B.7)) and the ground state is defined as:

$$\begin{aligned} E_{GS} &= \frac{\lambda}{2} - \sqrt{\frac{\lambda^2}{4} + a^2} = \frac{\lambda}{2} - R \\ |GS> &= \frac{1}{N}\begin{pmatrix} \frac{\lambda}{2} - R \\ a \end{pmatrix} \end{aligned} \tag{C.3}$$

Now, the normalization factor N has to be calculated:

$$\begin{aligned} &< GS|GS >= \frac{1}{N^2}\left[\left(\frac{\lambda}{2}-R\right)^2+a^2\right]=1 \Longrightarrow \\ &N^2=2R^2-\lambda R \rightarrow N=\sqrt{2R(R-\frac{\lambda}{2})} \end{aligned} \tag{C.4}$$

with R defined in Eq. (C.3). Using this definition, the expectation values of S^z and O can be calculated as:

$$\begin{cases} < S^z >=< GS|S^z|GS >= \frac{1}{2N^2}\left[\left(\frac{\lambda}{2}-R\right)-a^2\right]=-\frac{\lambda}{4R} \\ < O >=< GS|O|GS >= \frac{1}{N^2}a\,(1+c)\left(\frac{\lambda}{2}-R\right)=-\frac{a(1+c)}{2R} \end{cases} \tag{C.5}$$

Now, applying the condition for the constraint given by Eq. (B.24), I obtain an analytical expression for λ:

$$n-\frac{1}{2}=< S^z >=-\frac{\lambda}{4R} \tag{C.6}$$

Note that $\lambda = 0$ if the system is at half-filling, i.e. $n = 1/2$. In the non-correlated limit:

$$Z=1=< O >^2=\frac{a^2(1+c)^2}{4R^2} \tag{C.7}$$

Now, I square Eq. (C.6), then divide both Eq. (C.6) $\div$ Eq. (C.7), restoring the expression of R, and obtaining:

$$\frac{\lambda^2}{a^2}=4\,(1+c)^2\left(n-\frac{1}{2}\right)^2 \tag{C.8}$$

The expression extracted from Eq. (C.8) for λ will be used to obtain the correction λ^0 in Eq. (B.25). This is due to the fact that λ and λ^0 has to be equal (with a different sign) at $U = J_H = 0$ in order to cancel each other and reproduce the non-correlated limit, see **Appendix B**. Otherwise (generalizing to the multiorbital case), $\lambda_m \neq 0$ out of half-filling, resulting in unphysical additional crystal field splittings at $U = J_H = 0$.

Substituting the value of R in Eq. (C.3), and using Eq. (C.8), the expression for the gauge c can be obtained in terms of the filling n, which is the expression that I wanted to demonstrate:

$$\begin{aligned} &(1+c)^2=\frac{\lambda^2}{a^2}+4=4\,(1+c)^2\left(n-\frac{1}{2}\right)^2+4 \Longrightarrow \\ &(1+c)^2=\frac{1}{n(1-n)} \rightarrow c=\frac{1}{\sqrt{n(1-n)}}-1 \end{aligned} \tag{C.9}$$

In general, for a given number of orbitals m it can be shown, by using this procedure, that the results for $c_{m\sigma}$ and $\lambda^0_{m\sigma}$ for a given orbital filling per atom, spin and orbital $n_{m\sigma}$ are:

$$\begin{cases} c_{m\sigma} = \dfrac{1}{\sqrt{n_{m\sigma}(1-n_{m\sigma})}} - 1 \\ \lambda^0_{m\sigma} = -2|h_{m\sigma}|(n_{m\sigma} - \dfrac{1}{2})(1 + c_{m\sigma}) \end{cases} \tag{C.10}$$

As shown here, the expressions in Eq. (C.10) are obtained for the non-correlated limit, $U = J_H = 0$. There is no justification to consider that this quantities should vary with non-zero U and J_H. However, not doing so in the case of the gauge will produce an unphysical $Z > 1$ for $U > 0$, as shown in FIGURE C.1.

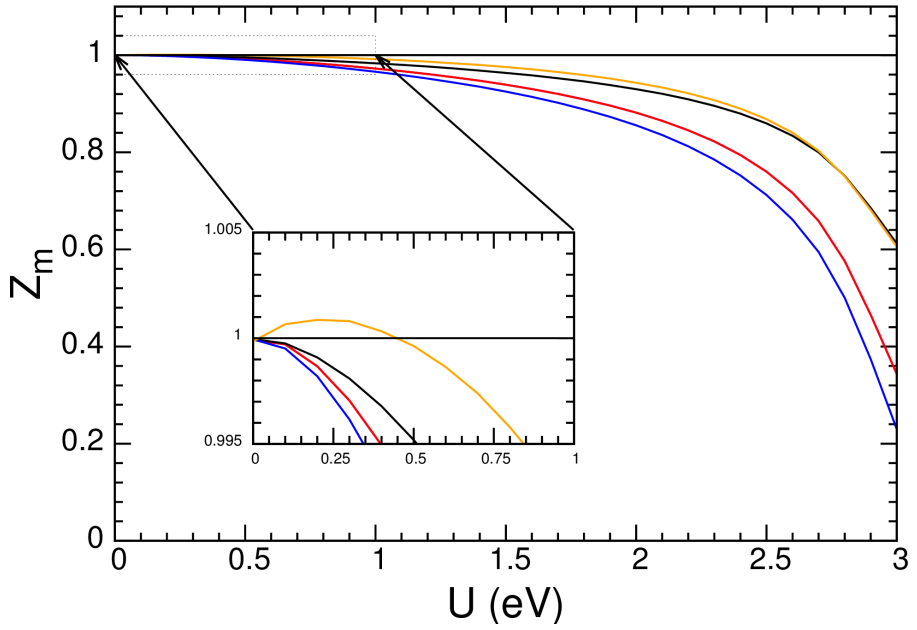

FIGURE C.1: Z_m in terms of U for $J_H = 0.25U$ for the *Graser et al.* [73] 5 d orbitals tight-binding model for $LaFeAsO$, where the filling per atom is $n_e = 6$. Z_2 formulation with $\tilde{c}_m$ fixed to $U = J_H = 0$ value, INSET shows a zoom into the unphysical solution $Z > 1$ for z^2.

During my thesis, I found the aforementioed analytical expression for $\lambda^0_{m\sigma}$. It coincides with previous calculations in which $\lambda^0_{m\sigma}$ was self-consistenly calculated in a first step, hence the analytical formula permits to save an important time when initializing the SSMF calculations.

C.2 Taylor expansion in $U(1)$ SSMF formulation

Let's see now how to obtain the Eq. (B.31) - Eq. (B.34). I am going to leave out all the indices (note that this derivation is the same if we include such indices). Then:

$$o^\dagger = P^+ S^+ P^- \tag{C.11}$$

By taking the expression of $P^\pm$ and applying a typical mean-field approach $S^z =< S^z > +\delta S^z \longleftrightarrow \delta S^z = S^z - < S^z >$, I obtain:

$$\begin{aligned} P^{\pm} &= \frac{1}{\sqrt{1/2 \pm S^z}} = \frac{1}{\sqrt{1/2 \pm (< S^z > + \delta S^z)}} \\ &= \frac{1}{\sqrt{1/2 \pm < S^z >}} \frac{1}{\sqrt{1 \pm \frac{\delta S^z}{1/2 \pm < S^z >}}} \end{aligned} \tag{C.12}$$

If the system is far from the fully-filled or fully-emptied situations, $\frac{1}{2} \pm < S^z > \sim \pm 1$, then $\frac{\delta S^z}{1/2 \pm S^z} << 1$ (because $\delta S^z << 1$). Now, a Taylor expansion can be performed:

$$\frac{1}{\sqrt{1 \pm x}} \approx 1 \mp \frac{1}{2} x + \frac{3}{8} x^2 - \cdots \tag{C.13}$$

Keeping up to linear terms:

$$\frac{1}{\sqrt{1 \pm \frac{\delta S^z}{\frac{1}{2} \pm < S^z >}}} \approx 1 \mp \frac{1}{2} \frac{\delta S^z}{1/2 \pm < S^z >} \tag{C.14}$$

An important result is obtained for $< P^{\pm} >$:

$$\begin{aligned} < P^{\pm} > &= \langle \frac{1}{\sqrt{1/2 \pm < S^z >}} \frac{1}{\sqrt{1 \pm \frac{\delta S^z}{1/2 \pm < S^z >}}} \rangle \\ &= \frac{1}{\sqrt{1/2 \pm < S^z >}} \langle \left(1 \mp \frac{1}{2} \frac{\delta S^z}{1/2 \pm < S^z >} \right) \rangle \\ &= \frac{1}{\sqrt{1/2 \pm < S^z >}} \mp \frac{1}{\sqrt{1/2 \pm < S^z >}} \frac{1}{2} \frac{< \delta S^z >}{1/2 \pm < S^z >} \\ &= \frac{1}{\sqrt{1/2 \pm < S^z >}} \end{aligned} \tag{C.15}$$

where I have used that $< \delta S^z >= \langle S^z - < S^z > \rangle = 0$. Also, note that, by using Eq. (B.33):

$$\begin{cases} < P^+ > = \dfrac{1}{\sqrt{n}} \\ < P^- > = \dfrac{1}{\sqrt{1-n}} \end{cases} \tag{C.16}$$

Then (considering that $\delta S^{z2} \approx 0$ and $\delta S^z \delta S^+ \approx 0$):

$$\begin{aligned} o^{\dagger} \approx & < P^+ > \left(1 - \frac{1}{2} < P^+ >^2 \delta S^z \right) S^+ < P^- > \left(1 + \frac{1}{2} < P^- >^2 \delta S^z \right) \\ = & < P^+ > S^+ < P^- > + < P^+ > S^+ < P^- > \frac{1}{2} \delta S^z \left(- < P^+ >^2 + < P^- >^2 \right) \\ = & < P^+ > S^+ < P^- > + < P^+ > < S^+ > < P^- > \frac{1}{2} \left(S^z - < S^z > \right) \left(-\frac{1}{n} + \frac{1}{1-n} \right) \\ = & \, O^{\dagger} + < O^{\dagger} > \eta \left[2S^z - (2n-1) \right] \end{aligned} \tag{C.17}$$

where I have defined:

$$\begin{cases} O^{\dagger} =< P^{+} > S^{+} < P^{-} > \\ \eta = \dfrac{1}{2}\dfrac{n-1/2}{n\,(1-n)} \end{cases} \tag{C.18}$$

And the expressions from Eq. (B.31) to Eq. (B.34) are obtained.

C.3 Implementation of the Zeeman field effect in SSMF

In this section, I will show the implementation of the Zeeman field term presented in **Chapter 5**, in the SSMF formalism. I include the Zeeman magnetic field term in the Hubbard-Kanamori hamiltonian of Eq. (1.22):

$$H = H_0 + H_{dens} + H_{add} + \underbrace{H \sum_{im} \left(d^{\dagger}_{im\uparrow} d_{im\uparrow} - d^{\dagger}_{im\downarrow} d_{im\downarrow} \right)}_{H_{Zeeman}} \tag{C.19}$$

where H_0 is the tight-binding, H_{dens} is the density-density interaction part and H_{add} encodes the pair-hopping and spin-flip terms. The Zeeman field H breaks the spin degeneracy, moving one spin $\uparrow$ upwards and the other one $\downarrow$ downwards. The majority spin band is labeled with $\downarrow$, and the minority spin band with $\uparrow$.

In the SSMF formalism, H_{Zeeman} is written in the basis of auxiliary fermion operators:

$$H_{Zeeman} = H \sum_{im} \left(\hat{n}^{f}_{im\uparrow} - \hat{n}^{f}_{im\downarrow} \right) \tag{C.20}$$

where $\hat{n}^{f}_{im\sigma} = f^{\dagger}_{im\sigma} f_{im\sigma}$. Then, H_{Zeeman} has to be added in the H_f of Eq. (B.23) or Eq. (B.35) as a spin-dependent onsite energy shift. In this situation, all the parameters $Z_{m\sigma}$, $\lambda_{m\sigma}$, etc. will depend explicitly on the spin index σ.

The implementation of the Zeeman field effect on SSMF is constraint to a specific regime. The discussion of next paragraphs works for equivalent orbitals systems which are out of half-filling and for small J_H. In **Chapter 5**, I precisely study this regime for a $N = 2$ equivalent orbitals system at quarter filling and $J_H = 0$.

I will consider that the total filling of the system is less than half-filling, and drop out the orbital index. Thus, when the Zeeman field H increases, the majority spin band is progressively filling, while the minority spin band is getting emptied (approaching 0 filling). This poses a problem when n_σ approaches 0 (band totally emptied) or to 1 (band totally filled). In this situation, Z_σ cannot be defined anymore for the band which is evolving to the totally filled/emptied situation, see **Section 1.2.2**. By following the numerical evolution of h_σ and c_σ for increasing H, it can be shown that when $n_\sigma \to 0$ or 1, $a_\sigma = h_\sigma(1 + c_\sigma) \to 0$, and H_{PS} is a block diagonal matrix. In the case of a single-orbital system:

$$H_{PS} = \begin{pmatrix} \lambda_\uparrow + \lambda_\downarrow + U & a_\downarrow & 0 & 0 \\ a_\downarrow & \lambda_\uparrow & 0 & 0 \\ 0 & 0 & \lambda_\downarrow & a_\downarrow \\ 0 & 0 & a_\downarrow & 0 \end{pmatrix} \tag{C.21}$$

Interestingly, the ground state $|GS>$ of Eq. (C.21), only depends on the parameters of the spin band $\downarrow$ (bottom right 2×2 block), i.e. the band which is not getting totally emptied. A similar demonstration can be done for $N = 2$ equivalent orbitals (not shown).

I will then proceed with the implementation of H_{Zeeman} in the SSMF calculations as follows: once one of the spin bands is totally emptied or filled, both spin channels are decoupled by neglecting the evolution of the spin band which is getting totally emptied/filled. This is done by simply re-formulating H_f and H_{PS} with respect to the spin band which remains in a finite filling. This spin decoupling has to be done in order to overcome possible oscillations in the filling of the totally empty/fill spin band, hence in all the other SSMF parameters.

C.4 Propagators in SSMF

Let's consider a single-orbital system in the local PM metal state. By taking the operators representation of Eq. (B.7) and the mean-field treatment, and the time-ordered propagators in the real space are:

$$G^d(ij,t) = G^f(ij,t)G^{PS}(ij,t) \tag{C.22}$$

where the superindices accounts for the different operators, ij is the relative position of the electron, t is the time and:

$$\begin{cases} G^d(ij,t) = -i< Td_{i\sigma}(t)d^\dagger_{j\sigma}(0) >^d \\ G^f(ij,t) = -i< Tf_{i\sigma}(t)f^\dagger_{j\sigma}(0) >^f \\ G^{PS}(ij,t) = < TO_{i\sigma}(t)O^\dagger_{j\sigma}(0) >^{PS} \end{cases} \tag{C.23}$$

These expressions can be Fourier transformed into $G^d(k,\omega)$, where k is the reciprocal space vector and ω is the frequency. $G^d(k,\omega)$ is found as the convolution of $G^f(k,\omega)$ and $G^{PS}(k,\omega)$:

$$G^d(k,\omega) = \int \frac{d\omega'}{2\pi}\frac{d^3\vec{k}'}{8\pi^3} G^f(k',\omega')G^{PS}(k-k',\omega-\omega') \tag{C.24}$$

After the second mean-field of Eq. (B.14), it can be seen that pseudospins are long-range ordered with $< O^\dagger_{i\sigma} >< O_{j\sigma} >\neq 0$ in the metallic phase. Then, at low frequencies ω, as required in FLT, $G^{PS}(k,\omega)$ can be divided into a small and large k and ω contributions:

$$G^{PS}(k,\omega) = Z_k\delta(k)\delta(\omega) + G^{PS,\,incoh}(k,\omega) \tag{C.25}$$

where the parameter Z_k is defined as the FT of $< O^{\dagger}_{i\sigma} >< O_{j\sigma} >$, and $G^{PS,\,incoh}(k,\omega)$ as the incoherent part, see **Section 1.2.2**. In a first approximation, $G^{PS,\,incoh}(k,\omega)$ can be neglected and:

$$G^{d}(k,\omega) = Z_k G^{f}(k,\omega) \tag{C.26}$$

H_f describes a non-interacting hamiltonian with a renormalized band structure. Hence, the Dyson equation for $G^{f}(k,\omega)$ can be written (note that $\Sigma^{f}(k,\omega) = 0$ in a non-interacting hamiltonian):

$$G^{f}(k,\omega) = \frac{1}{\omega - Z_k\varepsilon_k + \mu + \lambda_k - \lambda_k^0} \tag{C.27}$$

where λ_k and λ_k^0 are the FT Lagrange multipliers and correction energy shifts. Taking into account Eq. (C.26) and Eq. (C.27):

$$G^{d}(k,\omega) = \frac{Z_k}{\omega - Z_k\varepsilon_k + \mu + \lambda_k - \lambda_k^0} \tag{C.28}$$

Using the definition Eq. (1.9) for $G^{d}(k,\omega)$, the self-energy $\Sigma(k,\omega)$ of the interacting hamiltonian H can be obtained as:

$$\Sigma(k,\omega) = \underbrace{\mu - \frac{\mu + \lambda_k - \lambda_k^0}{Z_k}}_{Re\,\Sigma(k,0)} + \omega\left(1 - \frac{1}{Z_k}\right) \tag{C.29}$$

Hence, the linear-ω dependence of the $\Sigma(k,\omega)$ in the FLT is recovered if Z_k is defined as the FT of $< O^{\dagger}_{i\sigma} >< O_{j\sigma} >$, as anticipated. In the single-site approximation for a PM system, this condition reduces to $< O >^2 = Z$.

List of publications

1. Strong correlations and the search for high-T_c superconductivity in chromium pnictides and chalcogenides
   J. M. Pizarro, M. J. Calderón, J. Liu, M. C. Muñoz and E. Bascones
   Phys. Rev. B **95**, 075115 (2017)

2. Strong electronic correlations and Fermi surface reconstruction in the quasi-one dimensional iron superconductor $BaFe_2S_3$
   J. M. Pizarro and Elena Bascones
   Phys. Rev. Materials **3**, 014801 (2018)

3. The nature of correlations in the insulating states of twisted bilayer graphene
   J. M. Pizarro, M. J. Calderón and E. Bascones
   arXiv 1805.07303 (2018)

References

[1] Neil W. Ashcroft and N. Mermin. *Solid State Physics*. Cengage Learning, 1976. ISBN 978-0030839931. URL https://cengage.com.au/product/title/solid-state-physics/isbn/9780030839931. (Cited on pages 1 and 5).

[2] S. Raghu, Xiao-Liang Qi, Chao-Xing Liu, D. J. Scalapino, and Shou-Cheng Zhang. Minimal two-band model of the superconducting iron oxypnictides. *Phys. Rev. B*, 77: 220503, 2008. doi: 10.1103/PhysRevB.77.220503. URL https://link.aps.org/doi/10.1103/PhysRevB.77.220503. (Cited on pages 2, 25, 29, and 53).

[3] D.P. Jenkins. The electronic band structure of silicon. *Physica*, 20(7):967 – 970, 1954. doi: https://doi.org/10.1016/S0031-8914(54)80206-0. (Cited on page 2).

[4] Piers Coleman. *Introduction to Many-Body Physics*. Cambridge University Press, 2015. doi: 10.1017/CBO9781139020916. (Cited on pages 3, 7, 9, 11, 22, 23, 24, 27, 40, and 129).

[5] E. Bascones, M.J. Calderón, R. Aguado, B. Valenzuela, A. Cortijo, and R. Roldán. Emergence of quantum phases in novel materials. Teoría y Simulación de Materiales, Instituto de Ciencia de Materiales de Madrid, ICMM-CSIC, Sep 2017. (Cited on pages 3, 6, 7, 12, 13, 14, 15, 17, 20, 21, 29, 31, 39, 40, 41, 45, 53, 58, 59, and 129).

[6] Z. K. Liu, M. Yi, Y. Zhang, J. Hu, R. Yu, J.-X. Zhu, R.-H. He, Y. L. Chen, M. Hashimoto, R. G. Moore, S.-K. Mo, Z. Hussain, Q. Si, Z. Q. Mao, D. H. Lu, and Z.-X. Shen. Experimental observation of incoherent-coherent crossover and orbital-dependent band renormalization in iron chalcogenide superconductors. *Phys. Rev. B*, 92:235138, 2015. doi: 10.1103/PhysRevB.92.235138. URL https://link.aps.org/doi/10.1103/PhysRevB.92.235138. (Cited on pages 3, 21, 40, 51, 52, and 59).

[7] Warren E. Pickett. Electronic structure of the high-temperature oxide superconductors. *Rev. Mod. Phys.*, 61:433–512, 1989. doi: 10.1103/RevModPhys.61.433. URL https://link.aps.org/doi/10.1103/RevModPhys.61.433. (Cited on pages 3, 12, and 26).

[8] Patrik Fazekas. *Vol. 5: Lecture Notes on Electron Correlation and Magnetism*. WORLD SCIENTIFIC, 1999. ISBN 978-981-02-2474-5. URL https://www.worldscientific.com/doi/abs/10.1142/2945. (Cited on pages 3, 6, 12, 14, 17, 21, 23, 27, 90, 96, 101, 102, 103, 104, 106, 109, and 129).

[9] Elena Bascones, Belén Valenzuela, and María José Calderón. Magnetic interactions in iron superconductors: A review. *Comptes Rendus Physique*, 17 (1):36 – 59, 2016. doi: https://doi.org/10.1016/j.crhy.2015.05.004. URL

http://www.sciencedirect.com/science/article/pii/S1631070515000924. (Cited on pages 3, 20, 21, 23, 24, 28, 29, 39, 40, 41, 45, 51, 53, 54, 55, 57, 58, 59, 62, 65, 70, 71, 76, an

[10] Rafael Roldán, Luca Chirolli, Elsa Prada, Jose Angel Silva-Guillén, Pablo San-Jose, and Francisco Guinea. Theory of 2D crystals: graphene and beyond. *Chem. Soc. Rev.*, 46:4387–4399, 2017. doi: 10.1039/C7CS00210F. URL http://dx.doi.org/10.1039/C7CS00210F. (Cited on pages 3 and 32).

[11] Gunnar Schönhoff. *Coulomb interaction and phonons in doped semiconducting and metallic two-dimensional materials*. PhD thesis, Universität Bremen, 2017. (Cited on pages 3, 4, 32, and 125).

[12] Alexander Atland and Ben D. Simons. *Condensed Matter Field Theory*. Cambridge University Press, 2010. ISBN 9780521769754. URL https://www.cambridge.org/de/academic/subjects/physics/condensed-matter-physics-nanoscience-and-mesoscopic-physics/condensed-matter-field-theory-2nd-edition?format=HB&isbn=9780521769754. (Cited on page 5).

[13] Johannes Ferber. *Density Functional Theory and Dynamical Mean Field Theory: Applications to Correlated Materials*. PhD thesis, Johann Wolfgang Goethe-Universität, Frankfurt am Main, 2012. (Cited on pages 4, 11, and 125).

[14] Jan Kuneš, Ryotaro Arita, Philipp Wissgott, Alessandro Toschi, Hiroaki Ikeda, and Karsten Held. Wien2wannier: From linearized augmented plane waves to maximally localized Wannier functions. *Computer Physics Communications*, 181(11):1888 – 1895, 2010. doi: https://doi.org/10.1016/j.cpc.2010.08.005. URL http://www.sciencedirect.com/science/article/pii/S0010465510002948. (Cited on page 6).

[15] L. de' Medici. Hund's metals, explained. *ArXiv e-prints*, 2017. URL https://arxiv.org/abs/1707.03282. (Cited on pages 9, 20, 21, 39, 40, 41, 43, 45, 53, 55, 56, 57, 58, and 59).

[16] Christian Gross and Immanuel Bloch. Quantum simulations with ultracold atoms in optical lattices. *Science*, 357(6355):995–1001, 2017. doi: 10.1126/science.aal3837. URL http://science.sciencemag.org/content/357/6355/995. (Cited on page 12).

[17] Antoine Georges, Gabriel Kotliar, Werner Krauth, and Marcelo J. Rozenberg. Dynamical mean-field theory of strongly correlated fermion systems and the limit of infinite dimensions. *Rev. Mod. Phys.*, 68:13–125, 1996. doi: 10.1103/RevModPhys.68.13. URL https://link.aps.org/doi/10.1103/RevModPhys.68.13. (Cited on pages 14, 15, 16, 18, 19, 21, 39, 90, 96, 101, 102, 103, 104, 106, and 129).

[18] A. Sekiyama, H. Fujiwara, S. Imada, H. Eisaki, S. I. Uchida, K. Takegahara, H. Harima, Y. Saitoh, and S. Suga. Genuine electronic states of vanadium perovskites revealed by high-energy photoemission. *eprint arXiv:cond-mat/0206471*, 2002. URL https://arxiv.org/abs/cond-mat/0206471v2. (Cited on page 16).

[19] H. Park, K. Haule, and G. Kotliar. Cluster Dynamical Mean Field Theory of the Mott transition. *Phys. Rev. Lett.*, 101:186403, 2008. doi: 10.1103/PhysRevLett.101.186403. URL https://link.aps.org/doi/10.1103/PhysRevLett.101.186403. (Cited on pages 18, 19, 90, 96, 102, 103, 104, and 106).

[20] J. Vučičević, H. Terletska, D. Tanasković, and V. Dobrosavljević. Finite-temperature crossover and the quantum Widom line near the Mott transition. *Phys. Rev. B*, 88: 075143, 2013. doi: 10.1103/PhysRevB.88.075143. URL https://link.aps.org/doi/10.1103/PhysRevB.88.075143. (Cited on pages 90, 96, 101, and 106).

[21] T. Schäfer, F. Geles, D. Rost, G. Rohringer, E. Arrigoni, K. Held, N. Blümer, M. Aichhorn, and A. Toschi. Fate of the false Mott-Hubbard transition in two dimensions. *Phys. Rev. B*, 91:125109, 2015. doi: 10.1103/PhysRevB.91.125109. URL https://link.aps.org/doi/10.1103/PhysRevB.91.125109. (Cited on pages 18, 90, 96, 102, 103, 104, and 106).

[22] Elbio Dagotto. *Nanoscale phase separation and colossal magnetoresistance*. Springer-Verlag, 2002. ISBN 978-3-662-05244-0. URL https://www.springer.com/de/book/9783540432456. (Cited on page 19).

[23] C. Castellani, C. R. Natoli, and J. Ranninger. Metal-insulator transition in pure and cr-doped v_2o_3. *Phys. Rev. B*, 18:5001–5013, 1978. URL https://link.aps.org/doi/10.1103/PhysRevB.18.5001. (Cited on pages 20 and 40).

[24] Takashi Miyake, Kazuma Nakamura, Ryotaro Arita, and Masatoshi Imada. Comparison of ab initio low-energy models for lafepo, lafeaso, bafe2as2, lifeas, fese, and fete: Electron correlation and covalency. *Journal of the Physical Society of Japan*, 79(4): 044705, 2010. doi: 10.1143/JPSJ.79.044705. URL https://journals.jps.jp/doi/abs/10.1143/JPSJ.79.044705. (Cited on pages 20, 53, and 54).

[25] Rong Yu and Qimiao Si. $U(1)$ slave-spin theory and its application to Mott transition in a multiorbital model for iron pnictides. *Phys. Rev. B*, 86:085104, 2012. doi: 10.1103/PhysRevB.86.085104. URL https://link.aps.org/doi/10.1103/PhysRevB.86.085104. (Cited on pages 20, 21, 22, 53, 54, 129, 131, and 134).

[26] Philipp Werner, Emanuel Gull, Matthias Troyer, and Andrew J. Millis. Spin freezing transition and non-Fermi-liquid self-energy in a three-orbital model. *Phys. Rev. Lett.*, 101:166405, 2008. doi: 10.1103/PhysRevLett.101.166405. URL https://link.aps.org/doi/10.1103/PhysRevLett.101.166405. (Cited on pages 20, 39, 45, 58, and 59).

[27] K Haule and G Kotliar. Coherence,Äìincoherence crossover in the normal state of iron oxypnictides and importance of Hund's rule coupling. *New Journal of Physics*, 11(2):025021, 2009. URL http://stacks.iop.org/1367-2630/11/i=2/a=025021. (Cited on pages).

[28] Ansgar Liebsch and Hiroshi Ishida. Correlation-induced spin freezing transition in $FeSe$: A dynamical mean field study. *Phys. Rev. B*, 82:155106, 2010. doi: 10.1103/PhysRevB.82.155106. URL https://link.aps.org/doi/10.1103/PhysRevB.82.155106. (Cited on pages 51, 59, and 62).

[29] Hiroshi Ishida and Ansgar Liebsch. Fermi-liquid, non-fermi-liquid, and Mott phases in iron pnictides and cuprates. *Phys. Rev. B*, 81:054513, 2010. doi: 10.1103/PhysRevB.81.054513. URL https://link.aps.org/doi/10.1103/PhysRevB.81.054513. (Cited on pages 51, 59, 60, 62, 73, and 137).

[30] P. Hansmann, R. Arita, A. Toschi, S. Sakai, G. Sangiovanni, and K. Held. Dichotomy between large local and small ordered magnetic moments in iron-based superconductors. *Phys. Rev. Lett.*, 104:197002, 2010. doi: 10.1103/PhysRevLett.104.197002. URL https://link.aps.org/doi/10.1103/PhysRevLett.104.197002. (Cited on pages).

[31] Z. P. Yin, K. Haule, and G. Kotliar. Kinetic frustration and the nature of the magnetic and paramagnetic states in iron pnictides and iron chalcogenides. *Nature Materials*, 10:932, 2011. URL http://dx.doi.org/10.1038/nmat3120. (Cited on page 44).

[32] Philipp Werner, Michele Casula, Takashi Miyake, Ferdi Aryasetiawan, Andrew J. Millis, and Silke Biermann. Satellites and large doping and temperature dependence of electronic properties in hole-doped $BaFe_2As_2$. *Nature Physics*, 8:331, 2012. URL http://dx.doi.org/10.1038/nphys2250. (Cited on pages 51 and 59).

[33] Nicola Lanatà, Hugo U. R. Strand, Gianluca Giovannetti, Bo Hellsing, Luca de' Medici, and Massimo Capone. Orbital selectivity in Hund's metals: The iron chalcogenides. *Phys. Rev. B*, 87:045122, 2013. doi: 10.1103/PhysRevB.87.045122. URL https://link.aps.org/doi/10.1103/PhysRevB.87.045122. (Cited on pages 21, 41, 53, 55, and 59).

[34] Luca de' Medici, Gianluca Giovannetti, and Massimo Capone. Selective Mott physics as a key to iron superconductors. *Phys. Rev. Lett.*, 112:177001, 2014. doi: 10.1103/PhysRevLett.112.177001. URL https://link.aps.org/doi/10.1103/PhysRevLett.112.177001. (Cited on pages 21, 41, 51, 53, 54, 55, 56, 57, 59, 62, and 84).

[35] L. Fanfarillo and E. Bascones. Electronic correlations in Hund metals. *Phys. Rev. B*, 92:075136, 2015. doi: 10.1103/PhysRevB.92.075136. URL https://link.aps.org/doi/10.1103/PhysRevB.92.075136. (Cited on pages 30, 41, 44, 45, 46, 49, 51, 58, and 59).

[36] Luca de' Medici. *Weak and Strong Correlations in Fe Superconductors*. Springer International Publishing, 2015. ISBN 978-3-319-11254-1. doi: 10.1007/978-3-319-11254-1_11. URL https://doi.org/10.1007/978-3-319-11254-1_11. (Cited on pages 21, 40, and 53).

[37] Luca de' Medici and Massimo Capone. *Modeling Many-Body Physics with Slave-Spin Mean-FIeld: Mott and Hund's Physics in Fe-Superconductors*. Springer International Publishing, 2017. ISBN 978-3-319-56117-2. doi: 10.1007/978-3-319-56117-2_4. URL https://doi.org/10.1007/978-3-319-56117-2_4. (Cited on pages 20, 21, 39, 40, 45, 53, 55, 57, 58, and 59).

[38] L. de'Medici, A. Georges, and S. Biermann. Orbital-selective Mott transition in multiband systems: Slave-spin representation and dynamical mean-field theory. *Phys. Rev. B*, 72:205124, 2005. doi: 10.1103/PhysRevB.72.205124. URL https://link.aps.org/doi/10.1103/PhysRevB.72.205124. (Cited on pages 21, 22, 40, 41, 42, 51, 52, 59, 70, 129, 130, and 131).

[39] Luca de' Medici, S. R. Hassan, Massimo Capone, and Xi Dai. Orbital-Selective Mott Transition out of band degeneracy lifting. *Phys. Rev. Lett.*, 102:126401, 2009. doi: 10.1103/PhysRevLett.102.126401. URL https://link.aps.org/doi/10.1103/PhysRevLett.102.126401. (Cited on pages 41 and 52).

[40] Rong Yu and Qimiao Si. Orbital-Selective Mott Phase in multiorbital models for alkaline iron selenides $\mathbf{K}_{1-x}\mathrm{Fe}_{2-y}\mathrm{Se}_2$. *Phys. Rev. Lett.*, 110:146402, 2013. doi: 10.1103/PhysRevLett.110.146402. URL https://link.aps.org/doi/10.1103/PhysRevLett.110.146402. (Cited on pages).

[41] M. Yi, D. H. Lu, R. Yu, S. C. Riggs, J.-H. Chu, B. Lv, Z. K. Liu, M. Lu, Y.-T. Cui, M. Hashimoto, S.-K. Mo, Z. Hussain, C. W. Chu, I. R. Fisher, Q. Si, and Z.-X. Shen. Observation of temperature-induced crossover to an Orbital-Selective Mott Phase in $A_xFe_{2-y}Se_2$ (A=K, Rb) superconductors. *Phys. Rev. Lett.*, 110:067003, 2013. doi: 10.1103/PhysRevLett.110.067003. URL https://link.aps.org/doi/10.1103/PhysRevLett.110.067003. (Cited on pages 21, 40, 51, 52, and 59).

[42] Donghui Lu, Inna M. Vishik, Ming Z, Yulin Chen, Rob G. Moore, and Zhi-Xun Shen. Angle-Resolved Photoemission studies of quantum materials. *Annual Review of Condensed Matter Physics*, 3 (1):129–167, 2012. doi: 10.1146/annurev-conmatphys-020911-125027. URL https://doi.org/10.1146/annurev-conmatphys-020911-125027. (Cited on pages 21, 30, 41, 53, 55, 59, 66, and 73).

[43] H. Gretarsson, A. Lupascu, Jungho Kim, D. Casa, T. Gog, W. Wu, S. R. Julian, Z. J. Xu, J. S. Wen, G. D. Gu, R. H. Yuan, Z. G. Chen, N.-L. Wang, S. Khim, K. H. Kim, M. Ishikado, I. Jarrige, S. Shamoto, J.-H. Chu, I. R. Fisher, and Young-June Kim. Revealing the dual nature of magnetism in iron pnictides and iron chalcogenides using x-ray emission spectroscopy. *Phys. Rev. B*, 84:100509, 2011. doi: 10.1103/PhysRevB.84.100509. URL https://link.aps.org/doi/10.1103/PhysRevB.84.100509. (Cited on page 57).

[44] S. Lafuerza, H. Gretarsson, F. Hardy, T. Wolf, C. Meingast, G. Giovannetti, M. Capone, A. S. Sefat, Y.-J. Kim, P. Glatzel, and L. de' Medici. Evidence of Mott physics in iron pnictides from x-ray spectroscopy. *Phys. Rev. B*, 96:045133, 2017. doi: 10.1103/PhysRevB.96.045133. URL https://link.aps.org/doi/10.1103/PhysRevB.96.045133. (Cited on pages 21, 41, 53, 55, 57, and 59).

[45] Gabriel Kotliar and Andrei E. Ruckenstein. New functional integral approach to strongly correlated fermi systems: The Gutzwiller approximation as a saddle point. *Phys. Rev. Lett.*, 57:1362–1365, 1986. doi: 10.1103/PhysRevLett.57.1362. URL https://link.aps.org/doi/10.1103/PhysRevLett.57.1362. (Cited on pages 21, 22, and 129).

[46] Serge Florens and Antoine Georges. Slave-rotor mean-field theories of strongly correlated systems and the Mott transition in finite dimensions. *Phys. Rev. B*, 70:035114, 2004. doi: 10.1103/PhysRevB.70.035114. URL https://link.aps.org/doi/10.1103/PhysRevB.70.035114. (Cited on pages 21, 22, 51, 90, 96, 97, 98, 99, 106, and 129).

[47] S. R. Hassan and L. de' Medici. Slave spins away from half filling: Cluster mean-field theory of the Hubbard and extended Hubbard models. *Phys. Rev. B*, 81:035106, 2010. doi: 10.1103/PhysRevB.81.035106. URL https://link.aps.org/doi/10.1103/PhysRevB.81.035106. (Cited on pages 21, 22, 70, 129, and 131).

[48] Michael Tinkham. *Introduction to superconductivity*. McGraw-Hill, Inc., 1996. ISBN 0-07-064878-6. (Cited on page 22).

[49] Maddury Somayazulu, Muhtar Ahart, Ajay K Mishra, Zachary M. Geballe, Maria Baldini, Yue Meng, Viktor V. Struzhkin, and Russell J. Hemley. Evidence for superconductivity above 260 K in lanthanum superhydride at megabar pressures. *ArXiv e-prints*, 2018. URL https://arxiv.org/abs/1808.07695. (Cited on page 22).

[50] H. Breitzke, I. Eremin, D. Manske, E.V. Antipov, and K. Lüders. Formation of magnetic moments in the cuprate superconductor $Hg0.8Cu0.2Ba2Ca2Cu3O8 + \delta$ below Tc seen by NQR. *Physica C: Superconductivity*, 406(1):27 – 36, 2004. doi: https://doi.org/10.1016/j.physc.2004.02.183. URL http://www.sciencedirect.com/science/article/pii/S0921453404004988. (Cited on page 23).

[51] M.R. Norman. Unconventional Superconductivity. *ArXiv e-prints*, 2013. URL https://arxiv.org/abs/1302.3176. (Cited on pages 23, 24, 26, 27, and 28).

[52] Y. Kurosaki, Y. Shimizu, K. Miyagawa, K. Kanoda, and G. Saito. Mott transition from a spin liquid to a Fermi liquid in the spin-frustrated organic conductor $\kappa-(ET)_2Cu_2(CN)_3$. *Phys. Rev. Lett.*, 95:177001, 2005. doi: 10.1103/PhysRevLett.95.177001. URL https://link.aps.org/doi/10.1103/PhysRevLett.95.177001. (Cited on pages 23 and 24).

[53] Johnpierre Paglione and Richard L. Greene. High-temperature superconductivity in iron-based materials. *Nature Physics*, 6:645, 2010. URL http://dx.doi.org/10.1038/nphys1759. (Cited on pages 23 and 28).

[54] Alberto Martinelli, Fabio Bernardini, and Sandro Massidda. The phase diagrams of iron-based superconductors: Theory and experiments. *Comptes Rendus Physique*, 17(1):5 – 35, 2016. doi: https://doi.org/10.1016/j.crhy.2015.06.001. URL http://www.sciencedirect.com/science/article/pii/S1631070515001267. (Cited on pages 23 and 30).

[55] T. Yildirim. Origin of the 150 K anomaly in LaFeAsO: Competing antiferromagnetic interactions, frustration, and a structural phase transition. *Phys. Rev. Lett.*, 101:057010, 2008. doi: 10.1103/PhysRevLett.101.057010. URL https://link.aps.org/doi/10.1103/PhysRevLett.101.057010. (Cited on pages 25, 29, and 53).

[56] Peter J. Hirschfeld. Using gap symmetry and structure to reveal the pairing mechanism in *Fe*-based superconductors. *Comptes Rendus Physique*, 17(1):197 – 231, 2016. doi: https://doi.org/10.1016/j.crhy.2015.10.002. URL http://www.sciencedirect.com/science/article/pii/S1631070515001693. (Cited on pages 25, 31, 32, and 71).

[57] F. Steglich, J. Aarts, C. D. Bredl, W. Lieke, D. Meschede, W. Franz, and H. Schäfer. Superconductivity in the presence of strong Pauli paramagnetism: $CeCu_2Si_2$. *Phys. Rev. Lett.*, 43:1892–1896, 1979. doi: 10.1103/PhysRevLett.43.1892. URL https://link.aps.org/doi/10.1103/PhysRevLett.43.1892. (Cited on page 26).

[58] S. S. Saxena, P. Agarwal, K. Ahilan, F. M. Grosche, R. K. W. Haselwimmer, M. J. Steiner, E. Pugh, I. R. Walker, S. R. Julian, P. Monthoux, G. G. Lonzarich, A. Huxley, I. Sheikin, D. Braithwaite, and J. Flouquet. Superconductivity on the border of itinerant-electron ferromagnetism in UGe2. *Nature*, 406:587, 2000. URL http://dx.doi.org/10.1038/35020500. (Cited on page 26).

[59] Georg Knebel, Dai Aoki, and Jacques Flouquet. Antiferromagnetism and superconductivity in cerium based heavy-fermion compounds. *Comptes Rendus Physique*, 12(5):542 – 566, 2011. doi: https://doi.org/10.1016/j.crhy.2011.05.002. URL http://www.sciencedirect.com/science/article/pii/S1631070511001204. (Cited on page 26).

[60] J. G. Bednorz and K. A. Müller. Possible high Tc superconductivity in the Ba-La-Cu-Oba,àíla,àícu,àío system. *Zeitschrift für Physik B Condensed Matter*, 64

(2):189–193, 1986. doi: 10.1007/BF01303701. URL https://doi.org/10.1007/BF01303701. (Cited on page 26).

[61] M. K. Wu, J. R. Ashburn, C. J. Torng, P. H. Hor, R. L. Meng, L. Gao, Z. J. Huang, Y. Q. Wang, and C. W. Chu. Superconductivity at 93 K in a new mixed-phase Y-Ba-Cu-O compound system at ambient pressure. *Phys. Rev. Lett.*, 58:908–910, 1987. doi: 10.1103/PhysRevLett.58.908. URL https://link.aps.org/doi/10.1103/PhysRevLett.58.908. (Cited on page 26).

[62] C. W. Chu, L. Gao, F. Chen, Z. J. Huang, R. L. Meng, and Y. Y. Xue. Superconductivity above 150 K in HgBa2Ca2Cu3O8+d at high pressures. *Nature*, 365:323, 1993. URL http://dx.doi.org/10.1038/365323a0. (Cited on page 26).

[63] Neven Barišić, Mun K. Chan, Yuan Li, Guichuan Yu, Xudong Zhao, Martin Dressel, Ana Smontara, and Martin Greven. Universal sheet resistance and revised phase diagram of the cuprate high-temperature superconductors. *Proceedings of the National Academy of Sciences*, 110(30):12235–12240, 2013. doi: 10.1073/pnas.1301989110. URL http://www.pnas.org/content/110/30/12235. (Cited on pages 26 and 27).

[64] M. R. Norman, A. Kanigel, M. Randeria, U. Chatterjee, and J. C. Campuzano. Modeling the Fermi arc in underdoped cuprates. *Phys. Rev. B*, 76:174501, 2007. doi: 10.1103/PhysRevB.76.174501. URL https://link.aps.org/doi/10.1103/PhysRevB.76.174501. (Cited on page 27).

[65] A.-M. S. Tremblay, B. Kyung, and D. Sénéchal. Pseudogap and high-temperature superconductivity from weak to strong coupling. Towards a quantitative theory (review article). *Low Temperature Physics*, 32(4):424–451, 2006. doi: 10.1063/1.2199446. URL https://doi.org/10.1063/1.2199446. (Cited on pages).

[66] M. Civelli, M. Capone, S. S. Kancharla, O. Parcollet, and G. Kotliar. Dynamical breakup of the Fermi surface in a doped Mott insulator. *Phys. Rev. Lett.*, 95:106402, 2005. doi: 10.1103/PhysRevLett.95.106402. URL https://link.aps.org/doi/10.1103/PhysRevLett.95.106402. (Cited on page 27).

[67] C. M. Varma. Proposal for an experiment to test a theory of high-temperature superconductors. *Phys. Rev. B*, 61:R3804–R3807, 2000. doi: 10.1103/PhysRevB.61.R3804. URL https://link.aps.org/doi/10.1103/PhysRevB.61.R3804. (Cited on page 27).

[68] Yoichi Kamihara, Takumi Watanabe, Masahiro Hirano, and Hideo Hosono. Iron-based layered superconductor $La[O1-xFx]FeAs$ (x = 0.05,àí0.12) with $T_c = 26K$. *Journal of the American Chemical Society*, 130(11):3296–3297, 2008. doi: 10.1021/ja800073m. URL https://doi.org/10.1021/ja800073m. (Cited on page 28).

[69] Marianne Rotter, Marcus Tegel, and Dirk Johrendt. Superconductivity at 38 K in the iron arsenide $(Ba_{1-x}K_x)Fe_2As_2$. *Phys. Rev. Lett.*, 101:107006, 2008. doi: 10.1103/PhysRevLett.101.107006. URL https://link.aps.org/doi/10.1103/PhysRevLett.101.107006. (Cited on pages 28 and 29).

[70] S. Lebègue. Electronic structure and properties of the fermi surface of the superconductor $LaOFeP$. *Phys. Rev. B*, 75:035110, 2007. doi: 10.1103/PhysRevB.75.035110. URL https://link.aps.org/doi/10.1103/PhysRevB.75.035110. (Cited on pages 28 and 63).

[71] Verónica Vildosola, Leonid Pourovskii, Ryotaro Arita, Silke Biermann, and Antoine Georges. Bandwidth and fermi surface of iron oxypnictides: Covalency and sensitivity to structural changes. *Phys. Rev. B*, 78:064518, 2008. doi: 10.1103/PhysRevB.78.064518. URL https://link.aps.org/doi/10.1103/PhysRevB.78.064518. (Cited on pages 28, 30, and 63).

[72] Kazuhiko Kuroki, Seiichiro Onari, Ryotaro Arita, Hidetomo Usui, Yukio Tanaka, Hiroshi Kontani, and Hideo Aoki. Unconventional pairing originating from the disconnected fermi surfaces of superconducting $LaFeAsO_{1-x}F_x$. *Phys. Rev. Lett.*, 101:087004, 2008. doi: 10.1103/PhysRevLett.101.087004. URL https://link.aps.org/doi/10.1103/PhysRevLett.101.087004. (Cited on pages 28 and 63).

[73] S Graser, T A Maier, P J Hirschfeld, and D J Scalapino. Near-degeneracy of several pairing channels in multiorbital models for the Fe pnictides. *New Journal of Physics*, 11(2):025016, 2009. URL http://stacks.iop.org/1367-2630/11/i=2/a=025016. (Cited on pages 71, 137, and 142).

[74] M. J. Calderón, B. Valenzuela, and E. Bascones. Tight-binding model for iron pnictides. *Phys. Rev. B*, 80:094531, 2009. doi: 10.1103/PhysRevB.80.094531. URL https://link.aps.org/doi/10.1103/PhysRevB.80.094531. (Cited on pages 28, 29, 63, 64, 65, 66, 69, and 73).

[75] Helmut Eschrig and Klaus Koepernik. Tight-binding models for the iron-based superconductors. *Phys. Rev. B*, 80:104503, 2009. doi: 10.1103/PhysRevB.80.104503. URL https://link.aps.org/doi/10.1103/PhysRevB.80.104503. (Cited on page 30).

[76] P J Hirschfeld, M M Korshunov, and I I Mazin. Gap symmetry and structure of Fe-based superconductors. *Reports on Progress in Physics*, 74 (12):124508, 2011. URL http://stacks.iop.org/0034-4885/74/i=12/a=124508. (Cited on pages 31 and 71).

[77] I. I. Mazin, D. J. Singh, M. D. Johannes, and M. H. Du. Unconventional superconductivity with a sign reversal in the order parameter of $LaFeAsO_{1-x}F_x$. *Phys. Rev. Lett.*, 101:057003, 2008. doi: 10.1103/PhysRevLett.101.057003. URL https://link.aps.org/doi/10.1103/PhysRevLett.101.057003. (Cited on pages 29, 31, and 53).

[78] A. V. Chubukov, D. V. Efremov, and I. Eremin. Magnetism, superconductivity, and pairing symmetry in iron-based superconductors. *Phys. Rev. B*, 78:134512, 2008. doi: 10.1103/PhysRevB.78.134512. URL https://link.aps.org/doi/10.1103/PhysRevB.78.134512. (Cited on pages).

[79] V. Cvetkovic and Z. Tesanovic. Multiband magnetism and superconductivity in Fe-based compounds. *EPL (Europhysics Letters)*, 85(3):37002, 2009. URL http://stacks.iop.org/0295-5075/85/i=3/a=37002. (Cited on pages 29 and 53).

[80] Qimiao Si and Elihu Abrahams. Strong correlations and magnetic frustration in the high T_c iron pnictides. *Phys. Rev. Lett.*, 101:076401, 2008. doi: 10.1103/PhysRevLett.101.076401. URL https://link.aps.org/doi/10.1103/PhysRevLett.101.076401. (Cited on pages 29 and 53).

[81] Andres Castellanos-Gomez. Black phosphorus: Narrow gap, wide applications. *The Journal of Physical Chemistry Letters*, 6(21):4280–4291, 2015. doi: 10.1021/acs.jpclett.5b01686. URL https://doi.org/10.1021/acs.jpclett.5b01686. (Cited on page 33).

[82] Andres Castellanos-Gomez, Rafael Roldán, Emmanuele Cappelluti, Michele Buscema, Francisco Guinea, Herre S. J. van der Zant, and Gary A. Steele. Local strain engineering in atomically thin MoS2. *Nano Letters*, 13(11):5361–5366, 2013. doi: 10.1021/nl402875m. URL https://doi.org/10.1021/nl402875m. (Cited on page 33).

[83] B. Sipos, A. F. Kusmartseva, A. Akrap, H. Berger, L. Forró, and E. Tutis. From Mott state to superconductivity in 1T-TaS2. *Nature Materials*, 7:960, 2008. URL http://dx.doi.org/10.1038/nmat2318. (Cited on page 33).

[84] Yuan Cao, Valla Fatemi, Shiang Fang, Kenji Watanabe, Takashi Taniguchi, Efthimios Kaxiras, and Pablo Jarillo-Herrero. Unconventional superconductivity in magic-angle graphene superlattices. *Nature*, 556:43, 2018. URL http://dx.doi.org/10.1038/nature26160. (Cited on pages 33, 34, 89, 91, 93, 94, 96, 97, 105, 118, and 122).

[85] Yuan Cao, Valla Fatemi, Ahmet Demir, Shiang Fang, Spencer L. Tomarken, Jason Y. Luo, Javier D. Sanchez-Yamagishi, Kenji Watanabe, Takashi Taniguchi, Efthimios Kaxiras, Ray C. Ashoori, and Pablo Jarillo-Herrero. Correlated insulator behaviour at half-filling in magic-angle graphene superlattices. *Nature*, 556:80, 2018. URL http://dx.doi.org/10.1038/nature26154. (Cited on pages 33, 34, 35, 36, 37, 89, 91, 92, 94, 96, 97, 100, 101, 105, 118, and 122).

[86] S. Reich, J. Maultzsch, C. Thomsen, and P. Ordejón. Tight-binding description of graphene. *Phys. Rev. B*, 66:035412, 2002. doi: 10.1103/PhysRevB.66.035412. URL https://link.aps.org/doi/10.1103/PhysRevB.66.035412. (Cited on pages 34, 89, and 91).

[87] J. M. B. Lopes dos Santos, N. M. R. Peres, and A. H. Castro Neto. Graphene bilayer with a twist: Electronic structure. *Phys. Rev. Lett.*, 99:256802, 2007. doi: 10.1103/PhysRevLett.99.256802. URL https://link.aps.org/doi/10.1103/PhysRevLett.99.256802. (Cited on pages 89, 94, and 105).

[88] E. Suárez Morell, J. D. Correa, P. Vargas, M. Pacheco, and Z. Barticevic. Flat bands in slightly twisted bilayer graphene: Tight-binding calculations. *Phys. Rev. B*, 82:121407, 2010. doi: 10.1103/PhysRevB.82.121407. URL https://link.aps.org/doi/10.1103/PhysRevB.82.121407. (Cited on pages).

[89] Rafi Bistritzer and Allan H. MacDonald. Moiré bands in twisted double-layer graphene. 108(30):12233–12237, 2011. doi: 10.1073/pnas.1108174108. URL http://www.pnas.org/content/108/30/12233. (Cited on pages 34, 35, 89, 91, 94, and 105).

[90] Y. Cao, J. Y. Luo, V. Fatemi, S. Fang, J. D. Sanchez-Yamagishi, K. Watanabe, T. Taniguchi, E. Kaxiras, and P. Jarillo-Herrero. Superlattice-induced insulating states and valley-protected orbits in twisted bilayer graphene. *Phys. Rev. Lett.*, 117:116804, 2016. doi: 10.1103/PhysRevLett.117.116804. URL https://link.aps.org/doi/10.1103/PhysRevLett.117.116804. (Cited on pages 89 and 91).

[91] Shiang Fang and Efthimios Kaxiras. Electronic structure theory of weakly interacting bilayers. *Phys. Rev. B*, 93:235153, 2016. doi: 10.1103/PhysRevB.93.235153. URL https://link.aps.org/doi/10.1103/PhysRevB.93.235153. (Cited on pages 89, 91, 94, and 105).

[92] Luis A. Gonzalez-Arraga, J. L. Lado, Francisco Guinea, and Pablo San-Jose. Electrically controllable magnetism in twisted bilayer graphene. *Phys. Rev. Lett.*, 119:107201, 2017. doi: 10.1103/PhysRevLett.119.107201. URL https://link.aps.org/doi/10.1103/PhysRevLett.119.107201. (Cited on pages 89 and 91).

[93] Mikito Koshino, Noah F. Q. Yuan, Takashi Koretsune, Masayuki Ochi, Kazuhiko Kuroki, and Liang Fu. Maximally localized Wannier orbitals and the extended Hubbard model for twisted bilayer graphene. *Phys. Rev. X*, 8:031087, 2018. doi: 10.1103/PhysRevX.8.031087. URL https://link.aps.org/doi/10.1103/PhysRevX.8.031087. (Cited on pages 34, 35, 36, 90, 91, 94, 95, 97, 102, and 105).

[94] A. H. Castro Neto, F. Guinea, N. M. R. Peres, K. S. Novoselov, and A. K. Geim. The electronic properties of graphene. *Rev. Mod. Phys.*, 81:109–162, 2009. URL https://link.aps.org/doi/10.1103/RevModPhys.81.109. (Cited on page 34).

[95] G. Chen, L. Jiang, S. Wu, B. Lv, H. Li, K. Watanabe, T. Taniguchi, Z. Shi, Y. Zhang, and F. Wang. Gate-tunable mott insulator in trilayer graphene-boron nitride moiré superlattice. *ArXiv e-prints*, 2018. URL https://arxiv.org/abs/1803.01985. (Cited on page 34).

[96] J. M. Pizarro, M. J. Calderón, J. Liu, M. C. Muñoz, and E. Bascones. Strong correlations and the search for high-T_c superconductivity in chromium pnictides and chalcogenides. *Phys. Rev. B*, 95:075115, 2017. doi: 10.1103/PhysRevB.95.075115. URL https://link.aps.org/doi/10.1103/PhysRevB.95.075115. (Cited on pages 37, 60, 62, 64, 118, and 121).

[97] J. M. Pizarro and E. Bascones. Strong electronic correlations and fermi surface reconstruction in the quasi-one-dimensional iron superconductor $bafe_2s_3$. *Phys. Rev. Materials*, 3:014801, 2019. URL https://link.aps.org/doi/10.1103/PhysRevMaterials.3.014801. (Cited on pages 37, 75, 80, 81, 118, and 121).

[98] Ryotaro Arita, Hiroaki Ikeda, Shiro Sakai, and Michi-To Suzuki. Ab initio downfolding study of the iron-based ladder superconductor $BaFe_2S_3$. *Phys. Rev. B*, 92:054515, 2015. doi: 10.1103/PhysRevB.92.054515. URL https://link.aps.org/doi/10.1103/PhysRevB.92.054515. (Cited on pages 37, 75, 76, 79, 80, 81, 83, 84, 88, 118, and 121).

[99] J.M. Pizarro, M.J. Calderón, and E. Bascones. The nature of correlations in the insulating states of twisted bilayer graphene. *ArXiv e-prints*, 2018. (Cited on pages 37, 89, 95, 103, 118, and 122).

[100] Taichi Terashima, Nobuyuki Kurita, Motoi Kimata, Megumi Tomita, Satoshi Tsuchiya, Motoharu Imai, Akira Sato, Kunihiro Kihou, Chul-Ho Lee, Hijiri Kito, Hiroshi Eisaki, Akira Iyo, Taku Saito, Hideto Fukazawa, Yoh Kohori, Hisatomo Harima, and Shinya Uji. Fermi surface in KFe_2As_2 determined via de Haas–van Alphen oscillation measurements. *Phys. Rev. B*, 87:224512, 2013. doi: 10.1103/PhysRevB.87.224512. URL https://link.aps.org/doi/10.1103/PhysRevB.87.224512. (Cited on pages 39, 51, 58, 59, and 62).

[101] F. Hardy, A. E. Böhmer, D. Aoki, P. Burger, T. Wolf, P. Schweiss, R. Heid, P. Adelmann, Y. X. Yao, G. Kotliar, J. Schmalian, and C. Meingast. Evidence of strong correlations and coherence-incoherence crossover in the iron pnictide superconductor KFe_2As_2. *Phys. Rev. Lett.*, 111:027002, 2013. doi: 10.1103/PhysRevLett.111.027002. URL https://link.aps.org/doi/10.1103/PhysRevLett.111.027002. (Cited on pages).

[102] M. Nakajima, S. Ishida, T. Tanaka, K. Kihou, Y. Tomioka, T. Saito, C. H. Lee, H. Fukazawa, Y. Kohori, T. Kakeshita, A. Iyo, T. Ito, H. Eisaki, and S. Uchida. Normal-state charge dynamics in doped $BaFe2As2$: Roles of doping and necessary

ingredients for superconductivity. *Scientific Reports*, 4:5873 EP, 2014. URL http://dx.doi.org/10.1038/srep05873. (Cited on pages).

[103] Felix Eilers, Kai Grube, Diego A. Zocco, Thomas Wolf, Michael Merz, Peter Schweiss, Rolf Heid, Robert Eder, Rong Yu, Jian-Xin Zhu, Qimiao Si, Takasada Shibauchi, and Hilbert v. Löhneysen. Strain-driven approach to quantum criticality in $A\mathrm{Fe}_2\mathrm{As}_2$ with $A = \mathrm{K}$, *Rb*, and *Cs*. *Phys. Rev. Lett.*, 116:237003, 2016. doi: 10.1103/PhysRevLett.116.237003. URL https://link.aps.org/doi/10.1103/PhysRevLett.116.237003. (Cited on pages).

[104] F. Hardy, A. E. Böhmer, L. de' Medici, M. Capone, G. Giovannetti, R. Eder, L. Wang, M. He, T. Wolf, P. Schweiss, R. Heid, A. Herbig, P. Adelmann, R. A. Fisher, and C. Meingast. Strong correlations, strong coupling, and *s*-wave superconductivity in hole-doped $\mathrm{BaFe}_2\mathrm{As}_2$ single crystals. *Phys. Rev. B*, 94:205113, 2016. doi: 10.1103/PhysRevB.94.205113. URL https://link.aps.org/doi/10.1103/PhysRevB.94.205113. (Cited on pages 39, 51, 55, 57, 58, 59, and 62).

[105] J. Hubbard and B.H. Flowers. Electron correlations in narrow energy bands. *Proceedings of the Royal Society of London A: Mathematical, Physical and Engineering Sciences*, 276(1365):238–257, 1963. doi: 10.1098/rspa.1963.0204. URL http://rspa.royalsocietypublishing.org/content/276/1365/238. (Cited on page 39).

[106] Electron correlations in narrow energy bands. II. the degenerate band case. *Proceedings of the Royal Society of London A: Mathematical, Physical and Engineering Sciences*, 277(1369):237–259, 1964. doi: 10.1098/rspa.1964.0019. URL http://rspa.royalsocietypublishing.org/content/277/1369/237. (Cited on pages).

[107] Electron correlations in narrow energy bands III. an improved solution. *Proceedings of the Royal Society of London A: Mathematical, Physical and Engineering Sciences*, 281(1386):401–419, 1964. doi: 10.1098/rspa.1964.0190. URL http://rspa.royalsocietypublishing.org/content/281/1386/401. (Cited on pages).

[108] Electron correlations in narrow energy bands - IV. the atomic representation. *Proceedings of the Royal Society of London A: Mathematical, Physical and Engineering Sciences*, 285(1403):542–560, 1965. doi: 10.1098/rspa.1965.0124. URL http://rspa.royalsocietypublishing.org/content/285/1403/542. (Cited on page 39).

[109] Olle Gunnarsson, Erik Koch, and Richard M. Martin. Mott transition in degenerate Hubbard models: Application to doped fullerenes. *Phys. Rev. B*, 54:R11026–R11029, 1996. doi: 10.1103/PhysRevB.54.R11026. URL https://link.aps.org/doi/10.1103/PhysRevB.54.R11026. (Cited on page 41).

[110] S. Florens, A. Georges, G. Kotliar, and O. Parcollet. Mott transition at large orbital degeneracy: Dynamical mean-field theory. *Phys. Rev. B*, 66:205102, 2002. doi: 10.1103/PhysRevB.66.205102. URL https://link.aps.org/doi/10.1103/PhysRevB.66.205102. (Cited on page 42).

[111] E. Bascones, B. Valenzuela, and M. J. Calderón. Orbital differentiation and the role of orbital ordering in the magnetic state of *Fe* superconductors. *Phys. Rev. B*, 86:174508, 2012. doi: 10.1103/PhysRevB.86.174508. URL https://link.aps.org/doi/10.1103/PhysRevB.86.174508. (Cited on pages 51, 59, and 62).

[112] M. J. Calderón, L. de' Medici, B. Valenzuela, and E. Bascones. Correlation, doping, and interband effects on the optical conductivity of iron superconductors. *Phys. Rev.*

B, 90:115128, 2014. doi: 10.1103/PhysRevB.90.115128. URL https://link.aps.org/doi/10.1103/PhysRevB.90.115128. (Cited on pages 51, 59, and 62).

[113] Marcelo J. Rozenberg. Integer-filling metal-insulator transitions in the degenerate Hubbard model. *Phys. Rev. B*, 55:R4855–R4858, 1997. doi: 10.1103/PhysRevB.55.R4855. URL https://link.aps.org/doi/10.1103/PhysRevB.55.R4855. (Cited on pages 51, 90, 96, 97, 98, 99, 101, and 106).

[114] Ming Yi, Yan Zhang, Zhi-Xun Shen, and Donghui Lu. Role of the orbital degree of freedom in iron-based superconductors. *npj Quantum Materials*, 2(1):57, 2017. URL https://doi.org/10.1038/s41535-017-0059-y. (Cited on pages 57 and 85).

[115] M. Yi, Z.-K. Liu, Y. Zhang, R. Yu, J.-X. Zhu, J. J. Lee, R. G. Moore, F. T. Schmitt, W. Li, S. C. Riggs, J.-H. Chu, B. Lv, J. Hu, M. Hashimoto, S.-K. Mo, Z. Hussain, Z. Q. Mao, C. W. Chu, I. R. Fisher, Q. Si, Z.-X. Shen, and D. H. Lu. Observation of universal strong orbital-dependent correlation effects in iron chalcogenides. *Nature Communications*, 6, Jul 2015. URL https://doi.org/10.1038/ncomms8777. (Cited on page 57).

[116] Sang-Won Park, Hiroshi Mizoguchi, Katsuaki Kodama, Shin ichi Shamoto, Toshiya Otomo, Satoru Matsuishi, Toshio Kamiya, and Hideo Hosono. Magnetic structure and electromagnetic properties of $LnCrAsO$ with a $ZrCuSiAs$-type structure ($Ln = La, Ce, Pr$, and Nd). *Inorganic chemistry*, 52 23:13363–8, 2013. URL https://pubs.acs.org/doi/10.1021/ic401487q. (Cited on pages 60, 61, 64, 71, 73, and 74).

[117] B. J. Ramshaw, S. E. Sebastian, R. D. McDonald, James Day, B. S. Tan, Z. Zhu, J. B. Betts, Ruixing Liang, D. A. Bonn, W. N. Hardy, and N. Harrison. Quasiparticle mass enhancement approaching optimal doping in a high-tc superconductor. *Science*, 348 (6232):317–320, 2015. URL http://science.sciencemag.org/content/348/6232/317. (Cited on page 62).

[118] Philipp Werner, Michele Casula, Takashi Miyake, Ferdi Aryasetiawan, Andrew J. Millis, and Silke Biermann. Satellites and large doping and temperature dependence of electronic properties in hole-doped $BaFe_2As_2$. *Nature Physics*, 8:331, 2012. URL http://dx.doi.org/10.1038/nphys2250. (Cited on page 62).

[119] Takahiro Misawa, Kazuma Nakamura, and Masatoshi Imada. Ab initio evidence for strong correlation associated with Mott proximity in iron-based superconductors. *Phys. Rev. Lett.*, 108:177007, 2012. doi: 10.1103/PhysRevLett.108.177007. URL https://link.aps.org/doi/10.1103/PhysRevLett.108.177007. (Cited on page 62).

[120] Jin-Ke Bao, Ji-Yong Liu, Cong-Wei Ma, Zhi-Hao Meng, Zhang-Tu Tang, Yun-Lei Sun, Hui-Fei Zhai, Hao Jiang, Hua Bai, Chun-Mu Feng, Zhu-An Xu, and Guang-Han Cao. Superconductivity in quasi-one-dimensional $K_2Cr_3As_3$ with significant electron correlations. *Phys. Rev. X*, 5:011013, 2015. doi: 10.1103/PhysRevX.5.011013. URL https://link.aps.org/doi/10.1103/PhysRevX.5.011013. (Cited on page 62).

[121] J. W. Simonson, K. Post, C. Marques, G. Smith, O. Khatib, D. N. Basov, and M. C. Aronson. Gap states in insulating $LaMnPO_{1-x}F_x$ ($x = 0$–0.3). *Phys. Rev. B*, 84: 165129, 2011. doi: 10.1103/PhysRevB.84.165129. URL https://link.aps.org/doi/10.1103/PhysRevB.84.165129. (Cited on page 63).

[122] A. T. Satya, Awadhesh Mani, A. Arulraj, N. V. Chandra Shekar, K. Vinod, C. S. Sundar, and A. Bharathi. Pressure-induced metallization of $BaMn_2As_2$. *Phys. Rev. B*, 84:180515, 2011. doi: 10.1103/PhysRevB.84.180515. URL https://link.aps.org/doi/10.1103/PhysRevB.84.180515. (Cited on page 64).

[123] J. W. Simonson, Z. P. Yin, M. Pezzoli, J. Guo, J. Liu, K. Post, A. Efimenko, N. Hollmann, Z. Hu, H.-J. Lin, C.-T. Chen, C. Marques, V. Leyva, G. Smith, J. W. Lynn, L. L. Sun, G. Kotliar, D. N. Basov, L. H. Tjeng, and M. C. Aronson. From antiferromagnetic insulator to correlated metal in pressurized and doped $LaMnPO$. *Proceedings of the National Academy of Sciences*, 109(27):E1815–E1819, 2012. doi: 10.1073/pnas.1117366109. URL http://www.pnas.org/content/109/27/E1815. (Cited on pages).

[124] Jing Guo, J. W. Simonson, Liling Sun, Qi Wu, Peiwen Gao, Chao Zhang, Dachun Gu, Gabriel Kotliar, Meigan Aronson, and Zhongxian Zhao. Observation of antiferromagnetic order collapse in the pressurized insulator $LaMnPO$. *Scientific Reports*, 3:2555, 2013. URL http://dx.doi.org/10.1038/srep02555. (Cited on pages).

[125] Bayrammurad Saparov, David J. Singh, Vasile O. Garlea, and Athena S. Sefat. Crystal, magnetic, and electronic structures, and properties of new $BaMnPnF$ ($Pn = As, Sb, Bi$). *Scientific Reports*, 3:2154, 2013. URL http://dx.doi.org/10.1038/srep02154. (Cited on pages).

[126] A. Beleanu, J. Kiss, G. Kreiner, C. Köhler, L. Müchler, W. Schnelle, U. Burkhardt, S. Chadov, S. Medvediev, D. Ebke, G. Cordier, B. Albert, A. Hoser, F. Bernardi, T. I. Larkin, D. Pröpper, A. V. Boris, B. Keimer, and C. Felser. Large resistivity change and phase transition in $LiMnAs$. *ArXiv e-prints*, 2013. URL https://arxiv.org/abs/1307.6404. (Cited on pages).

[127] J. Lamsal, G. S. Tucker, T. W. Heitmann, A. Kreyssig, A. Jesche, Abhishek Pandey, Wei Tian, R. J. McQueeney, D. C. Johnston, and A. I. Goldman. Persistence of local-moment antiferromagnetic order in $Ba_{1-x}K_xMn_2As_2$. *Phys. Rev. B*, 87:144418, 2013. doi: 10.1103/PhysRevB.87.144418. URL https://link.aps.org/doi/10.1103/PhysRevB.87.144418. (Cited on pages).

[128] D. E. McNally, J. W. Simonson, K. W. Post, Z. P. Yin, M. Pezzoli, G. J. Smith, V. Leyva, C. Marques, L. DeBeer-Schmitt, A. I. Kolesnikov, Y. Zhao, J. W. Lynn, D. N. Basov, G. Kotliar, and M. C. Aronson. Antiferromagnetic exchange, Hund's coupling and the origin of the charge gap in $LaMnPO$. *ArXiv e-prints*, 2014. URL https://arxiv.org/abs/1402.6312. (Cited on pages).

[129] Shuai Dong, Wei Li, Xin Huang, and Elbio Dagotto. First principles study of the magnetic properties of $LaOMnAs$. *Journal of Applied Physics*, 115(17):17D723, 2014. doi: 10.1063/1.4867757. URL https://doi.org/10.1063/1.4867757. (Cited on pages).

[130] E. J. Wildman, N. Emery, and A. C. Mclaughlin. Electronic and magnetic properties of $Nd_{1-x}Sr_xMnAsO$ oxyarsenides. *Phys. Rev. B*, 90:224413, 2014. doi: 10.1103/PhysRevB.90.224413. URL https://link.aps.org/doi/10.1103/PhysRevB.90.224413. (Cited on pages).

[131] S. Calder, B. Saparov, H. B. Cao, J. L. Niedziela, M. D. Lumsden, A. S. Sefat, and A. D. Christianson. Magnetic structure and spin excitations in $BaMn_2Bi_2$. *Phys. Rev. B*, 89:064417, 2014. doi: 10.1103/PhysRevB.89.064417. URL https://link.aps.org/doi/10.1103/PhysRevB.89.064417. (Cited on pages).

[132] Dachun Gu, Xia Dai, Congcong Le, Liling Sun, Qi Wu, Bayrammurad Saparov, Jing Guo, Peiwen Gao, Shan Zhang, Yazhou Zhou, Chao Zhang, Shifeng Jin, Lun Xiong, Rui Li, Yanchun Li, Xiaodong Li, Jing Liu, Athena S. Sefat, Jiangping

Hu, and Zhongxian Zhao. Robust antiferromagnetism preventing superconductivity in pressurized $(Ba_{0.61}K_{0.39})Mn_2Bi_2$. *Scientific Reports*, 4:7342, 2014. URL http://dx.doi.org/10.1038/srep07342. (Cited on pages).

[133] Qiang Zhang, Wei Tian, Spencer G. Peterson, Kevin W. Dennis, and David Vaknin. Spin reorientation and Ce–Mn coupling in antiferromagnetic oxypnictide $CeMnAsO$. *Phys. Rev. B*, 91:064418, 2015. doi: 10.1103/PhysRevB.91.064418. URL https://link.aps.org/doi/10.1103/PhysRevB.91.064418. (Cited on pages).

[134] B. G. Ueland, Abhishek Pandey, Y. Lee, A. Sapkota, Y. Choi, D. Haskel, R. A. Rosenberg, J. C. Lang, B. N. Harmon, D. C. Johnston, A. Kreyssig, and A. I. Goldman. Itinerant ferromagnetism in the As $4p$ conduction band of $Ba_{0.6}K_{0.4}Mn_2As_2$ identified by x-ray magnetic circular dichroism. *Phys. Rev. Lett.*, 114:217001, 2015. doi: 10.1103/PhysRevLett.114.217001. URL https://link.aps.org/doi/10.1103/PhysRevLett.114.217001. (Cited on pages).

[135] Abhishek Pandey and D. C. Johnston. $Ba_{0.4}Rb_{0.6}Mn_2As_2$: A prototype half-metallic ferromagnet. *Phys. Rev. B*, 92:174401, Nov 2015. doi: 10.1103/PhysRevB.92.174401. URL https://link.aps.org/doi/10.1103/PhysRevB.92.174401. (Cited on pages).

[136] D. E. McNally, S. Zellman, Z. P. Yin, K. W. Post, Hua He, K. Hao, G. Kotliar, D. Basov, C. C. Homes, and M. C. Aronson. From hund's insulator to fermi liquid: Optical spectroscopy study of K doping in $BaMn_2As_2$. *Phys. Rev. B*, 92: 115142, 2015. doi: 10.1103/PhysRevB.92.115142. URL https://link.aps.org/doi/10.1103/PhysRevB.92.115142. (Cited on pages).

[137] Michael A. McGuire and V. Ovidiu Garlea. Short- and long-range magnetic order in $LaMnAsO$. *Phys. Rev. B*, 93:054404, 2016. doi: 10.1103/PhysRevB.93.054404. URL https://link.aps.org/doi/10.1103/PhysRevB.93.054404. (Cited on pages).

[138] Qiang Zhang, C. M. N. Kumar, Wei Tian, Kevin W. Dennis, Alan I. Goldman, and David Vaknin. Structure and magnetic properties of LnMnSbO (Ln = La and Ce). *Phys. Rev. B*, 93:094413, 2016. doi: 10.1103/PhysRevB.93.094413. URL https://link.aps.org/doi/10.1103/PhysRevB.93.094413. (Cited on pages).

[139] Manuel Zingl, Elias Assmann, Priyanka Seth, Igor Krivenko, and Markus Aichhorn. Importance of effective dimensionality in manganese pnictides. *Phys. Rev. B*, 94: 045130, 2016. doi: 10.1103/PhysRevB.94.045130. URL https://link.aps.org/doi/10.1103/PhysRevB.94.045130. (Cited on page 63).

[140] D. J. Singh, A. S. Sefat, M. A. McGuire, B. C. Sales, D. Mandrus, L. H. VanBebber, and V. Keppens. Itinerant antiferromagnetism in $BaCr_2As_2$: Experimental characterization and electronic structure calculations. *Phys. Rev. B*, 79:094429, 2009. doi: 10.1103/PhysRevB.79.094429. URL https://link.aps.org/doi/10.1103/PhysRevB.79.094429. (Cited on page 64).

[141] Yi Ding, Yanli Wang, and Jun Ni. Electronic and magnetic properties of 3d transition-metal selenides from first principles. *Solid State Communications*, 149(13):505 – 509, 2009. doi: https://doi.org/10.1016/j.ssc.2009.01.015. URL http://www.sciencedirect.com/science/article/pii/S0038109809000295. (Cited on page 64).

[142] Shu-Jun Hu and Xiao Hu. Half-metallic antiferromagnet bacrfeas2. *The Journal of Physical Chemistry C*, 114(26):11614–11617, 2010. doi: 10.1021/jp103328g. URL https://doi.org/10.1021/jp103328g. (Cited on page 64).

[143] S.-J. Hu and X. Hu. Half-metallic antiferromagnet sheets in $Sr_4M_2O_6CrFeAs_2$ ($M = Sc, Cr$) and their bulk form. *ArXiv e-prints*, 2010. URL https://arxiv.org/abs/1011.2576. (Cited on pages).

[144] K. Marty, A. D. Christianson, C. H. Wang, M. Matsuda, H. Cao, L. H. VanBebber, J. L. Zarestky, D. J. Singh, A. S. Sefat, and M. D. Lumsden. Competing magnetic ground states in nonsuperconducting $Ba(Fe_{1-x}Cr_x)_2As_2$ as seen via neutron diffraction. *Phys. Rev. B*, 83:060509, 2011. doi: 10.1103/PhysRevB.83.060509. URL https://link.aps.org/doi/10.1103/PhysRevB.83.060509. (Cited on page 64).

[145] U. B. Paramanik, R. Prasad, C. Geibel, and Z. Hossain. Itinerant and local-moment magnetism in $EuCr_2As_2$ single crystals. *Phys. Rev. B*, 89:144423, 2014. doi: 10.1103/PhysRevB.89.144423. URL https://link.aps.org/doi/10.1103/PhysRevB.89.144423. (Cited on page 64).

[146] Hao Jiang, Jin-Ke Bao, Hui-Fei Zhai, Zhang-Tu Tang, Yun-Lei Sun, Yi Liu, Zhi-Cheng Wang, Hua Bai, Zhu-An Xu, and Guang-Han Cao. Physical properties and electronic structure of $Sr_2Cr_3As_2O_2$ containing CrO_2 and Cr_2As_2 square-planar lattices. *Phys. Rev. B*, 92:205107, 2015. doi: 10.1103/PhysRevB.92.205107. URL https://link.aps.org/doi/10.1103/PhysRevB.92.205107. (Cited on page 64).

[147] J. C. Slater and G. F. Koster. Simplified LCAO method for the periodic potential problem. *Phys. Rev.*, 94:1498–1524, 1954. doi: 10.1103/PhysRev.94.1498. URL https://link.aps.org/doi/10.1103/PhysRev.94.1498. (Cited on page 65).

[148] Tetsuya Takimoto, Takashi Hotta, and Kazuo Ueda. Strong-coupling theory of superconductivity in a degenerate Hubbard model. *Phys. Rev. B*, 69:104504, 2004. doi: 10.1103/PhysRevB.69.104504. URL https://link.aps.org/doi/10.1103/PhysRevB.69.104504. (Cited on page 71).

[149] Katsunori Kubo. Pairing symmetry in a two-orbital Hubbard model on a square lattice. *Phys. Rev. B*, 75:224509, 2007. doi: 10.1103/PhysRevB.75.224509. URL https://link.aps.org/doi/10.1103/PhysRevB.75.224509. (Cited on page 71).

[150] Martin Edelmann, Giorgio Sangiovanni, Massimo Capone, and Luca de' Medici. Chromium analogs of iron-based superconductors. *Phys. Rev. B*, 95:205118, 2017. doi: 10.1103/PhysRevB.95.205118. URL https://link.aps.org/doi/10.1103/PhysRevB.95.205118. (Cited on page 74).

[151] Kai A. Filsinger, Walter Schnelle, Peter Adler, Gerhard H. Fecher, Manfred Reehuis, Andreas Hoser, Jens-Uwe Hoffmann, Peter Werner, Martha Greenblatt, and Claudia Felser. Antiferromagnetic structure and electronic properties of $BaCr_2As_2$ and $BaCrFeAs_2$. *Phys. Rev. B*, 95:184414, May 2017. doi: 10.1103/PhysRevB.95.184414. URL https://link.aps.org/doi/10.1103/PhysRevB.95.184414. (Cited on page 74).

[152] Jayita Nayak, Kai Filsinger, Gerhard H. Fecher, Stanislav Chadov, Ján Minár, Emile D. L. Rienks, Bernd Büchner, Stuart P. Parkin, Jörg Fink, and Claudia Felser. Observation of a remarkable reduction of correlation effects in $BaCr_2As_2$ by ARPES. *Proceedings of the National Academy of Sciences*, 114(47):12425–12429, 2017. doi: 10.1073/pnas.1702234114. URL http://www.pnas.org/content/114/47/12425. (Cited on pages).

[153] P. Richard, A. van Roekeghem, B. Q. Lv, Tian Qian, T. K. Kim, M. Hoesch, J.-P. Hu, Athena S. Sefat, Silke Biermann, and H. Ding. Is $\mathbf{BaCr_2As_2}$ symmetrical to $\mathbf{BaFe_2As_2}$ with respect to half $3d$ shell filling? *Phys. Rev. B*, 95:184516, 2017. doi: 10.1103/PhysRevB.95.184516. URL https://link.aps.org/doi/10.1103/PhysRevB.95.184516. (Cited on page 74).

[154] R.A. Jishi, J.P. Rodriguez, T.J. Haugan, and M.A. Susner. Prediction of antiferromagnetism in chromium-phosphide confirmed by synthesis. *ArXiv e-prints*, 2018. URL https://arxiv.org/abs/1807.03041. (Cited on page 74).

[155] H. Takahashi, A. Sugimoto, Y. Nambu, T. Yamauchi, Y. Hirata, T. Kawakami, V. Avdeev, K. Matsubayashi, Ch. Du, F.and Kawashima, H. Soeda, S. Nakano, Y. Uwatoko, Y. Ueda, T.J. Sato, and K. Ohgushi. Pressure-induced superconductivity in the iron-based ladder material $BaFe_2S_3$. *Nature Materials*, 14:1008, 2015. doi: 10.1038/nmat4351. URL https://www.nature.com/articles/nmat4351. (Cited on pages 75, 77, 78, 79, 87, and 88).

[156] Touru Yamauchi, Yasuyuki Hirata, Yutaka Ueda, and Kenya Ohgushi. Pressure-induced Mott transition followed by a 24-K superconducting phase in $BaFe_2S_3$. *Phys. Rev. Lett.*, 115:246402, 2015. doi: 10.1103/PhysRevLett.115.246402. URL https://link.aps.org/doi/10.1103/PhysRevLett.115.246402. (Cited on pages 75, 77, 79, and 88).

[157] Jianjun Ying, Hechang Lei, Cedomir Petrovic, Yuming Xiao, and Viktor V. Struzhkin. Interplay of magnetism and superconductivity in the compressed Fe-ladder compound $BaFe_2Se_3$. *Phys. Rev. B*, 95:241109, 2017. doi: 10.1103/PhysRevB.95.241109. URL https://link.aps.org/doi/10.1103/PhysRevB.95.241109. (Cited on pages 75, 77, 78, 79, and 87).

[158] J. M. Caron, J. R. Neilson, D. C. Miller, A. Llobet, and T. M. McQueen. Iron displacements and magnetoelastic coupling in the antiferromagnetic spin-ladder compound $BaFe_2Se_3$. *Phys. Rev. B*, 84:180409, 2011. doi: 10.1103/PhysRevB.84.180409. URL https://link.aps.org/doi/10.1103/PhysRevB.84.180409. (Cited on page 77).

[159] M. V. Medvedev, I. A. Nekrasov, and M. V. Sadovskii. Electronic and magnetic structure of a possible iron based superconductor $BaFe_2Se_3$. *JETP Letters*, 95(1): 33–37, 2012. doi: 10.1134/S0021364012010092. URL https://doi.org/10.1134/S0021364012010092. (Cited on pages).

[160] Qinlong Luo, Andrew Nicholson, Julián Rincón, Shuhua Liang, José Riera, Gonzalo Alvarez, Limin Wang, Wei Ku, German D. Samolyuk, Adriana Moreo, and Elbio Dagotto. Magnetic states of the two-leg-ladder alkali metal iron selenides AFe_2Se_3. *Phys. Rev. B*, 87:024404, 2013. doi: 10.1103/PhysRevB.87.024404. URL https://link.aps.org/doi/10.1103/PhysRevB.87.024404. (Cited on pages 77 and 80).

[161] Songxue Chi, Yoshiya Uwatoko, Huibo Cao, Yasuyuki Hirata, Kazuki Hashizume, Takuya Aoyama, and Kenya Ohgushi. Magnetic precursor of the pressure-induced superconductivity in Fe-ladder compounds. *Phys. Rev. Lett.*, 117:047003, 2016. doi: 10.1103/PhysRevLett.117.047003. URL https://link.aps.org/doi/10.1103/PhysRevLett.117.047003. (Cited on pages 77 and 80).

[162] Meng Wang, S. J. Jin, Ming Yi, Yu Song, H. C. Jiang, W. L. Zhang, H. L. Sun, H. Q. Luo, A. D. Christianson, E. Bourret-Courchesne, D. H. Lee, Dao-Xin Yao, and

R. J. Birgeneau. Strong ferromagnetic exchange interaction under ambient pressure in $BaFe_2S_3$. *Phys. Rev. B*, 95:060502, 2017. doi: 10.1103/PhysRevB.95.060502. URL https://link.aps.org/doi/10.1103/PhysRevB.95.060502. (Cited on page 77).

[163] V. Svitlyk, G. Garbarino, A. D. Rosa, E. Pomjakushina, A. Krzton-Maziopa, K. Conder, M. Nunez-Regueiro, and M. Mezouar. High-pressure polymorphism of $BaFe_2Se_3$. *ArXiv e-prints*, 2018. URL https://arxiv.org/abs/1808.03952. (Cited on page 78).

[164] Michi-To Suzuki, Ryotaro Arita, and Hiroaki Ikeda. First-principles study of magnetic properties in Fe-ladder compound $BaFe_2S_3$. *Phys. Rev. B*, 92:085116, 2015. doi: 10.1103/PhysRevB.92.085116. URL https://link.aps.org/doi/10.1103/PhysRevB.92.085116. (Cited on pages 77, 80, and 82).

[165] Yusuke Nambu, Kenya Ohgushi, Shunpei Suzuki, Fei Du, Maxim Avdeev, Yoshiya Uwatoko, Koji Munakata, Hiroshi Fukazawa, Songxue Chi, Yutaka Ueda, and Taku J. Sato. Block magnetism coupled with local distortion in the iron-based spin-ladder compound $BaFe_2Se_3$. *Phys. Rev. B*, 85:064413, 2012. doi: 10.1103/PhysRevB.85.064413. URL https://link.aps.org/doi/10.1103/PhysRevB.85.064413. (Cited on pages 77 and 79).

[166] J. M. Caron, J. R. Neilson, D. C. Miller, K. Arpino, A. Llobet, and T. M. McQueen. Orbital-selective magnetism in the spin-ladder iron selenides $Ba_{1-x}K_xFe_2Se_3$. *Phys. Rev. B*, 85:180405, 2012. doi: 10.1103/PhysRevB.85.180405. URL https://link.aps.org/doi/10.1103/PhysRevB.85.180405. (Cited on pages 77 and 78).

[167] Yasuyuki Hirata, Sachiko Maki, Jun-ichi Yamaura, Touru Yamauchi, and Kenya Ohgushi. Effects of stoichiometry and substitution in quasi-one-dimensional iron chalcogenide $BaFe_2S_3$. *Phys. Rev. B*, 92:205109, 2015. doi: 10.1103/PhysRevB.92.205109. URL https://link.aps.org/doi/10.1103/PhysRevB.92.205109. (Cited on page 78).

[168] Fei Du, Kenya Ohgushi, Yusuke Nambu, Takateru Kawakami, Maxim Avdeev, Yasuyuki Hirata, Yoshitaka Watanabe, Taku J Sato, and Yutaka Ueda. Stripelike magnetism in a mixed-valence insulating state of the Fe-based ladder compound $CsFe_2Se_3$. *Phys. Rev. B*, 85:214436, 2012. doi: 10.1103/PhysRevB.85.214436. URL https://link.aps.org/doi/10.1103/PhysRevB.85.214436. (Cited on page 79).

[169] Yang Zhang, Ling-Fang Lin, Jun-Jie Zhang, Elbio Dagotto, and Shuai Dong. Sequential structural and antiferromagnetic transitions in $BaFe_2Se_3$ under pressure. *Phys. Rev. B*, 97:045119, 2018. doi: 10.1103/PhysRevB.97.045119. URL https://link.aps.org/doi/10.1103/PhysRevB.97.045119. (Cited on page 80).

[170] D. Ootsuki, N. L. Saini, F. Du, Y. Hirata, K. Ohgushi, Y. Ueda, and T. Mizokawa. Coexistence of localized and itinerant electrons in $BaFe_2X_3$ (X = S and Se) revealed by photoemission spectroscopy. *Phys. Rev. B*, 91:014505, 2015. doi: 10.1103/PhysRevB.91.014505. URL https://link.aps.org/doi/10.1103/PhysRevB.91.014505. (Cited on page 80).

[171] Kou Takubo, Yuichi Yokoyama, Hiroki Wadati, Shun Iwasaki, Takashi Mizokawa, Teak Boyko, Ronny Sutarto, Feizhou He, Kazuki Hashizume, Satoshi Imaizumi, Takuya Aoyama, Yoshinori Imai, and Kenya Ohgushi. Orbital order and fluctuations in the two-leg ladder materials $BaFe_2X_3$ (X = S and Se) and $CsFe_2Se_3$. *Phys. Rev. B*, 96:115157, 2017. doi: 10.1103/PhysRevB.96.115157. URL https://link.aps.org/doi/10.1103/PhysRevB.96.115157. (Cited on page 80).

[172] Niravkumar D. Patel, Alberto Nocera, Gonzalo Alvarez, Ryotaro Arita, Adriana Moreo, and Elbio Dagotto. Magnetic properties and pairing tendencies of the iron-based superconducting ladder $bafe_2s_3$: Combined ab initio and density matrix renormalization group study. *Phys. Rev. B*, 94:075119, 2016. URL https://link.aps.org/doi/10.1103/PhysRevB.94.075119. (Cited on page 80).

[173] S. Li, N. Kaushal, Y. Wang, Y. Tang, G. Alvarez, A. Nocera, T. A. Maier, E. Dagotto, and S. Johnston. Nonlocal correlations in the orbital selective mott phase of a one-dimensional multiorbital hubbard model. *Phys. Rev. B*, 94:235126, 2016. URL https://link.aps.org/doi/10.1103/PhysRevB.94.235126. (Cited on page 80).

[174] L. Fanfarillo, G. Giovannetti, M. Capone, and E. Bascones. Nematicity at the hund's metal crossover in iron superconductors. *Phys. Rev. B*, 95:144511, 2017. URL https://link.aps.org/doi/10.1103/PhysRevB.95.144511. (Cited on page 84).

[175] Pablo Jarillo-Herrero. Magic-angle graphene superlattice. APS March meeting 2018 talk, Mar 2018. URL https://www.youtube.com/watch?v=O2HVCjhuJlE&t=. (Cited on pages 89 and 94).

[176] M. Yankowitz, S. Chen, H. Polshyn, K. Watanabe, T. Taniguchi, D. Graf, A. F. Young, and C.R. Dean. Tuning superconductivity in twisted bilayer graphene. *ArXiv e-prints*, 2018. URL https://arxiv.org/abs/1808.07865. (Cited on page 89).

[177] Noah F. Q. Yuan and Liang Fu. Model for the metal-insulator transition in graphene superlattices and beyond. *Phys. Rev. B*, 98:045103, 2018. doi: 10.1103/PhysRevB.98.045103. URL https://link.aps.org/doi/10.1103/PhysRevB.98.045103. (Cited on pages 89, 90, 91, 94, 96, 97, 98, 99, 102, 105, 106, and 107).

[178] Hoi Chun Po, Liujun Zou, Ashvin Vishwanath, and T. Senthil. Origin of Mott insulating behavior and superconductivity in twisted bilayer graphene. *Phys. Rev. X*, 8:031089, 2018. doi: 10.1103/PhysRevX.8.031089. URL https://link.aps.org/doi/10.1103/PhysRevX.8.031089. (Cited on page 107).

[179] Jian Kang and Oskar Vafek. Symmetry, maximally localized Wannier states, and a low-energy model for twisted bilayer graphene narrow bands. *Phys. Rev. X*, 8:031088, 2018. doi: 10.1103/PhysRevX.8.031088. URL https://link.aps.org/doi/10.1103/PhysRevX.8.031088. (Cited on pages 89, 91, 94, 102, 105, and 107).

[180] L. Rademaker and P. Mellado. Charge-transfer insulation in twisted bilayer graphene. *ArXiv e-prints*, 2018. URL https://arxiv.org/abs/1805.05294. (Cited on pages 90 and 91).

[181] J. E. Han, M. Jarrell, and D. L. Cox. Multiorbital Hubbard model in infinite dimensions: Quantum Monte Carlo calculation. *Phys. Rev. B*, 58:R4199–R4202, 1998. doi: 10.1103/PhysRevB.58.R4199. URL https://link.aps.org/doi/10.1103/PhysRevB.58.R4199. (Cited on pages 90, 96, 97, 98, 99, and 106).

[182] Luca de' Medici. Hund's coupling and its key role in tuning multiorbital correlations. *Phys. Rev. B*, 83:205112, 2011. doi: 10.1103/PhysRevB.83.205112. URL https://link.aps.org/doi/10.1103/PhysRevB.83.205112. (Cited on pages 90, 96, 97, 98, 99, and 106).

[183] J. F. Dodaro, S. A. Kivelson, Y. Schattner, X. Q. Sun, and C. Wang. Phases of a phenomenological model of twisted bilayer graphene. *Phys. Rev. B*, 98:075154,

2018. doi: 10.1103/PhysRevB.98.075154. URL https://link.aps.org/doi/10.1103/PhysRevB.98.075154. (Cited on pages 90, 96, 101, 104, and 106).

[184] C.-C. Liu, L.-D. Zhang, W.-Q. Chen, and F. Yang. Chiral SDW and d + id superconductivity in the magic-angle twisted bilayer-graphene. *ArXiv e-prints*, 2018. URL https://arxiv.org/abs/1804.10009. (Cited on pages 90, 96, 101, 104, and 106).

[185] Thomas Maier, Mark Jarrell, Thomas Pruschke, and Matthias H. Hettler. Quantum cluster theories. *Rev. Mod. Phys.*, 77:1027–1080, 2005. doi: 10.1103/RevModPhys.77.1027. URL https://link.aps.org/doi/10.1103/RevModPhys.77.1027. (Cited on pages 90, 96, 102, and 106).

[186] A. I. Poteryaev, A. I. Lichtenstein, and G. Kotliar. Nonlocal coulomb interactions and metal-insulator transition in Ti_2O_3: A Cluster LDA + DMFT approach. *Phys. Rev. Lett.*, 93:086401, 2004. doi: 10.1103/PhysRevLett.93.086401. URL https://link.aps.org/doi/10.1103/PhysRevLett.93.086401. (Cited on pages).

[187] S. Biermann, A. Poteryaev, A. I. Lichtenstein, and A. Georges. Dynamical singlets and correlation-assisted Peierls transition in VO_2. *Phys. Rev. Lett.*, 94:026404, 2005. doi: 10.1103/PhysRevLett.94.026404. URL https://link.aps.org/doi/10.1103/PhysRevLett.94.026404. (Cited on pages).

[188] Tomoko Kita, Takuma Ohashi, and Sei-ichiro Suga. Spatial fluctuations of spin and orbital nature in the two-orbital Hubbard model. *Phys. Rev. B*, 79:245128, 2009. doi: 10.1103/PhysRevB.79.245128. URL https://link.aps.org/doi/10.1103/PhysRevB.79.245128. (Cited on pages 102, 103, 104, 105, and 106).

[189] Yusuke Nomura, Shiro Sakai, and Ryotaro Arita. Multiorbital cluster dynamical mean-field theory with an improved continuous-time quantum Monte Carlo algorithm. *Phys. Rev. B*, 89:195146, 2014. doi: 10.1103/PhysRevB.89.195146. URL https://link.aps.org/doi/10.1103/PhysRevB.89.195146. (Cited on pages 105 and 106).

[190] Yusuke Nomura, Shiro Sakai, and Ryotaro Arita. Nonlocal correlations induced by Hund's coupling: A cluster DMFT study. *Phys. Rev. B*, 91:235107, 2015. doi: 10.1103/PhysRevB.91.235107. URL https://link.aps.org/doi/10.1103/PhysRevB.91.235107. (Cited on pages).

[191] Ansgar Liebsch and Wei Wu. Coulomb correlations in the honeycomb lattice: Role of translation symmetry. *Phys. Rev. B*, 87:205127, 2013. doi: 10.1103/PhysRevB.87.205127. URL https://link.aps.org/doi/10.1103/PhysRevB.87.205127. (Cited on pages 102 and 106).

[192] Qing-Xiao Li, Rong-Qiang He, and Zhong-Yi Lu. Correlated Dirac semimetal by periodized cluster dynamical mean-field theory. *Phys. Rev. B*, 92:155127, 2015. doi: 10.1103/PhysRevB.92.155127. URL https://link.aps.org/doi/10.1103/PhysRevB.92.155127. (Cited on pages 102 and 106).

[193] Tsutomu Momoi and Kenn Kubo. Ferromagnetism in the Hubbard model with orbital degeneracy in infinite dimensions. *Phys. Rev. B*, 58:R567–R570, 1998. doi: 10.1103/PhysRevB.58.R567. URL https://link.aps.org/doi/10.1103/PhysRevB.58.R567. (Cited on pages 103 and 106).

[194] Francisco H. Kim, Karlo Penc, Pierre Nataf, and Frédéric Mila. Linear flavor-wave theory for fully antisymmetric $SU(N)$ irreducible representations. *Phys. Rev. B*, 96:

205142, 2017. doi: 10.1103/PhysRevB.96.205142. URL https://link.aps.org/doi/10.1103/PhysRevB.96.205142. (Cited on pages).

[195] Caterina De Franco, Luca F. Tocchio, and Federico Becca. Metal-insulator transitions, superconductivity, and magnetism in the two-band Hubbard model. *Phys. Rev. B*, 98: 075117, 2018. doi: 10.1103/PhysRevB.98.075117. URL https://link.aps.org/doi/10.1103/PhysRevB.98.075117. (Cited on pages).

[196] Zhichao Zhou, Da Wang, Zi Yang Meng, Yu Wang, and Congjun Wu. Mott insulating states and quantum phase transitions of correlated SU($2N$) Dirac fermions. *Phys. Rev. B*, 93:245157, 2016. doi: 10.1103/PhysRevB.93.245157. URL https://link.aps.org/doi/10.1103/PhysRevB.93.245157. (Cited on pages).

[197] Philippe Corboz, Miklós Lajkó, Andreas M. Läuchli, Karlo Penc, and Frédéric Mila. Spin-orbital quantum liquid on the honeycomb lattice. *Phys. Rev. X*, 2:041013, 2012. doi: 10.1103/PhysRevX.2.041013. URL https://link.aps.org/doi/10.1103/PhysRevX.2.041013. (Cited on pages).

[198] D. Jakab, E. Szirmai, M. Lewenstein, and G. Szirmai. Competing valence bond and symmetry-breaking Mott states of spin-$\frac{3}{2}$ fermions on a honeycomb lattice. *Phys. Rev. B*, 93:064434, 2016. doi: 10.1103/PhysRevB.93.064434. URL https://link.aps.org/doi/10.1103/PhysRevB.93.064434. (Cited on pages).

[199] Philippe Corboz, Andreas M. Läuchli, Karlo Penc, Matthias Troyer, and Frédéric Mila. Simultaneous dimerization and SU(4) symmetry breaking of 4-color fermions on the square lattice. *Phys. Rev. Lett.*, 107:215301, 2011. doi: 10.1103/PhysRevLett.107.215301. URL https://link.aps.org/doi/10.1103/PhysRevLett.107.215301. (Cited on pages 90, 96, 102, and 106).

[200] H.C. Po, L. Zou, T. Senthil, and A. Vishwanath. Faithful tight-binding models and fragile topology of magic-angle bilayer graphene. *ArXiv e-prints*, 2018. URL https://arxiv.org/abs/1808.02482. (Cited on pages 91, 102, and 107).

[201] Yu Saito, Tsutomu Nojima, and Yoshihiro Iwasa. Highly crystalline 2D superconductors. *Nature Reviews Materials*, 2:16094, 2016. URL http://dx.doi.org/10.1038/natrevmats.2016.94. (Cited on page 93).

[202] Dmitry K. Efimkin and Allan H. MacDonald. Helical network model for twisted bilayer graphene. *Phys. Rev. B*, 98:035404, 2018. doi: 10.1103/PhysRevB.98.035404. URL https://link.aps.org/doi/10.1103/PhysRevB.98.035404. (Cited on pages 94 and 105).

[203] Cenke Xu and Leon Balents. Topological superconductivity in twisted multilayer graphene. *Phys. Rev. Lett.*, 121:087001, 2018. doi: 10.1103/PhysRevLett.121.087001. URL https://link.aps.org/doi/10.1103/PhysRevLett.121.087001. (Cited on pages).

[204] Huaiming Guo, Xingchuan Zhu, Shiping Feng, and Richard T. Scalettar. Pairing symmetry of interacting fermions on a twisted bilayer graphene superlattice. *Phys. Rev. B*, 97:235453, 2018. doi: 10.1103/PhysRevB.97.235453. URL https://link.aps.org/doi/10.1103/PhysRevB.97.235453. (Cited on pages 94 and 105).

[205] Pilkyung Moon and Mikito Koshino. Optical absorption in twisted bilayer graphene. *Phys. Rev. B*, 87:205404, 2013. URL https://link.aps.org/doi/10.1103/PhysRevB.87.205404. (Cited on page 95).

[206] Yusuke Nomura, Shiro Sakai, Massimo Capone, and Ryotaro Arita. Exotic s -wave superconductivity in alkali-doped fullerides. *Journal of Physics: Condensed Matter*, 28(15):153001, 2016. URL http://stacks.iop.org/0953-8984/28/i=15/a=153001. (Cited on pages 98 and 106).

[207] Yujun Deng, Yijun Yu, Yichen Song, Jingzhao Zhang, Nai Zhou Wang, Zeyuan Sun, Yangfan Yi, Yi Zheng Wu, Shiwei Wu, Junyi Zhu, Jing Wang, Xian Hui Chen, and Yuanbo Zhang. Gate-tunable room-temperature ferromagnetism in two-dimensional Fe_3GeTe_2. *Nature*, 563(7729):94–99, 2018. URL https://doi.org/10.1038/s41586-018-0626-9. (Cited on pages 108, 109, and 116).

[208] Zaiyao Fei, Bevin Huang, Paul Malinowski, Wenbo Wang, Tiancheng Song, Joshua Sanchez, Wang Yao, Di Xiao, Xiaoyang Zhu, Andrew F. May, Weida Wu, David H. Cobden, Jiun-Haw Chu, and Xiaodong Xu. Two-dimensional itinerant ferromagnetism in atomically thin Fe_3GeTe_2. *Nature Materials*, 17(9):778–782, 2018. URL https://doi.org/10.1038/s41563-018-0149-7. (Cited on pages 108, 109, and 116).

[209] Hans-Jŕg Deiseroth, Krasimir Aleksandrov, Christof Reiner, Lorenz Kienle, and Reinhard K. Kremer. Fe_3GeTe_2 and Ni_3GeTe_2 ,Äì two new layered transition-metal compounds: Crystal structures, HRTEM investigations, and magnetic and electrical properties. *European Journal of Inorganic Chemistry*, 2006(8):1561–1567, 2006. URL https://onlinelibrary.wiley.com/doi/abs/10.1002/ejic.200501020. (Cited on page 108).

[210] Bin Chen, JinHu Yang, HangDong Wang, Masaki Imai, Hiroto Ohta, Chishiro Michioka, Kazuyoshi Yoshimura, and MingHu Fang. Magnetic properties of layered itinerant electron ferromagnet Fe_3GeTe_2. *Journal of the Physical Society of Japan*, 82(12):124711, 2013. URL https://doi.org/10.7566/JPSJ.82.124711. (Cited on pages).

[211] Jian-Xin Zhu, Marc Janoschek, D. S. Chaves, J. C. Cezar, Tomasz Durakiewicz, Filip Ronning, Yasmine Sassa, Martin Mansson, B. L. Scott, N. Wakeham, Eric D. Bauer, and J. D. Thompson. Electronic correlation and magnetism in the ferromagnetic metal Fe_3GeTe_2. *Phys. Rev. B*, 93:144404, 2016. doi: 10.1103/PhysRevB.93.144404. URL https://link.aps.org/doi/10.1103/PhysRevB.93.144404. (Cited on pages 110 and 112).

[212] Jieyu Yi, Houlong Zhuang, Qiang Zou, Zhiming Wu, Guixin Cao, Siwei Tang, S A Calder, P R C Kent, David Mandrus, and Zheng Gai. Competing antiferromagnetism in a quasi-2D itinerant ferromagnet: Fe_3GeTe_2. *2D Materials*, 4(1):011005, 2017. URL http://stacks.iop.org/2053-1583/4/i=1/a=011005. (Cited on pages).

[213] Yun Zhang, Haiyan Lu, Xiegang Zhu, Shiyong Tan, Wei Feng, Qin Liu, Wen Zhang, Qiuyun Chen, Yi Liu, Xuebing Luo, Donghua Xie, Lizhu Luo, Zhengjun Zhang, and Xinchun Lai. Emergence of Kondo lattice behavior in a van der Waals itinerant ferromagnet, Fe_3GeTe_2. *Science Advances*, 4(1), 2018. URL http://advances.sciencemag.org/content/4/1/eaao6791. (Cited on pages 108 and 110).

[214] N. D. Mermin and H. Wagner. Absence of ferromagnetism or antiferromagnetism in one- or two-dimensional isotropic heisenberg models. *Phys. Rev. Lett.*, 17:1133–1136, 1966. URL https://link.aps.org/doi/10.1103/PhysRevLett.17.1133. (Cited on page 109).

[215] Anna E Böhmer and Andreas Kreisel. Nematicity, magnetism and superconductivity in Fe Se. *Journal of Physics: Condensed Matter*, 30(2):023001,

2017. URL https://iopscience.iop.org/article/10.1088/1361-648X/aa9caa/meta. (Cited on page 110).

[216] Daniel Guterding, Harald O. Jeschke, I. I. Mazin, J. K. Glasbrenner, E. Bascones, and Roser Valentí. Nontrivial role of interlayer cation states in iron-based superconductors. *Phys. Rev. Lett.*, 118:017204, 2017. URL https://link.aps.org/doi/10.1103/PhysRevLett.118.017204. (Cited on page 110).

[217] A. A. Mostofi, J. R. Yates, G. Pizzi, Y.-S. Lee, I. Souza, D. Vanderbilt, and N. Marzari. An updated version of wannier90: A tool for obtaining maximally-localised wannier functions. *Comput. Phys. Commun.*, 185:2309, 2014. doi: 10.1016/j.cpc.2014.05.003. URL http://dx.doi.org/10.1016/j.cpc.2014.05.003. (Cited on pages 125 and 128).

[218] P. Hohenberg and W. Kohn. Inhomogeneous electron gas. *Phys. Rev.*, 136:B864–B871, 1964. doi: 10.1103/PhysRev.136.B864. URL https://link.aps.org/doi/10.1103/PhysRev.136.B864. (Cited on page 125).

[219] W. Kohn and L. J. Sham. Self-consistent equations including exchange and correlation effects. *Phys. Rev.*, 140:A1133–A1138, 1965. doi: 10.1103/PhysRev.140.A1133. URL https://link.aps.org/doi/10.1103/PhysRev.140.A1133. (Cited on page 125).

[220] D. M. Ceperley and B. J. Alder. Ground state of the electron gas by a stochastic method. *Phys. Rev. Lett.*, 45:566–569, 1980. doi: 10.1103/PhysRevLett.45.566. URL https://link.aps.org/doi/10.1103/PhysRevLett.45.566. (Cited on page 126).

[221] John P. Perdew and Yue Wang. Accurate and simple analytic representation of the electron-gas correlation energy. *Phys. Rev. B*, 45:13244–13249, 1992. doi: 10.1103/PhysRevB.45.13244. URL https://link.aps.org/doi/10.1103/PhysRevB.45.13244. (Cited on page 126).

[222] A. D. Becke. Density-functional exchange-energy approximation with correct asymptotic behavior. *Phys. Rev. A*, 38:3098–3100, 1988. doi: 10.1103/PhysRevA.38.3098. URL https://link.aps.org/doi/10.1103/PhysRevA.38.3098. (Cited on page 126).

[223] Gregory H. Wannier. The structure of electronic excitation levels in insulating crystals. *Phys. Rev.*, 52:191–197, 1937. doi: 10.1103/PhysRev.52.191. URL https://link.aps.org/doi/10.1103/PhysRev.52.191. (Cited on page 127).

[224] Nicola Marzari and David Vanderbilt. Maximally localized generalized wannier functions for composite energy bands. *Phys. Rev. B*, 56:12847–12865, 1997. doi: 10.1103/PhysRevB.56.12847. URL https://link.aps.org/doi/10.1103/PhysRevB.56.12847. (Cited on page 128).

[225] Luca de'Medici. *Private communication*. (Cited on page 130).

[226] C. G. Broyden. A class of methods for solving nonlinear simultaneous equations. *Math. Comp.*, 19:577–593, 1965. URL http://www.ams.org/journals/mcom/1965-19-092/S0025-5718-1965-0198670-6/home.html. (Cited on page 139).